INVESTIGATION OF SPATIALLY AND TEMPORALLY VARYING BROADBAND WIRELESS URBAN CHANNELS

BY

S. TOAUTACHONE

Ph.D 2015

THE UNIVERSITY OF PORTSMOUTH
School of Engineering

INVESTIGATION OF SPATIALLY AND TEMPORALLY VARYING BROADBAND WIRELESS URBAN CHANNELS

by

Somboon Toautachone

April 2015

This thesis is submitted in partial fulfilment of the requirements for the award of the degree of Doctor of Philosophy at the University of Portsmouth

To my parents for their unconditional and relentless support, to my supervisor, Dr David L Ndzi, and to all of my friends, I could not have done it without all of you.

Investigation of Spatially and Temporally Varying Broadband Wireless Urban Channels

by

Somboon Toautachone

Abstract

The use of wireless communication systems is rapidly expanding due to its flexibility, mobility and, low installation and maintenance costs. However as the number of services over wireless networks increase, users expect the same quality of service as on wired networks. Compared to wired channels, a wireless channel is influenced by static and mobile objects in its surroundings. A detailed understanding of these influences are required in order to develop adequate models that can be used to support high data rate services, especially in urban environments where network antennas are frequently installed below surrounding object (building and trees) heights.

The research reported in this thesis was carried out to study the impact of mobile objects (vehicle) on wideband channels in urban environment and the signal variations in a picocell. To conduct this study, a wideband channel sounder that transmits a flat spectrum Pseudo-Random Gaussian Noise (PRGN) signal over a bandwidth of 200 MHz at a carrier frequency of 2 GHz was used. The implemented data acquisition strategy enabled channel measurements to be made every 184.32 μs (equivalent to channel sampling rate of 5.4 kHz). This speed is indispensable for studying fast varying channels. A series of controlled experiment were conducted and reported in this thesis to test the capabilities of the channel sounder and to gain an understanding of the impact of passing vehicles on wideband channels. A number of experimental measurements were then carried out to study static and dynamic channels and the results are reported in this thesis. To gain a detailed understanding of the channel variations, an algorithm that can resolve closely spaced multipath components was required. Singular Value Decomposition Prony (SVDP) algorithm has been developed and tested. Test results show that it achieves time delay resolution of up to 1 ns, a factor of 5 better than Fast Fourier Transform (FFT) algorithm.

Analysis of the signal variations with distance shows that none of the proposed path loss model can be used to predict signal variation with distance in picocell environment, for path length up to 30 m. A linear model is found to provide the best prediction and is

proposed for picocell channels. In addition, Rice probability density function is found to provide the best fit to temporal signal variation with increasing standard deviation as the path length increases. The increase in standard deviation is also reflected in the increase of root mean square delay spread and a reduction in channel coherence bandwidth with increasing path length.

Overall, this research has shown that a greater attention needs to be paid to the impact of mobile traffic in urban environments than it was initially thought. Passing vehicles have been shown to cause severe fading within the bandwidth of up to 40 dB but only manifest as between 1 dB and 4 dB fade in the averaged signal power across the bandwidth. This type of fade will introduce error burst in digital communication systems and vary in time and space, especially if either the receiver or object is moving.

In addition to the results mentioned, one of the key contributions of this research is that it shows that a greater attention has to be paid to moving objects in the channel irrespective of their positions relative to the transmitter to receiver path. The sounder used employs technology which allows measurement speeds that have, up until now, not been possible over large bandwidths. Together with SVDP algorithm developed, they present an opportunity for more detailed study to be carried out. This research has also laid the foundation for this to be carried out.

Acknowledgements

I would really like to pay tribute to my supervisor Dr D. L. Ndzi for his help, support and encouragement from the beginning through to the end of my study for this research project. And I would like to say thank you to Dr K. Stuart and Mohamed Samir Al-Jabban for their support and contributions. Many thanks as well to lecturers, technical and administrative staffs in School of Engineering for their contribution and staffs from IS help desk service for all technical supports. Finally I would like to say thank you to all of my friends for your friendship and fun.

DECLARATION

“While registered as a candidate for the above degree, I have not been registered for any other research award. The results and conclusions embodied in this thesis are the work of the named candidate and have not been submitted for any other academic award.”

Table of Contents

List of Figures

List of Tables

List of Abbreviations

ABCs	Absorbing boundary condition
ADC	Analogue to Digital Converter
AIC	Akaike Information Criterion
AOA	Angle-of-Arrival
AR	Autoregressive
ARMA	Autoregressive-Moving Average
AWGN	Additive White Gaussian Noise
AWS	Arbitrary Waveform Synthesiser
BER	Bit Error Ratio
BFWA	Broadband Fixed Wireless Access
BLP	Backward Linear Predictor
BW	Bandwidth
CAT	Criterion Autoregressive Transfer
COST	European Cooperation in the Field of Scientific and Technical Research
CW	Continuous Wave
dB	Decibel
dBm	Decibel relative to a milliwatt
DC	Direct Current
DDMA	Demand-Mode Direct Memory Access
DFT	Discrete Fourier Transform
DRA	Data Ready for Channel A of the AD12400
DRB	Data Ready for Channel B of the AD 12400
DSP	Digital Signal Processing
ECC	Electronic Communication Committee
EFIE	Electric Field Integral Equation
EMC	Electro-Magnetic Compatibility
ERP	Effective Radiated Power
ETSI	European Telecommunications standards Institute
FBLP	Forward-Backward Linear Predictor
FDTD	Finite Difference in Time Domain
FEM	Finite Element Method

FFT	Fast Fourier Transform
FIFO	First-In-First-Out
FLP	Forward Linear Predictor
FPGA	Field Programmable Gate Array
FT	Fourier Transform
FWA	Fixed Wireless Access
GHz	Gigahertz
GO	Geometrical Optic
GTD	Geometrical Theory of Diffraction
HF	High Frequency
HiperLAN	High Performance Local Area Network
HiperMAN	High Performance Radio metropolitan Area Network
Hz	Hertz
IEEE	Institute of Electrical and Electronic Engineers
IF	Intermediate Frequency
ISI	Inter-Symbol Interference
ITU	International Telecommunication Union
JTAG	Joint Test Action Group
kHz	Kilohertz
km	Kilometre
KS	Kolmogorov-Smirnov
LAN	Local Area Network
LMCS	Local Multipoint Communication System
LOS	Line of Sight
LS	Least Square
m	Metre
m/s	Metre per Second
Mb/s	Megabit per second
MDL	Minimum Description Length
MFIE	Magnetic Field Integral Equation
MHz	Megahertz
MIMO	Multiple-Input and Multiple Output
MLSE	Maximum Likelihood Sequence Estimation

MMDS	Multipoint Microwave Distribution System
MOM	Method of Moment
MS/s	Megasamples per second
MTL	Modal Transmission-Line
mW	Milliwatt
NLOS	Non-Line of Sight
OFDM	Orthogonal Frequency-Division Multiplexing
PCI	Peripheral Component Interconnect
PDF	Probability Density Function
PO	Physical Optic
PLL	Phase-Locked-Loop
PMC	Peripheral Component Interconnect Mezzanine Card
PRBS	Pseudo Random Binary Sequence
PRGN	Pseudo Random Gaussian Noise
PROM	Programmable Read only Memory
QoS	Quality of Service
RF	Radio Frequency
RMS	Root Mean Square
RMSE	Root Mean Square Error
RT	Ray Tracing
Rx	receiver
SF	Scatter Function
SHF	Super High Frequency
SINR	Signal-to-Intermodulatio and Noise Ratio
SMS	Short Messaging Service
SNR	Signal-to-Noise Ratio
SSTA	Spread Spectrum Time Averaging
SUI	Stanford University Interim
SVD	Singular Value Decomposition
SVDP	Singular Value Decomposition Prony
TF	Transfer Function
Tx	Transmitter
UHF	Ultra High Frequency

UMTS	Universal Mobile Telecommunication System
UTD	Uniform Theory of Diffraction
VHDL	Very High Speed Integrated Circuit Hardware Description Language
VHF	Very High Frequency
WiMAX	Worldwide Interoperability for Microwave Access
WLAN	Wireless Local Area Network
WSS	Wide-Sense Stationary
WSSUS	Wide-Sense Stationary Uncorrelated Scattering

List of Symbols

$\boldsymbol{A}$	Dominant component
$\boldsymbol{A_{bm}}$	Basic median path loss
$\boldsymbol{A_{fs}}$	Free space attenuation
$\boldsymbol{A_{mu}}$	Median attenuation
$\boldsymbol{B_s}$	Signal bandwidth
$\boldsymbol{b}$	Slope
$\boldsymbol{c}$	Velocity of light
$\boldsymbol{D}$	The greatest distance different between two data
$\boldsymbol{d}$	Distance
$\boldsymbol{d_0}$	Reference distance
$\boldsymbol{d_b}$	Distance between Building
$\boldsymbol{d_g}$	Distance for ground reflected propagation path
$\boldsymbol{d_{LOS}}$	Distance for line-of-sight propagation path
$\boldsymbol{d_{t-r}}$	Transmitter-receiver separation distance
$\boldsymbol{E}$	Electric field
$\boldsymbol{e_{rms}}$	Root-Mean-Square fitting error
$\boldsymbol{F[n]}$	Discrete Fourier transform in frequency domain
$\boldsymbol{f_s}$	Nyquist sampling rate
$\boldsymbol{f_c}$	Carrier frequency
$\boldsymbol{f_d}$	Doppler frequency shift
$\boldsymbol{f[k]}$	Discrete Fourier transform in time domain
$\boldsymbol{G_{mea}}$	Output signal in frequency domain
$\boldsymbol{G_r}$	Receiver antenna gain
$\boldsymbol{G_{ref}^{'}}$	Calibrated output
$\boldsymbol{H}$	Magnetic field
$\boldsymbol{H_{channel}}$	Transfer function of the channel
$\boldsymbol{H_i}$	Forward linear predictor
$\boldsymbol{H_i^*}$	Backward linear predictor
$\boldsymbol{H_R}$	Transfer function of receiver system
$\boldsymbol{H_{Rant}}$	Transfer function of receiver antenna

H_{Rx}	Transfer function of transmitter
H'_{ref}	Reference channel transfer function
H_{ru}	Receiver gain
H_{spu}	Transfer function of data acquisition unit
H_T	Transfer function of transmitter system
H_{Tant}	Transfer function of transmitter antenna
H_{Tx}	Transfer function of transmitter
H_{tu}	Transmitter gain
$\bar{H}$	Estimated transfer function
$H(j\omega)$	Complex transfer function
h_b	Building height
h_c	Critical height of surface protuberances
h_{mobile}	Height of mobile antenna
h_r	Height of receiving antenna
h_{roof}	Height of roof
h_t	Height of transmitting antenna
$h(t)$	Impulse response of system
K	Ratio of direct component power to multipath components power
K_{cf}	Correction factor
L_{50}	The 50^{th} percentile value of path loss
L_{ex}	Excess loss over the free space
L_{FSL}	Free space loss
L_{msd}	Multiple screen diffraction
L_P	Path loss
L_{rts}	Rooftop street loss
N	Number of sampled data
N_a	Number of average
N_g	Number of
N_s	Length of the sequence
P	Poynting's vector
P_N	Total noise
$\overline{P_N}$	Mean noise power level

P_r	Received power
P_s	Total signal power
$\overline{P_s}$	Mean output power
p_i	Power of the ith path
$p(z)$	Predictor polynomial
$R(\Delta f)$	Spaced-frequency correlation function
$R(\Delta t)$	Spaced-time correlation function
$RMSE$	Root Mean Square Error
S	Data matrix
$S(\tau)$	Multipath intensity profile
$S_{N\backslash RWB}$	Noise power spectral density
S_{PRGN}	Input signal
T_{as}	Time to capture one averaged snapshot
T_c	Coherence time
T_{db}	Time to capture one data block
T_{df}	Time to capture one data file
T_m	Maximum excess delay time
T_s	Symbol time
T_{sg}	Time to between snapshot
t	Time
v	Velocity
w	Street width
X_f	Frequency correction factor
X_r	Correction factor of receiver antenna height
$X(\omega)$	Continuous Fourier transform in frequency domain
$x(t)$	Continuous Fourier transform in time domain
Y	Data vector
$\hat{y}$	Estimated/fitted line
$\Gamma(m)$	Gamma function
$\Gamma_{\parallel}$	Fresnel's vertical polarization reflection coefficient
$\Gamma_{\perp}$	Fresnel's horizontal polarization reflection coefficient
Δ	Excess path length

ΔSNR	Signal-to-Noise Ratio Improvement
α	AR coefficient vector
β_0	Intercept
β_1	Slope
γ	Path loss exponent
ε	Permittivity
ε_0	Free space permittivity
ε_r	Relative permittivity
η	Refractive index
θ_i	Angle of incidence
θ_r	Angle of refraction
λ	wavelength
μ	Permeability
μ_0	Free space permeability
μ_r	Relative permeability
π	pi
σ	Standard deviation
σ^2	Variance
σ_d	Root Mean Square delay spread
τ	Delay time
$\langle\tau\rangle$	Average delay
$\langle\tau^2\rangle$	Mean square delay
φ	Street orientation angle
ω	Radian

CHAPTER 1

Background and Introduction

Abstract:

This chapter introduces the problems associated with high data rate transmissions through wireless channels. It outlines the objectives of the research reported in this thesis and provides a summary of the work that has been conducted as part of the project. It concludes with an overview of the layout of the rest of the thesis.

1.1 Introduction

Wireless technology has become the dominant means of communication in the past decade. The growth of wireless communication systems can be attributed to its convenience, flexibility, seamless connectivity and the fact that wireless connectivity can easily be provided in areas where no wired communication infrastructure existed. A report by Microsoft shows that in 2011 there were more than 4 billion mobile phone users of which 1.03 billion were smart-phones [1.1]. Of all the 4 billion mobile phones, 3.05 billion were Short Messaging Service (SMS) enabled. It forecasted that by late 2013 mobile internet users will exceed desktop internet users. The demand on wireless communication systems is both, in terms of connectivity and data rates, over the limited available bandwidth. There has also been an explosion in the number of high data applications (e.g. high definition video) on mobile services. This has led to an urgent need to fully understand communication impairments in order to maximise channel capacity and spectrum usage. In addition, the telecommunication pricing model has shifted from connectivity based model to quality of service (connection speed) thus renewing impetus in channel capacity optimisation research.

Unlike in wired communication where the characteristics of the transmission medium is well known, in wireless systems the channel is subject to both spatial and temporal variations which require dynamic coding and modulation to maintain communication. The complexity arises from the fact that these changes/variations can occur independently or combined, influenced by a wide range of factors. This also depends on whether any or all the parts of the system are moving, objects and people within the environment, whether they are fixed or mobile and the presence of static objects such as

buildings and trees. In almost all cases, the received signal in a wireless system is a combination of multiple replicas (multipaths) of the transmitted signal that have travelled through different paths and experienced different levels of attenuation. The received signal may have Line of Sight (LOS) component and Non-Line of Sight (NLOS) components. In some cases, there may not be a LOS signal.

Multipath propagation results in frequency selective fading and inter-symbol interference (ISI) [1.2][1.3] that introduces an irreducible Bit Error Rate (BER) in digital communication systems [1.4][1.5]. Many techniques such as adaptive equalization, antenna diversity, coding techniques, maximum likelihood sequence estimation (MLSE), spread spectrum techniques and orthogonal frequency-division multiplexing (OFDM) have been developed to mitigate the effects of multipath signals. However, most adaptive techniques are still relatively slow to compensate for changes in a highly dynamic high bit rate wireless communication channel [1.2][1.6] and thus there is a need to gain a better understanding of the channel and to develop models so that suitable mitigation techniques can be implemented. This is particularly important in urban environments where users may be moving and objects, including cars and people, are also moving thereby changing the channel characteristics.

Most wireless communications channel models enable the prediction of path loss over given distances [1.7]-[1.12] taking into account shadowing and fading. However in multipath propagation, each radio signal (multipath component) will travel through a different path and may experience different propagation mechanisms (reflection, diffraction, refraction and scattering) resulting in different amplitudes and phases (time delay). To improve the Quality of Service (QoS), a number of wireless devices use smart antennas incorporating diversity reception as a means of enhancing the signal quality. The associated models describe the dispersion of signal power both in time and angles of arrival [1.13]-[1.20]. Directional information can be used to improve signal quality [1.21][1.22]. The definition of the Broadband Fixed Wireless Access (BFWA) standards in the 2 to 11 GHz frequency band renewed interest and research in site specific channel models using methods such as ray tracing and statistical methods to evaluate and characterise wireless channels [1.23]-[1.27]. Although some work have been done to describe the dynamics of multipath fading, studies to assess channel dynamics for high data rate services at picocell level has not been carried out.

As forecasted in [1.1] wireless communication will become more high data rate driven. Limitations in user capacity and bandwidth can be augmented with picocellular network deployment. However burst errors introduced by localised objects will remain an important QoS influencing factor. The application of technologies such as Multiple-Input and Multiple-Output (MIMO) [1.28]-[1.30] can address some of the communication impairment but at the cost of device complexity, size and power consumption which do not fair well in mobile consumer devices. For fixed devices where size and power consumption is not too important, MIMO technology has becoming an important part. These include devices based on wireless communication standards such as IEEE 802.11n (Wi-Fi) and Worldwide Interoperability for Microwave Access (WiMAX) [1.15][1.31].

1.2 Gaps in Research

Significant research has been conducted into wireless communication channels ranging from transhorizon to indoor picocell channels for both narrow and wideband communications [1.32][1.33]. Often, the channel characteristics are described using parameters such as signal levels, Root Mean Square (RMS) delay spread and coherence bandwidth [1.34][1.35] [1.36]. Signal fading is divided into large-scale used to estimate the averaged received power in large areas, and small-scale fading due to changes in signal amplitudes and phases as a result of small changes in the channel [1.3][1.4][1.37][1.38]. A number of models have been proposed to model large-scale path loss with distance which include the Okumula [1.9], Hata [1.10] and Walfisch-Ikegami [1.26] path loss models. Small-scale signal fading is usually modelled using statistical distributions such as Rayleigh [1.3][1.4] and Rice distributions [1.39]-[1.47]. Most of these models have been sufficient for macrocell channel modelling (cell sizes grater than 2 km) and for comparatively low data rate transmissions. However, due to the increase in demand for wireless communication connectivity and data rates over limited spectrum, the most feasible approach to meet this demand has been to reduce cell sizes such that most base station antennas are at heights comparable to building heights. The increased data rate also means that small changes in the channel which were previously inconsequential now have significant impact on communication QoS.

To study fast changing channels, high speed channel sampling equipment is required. Channel measurement systems, e.g. channel sounders have failed to keep pace with the speed at which communication data rate demands are evolving. Therefore very few

studies have been conducted into fast channel evolution in areas such as urban environment where the movement of people and vehicles may have significant impact on sustainable data rates. Where fast measurement systems have been used, the bandwidth is small offering poor multipath resolution that does not enable detailed evolution of the channel to be observed and hence studied. To develop fade mitigation techniques for future systems, this type of knowledge is required.

1.3 Research Objectives

The main aim of this research project has been to develop the tools to study the impact of spatial and temporal channel variations on high data wireless communication systems in picocell urban environment. The research will have application in both fixed (e.g. WiMAX [1.31][1.48], WIFI and High Performance Radio Metropolitan Area Network-HiperMAN [1.49]) and mobile communication systems as it will enable the influences of off-path objects (e.g. trees, passing vehicle) on communication systems to be studied [1.50]-[1.53]. In this research project therefore, the main objectives included:

1) To investigate a suitable data acquisition (measurement) strategy to study the effects of vehicles on fixed and mobile high data rate wideband channels;
2) To implement a suitable data calibration technique and data processing procedure;
3) To investigate and develop a suitable channel impulse response estimating algorithm and evaluate its performance using simulated and measured data;
4) To investigate and develop a suitable procedure to process large volumes of measured channel data ;
5) To carry out a qualitative and quantitative study of small and large scale fading due to the movement of vehicles in urban environment; and
6) To develop and evaluate a model for spatial and temporal varying picocell urban wireless communication channel.

1.4 Overview of Work Undertaken and Achievements

- The 200 MHz bandwidth wideband channel sounder that employs Spread Spectrum Time Averaging (SSTA) was evaluated and found to be suitable for use to study fast varying channels [1.54]. The channel sounder employs Field

Programmable Gate Arrays (FPGA), is compact in size and light weight making it ideal for channel measurements. It also offers real-time averaging which enables processing gains up to 30 dB to be achieve (1024 averages). This is important in low signal to noise ratio channel measurement conditions. It offers continuous channel measurement speeds of up to 5.43 kHz (channel transfer measurement every 184 μs) which is ideal for studying fast changing channels. The only drawback of the system is the fact that it currently transmits at a centre frequency of 2 GHz and, although the spectrum is designed to discriminate other frequencies, the UMTS transmission in the 1.9 GHz band is still visible in the measured channel transfer function. However, analysis has shown that this is discriminated when the transfer function is processed [1.57].

- To study fast varying channels, a data acquisition strategy that measures 240 channel transfer functions at 184 μs time intervals and then stops for 252 ms to allow the data to be transferred from the data acquisition card onto the computer hard drive was implemented as the optimum strategy. Slower channel measurement speeds can also be implemented for non-fast varying channels.
- Using a Fast Fourier Transform method to compute the channel impulse response, a maximum time delay resolution of 5 ns would be achieved based on the 200 MHz signal bandwidth. However, the author researched and developed a parametric channel estimating algorithm called Singular Value Decomposition Prony (SVDP) that achieves impulse response delay resolution of up to 1ns [1.55][1.56]. This algorithm has been used to process the measured channel transfer functions.
- Large-scale channel variation has been studied and found to be linear rather than follow any of the models that have been reported in open literature. Analyses of small-scale signal variations have shown that signal variations are best described by Rice distributions [1.58][1.59].
- Overall, this research has shown that a vehicle passing parallel to the LOS path has significant impact on the channel. On average fading caused by vehicles vary between 0.5 dB and 5 dB but can be up to 30 dB within the signal bandwidth.

Overall, the objectives of the research as listed in Section 1.3, have been achieved. This research has provided the necessary tools that can be used to investigate a wide range of space-time variant channels that will support current and future wireless systems.

References

[1.1] Microsoft, “Mobile users statistics 2011”, http://www.digitalbuzzblog.com/2011-mobile-statistics-stats-facts-marketing-infographic/, accessed: 28 March 2012

[1.2] Shankar P. M., “Introduction to Wireless Systems”, John Wiley & Sons, Inc., USA, 2002.

[1.3] Sklar B., “Rayleigh Fading Channels in Mobile Digital Communication Systems Part I: Characterisation”, IEEE Communications Magazine, Vol. 35, No. 7, July 1997, pp. 90-100.

[1.4] Sklar B., “Rayleigh Fading Channels in Mobile Digital Communication Systems Part II: Mitigation”, IEEE Communication Magazine, Vol. 35, No. 7, July 1997, pp.102-109.

[1.5] Young Yong Kim, San-qi Li, “ Modeling Multipath Fading Channel Dynamics for Packet Data Performance Analysis”, Wireless Networks, Vol. 6, No. 6, December 2000, pp. 481-492.

[1.6] Shafi M., Hashimoto A., Umehira M., Ogose S., Murase T., “Wireless Communications in the Twenty-First Century: A Perspective”, IEEE Proceedings, Vol. 85, No. 10, October 1997, pp. 1622-1638.

[1.7] Rummler W., Coutts R., Liniger M., “Multipath Fading Channel Models for Microwave Digital Radio”, IEEE Communication Magazine, Vol. 24, No. 11, November 1986, pp. 30-42.

[1.8] Greenstein L. J., Andersen J. B., Bertoni H. L., Kozono S., Michelson D.G., Tranter W. H., “Guest Editorial Channel and Propagation Models for Wireless System Design I”, IEEE Journal on Selected Areas in Communications, Vol. 20, No. 3, April 2002, pp. 493-495.

[1.9] Okumura Y., Ohmori E., Kawano T., Fukuda K., “Field Strength and Its Variability in VHF and UHF Land Mobile Radio Services”, Review of the Electrical Communications Laboratory, Vol. 16, September - October 1968, pp. 825-873.

[1.10] Hata M., “Empirical Formula for Propagation Loss in Land Mobile Radio Services”, IEEE Transactions on Vehicular Technology, Vol. 29, No. 3, March 1980, pp. 317-325.

[1.11] Riback M., Medbo J., Berg J. E., Harrysson F., Asplund H., “Carrier Frequency Effects on Path Loss”, IEEE 63rd Vehicular Technology Conference 2006: VTC 2006-Spring, Vol. 6, 7-10 May 2006, pp. 2717-2721.

[1.12] Erceg V., Greenstein L. J., Tjandra S. Y., Parkoff S. R., Gupta A., Kulic B., Julius A. A., Bianchi R., “An Empirically Based Path Loss Model for Wireless Channels in Suburban Environments”, IEEE Journal on Selected Areas in Communications, Vol. 17, No. 7, July 1999, pp. 1205-1211.

[1.13] Calcev G., Chizhik D., Goransson B., Howard S., Huang H., Kogianthis A., Molisch A. F., Moustakas A. L., Reed D., Xu Hao, “A Wideband Spatial Channel

Model for System-Wide Simulations", IEEE Transactions on Vehicular Technology, Vol. 56, No. 2, March 2007, pp. 389-403.

[1.14] Anderson H. R., "A Ray-Tracing Propagation Model for Digital Broadcast Systems in Urban Areas", IEEE Transactions on Broadcasting, Vol. 39, No. 3, September 1993, pp. 309-317.

[1.15] Milanovic J., Rimac-Drlje S., Bejuk K., "Comparison of Propagation Models Accuracy for WiMAX on 3.5 GHz", IEEE International Conference on Electronics, Circuits and Systems, ICECS 2007 14th, 11-14 December 2007, pp. 111-114.

[1.16] Greenstein L. J., "A Multipath Fading Channel Model for Terrestrial Digital Radio Systems", IEEE Transactions on Communications, Vol. 26, No. 8, August 1978, pp. 1247-1250.

[1.17] Narandzic M., Kyosti P., Meinila J., Hentila L., Alatossava M., Rautiainen T., De Jong Y. L. C., Schneider C., Thoma R. S., "Advances in "WINNER" Wideband MIMO System-Level Channel Modelling", The Second European Conference on Antennas and Propagation, EuCAP 2007, 11-16 November 2007, pp. 1-7.

[1.18] Parsons J. D., Bajwa A. S., "Wideband Characterisation of Fading Mobile Radio Channels", IEE Proceeding Communications, Radar and Signal Processing, Vol. 129, Pt. F, No. 2, April 1982, pp. 95-101.

[1.19] Biglieri E., Proakis J., Shamai S., "Fading Channels: Information-Theoretic and Communications Aspects", IEEE Transaction on Information Theory, Vol. 44, No. 6, October 1998, pp. 2619-2692.

[1.20] Greenstein L. J., Ghassemzadeh S. S., "Comparing Three Models for UWB Indoor Power Delay Profile", 40th Annual Conference on Information Sciences and Systems 2006, 22-24 March 2006, pp.626-631.

[1.21] Samukic A., "UMTS Universal Mobile Telecommunications System: Development of Standards for the Third Generation", IEEE Global Telecommunications Conference 1998: GLOBECOM '98 The Bridge to Global Integration, Vol. 4, No. 4, 8-12 November 1998, pp. 1976-1983.

[1.22] Kruys J., "HIPERLAN, Applications and Requirements", IEEE 3th International Symposium on Personal, Indoor and Mobile Radio Communications 1992 Proceedings: PIMRC '92, 19-21 October 1992, pp. 133-138.

[1.23] Gans M. J., Amitay N., Yeh Y. S., Damen T. C., Valenzuela R. A., Choelhang Cheon, Jeho Lee, "Propagation Measurements for Fixed Wireless Loops (FWL) in a Suburban Region with Foliage and Terrain Blockages", IEEE Transactions on Wireless Communications, Vol. 1, No. 2, April 2002, pp. 302-310.

[1.24] Ahumada L., Feick R., Valenzuela R. A., Morales C., "Measurement and Characterization of the Temporal Behavior of Fixed Wireless Links", IEEE Transactions on Vehicular Technology, Vol. 54, No. 6, November 2005, pp. 1913-1922.

[1.25] Torres R. P., Cobo B., Mavares D., Medina F., Loredo S., Engels M., “Measurement and Statistical Analysis of the Temporal Variations of a Fixed Wireless Link at 3.5 GHz”, Wireless Personal Communications: Springer 2006, Vol. 37, 2006, pp. 41-59.

[1.26] Erceg V., Hari K. V. S., Smith M. S., Baum D. S., Soma P., Greenstein L. J., Michelson D. G., Ghassemzadeh S., Rustako A. J., Roman R. S., Sheikh K. P., Tappenden C., Costa J. M, Bushue C., Sarajedini A., Schwartz R., Branlund D., Kaitz T., Trinkwon D., “Channel Models for Fixed Wireless Applications”, Contribution IEEE 802.16a-03/01, June 2003.

[1.27] Athanasiadou G. E., Nix A. R., McGeehan J. P., “A Microcellular Ray-Tracing Propagation Model and Evaluation of its Narrow-Band and Wide-Band Predictions”, IEEE Journal on Selected Areas in Communications, Vol. 18, No. 3, March 2000, pp. 322-335.

[1.28] Gu X., Peng X-H., Zhang G. C., “MIMO Systems for Broadband Wireless Communications”, BT Technology Journal, Vol. 24, No. 2, April 2006, pp. 90-96.

[1.29] Kafle P. L., Intarapanich A., Sesay A. B., McRory J., Davies R. J., “Spatial Correlation and Capacity Measurements for Wideband MIMO Channels in Indoor Office Environment”, IEEE Transactions on Wireless Communications, Vol. 7, No. 5, May 2008, pp.1560-1571.

[1.30] Xiantao Sun, Cimini L. J., Greenstein L. J., Chan D. S., “ICI/ISI Aware Beamforming for MIMO-OFDM Wireless System”, CISS 2009. 43rd Annual Conference on Information Sciences and Systems 2009, 18-20 March 2009, pp. 103 - 107.

[1.31] Marin J., Bo Li, Pressly W., Westall J., “WiMAX Performance at 4.9 GHz”, IEEE Aerospace Conference 2010, 6-13 March 2010, pp. 1-8.

[1.32] Ndzi, D., Austin, J., Vilar, E., "Wideband transhorizon channel characterization", Radio Science, Vol. 36 , No. 5 , May 2001, pp. 965-981

[1.33] Ndzi D., Savage N., Gremont B., "Spatial and Temporal Variation of Wideband Indoor Channels", International Journal of Antennas and Propagation, Vol. 2010, Article ID 735434, 11 pages, 2010. doi:10.1155/2010/735434

[1.34] Greenstein L. J., Erceg V., Michelson D. G., “Modelling Diversity Reception over Narrowband Fixed Wireless Channels”, Electronics Letters, Vol. 34, No. 11, 28 May 1998, pp. 1146-1147.

[1.35] Proakis J. G., “Digital Communications”, McGraw-Hill, Singapore, 1983.

[1.36] Bultitude R. J. C., Bedal G. K., “Propagation Characteristics on Microcellular Urban Mobile Radio Channels at 910 MHz”, IEEE Journal on Selected Areas in Communications, Vol. 7, No. 1, January 1989, pp. 31-39.

[1.37] Heidari A., Khandani A. K., McAvoy D., “Adaptive Modelling and Long-Range Prediction of Mobile Fading Channels”, IET Communications, Vol. 4, No. 1, January 2010, pp. 39-50.

[1.38] Prabhu G. S., Shankar P. M., “Simulation of Flat Fading Using MATLAB for Classroom Instruction”, IEEE Transactions on Education, Vol. 45, No. 1, February 2002, pp. 19-25.

[1.39] Abdi A., Tepedelenlioglu C., Kavh M., Giannakis G., “On the Estimation of the K Parameter for the Rice Fading Distribution”, IEEE Communications Letters, Vol. 5, No. 3, March 2001, pp. 92-94.

[1.40] Bo-Chieh Liu, Ken-Huang Lin, Ju-Ya Chen, “Ricean K-factor Estimation in Cellular Communications Using Kolmogorov-Smirnov Statistic”, Asia-Pacific Conference on Communications 2006: APCC’06, August 2006, pp. 1-5.

[1.41] Tepedelenlioglu C., Abdi A., Giannakis G. B., “The Ricean K Factor: Estimation and Performance Analysis”, IEEE Transactions on Wireless Communications, Vol. 2, No. 4, July 2003, pp. 799-810.

[1.42] Po-Ying Chen, Hsueh-Jyh Li, “An Iterative Algorithm for Doppler Spread Estimation in LOS Environments”, IEEE Transactions on Wireless Communications, Vol. 5, No. 6, June 2006, pp. 1223-1228.

[1.43] Hewitt A., Vilar E., “Selective Fading on LOS Microwave Links: Classical and Spread-Spectrum Measurement Techniques”, IEEE Transactions on Communications, Vol. 36, No. 7, July 1988, pp. 789-796.

[1.44] Hammoudeh A., Haslett C., “Characterisation and Modelling of Obstructed Line-of-Sight Millimetre Wave Mobile Radio Signals”, 9th International Conference on Antennas and Propagation 1995 (Conf. Publ. No. 407), Vol. 2, 4-7 April 1995, pp. 283-287.

[1.45] Feng Wang, Xia Liu, Bialkowski M. E., “Investigation into SVD Based Beamforming over Rician MIMO Channels”, IEEE 5th International Conference on Wireless Communications, Networking and Mobile Computing 2009: WiCom’09, 24-26 September 2009, pp. 1-4.

[1.46] Rustoko A. J., Amitay N., Owens G. J., Roman R. S., “Radio Propagation at Microwave Frequencies for Line-of-Sight Microcellular Mobile and Personal Communications”, IEEE Transactions on Vehicular Technology, Vol. 40, No. 1, February 1991, pp. 203-210.

[1.47] Liberti J. C., Rappaport T. S., “A Geometrically Based Model for Line-of-Sight Multipath Radio Channels”, IEEE 46th Vehicular Technology Conference 1996 Mobile Technology for the Human Race, Vol. 2, 28 April-1 May 1996, pp. 844-848.

[1.48] Pareit D., Lannoo B., Moerman I., Demeester P., “The History of WiMAX: A Complete Survey of the Evolution in Certification and Standardization for IEEE 802.16 and WiMAX”, IEEE Communications Surveys & Tutorials, Vol. PP, No. 99, pp. 1-29.

[1.49] Vaughan-Nichols S. J., “Achieving Wireless Broadband with WiMax”, Computer, Vol. 37, No. 6, June 2004, pp. 10-13.

[1.50] Mahmoud S. S., Hussain Z. M., O'Shea P. J., "Space-Time Geometrical-Based Channel Models: A Comparative Study", Australian Telecommunications, Networks and Applications Conference, March 2003.

[1.51] Van Rheeden D. R., Gupta S. C., "A Geometric Model for Fading Correlation in Multipath Radio Channels", IEEE International Conference on Communications 1998: ICC 98, Vol. 3, 7-11 June 1998, pp. 1655-1659.

[1.52] Norklit O., Andersen J. B., "Mobile Radio Environments and Adaptive Arrays", IEEE 5th International Symposium on Personal, Indoor and Mobile Radio Communications 1994: Wireless Networks - Catching the Mobile Future, Vol. 2, 18-23 September 1994, pp. 725-728.

[1.53] Petrus P., Reed J. H., Rappaport T. S., "Geometrical-Based Statistical Macrocell Channel Model for Mobile Environments", IEEE Transactions on Communications, Vol. 50, No. 3, March 2002, pp. 495-502.

[1.54] Austin J., Ditmar W. P. A., Lam W. K., Vilar E., Wan K. W., "A Spread Spectrum Communication Channel Sounder", IEEE Transaction on Communications, Vol. COM-45, No. 7, July 1997, pp. 840-847.

[1.55] Lau W. H., Austin J., Hewitt A., Vilar E., Martin L., "Analysis of the Time Variant Structure of Microwave Line-of-Sight Multipath Phenomena", IEEE Transactions on Communications, Vol. 39, No. 6, June 1991, pp. 847-855.

[1.56] Hewitt A., Lau W. H., Austin J., Vilar E., "An Autoregressive Approach to the Identification of Multipath Ray Parameters from Field Measurements", IEEE Transactions on Communications, Vol. 37, No. 11, November 1989, pp. 1136-1143.

[1.57] Ndzi D. L., Stuart K., Toautachone S., Yang Y., Dunn V., "An FPGA-Based Adaptable 200 MHz Bandwidth Channel Sounder for Wireless Communication Channel Characterisation", International Journal of Reconfiguable Computing, Vol. 2011, Article ID 894530, 14 pages, 2011.

[1.58] Ndzi D. L., Stuart K., Toutaouchone S., Vuksanovic B., Sanders D. A., "Wideband sounder for dynamic and static wireless channel characterisation: urban picocell channel model," Progress In Electromagnetics Research, Vol. 113, 285-312, 2011.

[1.59] Toutaouchone S., D. Ndzi, K. Stuart, R. Khusainov, "Spatial and Temporal Variation of Urban Wideband Channels due to Automotive Traffic", International Conference on Electrical, Computer and Communication Engineering (ICECCE-2011), Paris, France, 27-29 July 2011

CHAPTER 2

Signal Propagation Theory and Channel Characterisation

Abstract:

This chapter presents a brief introduction of wireless systems and fundamental theory of electromagnetic wave propagation. The different signal propagation mechanisms are explained. Signal fading experienced by propagating radio waves are presented in detail together with some of the parameters that are widely used to characterise communication channels.

2.1 Introduction

Many research projects in wireless communications have led to the rapid evolution of wireless technologies and systems. Broadband Fixed Wireless Access (BFWA) technology is also gaining in popularity. To support and improve high data rate wireless communication, MIMO technique has been adopted in IEEE 802.11n and WiMAX for public wireless access point. There are many advantages of wireless over wired communication. However, wireless channels suffer from space and time variations.

Temporal variation of the received signal has been studied by Torres et al. [2.1] to investigate the effects of moving vehicles when there is no LOS signal and when LOS signal is blocked intermittently by moving vehicles. The results show that NLOS signals scattering from moving vehicles can be a dominant part of the received signal when the LOS signal is blocked. When vehicles are not blocking the transmitter to receiver path, they still affect the received signal resulting in both fading and enhancements. Results of scattered signals from moving vehicles have been analysed in terms of Doppler shift. They show that when scattered signal components are a dominant part of the received signal, Doppler shift increases. In [2.2] to improve the performance of Local Multipoint Communication System (LMCS) for fixed broadband wireless systems, Naz and Falconer studied the temporal variation of signals in two scenarios: foliage movements due to wind and passing vehicles. Results show that the effects from foliage movements can cause a small range of continuous attenuation whilst the effects from moving vehicles cause intermittent deep fading depending on vehicle size, speed and distance

between the receiving antenna and passing vehicles. The results also show that Rayleigh and Ricean distribution can be used to represent the distribution of measured data from both scenarios. In addition, it was found that narrowband signals undergo fades more rapidly than wideband signals and that Doppler is not an important factor for bit rates greater than 1 Mb/s.

The Fourier Transform (FT) is a traditional method that can be used to transform a signal between the time and frequency domains to examine the impulse response and transfer function. Singular Value Decomposition Prony (SVDP) algorithm [2.3][2.4] has been used in [2.5] to compute the impulse response from the measured channel transfer function to analyse the temporal variations induced by people in indoor wideband channels. The results show that the number of people and their positions within the room can induce both signal enhancement and fading whilst room size can be a significant factor in the channel response. Temporal variations induced by people on indoor radio channels have also been studied by Mainier et al. [2.6] for high data rate broadband applications over wireless LAN. The results show that motion affects the received multipath power and the RMS delay spread. However people moving is not the only thing that has a strong effect on the characteristics of indoor wireless channels but also antenna heights and radiation patterns which can influence channel fading. A spatial-temporal model for multipath propagation channels based on physical propagation processes has been presented by Ming Lu et al. [2.7] for generating a set of spatially distributed reflectors or scatterers which behave as sources of multipath signals arriving at the receiver with a set of delay times and angles-of-arrival. When an antenna array system was used, results show that the number of multipath components largely depends on the measurement bandwidth and receiver sensitivity (threshold). The RMS delay spread of multipath signals increases with the distance separating the transmitter and receiver, and depends on the beamwidth. The application of antenna arrays in wireless cellular systems can improve the quality of systems by combining multiple signal components [2.8]. Moreover, the use of antenna arrays at both transmitter and receiver can help to increase the channel capacity. To analyse, design and model multi-element antenna systems based on the correlation between channel impulse responses caused by the scattering of the signal in the mobile channel, Abdi and Kaveh [2.9] proposed a space-time correlation model. This includes angular spread at the base and mobile station, distance between the base and mobile station, mean directions of the signal

arrivals, array configurations, Doppler spread, angle-of-arrival (AOA) and scattering scenario, including isotropic and non-isotropic scattering model. Ertel et al. [2.10] provided an overview of spatial channel models for antenna arrays that could be used to reduce the effects of channel fading caused by multipath signals from different paths with different amplitudes, phase shifts, time delays, AOAs, and Doppler shift as time-varying parameters.

2.2 Electromagnetic Wave Propagation

Electromagnetic waves are created by the vibration of an electric charge, producing both electric and magnetic fields. The fundamental principle of electromagnetic wave propagation in a homogeneous medium is described by Maxwell's equations [2.11]. Electric field, E, when propagating in a non-conductive medium with zero charge and current density having the permittivity ε and permeability μ can be described by

$$\nabla^2 E = \varepsilon\mu \frac{\partial^2 E}{\partial t^2} \tag{2.1}$$

For magnetic field H an identical equation form can also be obtained. The parameter ε and μ can be expressed by the overall components which include the free space value and the relative value as $\varepsilon_0\varepsilon_r$ and $\mu_0\mu_r$, respectively. A solution given for boundary conditions is for a plane wave propagating through the medium with a velocity v where

$$v = \frac{1}{\sqrt{\varepsilon\mu}} \tag{2.2}$$

And the velocity is relative to free space given by

$$\frac{c}{v} = \sqrt{\frac{\varepsilon\mu}{\varepsilon_0\mu_0}} = \sqrt{\varepsilon_r\mu_r} \tag{2.3}$$

For free space $\mu_r = \varepsilon_r = 1$ then $\mu_0\varepsilon_0 = c^{-2}$, where c is the velocity (speed) of light in a vacuum, 3×10^8 m/s. The relationship between the velocities in free space and medium c/v can be defined as the refractive index η of the medium. At the boundary between two media (substances) with different refractive indices, the direction of propagation of wave energy is governed by Snell's law,

$$\eta_1 \sin\theta_1 = \eta_2 \sin\theta_2 \tag{2.4}$$

where η_1 and η_2 are the refractive indices of medium 1 and 2 respectively, and θ_1 and θ_2 are the angle of incidence and angle of refraction to the normal in the two media. The magnitude and direction of an electromagnetic wave propagating in space is given by Poynting's vector $\boldsymbol{P} = \boldsymbol{E} \times \boldsymbol{H}$. It assumes that at long distances from the source, the curvature of the wavefront is negligible and can be represented with a plane wave and thus, the directional propagation is parallel to the normal of the plane.

2.3 Signal Propagation Mechanisms

The quality of wireless signal is degraded by attenuation and multipath propagation as it travels along the path from the transmitter to the receiver [2.12]-[2.15]. The three basic propagation mechanisms are reflection, diffraction and scattering.

- **Reflection** occurs when propagating electromagnetic waves impinge on smooth surface that is much larger than the signal's wavelength.
- **Diffraction** occurs when travelling radio waves impinge on an edge of an obstacle which results in the bending of the radio waves around the obstacle.
- **Scattering** mechanism occurs when the electromagnetic waves come into contact with objects which are smaller than the signal's wavelength. Normally this mechanism happens when electromagnetic waves travel through a medium such as vegetation.

Figure 2.1 illustrates a scenario where the mechanisms described may prevail. In wireless propagation, LOS signal might be blocked but a number of NLOS signals may still reach the receiver due to multipath propagation. A combination of multipath signal components can result in either enhancement or degradation of the received signal power. Empirical and statistical modelling [2.2][2.16]-[2.18] are widely used to describe the received signal as a function of distance.

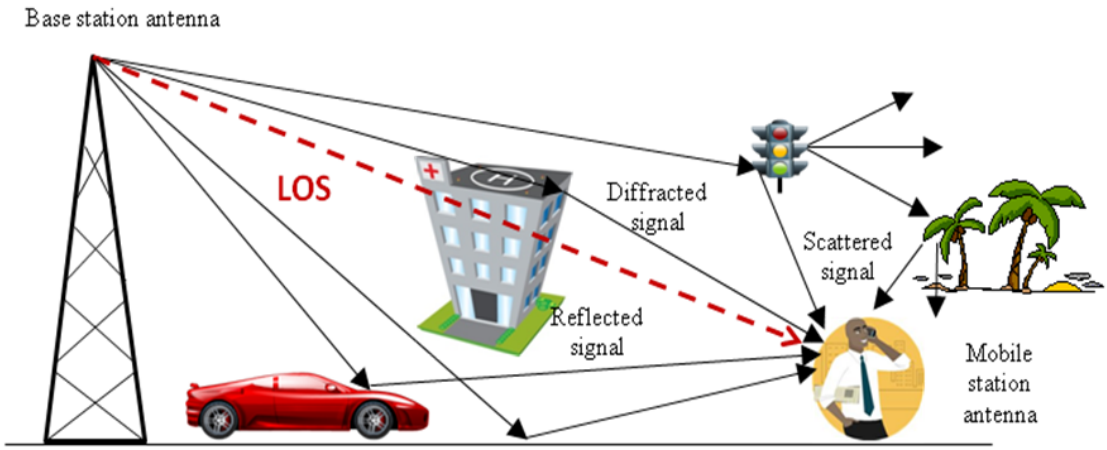

Figure 2.1 Signal propagation mechanisms

2.3.1 Free Space Path Loss

In an ideal case, free space loss refers to signal loss when radio waves propagate in a vacuum. The received signal power from the transmitter antenna to the receiver antenna depends on the distance between the transmitter and receiver, and follows the inverse square law [2.12]. That is, the received signal power, P_r, can be represented as

$$P_r \propto d^{-2} \tag{2.5}$$

where parameter d is the distance, in metres, between the transmitter and the receiver. Normally the received power at distance d, $P_r(d)$, is given by

$$P_r(d) = \frac{P_t G_r G_t \lambda^2}{(4\pi)^2 d^2} \quad , d > 0 \tag{2.6}$$

where parameter P_t is the transmitted power in watts (W), G_r and G_t are the receiver antenna gain and the transmitter antenna gains respectively with distance d in metres (m), and $\lambda = c/f$ is the wavelength in metres (m) with frequency f in hertz (Hz). The velocity of the electromagnetic wave in free space, c, is 3×10^8 m/s and f is the carrier frequency (Hz). The free space loss, L_{free}, in decibel (dB) is given by

$$L_{free}(dB) = 32.44 + 20\log_{10}(f) + 20\log_{10}(d) \tag{2.7}$$

2.3.2 Reflection

Reflection occurs when an electromagnetic wave impinges on the surface of another medium whose surface roughness is small compared to the wavelength of the signal. At the boundary between the two media, part of the wave will be reflected away from the second medium whilst part will pass into the medium. The amplitudes of these two waves can be computed relative to the amplitude of the incident wave using Fresnel's reflection and transmission coefficients based on the electromagnetic properties of the materials [2.19]. For the case where the first medium is free space and $\mu_1 = \mu_2$, the reflection coefficients of two cases for parallel and perpendicular polarization to the plane of incidence can be simplified as,

$$\Gamma_{\parallel} = \frac{-\varepsilon_r \sin\theta_i + \sqrt{\varepsilon_r - \cos^2\theta_i}}{\varepsilon_r \sin\theta_i + \sqrt{\varepsilon_r - \cos^2\theta_i}} \tag{2.8}$$

and

$$\Gamma_{\perp} = \frac{\sin\theta_i - \sqrt{\varepsilon_r - \cos^2\theta_i}}{\sin\theta_i + \sqrt{\varepsilon_r - \cos^2\theta_i}} \tag{2.9}$$

respectively. When the second medium surface is irregular, the specular reflected signal will be further attenuated [2.20]. Most received signals, irrespective of whether there is a LOS or not, include reflected and scattered components. Figure 2.2 shows the plane earth propagation path of two waves travelling from the transmitter to the receiver, where d_{LOS} is the distance for the LOS path, d_g is the distance of the ground reflected path and d_{t-r} is the distance between the transmitter and receiver in metre.

The path lengths of d_{LOS} and $d_g$can be calculated using the following

$$d_{LOS} = \sqrt{d_{t-r}^2 + (h_t - h_r)^2} \tag{2.10}$$

and

$$d_g = \sqrt{d_{t-r}^2 + (h_t + h_r)^2} \tag{2.11}$$

When a signal is transmitted with power, P_t, the received signal power is given by

$$P_r = P_t G_t G_r \left(\frac{h_t h_r}{d_{t-r}^2}\right)^2 \tag{2.12}$$

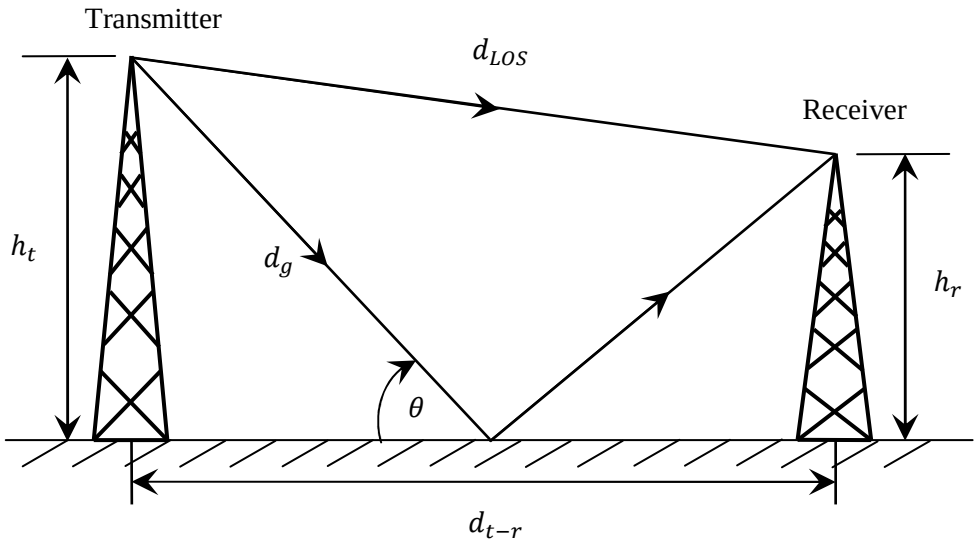

Figure 2.2 Propagation over the plane earth

Equation (2.12) is known as the plane earth propagation equation which is suitable for large-scale propagation modelling. It is different from the free space path loss model in Equation (2.6). The received power is inversely proportional to d_{t-r}^4. The path loss becomes frequency independent (only if the antenna gain remains constant) if the distance between the transmitter and receiver is much greater than the antenna height. For small distance separation such as in microcell environments, Equation (2.13) is used as it will give alternate maxima and minima in the signal strength [2.21] with the assumption of the ground being in the first Fresnel zone that will make it much more useful in microcell path loss models [2.22].

$$P_r = 4P_t \left(\frac{\lambda}{4\pi d_{t-4}}\right)^2 G_t G_r sin^2 \left(\frac{2\pi h_t h_r}{\lambda d_{t-r}^2}\right)^2 \tag{2.13}$$

2.3.3 Diffraction

Diffraction occurs when an electromagnetic wave encounters an edge of an object which has dimension greater than the wavelength of the signal. This results in an apparent bending of the radio waves around the obstacle. Huygens' principle stated that all points of a wavefront can be considered as a point source that can produce secondary wavelets and these wavelets combine to form a new wavefront in the direction of propagation, so

that the magnitude of diffracted energy, as shown in Figure 2.3, in the shadow region is depended on the point of observation and the frequency. Based on the Geometrical Theory of Diffraction (GTD) [2.23][2.26] and the Uniform Theory of Diffraction (UTD) [2.24], diffracted fields can be calculated, whilst the Fresnel-Kirchhoff theory gives the scalar value of the field behind an ideal conducting knife-edge [2.25].

By considering a plane normal to the LOS path at a point between the transmitter and receiver, if on this plane are circles of arbitrary radius expanding out from the middle along the LOS path, and signal propagate to the receiver via any point on these circles as shown in Figure 2.4(a), the complete path from the transmitter will be longer than the LOS path. From Figure 2.4(b), it shows that from the geometry the excess path length denoted as Δ is given by

$$\Delta \simeq \frac{h^2}{2}\left(\frac{d_1 + d_2}{d_1 d_2}\right) \tag{2.14}$$

Assuming that $h \ll d_1, d_2$. Thus the phase difference between the LOS path and the diffracted path is given by

$$\phi = \frac{2\pi\Delta}{\lambda} \tag{2.15}$$

Normally it is written in terms of a parameter v, as

$$v = h\sqrt{\frac{2(d_1 + d_2)}{\lambda d_1 d_2}} \tag{2.16}$$

then

$$\phi = \frac{\pi}{2}v^2 \tag{2.17}$$

This is known as the Fresnel-Kirchhoff diffraction parameter. However in the case of high data rate wireless communications systems in urban environments typical obstacles are not perfect knife-edge and are more likely to result in more losses than the knife-edge equation predicts.

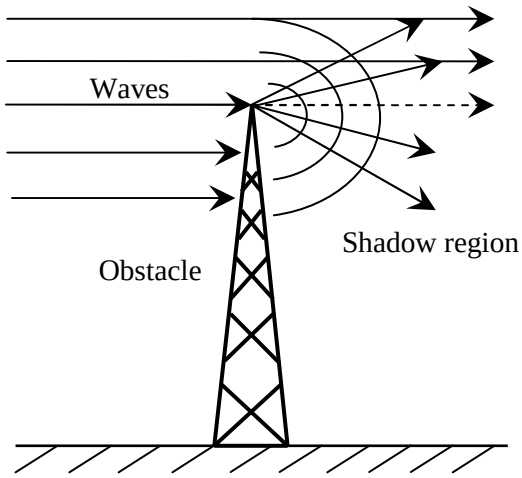

Figure 2.3 Diffraction at the edge of an obstacle

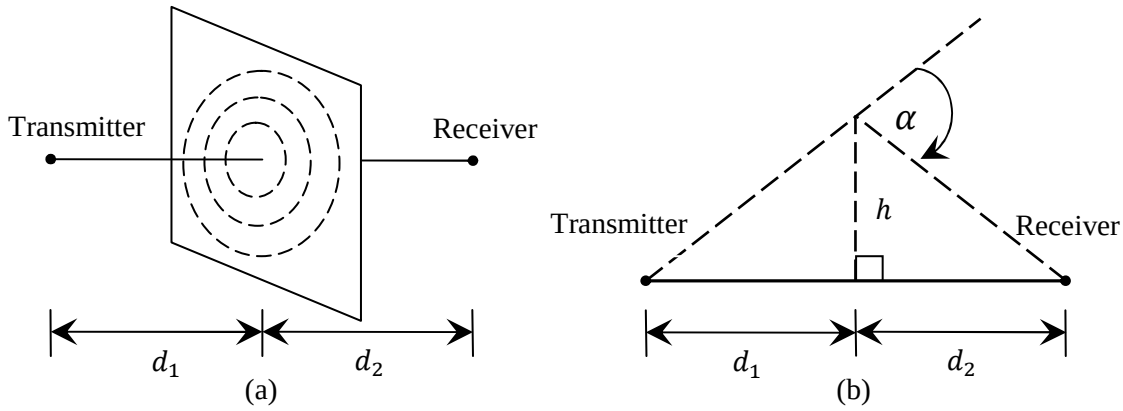

Figure 2.4 (a) Family of circles defining the limits of the Fresnel zones at a given point on the radio propagation path, (b) The geometry of knife-edge diffraction

2.3.4 Scattering

Scattering happens when travelling electromagnetic waves impinge on an object with dimension smaller than its wavelength and also having irregular surface roughness. In urban wireless communications channels, examples of objects that can cause scattering effects include trees and lampposts. Sometime scattering components can be negligible however if there are a large number of scattered signals, they may significantly influence the fluctuation of the received signal. In addition, scattering can also occur if the electromagnetic wave impinges on objects with irregular surface that is smaller than the wavelength of electromagnetic wave. Rayleigh criterion is widely used to determine when a surface can be defined as electromagnetically rough [2.27]. This is used to define the critical height of surface protuberances, h_c, for a given angle of incidence given by

$$h_c = \frac{\lambda}{8 \sin \theta_i} \tag{2.18}$$

An object will be considered smooth if its protuberance height is less than h_c. If the protuberance height is greater than h_c the surface will be considered rough.

2.3.5 Fresnel Zone

The Fresnel zone can be specified by drawing a family of circles between the transmitter and receiver for which the total path length from the transmitter to the receiver of each circle is longer than the LOS path by $n\lambda/2$, where n is an integer. The innermost circle would represent the case for which $n = 1$. Thus the excess path length is $\lambda/2$ whilst the other circles are $\lambda, 3\lambda/2$, and so on. The loci of the points for the excess path length define a number of ellipsoids as shown in Figure 2.5.

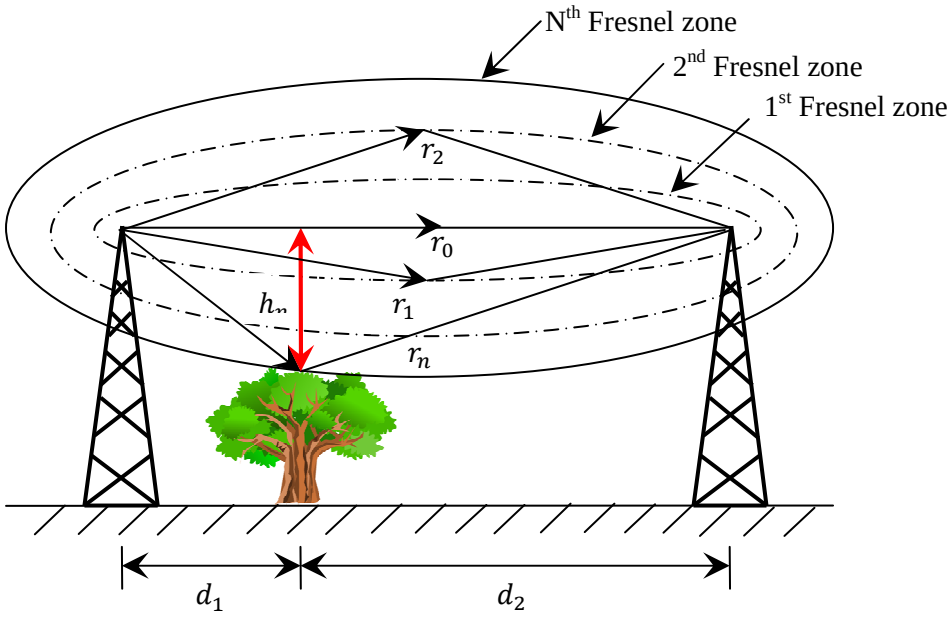

Figure 2.5 Fresnel zone

The radius of each specific ellipsoid can be expressed by

$$h_n = \sqrt{\frac{n\lambda d_1 d_2}{d_1 d_2}} = \sqrt{n\lambda} \tag{2.19}$$

It is clear that the radii of the Fresnel zone ellipsoids depend on the operating frequency, the distance and the order of the Fresnel zone.

2.4 Channel Fading

In wireless communications, the frequency band covering 3 - 30 MHz (high frequency) is widely used for ionospheric communications, whilst 300 MHz - 3 GHz (ultra high frequency) and 3-30 GHz (super high frequency) bands are for tropospheric communications. Idealistic wireless channel models consider only Additive White Gaussian Noise (AWGN) which does not exist in practice. Wireless channels are characterised by external interference signals and are also influenced by multipath signals. Internal interference due to thermal noise might be ignored when compared to the effects caused by the external interference signals. Multipath signals manifest as frequency selective fading causing Inter-Symbol Interference (ISI). A wireless channel is called as space-time variant channel if its characteristics change in time and space (distance) that may cause different number of multipath signals to arrive at the receiver. At the receiver, the received signal is a superposition of multiple copies of the transmitted signal that has travelled through different paths and experienced different attenuation levels, delays and phase shifts. The result of these multiple copies can be either constructive or destructive.

The free space path loss model can be used to estimate the received signal power as a function of distance. It assumes the channel to be free of all objects that might absorb or reflect radio frequency (RF) energy.

However, most practical channels experience fading [2.28]. In this case, the free space path loss model is inadequate to describe the channel and predict system performance. Therefore the channel's propagation characteristics need to be scrutinised. Fading manifestations can be represented as shown in Figure 2.6 [2.28][2.29]. Fading can be described as large-scale fading, small-scale fading, frequency selective fading, flat fading, and also fast fading and slow fading as classified in Figure 2.6.

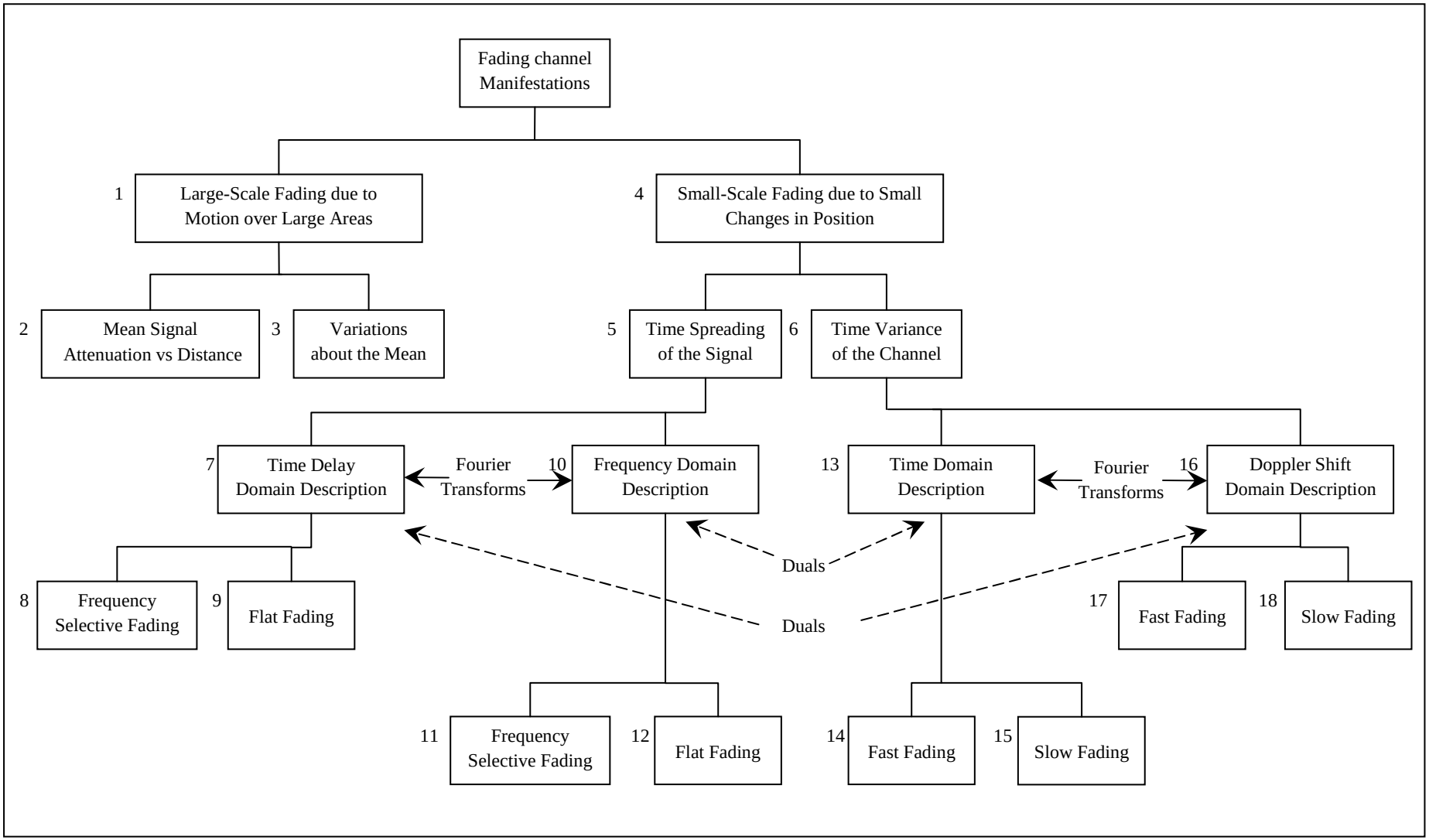

Figure 2.6 Fading channel characterisation

2.4.1 Large-Scale Fading and Small-Scale Fading

Figure 2.6 represents a classification of channel fading. Based on the distance between the transmitter and receiver, there are two types of fading: large-scale fading and small-scale fading [2.28]-[2.30].

Large-scale fading is used to represent the variations of the mean amplitude or mean power of the received signals as a function of distance between the transmitter and receiver over large areas as shown in blocks 1, 2 and 3. The mean power is considered to be constant within a particular interval of time or space. This interval is considered to be around a few tens of wavelength [2.31] when considering outdoor mobile radio channels. Large-scale fading can be affected by hills, forests and buildings located between the transmitter and receiver. The LOS signal path might be partially or completely blocked causing large-scale fading or shadowing effect.

Small-scale fading is used to represent a small and rapid variation of signal amplitudes when the receiver is considered to have moved only a short distance or changes over a short time period. Small-scale fading is often superimposed on large scale fading. Overall small-scale fading [2.28] can be referred to as changes in signal amplitude and phase as a result of small changes. Small-scale fading is often called Rayleigh fading especially when LOS signal is obstructed. The envelope of the received signal is statistically represented by Rayleigh Probability Density Function (PDF). In the presence of LOS path, signal components arriving at the receiver can often be described by Rician PDF.

Small-scale fading is categorised into two groups according to time spreading of the signal (or signal dispersion) and time variance of the channel as shown in blocks 4, 5 and 6 in Figure 2.6. Channel characteristics are usually represented in time and frequency domain as indicated in blocks 7, 10, 13 and 16. Fourier transform shows the relationship between two domains. Signal degradation due to fading can be categorised as frequency selective fading and frequency non-selective fading (flat fading) as shown in blocks 8, 9, 11 and 12.

2.4.2 Frequency Selective Fading and Flat Fading Channel

Due to the dispersive nature of the channel, fluctuation of the received signal power is not the only effect of multipath propagation. Fading may also affect the shape of the pulse after it is transmitted through the channel [2.32]-[2.34]. Bello [2.35] proposed the

notion of Wide-Sense Stationary Uncorrelated Scattering (WSSUS) in 1963 as a simple way to model the fading phenomenon. Functions of multipath-intensity profile, spaced-frequency correlation function, spaced-time correlation function and Doppler power spectrum of the channel response, as shown in Figure 2.7, make up this model [2.35][2.41]. They have been used to describe the relationship between time and frequency of fading channels.

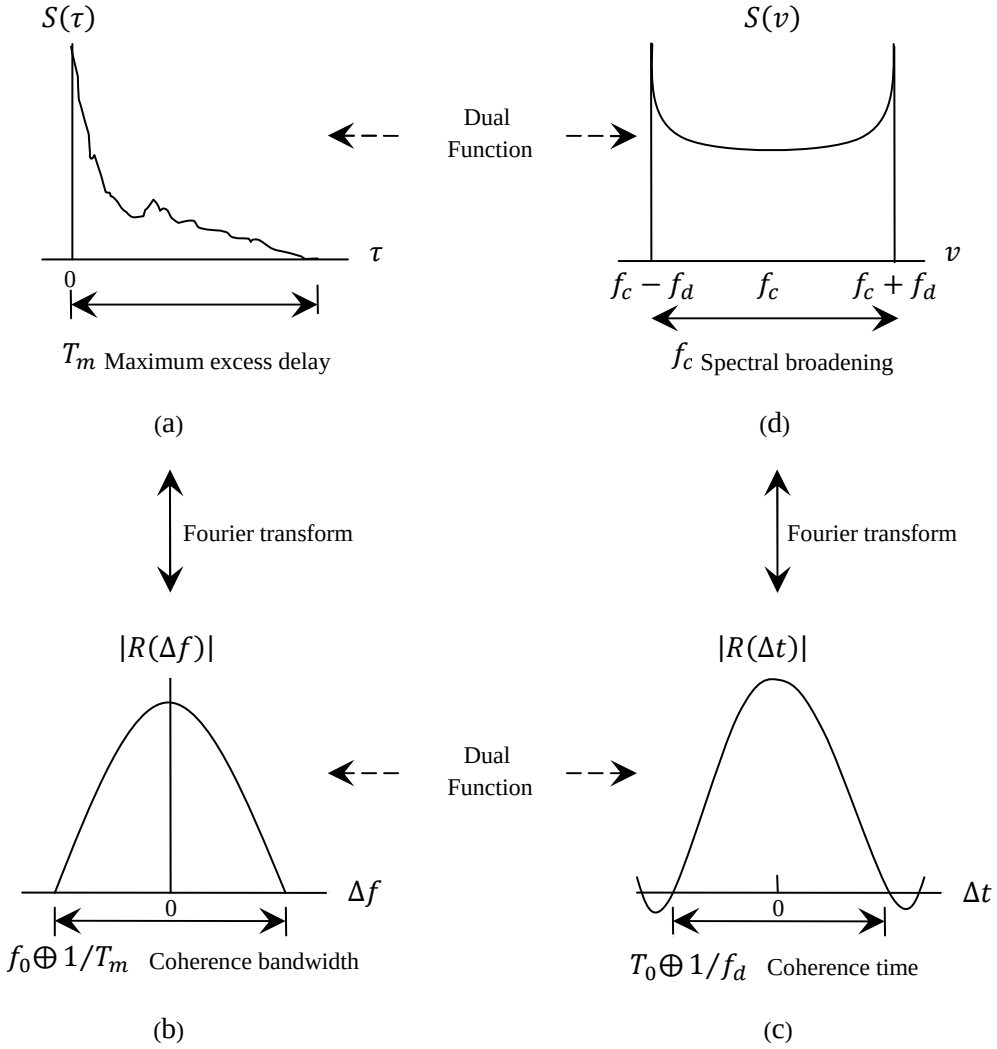

Figure 2.7 Relationships between channel correlation functions and power density functions (a) multipath intensity profile, (b) spaced-frequency correlation function, (c) spaced-time correlation function, and (d) Doppler power spectrum

Considering the time-delay domain for a fading channel, in Figure 2.7(a) a multipath-intensity profile, $S(\tau)$ versus time delay τ is plotted. The term, maximum excess delay time, T_m, has been used to refer to the maximum excess delay between the first and last received component due to a single transmitted impulse. The relationship between the maximum excess delay time, T_m, and symbol time, T_s, can be used to determine whether

the channel is frequency selective or frequency non-selective (flat fading) as indicated in blocks 8 and 9 in Figure 2.6. When $T_m > T_s$ it indicates that the received multipath components of a symbol extend beyond the symbol's time duration and the channel will experience frequency-selective fading. These multipath signals are represented as multiple copies of the transmitted signal when these pulses arrive and combine to produce a broadened pulse that can cause ISI. On the other hand, the channel is said to experience frequency non-selective fading or flat fading when $T_m < T_s$ meaning that all multipath components are received within the symbol time duration.

In the frequency domain, a spaced-frequency correlation function $R(\Delta f)$ which, is the Fourier transform of a multipath intensity profile $S(\tau)$, represents the correlation between the channel responses. It is a function of the frequency difference, $\Delta f = (f_1 - f_2)$ between two signals [2.28][2.41]. In Figure 2.7(b), function $|R(\Delta f)|$ is plotted to represent an absolute value of a spaced-frequency correlation function. The parameter, coherence bandwidth, f_0 has been defined as a statistical measure of the range of frequencies over which the channel can pass all spectral components with approximately equal gain and linear phase. The coherence bandwidth is often expressed as being inversely proportional to the maximum excess delay time, T_m, given by

$$f_0 \propto \frac{1}{T_m} \quad . \tag{2.20}$$

However the maximum excess delay time T_m is not the best indicator because different channels can have the same value of T_m but exhibit very different profiles of signal intensity over the delay time span. A more useful parameter is the Root-Mean-Squared (RMS) delay spread σ_d which represents the average time taken by pulses (multipath signals) due to dispersive behaviour of the channel to arrive at the receiver. The time difference between multipath signals depend on the scenarios; small in rural area and diverse in urban area due to the influence of high buildings and other objects within the environment [2.12][2.36][2.37]. To calculate the RMS delay spread, σ_d, the average delay $\langle\tau\rangle$ is first computed using the following equation,

$$\langle\tau\rangle = \sum_{i=1}^{N} p_i \tau_i \Big/ \sum_{i=1}^{N} p_i \tag{2.21}$$

where p_i is the power of the i^{th} component (path), and τ_i is its time delay. The RMS delay spread σ_d is given by,

$$\sigma_d = \sqrt{\langle \tau^2 \rangle - \langle \tau \rangle^2} \tag{2.22}$$

If σ_d is very high, that channel is expected to have considerable pulses broadening. From the property of σ_d, therefore, it is possible to define the lowpass bandwidth of the channel and the coherence bandwidth can be approximately defined as,

$$f_0 \approx \frac{1}{5\sigma_d} \tag{2.23}$$

This is a more popular approximation of f_0 presenting the case that coherence bandwidth is defined as the frequency interval over which the channel transfer function has a correlation of at least 0.5 [2.38] instead of at least 0.9 of which the coherence bandwidth becomes approximately [2.39]-[2.42],

$$f_0 \approx \frac{1}{50\sigma_d} \tag{2.24}$$

Where the symbol rate, $1/T_s$, is taken to be equal to the signal bandwidth B_s. When the coherence bandwidth f_0 is larger than the signal bandwidth B_s, all of the frequency components will arrive at the receiver nearly within the same time with negligible distortion. In contrast, if the signal bandwidth B_s is much larger than the coherence bandwidth the frequency components of the signal will be disperse resulting in pulse broadening.

2.4.3 Slow Fading and Fast Fading Channel

The effects of signal dispersion have been explained in the previous section, however the effects of time varying channel caused by relative motion of the transmitter and receiver, and/or the movement of objects within the channel is different. A radio channel is considered to be time variant when its characteristics changes over time irrespective of whether the transmitter or receiver or both are moving. Figure 2.7(c) shows the function $R(\Delta t)$ which is designated as the spaced-time correlation function. This function is the autocorrelation function of the channel's response to a sinusoid and it is used to specify the extent to which there is correlation between the channel's response to a sinusoid sent

at time t_1 and the channel's response to a similar sinusoid sent at time t_2, where $\Delta t = t_2 - t_1$. A measure of the expected time duration over which the channel's response is considerably invariant is called the coherence time T_c [2.28].

The concept of duality is used to explain when the behaviour of one function (or system) in the time domain (time or time delay) can be used to infer the behaviour of another function in the frequency domain (frequency or Doppler shift) as shown in Figure 2.6 between blocks 7 and 16 as well as between blocks 10 and 13. As such, functions $R(\Delta f)$ and $R(\Delta t)$ in Figure 2.7(b) and (c) can be used to characterise signal dispersion in the frequency domain and fading rate in the time domain, respectively.

In the time domain, as shown in Figure 2.6 block 13, the degradation of signals in a time variant channel can be categorised into two groups: fast fading and slow fading. Fast fading is used to describe channels in which $T_0 < T_s$, where T_0 is the coherence time and T_s is the symbol time. This can cause synchronisation problems (failure of phase-locked-loop receivers). A channel is described as slow fading when $T_0 > T_s$, which means that the channel remains unchanged during the symbol transmission period.

In the Doppler shift domain, Figure 2.6 block 16, characterisation of the time variant channel can be represented in terms of the Doppler shift (frequency domain). A Doppler power spectral density $S(v)$, Figure 2.7(d), is plotted as a function of Doppler frequency shift v. According to the case of the dense-scatterer model, a vertical receive antenna with a constant azimuthal gain, a uniform distribution of signals arrival throughout the range $(0,2\pi)$ at an isotropic antenna, and an un-modulated Continuous Wave (CW) signal, the signal spectrum at the antenna terminals is given by [2.43]

$$S(v) = \frac{1}{\pi f_d \sqrt{1 - \left(\frac{v}{f_d}\right)^2}} \tag{2.25}$$

In Figure 2.7(d) the sharpness and steepness of the Doppler spectrum boundaries are due to the upper limit on the Doppler shift that are observed. The largest magnitude of Doppler power spectral density $S(v)$ will occur when the scatterer is directly ahead or behind of the moving antenna platform.

The Doppler frequency shift, f_d, is given by,

$$f_d = \frac{v}{\lambda} \tag{2.26}$$

where v is the speed of a mobile unit travelling (m/s) and λ is the wavelength of the electromagnetic wave.

Slow and fast fading can be expressed in term of the coherence time T_c of the channel [2.44], which is given by,

$$T_c \approx \frac{9}{16\pi f_d} \tag{2.27}$$

If the pulse duration of the signal is smaller than T_c (having large message bandwidth) the pulse will not experience any distortion. However if it is larger than the coherence time, it will experience fast fading and be distorted. Fast fading is therefore a frequency dispersive property of the channel.

Figure 2.8 shows the overall effects of small-scale fading such as ISI, loss in SNR, Doppler shift, Phase-Locked-Loop (PLL) and BER that might occur when signals propagate through the channel.

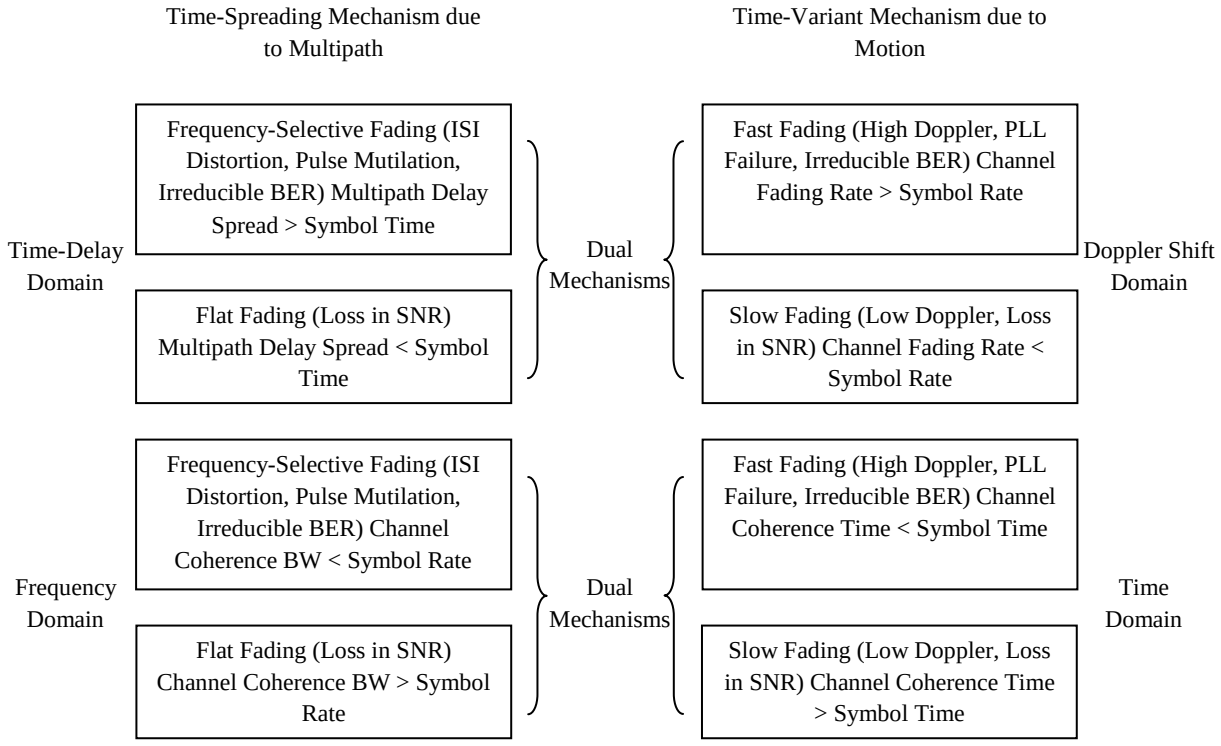

Figure 2.8 Classification of small-scale fading: mechanisms and effects

2.5 Summary

Electromagnetic wave propagation principles have been discussed in this chapter. The phenomena of radio wave propagation, namely scattering, refraction, diffraction and reflection have been presented. Radio signal fading due to the propagation media are introduced together with how fading affects the signal and the parameters that are used to quantify them. Chapter 3 will introduce the channel models that have been developed and proposed in open literature for a range of wireless communication systems.

References

[2.1] Torres R. P., Cobo, B., Mavares, D., et al., “Measurement and Statistical Analysis of the Temporal Variations of a Fixed Wireless Link at 3.5 GHz”, Wireless Personal Communications: Springer 2006, Vol. 37, 2006, pp. 41-59.

[2.2] Naz N., Falconer, D. D., “Temporal Variations Characterization for Fixed Wireless at 29.5 GHz”, IEEE 51st, Vehicular Technology Conference Proceeding, Tokyo, Vol. 3, August 2002, pp. 2178 - 2182.

[2.3] Lau W. H., Austin, J., Hewitt, A., et al., “Analysis of the Time Variant Structure of Microwave Line-of-Sight Multipath Phenomena”, IEEE Transactions on Communications, Vol. 39, No. 6, June 1991, pp. 847-855.

[2.4] Hewitt A., Lau, W. H., Austin, J., Vilar, E., “An Autoregressive Approach to the Identification of Multipath Ray Parameters from Field Measurements”, IEEE Transactions on Communications, Vol. 37, No. 11, November 1989, pp. 1136-1143.

[2.5] Ndzi D. L, Savage, N., Gremont, B., “ Spatial and Temporal Variation of Wideband Indoor Channels”, International Journal of Antennas and Propagation, Vol. 2010, Article ID 735434, 11 pages, 2010.

[2.6] Marinier P., Delisle, G. Y., Despins, C. L., “Temporal Variations of the Wideband Indoor Wireless Millimetre-Wave Channel”, IEEE Transactions on Antennas and Propagation, Vol. 46, No. 6, June 1998, pp. 928-934.

[2.7] Ming Lu, Lo, T., Litya, J., “A Physical Spatio-Temporal Model of Multipath Propagation Channels”, IEEE 47th Vehicular Technology Conference 1997, Vol. 2, 4-7 May1997, pp. 810-814.

[2.8] Winters J. H., “Smart Antennas for Wireless Systems”, IEEE Personal Communications, Vol. 5, No. 1, February 1998, pp. 23-27.

[2.9] Abdi A., Kaveh, M., “Space-Time Correlation Modeling of Multielement Antenna Systems in Mobile Fading Channels”, IEEE International Conference on Acoustics, Speech, and Signal Processing 2001 Proceedings: ICASSP’01, Vol. 4, 7-11 May 2001, pp. 2505-2508.

[2.10] Ertel R. B., Cardieri, P., Sowerby, K. W., et al., “Overview of Spatial Channel Models for Antenna Array Communication Systems”, IEEE Personal Communications, Vol. 5, No. 1, February 1998, pp. 10-22.

[2.11] Lorrain P., Corson D. R., “Electromagnetic Fields and Waves”, W. H. Freeman San Francisco, USA, 1970.

[2.12] Shankar P. M., “Introduction to Wireless Systems”, John Wiley & Sons, Inc., USA, 2002.

[2.13] IEEE Vehicular Technology Society Committee on Radio Propagation., “Coverage Prediction for mobile Radio Systems Operating in The 800/900 MHz Frequency Range”, IEEE Transactions on Vehicular Technology, Vol. 37, No. 1, February 1988, pp. 3 - 44.

[2.14] Delisle G. Y., Lefevre, J., Lecours, M., Chouinard, J., “Propagation Loss Prediction: A Comparative Study with Application to Mobile Radio Channles”,

IEEE Transactions on Vehicular Technology, Vol. VT-34, No. 2, May 1985, pp. 86 - 96.

[2.15] Cheung K., Sau, J. H. M., Murch, R. D., "A New Empirical Model for Indoor Propagation Prediction", IEEE Transactions on Vehicular Technology, Vol. 47, No. 3, August 1998, pp. 996 - 1001.

[2.16] Bultitude R.J.C., "Measurement, Characterization and Modeling of Indoor 800/900 MHz Radio Channels for Digital Communications", IEEE Communication Magazine, Vol. 25, No. 6, June 1987, pp. 5 - 12.

[2.17] Gans M. J., Amitay, N., Yeh, Y. S., et al., "Propagation Measurements for Fixed Wireless Loops (FWL) in A Suburban Region with Foliage and Terrain Blockages", IEEE Transactions on Wireless Communications, Vol. 1, No. 2, April 2002, pp. 302 - 310.

[2.18] Gilbert E. N., "Energy Reception for Mobile Radio", Bell Syst. Tech. J., Vol. 44, October 1965, pp. 1779 - 1803.

[2.19] Jackson J. D., "Classical Electrodynamics", Wiley, New York, USA, 1998.

[2.20] Ament W. S., "Toward a Theory of Reflection by a Rough Surface", IRE Proceedings, Vol. 41, No. 1, January 1953, pp. 142-146.

[2.21] Parsons J. D., "The Mobile Radio Propagation Channel", John Wiley & Sons Ltd., Chichester, U.K., 2000.

[2.22] Feuerstein M. J., Blackard K. L., Rappaport T. S., Seidel S. Y., Xia H. H., "Path Loss Delay Spread, and Outage Models as Functions of Antenna Height for Microcellular System Design", IEEE Transaction on Vehicular Technology, Vol. VT-43, No. 3, August 1994, pp. 487-498.

[2.23] Keller J. B., "Geometrical Theory of Diffraction", Journal of the Optical Society of America, Vol. 52, No. 2, February 1962, pp. 116-130.

[2.24] Kouyoumjian R. G., Pathak P. H., "A Uniform Theory of Diffraction for an Edge in Perfectly Conducting Surface", IEEE Proceedings, Vol. 62, No. 11, November 1974, pp. 1448-1461.

[2.25] Mokhtari H., Lazaritis P., "Comparative Study of Lateral Profile Knife-Edge Diffraction and Ray Tracing Technique Using GTD in Urban Environment", IEEE Transactions on Vehicular Technology, Vol. VT-48, No. 2, March 1999, pp. 589-592.

[2.26] Luebbers R., "Finite Conductivity Uniform GTD versus Knife Edge Diffraction in Prediction of Propagation Path Loss", IEEE Transactions on Antennas and Propagation, Vol. 32, No. 1, January 1984, pp. 70-76.

[2.27] Rappaport T. S., "Wireless Communications: Principles and Practice", Prentice Hall, New Jersey, USA, 2002.

[2.28] Sklar B., "Rayleigh Fading Channels in Mobile Digital Communication Systems Part I: Characterisation", IEEE Communications Magazine, Vol. 35, No. 7, July 1997, pp. 90-100.

[2.29] Sklar B., "Rayleigh Fading Channels in Mobile Digital Communication Systems Part II: Mitigation", IEEE Communication Magazine, Vol. 35, No. 7, July 1997, pp.102 - 109.

[2.30] Smulders P., Jevrosimovic, M., Herben, M., Savov, S., Martijn, E., “Deliverable D2.1: State of the Art Channel Models”, Broadband Radio@Hand B4 Public, June 2002, pp. 1 - 46.

[2.31] Parsons J. D., Bajwa, A. S., “Wideband Characterisation of Fading Mobile Radio Channels”, IEE Proceedings on Communications, Radar and Signal Processing, Vol. 129, No. 2, Part F, April 1982, pp. 95 - 101.

[2.32] Cox D., “Delay Doppler Characteristics of Multipath Propagation at 910 MHz in a Suburban Mobile Radio Environment”, IEEE Transactions on Antennas and Propagation, Vol. 20, No. 5, September 1972, pp. 625 - 635.

[2.33] Cox D., Leck, R., “Correlation Bandwidth and Delay Spread Multipath Propagation Statistics for 910-MHz Urban Mobile Radio Channels”, IEEE Transactions on Communications, Vol. 23, No. 11, November 1975, pp. 1271 - 1280.

[2.34] Hashemi H., “Simulation of the Urban Radio Propagation Channel”, IEEE Transaction on Vehicular Technology, Vol. 28, No. 2, August 1979, pp. 213 - 225.

[2.35] Bello P., “Characterization of Randomly Time-Variant Linear Channels”, IEEE Transactions on Communications Systems, Vol. 11, No. 4, December 1963, pp. 360 - 393.

[2.36] Akaiwa Y., “Introduction to Digital Mobile Communication”, John Wiley & Sons, New York, 1998.

[2.37] Hashemi H., Tholl, D., Morrison, G., “Statistical Modeling of the Indoor Radio Propagation Channel. I”, IEEE Vehicular Technology Conference 42nd, Vol. 1, May 1992, pp. 338-342.

[2.38] Rappaport T. S., “Wireless Communications”, Prentice Hall, NJ USA, 1996.

[2.39] Lee W. Y. C., “Mobile Cellular Communications, McGraw-Hill, New York USA, 1983.

[2.40] Rummler W., Coutts, R., Liniger, M., “Multipath Fading Channel Models for Microwave Digital Radio”, IEEE Communication Magazine, Vol. 24, No. 11, November 1986, pp. 30 - 42.

[2.41] Proakis J. G., “Digital Communications”, McGraw-Hill, Inc., Singapore, 1983.

[2.42] Biglieri E., Proakis, J., Shamai, S., “Fading Channels: Information-Theoretic and Communications Aspects”, IEEE Transactions on Information Theory, Vol. 44, No. 6, October 1998, pp. 2619-2692.

[2.43] Clarke R. H., “A Statistical Theory of Mobile Radio Reception”, Bell Sys. Tech. J., Vol. 47, No. 6, July - August 1968, pp. 957 - 1000.

[2.44] Stein S., “Fading Channel Issues in System Engineering”, IEEE Journal on Selected Areas in Communications, Vol. 5, No. 2, February 1987, pp. 68 - 89.

CHAPTER 3

Propagation Channel Modelling

Abstract:

This chapter presents channel modelling techniques that are in use. It also presents detailed literature review of channel models that have been developed for path loss prediction in urban environment. A list of channel models is also described.

3.1 Introduction

In wireless communication, radio wave propagation models are mathematical expressions that can be used to describe the behaviour of electromagnetic waves through the channel (where they may interact with objects like vehicles, buildings, foliages and also people in the environment) to the receiving antenna [3.1]. A number of mathematical expressions have been proposed as models. These can be categorised into deterministic, statistical and empirical, and combined statistical and deterministic models. Most techniques that are used relate to the approximations of Maxwell's equations, especially the ray tracing technique [3.2]-[3.7]. The main disadvantage of ray tracing technique is its requirement for details of actual environment which makes it computationally expensive and slow. For this reason, statistical and empirical models have gain wider acceptance in many areas of wireless channel analyses [3.8]. Propagation models that are designed to describe specific environments are less amenable or appropriate for generalisation. Accurate channel models are useful and essential to estimate the received signal in order to assess the performances of communication system so as to develop fade mitigation techniques.

3.2 Conventional Channel Modelling Approaches

Conventional modelling approaches that are used to model radio channels are based on deterministic and stochastic techniques [3.2]. Stochastic techniques have gained wide spread popularity because of the random nature of many wireless channels. In general stochastic approach has been used extensively in developing wireless cellular network systems [3.9]-[3.12].

In combined statistical and deterministic modelling approach, it is often assumed that large objects within the environment are known but their positions and movements may vary within certain defined limits. From these details, the dominant rays can be modelled using the deterministic approach whilst the rests of the multipath signals that have lower power amplitudes are modelled using the stochastic approach.

3.2.1 Deterministic Modelling

Ray tracing is a dominant deterministic technique which is used to model the radio channel by tracking each ray from the transmitting antenna to the receiving antenna. For this approach, detailed knowledge of the environment is extremely important as it is required to determine magnitudes, phases and time delays of each ray that reaches the receiver. Electromagnetic wave theory, Maxwell's equation, and propagation mechanisms (reflection, diffraction, refraction and scattering) are used to describe the phenomena that affect the ray in-flight. Deterministic techniques have often been used in indoor applications. In outdoor environment, its complexity expands several times over leading to large scale approximation to reduce computational time.

Deterministic models are suitable for cases where high accuracy is required, such as in radio network planning. Normally this type of modelling will be used as a benchmark that others can be compared against. For deterministic modelling to be a viable option, there are two major challenges that need to be overcome: firstly a substantial computing power is required and; secondly detailed knowledge of the physical environment is needed [3.13]. Deterministic modelling can be divided into two groups [3.1] the first one is full wave methods that are suitable for low frequency and resonant frequency applications whilst the other one is the asymptotic methods that are suitable for high frequency applications. The full wave methods are subdivided into three subgroups: integral equations, differential equations, and series representations. Whilst in the second group the dominant methods are physical optics and UTD method.

3.2.1.1 Electric Field and Magnetic Field Integral Methods

Integral equations are suitable for describing wave propagation through an inhomogeneous media where the wave can be embedded into infinite homogeneous medium. Normally the equivalent theorem is used to replace the areas and surfaces with the problems of unknown equivalent electric and magnetic current distribution.

Generally, these two equations can be marked as a couple however in some special cases, for example, in perfect conductors they can be decoupled or separated into the electric field integral equation (EFIE) and magnetic field integral equation (MFIE). After getting an appropriate discretisation of the integration area, the matrix equations can be used to represent these integral equations. This results in dense matrices, the main disadvantage of this method. The Method of Moments (MOM) is the most common numerical procedure that is used to solve the integral equations. To improve the efficiency of this method, many techniques can be used such as the impedance matrix localisation method which replaces the impedance matrix with a sparser N-diagonal matrix [3.14] or a sparser triangular form [3.15].

3.2.1.2 Finite Element and Finite Difference Methods

Another deterministic technique is differential equations. There are many different methods the first one is finite difference method, the second one is finite element method and the third one is parabolic equation method. For the finite difference method, this method also discretizes the computational domain, followed by the calculation of the fields at each lattice according to the restrictions of the governing equations, Maxwell's equations or alternatively the wave equations. The most popular method version is the Finite Difference in Time Domain (FDTD), which is suitable for wideband applications. The main drawback of the method is that due to the boundary conditions, it may give the correct results for normal incident waves but not for grazing incident waves. The Finite Element Method (FEM) is similar to the previous one but it offers more flexibility within the partition of the space for general inhomogeneous problems. The last method, the parabolic equation, is an estimation of the hyperbolic wave equation. This method has no restrictions of the step-size in the horizontal direction compared to the finite difference method and thus the step-size can be expanded significantly to reduce computational time. However this method suffers from wide angle scattering problem.

3.2.1.3 Series Representations Method

Series representations method is used in many electromagnetic problems that have simple geometries with normal boundaries that allow the use of characteristic modes like waveguide problems. Floquet space-harmonics can be employed to handle series expansion of the fields in different regions. An example of the application of this method has been used to solve an EMC problem [3.16].

3.2.1.4 Physical Optics and Geometrical Optics Method

Unlike the methods described above, the asymptotic method is suitable for high frequency applications. It can also be separated into two main groups; physical optics and geometrical optics. The Physical Optics (PO) method is related to the parabolic equation method provided the field distribution is known in the aperture plane. It offers an opportunity to compute the far-field distance using a double integration procedure. For a number of cases this integral can be solved analytically, however for most cases it must be computed numerically. Geometrical Optics (GO) method is another popular high-frequency technique which has been used to replaces waves with rays. It is relies on three types of rays; direct, reflected and refracted rays. The observation is a superposition of the fields which are associated with all of these rays. However within the shadow area the observed field cannot be described using only these three kinds of rays. Diffracted rays must also be taken into account Geometrical Theory of Diffraction (GTD). This technique usually have problems in the shadow boundaries, however in such transition regions, this can be solved using Uniform Theory of Diffraction (UTD) which improves its performances.

3.2.1.5 Deterministic Modelling Applications

This section provides some beneficial applications of deterministic modelling approaches that can be used to investigate and analyse the propagation channels. According to the based methods, including of full wave methods and asymptotic methods, the brief applications of deterministic modelling approaches can be used for modelling both indoor and outdoor signal propagation.

Ray tracing known as masterpiece method of deterministic modelling can be used to approximate the behaviour of electromagnetic waves as a fairly accurate prediction tool for indoor environments [3.17]. Studies based on ray tracing techniques show that it is a reliable prediction method that can be used to determine the average received power and delay spread.

Overall, ray tracing algorithms can be classified into two general types; imaging method and the ray launching method. For the imaging method, geometric optics from a combination of transmission positions, receiving positions and reflecting surfaces are used to derive the propagation path. On the other hand, for the ray launching method, the propagation path is derived using rays that are discretely launched and traced to the

received position. The propagation characteristics that are estimated when using ray tracing generally require three parameters; propagation distance, incident angle of rays, and complex permittivity of the surfaces. The first two parameters can be derived from ray tracing estimation results whilst the last is a predetermined static parameter that depends on the material. Ray tracing accuracy can be increased by increasing the number of reflections, diffractions, or penetrations when using the imaging method. For the ray launching method, greater accuracy can be achieved by increasing the number of rays. Both schemes increase the computation time of the algorithms. Ray tracing technique has been extensively used in radio propagation models such as for MIMO systems [3.18] to estimate channel characteristics correctly.

3.2.2 Statistical and Empirical Channel Modelling

Due to the complication of deterministic modelling approaches by which the detailed knowledge of environmental geometry and wave theory are indispensable, most propagation channel models in open literature are based on experimental studies. The measured data captured from the measurement systems are statistically analysed on the basis of mathematics. Channel models such as Okumura model, Hata model, and COST231 Walfisch-Ikegami model have been accepted as benchmarks and used to compare with other propagation models. Although some of these models have been designed to estimate path loss of radio channels for far field communications, in this thesis these models will be used to analyse the radio channels performances in the urban area affected by passing vehicles.

3.2.2.1 Okumura Model

The Okumura model is a radio propagation model developed from experimental studies of signal propagations in Tokyo city which was widely accepted as a benchmark and is often used to assess other models. It is an empirical prediction model which can provide the median attenuation relative to free space path loss model. The use of the Okumura model [3.19] to analyse radio propagation channels requires parameters such as the frequency, mobile station antenna height, base station antenna height and link distance. It is applicable for frequencies from 150 MHz to 1920 MHz, mobile station antenna heights between 1 m and 10 m, base station antenna heights between 30 m and 1000 m and link distances between 1 km and 100 km. The Okumura model is given by Equation (3.1).

$$L_{50}(dB) = L_{free} + A_{mu} + H_{tu} + H_{ru} + K_{cf} \quad (3.1)$$

Where $L_{50}(dB)$ is the 50th percentile (i.e. median) value of path loss in decibel (dB), L_{free} is free space path loss in decibel (dB), A_{mu} is median attenuation in decibel (dB), H_{tu} and H_{ru} are transmitter and receiver antenna gains and K_{cf} is a correction factor for the type of environment. For an urban area over quasi-smooth terrain with a transmitter effective antenna height of 200 m and a receiver antenna height of 3 m, extensive measurements curves were developed for vertical omni-directional antennas at both the transmitter and receiver antennas. The curves are plotted as a function of frequency in the range 100 MHz to 1920 MHz and also as a function of distance from 1 km to 100 km. To use the model to determine path loss,

- first the free space path loss between the points of interest is determined; and
- the value of $A_{mu}(f, d)$ shown in term of frequency and distance is added along side its correction factor based on the type of environment e.g. urban, suburban and rural areas, and over irregular terrain which can be added or subtracted as appropriate.

The Okumura model is based on measured data and does not give any analytical explanation. Thus the derived curves, in many situations, can be extended outside the measurement range based on the circumstances and profile of the curve. Figure 3.1 shows the graphs of the attenuation and correction factor proposed by Okumura.

The Okumura model has been widely used for system planning to assess signal power fading in modern terrestrial mobile radio systems for urban areas. Based on its effective distance which is from 1 km to 1000 km and its frequency range which is from 100 MHz to 1920 MHz, the model is not suitable for assessing urban high data rate wireless channel such as WLAN hotspot.

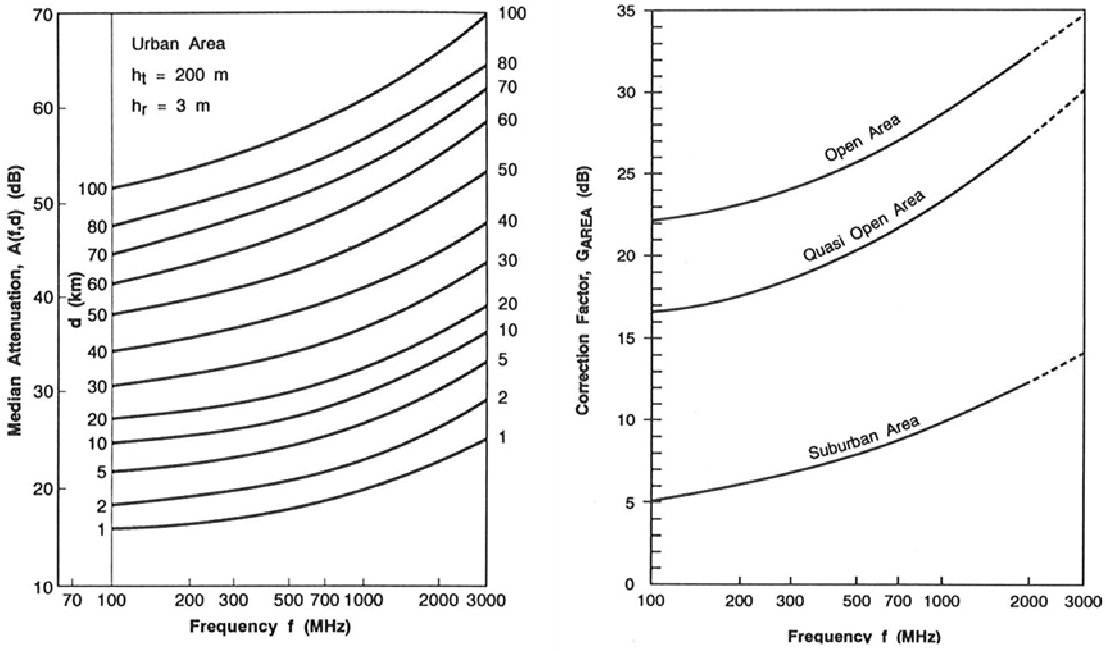

Figure 3.1 Graphs of median attenuation and correction factor proposed by Okumura

3.2.2.2 Hata Model

Another one of the most widely used models for predicting propagation signal path loss is Hata model [3.20]. It is also a well-known empirical model based on the graphical path loss data derived from the Okumura's report in [3.19] that was developed to make the Okumura propagation prediction method easier for practical computational use. To use the Okumura's prediction method for system planning, it is necessary to select the curves according to the frequency, transmitter and receiver antenna heights. It was cumbersome and awkward to use the curves which represented 1 kW effective radiated power (ERP) per dipole, and therefore it was necessary to convert the transmit power into a parameter that can be varied for system planning.

The Hata model is also known as the Okumura-Hata model because it was a modification of the Okumura model. It makes provisions for 3 scenarios: urban, suburban, and open areas. This model is valid for a frequency range from 150 MHz to 1500 MHz. In this model, the propagation path loss can be calculated by standard formulas and correction factors are prepared for different environments. The formula for median propagation path loss in urban areas is given by,

$$L_{P_{50}}(\text{dB}) = 69.55 + 26.16\log_{10} f_c - 13.82\log_{10} h_t - a(h_r) + (44.9 - 6.55\log_{10} h_t)\log_{10} d_{t-r} \quad (3.2)$$

where f_c is the frequency in MHz from 150 MHz to 1500 MHz, h_t is the transmitter antenna height ranging from 30 m to 200 m, h_r is the receiver antenna height ranging from 1 m to 10 m, and d_{t-r} represents the transmitter to receiver separation distance in kilometres between 1 km and 20 km. The correction factor $a(h_r)$ for effective mobile antenna depends on the size of city. The correction factors for small to medium and large cities are given by Equation (3.3) and (3.4) respectively.

$$a(h_r) = (1.1 \log_{10} f_c - 0.7)h_r - (1.56 \log_{10} f_c - 0.8) \tag{3.3}$$

$$a(h_r) = \begin{cases} 8.29(\log_{10} 1.54\, h_r)^2 - 1.1 & ;if\ \ 150 \le f_c \le 200\ MHz \\ 3.2\ (\log_{10} 11.75\, h_r)^2 - 4.97 & ;if\ 200 < f_c \le 1500\ MHz \end{cases} \tag{3.4}$$

The formula for median path loss in suburban areas is given by,

$$L_{PS}(dB) = L_P\{Urban\ area\} - 2\{\log_{10}(f_c/28)\}^2 - 5.4 \tag{3.5}$$

and the formula for median path loss in open areas is given by,

$$L_{PO}(dB) = L_P\{Urban\ area\} - 4.78(\log_{10} f_c)^2 + 18.33 \log_{10} f_c - 40.94 \tag{3.6}$$

The correction factor of the Hata model in Equation (3.3) would be applicable for wireless communication of WLAN hotspot access point but the cell size designed is started from 1 km according to the commencement of the Okumura model. That is larger than WLAN hotspot coverage area which often has a range around 300 m or less depending on the location. Because of the Hata model which was designed and upgraded from the Okumura model, it is viewed to have enhanced the practical application of the Okumura model. Comparisons have been made and presented in [3.21] and [3.22] which show that the Okumura model can provide better accuracy even though it is a more complex model to use due to the requirement of attenuation and correction factor graphs to compensate the error influenced by the model.

3.2.2.3 COST231 – Hata Model

The Hata model [3.20] and the classical Okumura model [3.19] have limitations in terms of frequency range (150 MHz to 1500 MHz), transmitter and receiver antenna heights, and path length which is longer than that of most wireless systems. Therefore, they are not suitable for WLAN and cellular networks which operate in the range of frequency between 1800 MHz and 2.5 GHz. COST231-Hata model [3.23] is applicable for urban

areas. It can also be used to evaluate path loss in suburban or rural quasi-open/open areas. The COST231 - Hata model was initiated as an extension of Hata model by the European COST231 programme with the expansion of the Okumura curves in the upper frequency range. This model, the COST231 - Hata model, is designed for use in the frequency range of 1500 MHz to 2 GHz. The availability of the correction factors for urban, suburban and rural areas has resulted in the COST231–Hata model been widely used for path loss prediction [3.24]-[3.26]. Its basic path loss equation is given by,

$$L_p(dB) = 46.3 + 33.9\log_{10} f_c - 13.82\log_{10} h_t - a(h_r) + (44.9 - 6.55\log_{10} h_t)\log_{10} d_{t-r} + c_m \quad (3.7)$$

where f_c is the frequency in MHz from 1500 MHz to 2000 MHz and the parameters h_t, h_r, d_{t-r} and $a(h_r)$ are the transmitter antenna height in metres, the receiver antenna height in metres, the transmitter to receiver separation distance in kilometres and the correction factor similar to that of the Hata model. The parameter c_m has different values based on the different environment defined as 0 dB for suburban areas and 3 dB for urban areas. This model has a limited frequency range because it was developed for mobile cellular network planning. In addition the model was developed for environments where the transmitter antenna is mounted at rooftop level. As such its application is limited.

3.2.2.4 Stanford University Interim (SUI) Model

The IEEE 802.16 standards for broadband wireless access for the frequency band below 11 GHz adopted the channel model developed by Stanford University, called the SUI models [3.26]-[3.28]. The SUI model has been developed from the extension of the Hata model for frequencies greater than 1900 MHz with the correction factors that extend the model up to 3.5 GHz. In the United States of America, this model is also defined for Multipoint Microwave Distribution System (MMDS) which uses the frequency band between 2.5 GHz and 2.7 GHz [3.26]. The antenna height of the transmitter station of SUI model is from 10 m to 80 m whilst the receiver antenna height is from 2 m to 10 m for cell size radii from 0.1 km to 8 km [3.28]. Three types of environments have been proposed in this model; terrain A, B and C. Terrain A represents a hilly area with moderate or very dense vegetation. Terrain B represents a hilly terrain having rare vegetation or flat terrains scenarios with moderate or heavy tree densities. And the last

one, terrain C is flat terrain or rural areas having light vegetation. From these three scenarios, the results of path loss can be specified based on the type of scenarios.

The SUI model with its correction factors is given by [3.26][3.27],

$$PL = A + 10\gamma \log_{10}(d/d_0) + X_f + X_r + s \quad for\ d > d_0 \tag{3.8}$$

where A is defined as

$$A = 20 \log_{10}(4\pi d_0/\lambda) \tag{3.9}$$

and the path loss exponent γ is given by

$$\gamma = a - bh_t + (c/h_t) \tag{3.10}$$

Table 3.1 The parameter values of SUI model for different terrain

Model Parameter	Terrain Type A	Terrain Type B	Terrain Type C
a	4.6	4.0	3.6
$b(m^{-1})$	0.0075	0.0065	0.005
$c(m)$	12.6	17.1	20

The parameter d is the distance between the transmitter and receiver antenna in metre (m), d_0 is reference distance at 100 m, λ is wavelength, X_f is the correction factor for frequency over 2 GHz in MHz, X_r is the correction factor for receiver antenna height, s is correction factor for shadowing in dB. The random variables are computed using a statistical procedure for path loss exponent, γ, and weak fading standard deviation s between 8.2 dB and 10.6 dB. The constant a, b, and c depend on the types of terrain that are given in Table 3.1.

The value of parameter γ is 2 for an urban area assuming free space propagation, $3 < \gamma < 5$ in an urban area for NLOS propagation, and $\gamma > 5$ for indoor environment [3.28]. The frequency correction factor X_f and the correction factor of the receiver antenna height X_r, are given by,

$$X_f = 6.0 \log_{10}(f/2000) \tag{3.11}$$

and

$$X_r = \begin{cases} -10.8\log_{10}(h_r/2000) & for\ terrain\ type\ A\ and\ B \\ -20.0\log_{10}(h_r/2000) & for\ \ terrain\ type\ C \end{cases} \quad (3.12)$$

where parameter f is the frequency in MHz and $h_r$is the receiver antenna height in metre. Given the above correction factors, the SUI model is extensively used for predicting path loss in rural, urban and suburban environments.

3.2.2.5 Hata-Okumura Extended Model (ECC-33 Path Loss Model)

Due to differences in the characteristics of dense urban environments, and in comparison with European cities, the medium city Okumura model has been recommended for European cities [3.29][3.30]. The Okumura, the Hata and the COST231 Hata model have been extensively used to model mobile receiver systems with omni-directional antennas at heights that are less than 3 m above ground level. It assumes that the users are mainly static relative to the transmitter or are moving at low speed when connected to the wireless network in urban areas. This assumption makes the model not to be directly applicable in mobile fast varying high data supporting channel. A model that can overcome some of these problems has been developed by extrapolating the original Okumura model. Whilst the original Okumura model did not provided for frequencies greater than 3 GHz, an extrapolated method has been applied to it enable the model to be used for frequencies greater than 3 GHz. For Fixed Wireless Access (FWA) system the Okumura model has been modified to create the ECC-33 model [3.31] given by

$$L_p(dB) = A_{fs} + A_{bm} - G_t - G_r \quad (3.13)$$

where parameters A_{fs}, A_{bm}, G_t and G_r are the free space attenuation in dB, the basic median path loss in dB, the transmitter height gain factor and the receiver height gain factor respectively. These factors can be separately described and represented by,

$$A_{fs} = 92.4 + 20\log_{10} d_{t-r} + 20\log_{10} f_c \quad (3.14)$$

$$A_{bm} = 20.41 + 9.83\log_{10} d_{t-r} + 7.894\log_{10} f_c + 9.56(\log_{10} f_c)^2 \quad (3.15)$$

$$G_t = \log_{10}(h_t/200)\{13.958 + 5.8(\log_{10} d_{t-r})^2\} \quad (3.16)$$

and for medium cities G_r is given by,

$$G_r = [42.57 + 13.7\log_{10} f_c][\log_{10} h_r - 0.585] \quad (3.17)$$

For large cities

$$G_r = 0.759h_r - 1.862 \tag{3.18}$$

where f_c is the frequency in GHz, d_{t-r} is the distance between transmitter and receiver in km, h_t is the transmitter antenna height in metres and h_r is the receiver antenna height in metres. It is important to note that predictions using the ECC-33 model do not follow a straight line when plotted against distance in a log-scale like the other models. The medium city model is appropriate for European cities but the large city model should be used in cities consisting of tall buildings.

3.2.2.6 COST231 Walfisch-Ikegami Model

The COST231 Walfisch-Ikegami model [3.27] is an empirical model which is a combination of the Walfisch-Bertroni method [3.32] and Ikegami model [3.34]. This model was enhanced by the COST231 project to improve path loss estimation by considering data for the height of buildings in the vertical plane between the transmitter and the receiver, street widths, building separation and street orientation with respect to the LOS path. The model has been distinguished for 2 cases depending on whether there is a LOS path or not. This model is valid for frequencies from 800 MHz to 2000 MHz, transmitter heights from 4 m to 50 m, receiver heights from 1 m to 3 m and transmitter-receiver separation distance between 20 m to 5 km. For LOS condition the model is expressed as

$$L_P(dB) = 42.6 + 26\log_{10} d_{t-r} + 20\log_{10} f_c \tag{3.19}$$

where d_{t-r} is the distance between transmitter and receiver antenna in metres and f_c is frequency in GHz. For NLOS condition the model is given by

$$L_P(dB) = \begin{cases} L_{FSL} + L_{rts} + L_{msd} & for\ urban\ and\ suburban \\ L_{FS} & if\ L_{rts} + L_{msd} > 0 \end{cases} \tag{3.20}$$

The NLOS equation is more complex because it is a summation of the free space loss L_{FSL}, multiple screen diffraction loss L_{msd} and the rooftop to street loss L_{rts}. The free space loss L_{FSL} is given by,

$$L_{FSL} = 32.45 + 20\log_{10} d_{t-r} + 20\log_{10} f_c \tag{3.21}$$

where the rooftop to street diffraction loss L_{rts}, originally from the Ikegami model and extended by COST231 project, determines the loss which occurs when the wave couples into the street where the mobile receiver is located. This is given by,

$$L_{rts} = \begin{cases} -16.9 - 10\log_{10} w + 10\log_{10} f_c + 20\log_{10} \Delta h_{mobile} \\ \qquad + L_{ori} & for\ h_{roof} > h_{mobile} \\ 0 & for\ L_{rts} < 0 \end{cases} \tag{3.22}$$

where w is the street width in metres and parameter L_{ori} is given by,

$$L_{ori} = \begin{cases} -10 + 0.354\varphi & for\ 0 \le \varphi < 35 \\ 2.5 + 0.075(\varphi - 35) & for\ 35 \le \varphi \le 55 \\ 4 - 0.114(\varphi - 55) & for\ 55 \le \varphi \le 90 \end{cases} \tag{3.23}$$

where φ is street orientation angle with respect to the direct signal path, $\Delta h_{mobile} = h_{roof} - h_{mobile}$ and $\Delta h_{base} = h_{base} - h_{roof}$.

An approximation for the multi-screen diffraction loss L_{msd} in [3.32] and modified by COST231 for employing with base antenna height below rooftop level is given by,

$$L_{msd} = \begin{cases} L_{bsh} + k_a + k_d \log_{10} d_{t-r} + k_f \log_{10} f_c - 9\log_{10} f_c \\ \qquad -9\log_{10} B & for\ L_{msd} > 0 \\ 0 & for\ L_{msd} < 0 \end{cases} \tag{3.24}$$

where B is building to building distance in metres whilst L_{bsh} is given by,

$$L_{bsh} = \begin{cases} -18\log_{10}(1 + \Delta h_{base}) & for\ h_{base} > h_{roof} \\ 0 & for\ h_{base} \le h_{roof} \end{cases} \tag{3.25}$$

where k_a is given by,

$$k_a = \begin{cases} 54 & for\ h_{base} > h_{roof} \\ 54 - 0.8\Delta h_{base} & for\ d \ge 0.5km\ and\ h_{base} \le h_{roof} \\ 54 - 0.8\Delta h_{base}\left(\dfrac{d_{t-r}}{0.5}\right) & for\ d < 0.5km\ and\ h_{base} \le h_{roof} \end{cases} \tag{3.26}$$

and $k_d$is given by,

$$k_d = \begin{cases} 18 & for\ h_{base} > h_{roof} \\ 18 - 15\left(\dfrac{\Delta h_{base}}{h_{roof}}\right) & for\ h_{base} \le h_{roof} \end{cases} \tag{3.27}$$

k_f is given by,

$$k_f = \begin{cases} -4 + 0.7\left(\frac{f_c}{925} - 1\right) & for\ suburban\ or\ medium\ size\ cities \\ & with\ moderate\ tree\ density \\ -4 + 1.5\left(\frac{f_c}{925} - 1\right) & for\ metropolitan/urban \end{cases} \quad (3.28)$$

The parameters k_d and k_f control the dependence of the multiscreen diffraction loss versus the distance and frequency whilst the parameter k_a shows the increase of the path loss for base stations below the rooftop.

For fixed wireless access networks like WLAN where the wireless access point is installed at heights of around 3m and mobile devices at about 1-1.5 m above the ground, the COST231 Walfisch-Ikegami model for LOS condition is seemingly more appropriate to estimate the path loss of signal.

3.2.2.7 Ericsson Model

For network planning of mobile wireless systems and to predict path loss in the propagation scenarios, Ericsson developed a modified version of the Okumura-Hata model for engineers to use for network planning and analysis [3.28]. This model allows users to change parameters according to the propagation environments. The Ericsson path loss model is given by,

$$L_P(dB) = a_0 + a_1 \log_{10} d_{t-r} + a_2 \log_{10} h_t + a_3 \log_{10} h_t \,.\log_{10} d_{t-r} - 3.2 \log_{10}(11.75h_r)^2 + g(f_c) \quad (3.29)$$

where function $g(f_c)$ is defined as,

$$g(f_c) = 44.49 \log_{10} f_c - 4.78(\log_{10} f_c)^2 \quad (3.30)$$

where parameter d_{t-r} is the distance between the transmitter and the receiver in metre, f_c is the frequency in MHz, h_t is the transmitter antenna height and h_r is the receiver antenna height. The default values for parameters a_0, a_1, a_2 and a_3 are classified according to the different terrains given in Table 3.2.

Table 3.2 Parameters' value for Ericsson model [3.35].

Environment	a_0	a_1	a_2	a_3
Urban	36.2	30.2	12.0	0.1
Suburban	43.20	68.93	12.0	0.1
Rural	45.95	100.6	12.0	0.1

3.2.2.8 WINNER II Channel Models

WINNER II project was a continuation of WINNER I [3.36]. For WINNER II, frequency range of interest was between 2 GHz to 6 GHz whilst WINNER I is focused only at 5 GHz. Many propagation scenarios was studied in WINNER I and II such as indoor, urban micro-cell, urban macro-cell, sub-urban macro-cell and rural macro-cell.

According to the data measured from the actual environments, the received signals will always have line-of-sight (LOS) component, so two radio propagation models, WINNER B1 and B3, from WINNER II are selected to estimate the channel performance. WINNER B1 has been designed for urban micro-cell scenarios wher the transmitting and receiving antenna heights are below the top of building. WINNER B3 has been designed for indoor hotspot such as conference halls, factories, train stations and airports. Normally typical dimensions of areas are from 20 m x 20 m up to 100 m in length and width.

Path loss models for various WINNER scenarios have been developed based on results from experiments and open literature as shown in equation (3.31).

$$PL = A\log_{10}(d[m]) + B + C\log_{10}\left(\frac{f_c[GHz]}{5.0}\right) + X \tag{3.31}$$

Where d is the distance between the transmitter and the receiver in metre (m), f_c is the system frequency in GHz whilst the fitting parameter A includes the path loss exponent, parameter B represents as the intercept, parameter C describes the path loss frequency dependence, and finally X is an optional attenuation from wall, surface, etc. Parameters in cases of LOS link have been defined as $A = 22.7$, $B = 41.0$, and $C = 20$ for WINNER B1 and $A = 13.9$, $B = 64.4$, and $C = 20$ for WINNER B3.

A list of empirical radio propagation models and their details including frequency, antenna height, and link distance have been summarised in Table 3.3.

Table 3.3 List of channel propagation models

Model	Frequency (MHz)	Base antenna height (m)	Mobile antenna height (m)	Link distance (km)
Okumura	150 – 1920	30 – 1000	1 – 10	1 – 10
Hata	150 – 1500	30 – 200	1 – 10	1 – 20
COST231-Hata	1500 – 2000	30 – 200	1 – 10	1 – 20
Stanford University Interim (SUI)	>1900 - 3500	10 – 80	2 – 10	0.1 – 8
ECC-33	150 - > 3000	N/A	N/A	N/A
COST231 Walfisch-Ikegami	800 – 2000	4 – 50	1 – 3	0.02 – 5
Ericsson	N/A	N/A	N/A	N/A
WINNER II	2000 – 6000	N/A	N/A	N/A

Each of these empirical channel propagation model can be used in different scenarios to assess the channel propagation performances.

3.2.3 Combined Statistical and Deterministic Modelling

Current available ray tracing techniques are powerful to track the dominant signal components travelling from the transmitter to the receiver. Ray tracing algorithms are generally based on electromagnetic wave propagation mechanisms in LOS signals involving reflections, diffraction, scattering and refraction. In a number of scenarios and environments, the complex interactions of these mechanisms make it difficult to explain the observed channel measurements and the channel properties or characteristics.

In wireless communication systems, especially in the outdoor microcellular scenarios, it is very difficult to determine, with certainty, the propagation mechanisms and hence the number of multipath components that will be received. Small-scale modelling of picocellular scenarios such as indoor channels can offer better accuracies. Understanding signals propagation in radio channels become more complicated when the objects in the

propagation channel are moving. Moreover when the mobile radio systems are also moving, the propagation mechanisms, their complex interactions and number of signal components become space and time variant. A combination of statistical and deterministic modelling can improve and fulfil the performance of an individual-existing statistical or deterministic model by representing the dominant rays with deterministic model and representing the rests of the multipath signals with statistical methods.

3.2.4 Statistical Probability Density Function Models

Multipath signals arrive at the receiver after experiencing one or more propagation mechanisms; reflection, refraction, diffraction and scattering. Signal components experience a complex alteration of power (amplitude), phase and also in terms of the number of components that will arrive at the receiver. Statistical probability density (PDF) function is one technique that is widely used to describe the channel characteristics and responses by considering the envelope of the averaged received signals which is often a summation of multipath signals. The received signal might include the LOS signal or might have only NLOS signals. Statistical distributions can be fitted to measured data without any knowledge of the channel response but they are critical to the development of channel coding techniques and link margin determination. The following sections describe some of the PDFs that are frequently used.

3.2.4.1 Rayleigh Distribution

Rayleigh distribution is commonly used to describe the time varying channel for small scale fading. It is assumed that the amplitude distribution of signal power travelling through the channel will spread out randomly according to Rayleigh distribution in the case of random complex numbers whose real and imaginary components are independently and identically distributed (i.i.d.) Gaussian random variables by virtue of the Central Limit Theorem[3.37]-[3.39]. The Rayleigh distribution has a probability density function given by

$$p(r) = \begin{cases} \frac{r}{\sigma^2} e^{\left(\frac{r^2}{2\sigma^2}\right)} & for(0 \le r \le \infty) \\ 0 & for(r < 0) \end{cases} \tag{3.32}$$

Where σ is the standard deviation of the random received signal, r. This is the amplitude distribution of the variable r which is uncorrelated rotating vectors with amplitudes and uniformly distributed phase in the interval (0,2π).

3.2.4.2 Rice Distribution

The Rice distribution describes the amplitude distribution of the variable r composed of multipath components form an underlying Rayleigh distribution and added with one dominant LOS signal component. The Rice distribution function is given by

$$p(r) = \begin{cases} \frac{r}{\sigma^2} e\left(-\frac{r^2 + A^2}{2\sigma^2}\right) I_0\left(\frac{Ar}{\sigma^2}\right) & for(A \geq 0, r \geq 0) \\ 0 & for(r < 0) \end{cases} \quad (3.33)$$

Where A is the peak amplitude of the dominant component, σ^2 is its variance, and $I_0(.)$ is the modified Bessel function of the first kind, order zero. The Ricean PDF is normally characterised by the ratio of the power of the dominant component to the power of the multipath components and is given by

$$\text{K}=10\log_{10}\frac{A^2}{2\sigma^2}\ dB \quad (3.34)$$

The Rice distribution becomes Rayleigh distribution when there is no LOS signal component and K approaches negative infinity.

3.2.4.3 Lognormal Distribution

The shadowing effect can be described by the lognormal distribution when the LOS path is completely blocked by obstacles like hills and buildings. In this situation, the reflected and scattered components are considered as the dominant components. The lognormal distribution is given by

$$p(r) = \begin{cases} \frac{1}{r\sigma\sqrt{2\pi}} e\left[-\frac{(\ln(r) - m)^2}{2\sigma^2}\right] & for(0 \leq r \leq \infty) \\ 0 & for(r < 0) \end{cases} \quad (3.35)$$

where m and σ are the mean and standard deviation of $\ln(r)$, respectively [3.39].

3.2.4.4 Nakagami Distribution

The Rayleigh distribution is a special case of the Nakagami distribution when $m = 1$. Moreover for higher values of m the Nakagami distribution is similar to the Ricean distribution. The Nakagami distribution is given by

$$f(r) = \begin{cases} \frac{2m^m r^{2m-1}}{\Gamma(m)\Omega^{\mathrm{m}}} e^{-(m/\Omega)r^2} & for(r \geq 0) \\ 0 & for(r < 0) \end{cases} \tag{3.36}$$

where $\Gamma(m)$ is the Gamma function, $\Omega = E\{r^2\}$ controls the spread of the distribution and m is the shape parameter given by

$$m = \frac{\Omega^2}{E[(r^2 - \Omega)^2]} \quad for\ m \geq \frac{1}{2} \tag{3.37}$$

The distribution describes the summation of m orthogonal independent Rayleigh distributed random variables for integer values of m. This means that for N Rayleigh distributed random variables (X_i) the PDF of the random variable Y given by

$$Y = \sqrt{\sum_{i=1}^{N} X_i^2} \tag{3.38}$$

which is a Nakagami distribution for $m = N$. Thus the Nakagami probability density function is general enough to cover both the Rayleigh and Ricean distributions.

3.2.4.5 Normal Distribution

The Normal distribution is often used to model a number of naturally emerging events. In communication, Normal distribution has been used to model noise (AWGN: Additive White Gaussian Noise). Its probability density function is controlled by the mean μ, standard deviation σ, and variance σ^2. The probability density function is given by

$$p(r) = \frac{1}{\sigma\sqrt{(2\pi)}} e\left(-\frac{(r-\mu)^2}{2\sigma^2}\right) \quad for(-\infty \leq r \leq \infty) \tag{3.39}$$

3.2.4.6 Loo's Distribution

Loo's distribution model is a statistical model. It is a model that is used for land mobile satellite propagation based on the probability density functions of multipath and shadowing propagation developed by Loo [3.40][3.41]. It is described by

$$p(r) = \frac{\sqrt{2}\overline{K}r}{sA\sqrt{\pi}} e\left[-\frac{(\ln(r)-m)^2}{2s^2} - \overline{K}(r^2+A^2)\right] I_0(2\overline{K}rA) \tag{3.40}$$

Loo's distribution is a combination of Rician and Lognormal PDF where s is standard deviation for lognormal fading, $\overline{K} = 1/2\sigma^2$. A is the dominant component or LOS signal and r is the received signal variable.

3.3 Summary

Conventional channel modelling approaches described in this chapter have been categorised into three groups; deterministic, statistical and empirical, and combined statistical and deterministic modelling approaches. Deterministic modelling approach is considered to be the best for estimating radio channel properties. However this method is very complicated to use because it requires details of environment. Statistical and empirical channel modelling approach is become the most powerful and beneficial method for researchers to estimate radio signal power in actual environments whilst the combined statistical and deterministic modelling approach is another method that details of real radio channel are required. Empirical channel models include the Okumura, Hata, COST231 Walfisch-Ikegami, Stanford University Interim (SUI), ECC-33, and Ericsson or WINNER project models described as well known models using to predict the signal power along the measurement path even though they are not suitable for the study in this thesis. As it will be presented in chapter 7, linear model combined with one of statistical probability functions can be used to represent the signal power spreading in urban area for path lengths less than 20 m.

References

[3.1] Smulders P., Jevrosimovic M., Herben M., Savov S., Martijn E., "Deliverable D2.1: State of the Art Channel Models", Broadband Radio@Hand B4 Public, June 2002, pp. 1 - 46.

[3.2] Domazetovic A., Greenstein L. J., Mandayam N. B., Seskar I., "Propagation Models for Short-Range Wireless Channels with Predictable Path Geometries", IEEE Transactions on Communications, Vol. 53, No. 7, July 2005, 1123 - 1126.

[3.3] Valenzuela R. A., "A Ray Tracing Approach to Predicting Indoor Wireless Transmission", IEEE Proceedings 43rd on Vehicular Technology Conference, May 1993, pp. 214 - 218.

[3.4] Valenzuela R. A., Greenstein L, J., "Performance Evaluations for Urban Line-of-Sight Microcells at 900 MHz Using a Multi-Ray Propagation Model", Global Telecommunications Conference GLOBECOM, Vol. 3, December 1991, pp. 1947 - 1952.

[3.5] Seong-Cheol B. J., Guarino B. J. Jr., Willis T. M. III, Erceg V., Fortune, S. J., Valenzuela, R. A., Thomas, L.W., Ling, J., Moore, J.D., "Radio Propagation Measurements and Prediction Using Three-Dimensional Ray Tracing in Urban Environments at 908 MHz and 1.9 GHz", IEEE Transactions on Vehicular Technology, Vol. 48, No. 3, May 1999, pp. 931 - 946.

[3.6] Seidel S. Y., Rappaport T. S., "Site-Specific Propagation Prediction for Wireless In-Building Personal Communication System Design", IEEE Transactions on Vehicular Technology, Vol. 43, No. 4, November 1994, pp. 879 - 891.

[3.7] Seidel S. Y., Rappaport T. S., "A Ray Tracing Technique to Predict Path Loss and Delay Spread inside Building", IEEE Global Telecommunications Conference GLOBECOM'92, Vol. 2, pp. 649 - 653.

[3.8] Greenstein L. J., Andersen J. B., Bertoni H. L., Kozono S., Michelson D.G., Tranter W. H., "Guest Editorial Channel and Propagation Models for Wireless System Design I", IEEE Journal on Selected Areas in Communications, Vol. 20, No. 3, April 2002, pp. 493 - 495.

[3.9] Erceg V., Greenstein L. J., Tjandra S. Y., Parkoff S. R., Gupta A., Kulic B., Julius A. A., Bianchi R., "An Empirically Based Path Loss Model for Wireless Channels in Suburban Environments", IEEE Journal on Selected Areas in Communications, Vol. 17, No. 7, July 1999, pp. 1205 - 1211.

[3.10] Greenstein L. J., Erceg V., Yeh Y. S., Clark M. V., "A New Path-Gain/Delay-Spread Propagation Model for Digital Cellular Channels", IEEE Transactions on Vehicular Technology, Vol. 46, No. 2, February 1997, pp. 477 - 485.

[3.11] Hata M., "Empirical Formula for Propagation Loss in Land Mobile Radio Services", IEEE Transactions on Vehicular Technology, Vol. 29, No. 3, March 1980, pp. 317 - 325.

[3.12] Asplund H., Molisch A. F., Steinbauer M., Mehta N. B., "Clustering of Scatterers in Mobile Radio Channels-Evaluation and Modelling in the COST259 Directional Channel Model", IEEE International Conference onCommunications, ICC 2002, Vol. 2, 2002, pp. 901 - 905.

[3.13] Molisch A. F., "Wireless Communications 2nd", John Wiley & Sons Ltd., United Kingdom, 2011.

[3.14] Canning F. X., "The Impedance Matrix Localization (IML) Method for Moment-Method Calculations", IEEE Antennas and Propagation Magazine, Vol. 32, No. 5, October 1990, pp. 18 - 30.

[3.15] Hviid J. T., Andersen J. B., Toftgard J., Bojer J., "Terrain-Based Propagation Model for Rural Area-An Integral Equation Approach", IEEE Transactions on Antennas and Propagation, Vol. 43, No. 1, January 1995, pp. 41 - 46.

[3.16] Savov S. V., Herben M. H. A. J., "Modal Transmission-Line Calculation of Shielding Effectiveness of Composite Structures", Electronics Letters, Vol. 37, No. 8, April 2001, pp. 487 - 488.

[3.17] Hao X., Kukshya V., Rappaport T.S., "Spatial and Temporal Characterization of 60 GHz Indoor Channels", IEEE VTS-Fall VTC 2000. 52, Vol.1, Sept. 2000, pp. 6 - 13.

[3.18] Savov S. V., Herben M. H. A. J., "Modal Transmission-Line Modeling of Propagation of Plane Radiowaves through Multilayer Periodic Building Structures", IEEE Transactions on Antennas and Propagation, Vol. 51, No. 9, September 2003, pp. 2244 - 2251.

[3.19] Okumura Y., Ohmori E., Kawano T., Fukuda K., "Field Strength and Its Variability in VHF and UHF Land Mobile Radio Services", Review of the Electrical Communications Laboratory, Vol. 16, September - October 1968, pp. 825 - 873.

[3.20] Hata M., "Empirical Formula for Propagation Loss in Land Mobile Radio Services", IEEE Transactions on Vehicular Technology, Vol. 29, No. 3, August 1980, pp. 317 - 325.

[3.21] Delisle G. Y., Lefevre J. P., Lecours M., Chouinard J. Y., "Propagation Loss Prediction: A Comparative Study with Application to the Mobile Radio Channel", IEEE transactions on Vehicular Technology, Vol. 34, No. 2, May 1985, pp. 86 - 89.

[3.22] Aurand J. F., Post R. E., "A Comparison of Prediction Methods for 800 MHz Mobile Radio Propagation", IEEE Transactions on Vehicular Technology, Vol. 34, No. 4, November 1985, pp. 149-153.

[3.23] COST Action 231, "Digital Mobile Radio Towards Future Generation Systems", Final Report, European Commission, EUR 18957, 1999.

[3.24] Samukic A., "UMTS Universal Mobile Telecommunications System: Development of Standards for the Third Generation", IEEE Transactions on Vehicular Technology, Vol. 47, No. 4, November 1998, pp. 1099 - 1104.

[3.25] Melin L., Ronnlund M., Angbratt R., "Radio Wave Propagation: A Comparison between 900 and 1800 MHz", IEEE 43rd Vehicular Technology Conference, New Jersey, USA, May 1993, pp. 250-252.

[3.26] Abhayawardhana V. S., Wassell I. J., Crosby D., Sellars M. P., Brown M. G., "Comparison of Empirical Propagation Path Loss Models for Fixed Wireless Access Systems", IEEE 61st Vehicular Technology Conference, Vol. 1, May - June 2005, pp. 73-77.

[3.27] Erceg V., Hari K. V. S., Smith M. S., Sheikh K. P., Tappenden C., Costa J. M., Baum D. S., Bushue C., "Channel Models for Fixed Wireless Applications", IEEE 802.16 Broadband Wireless Access WG http://ieee802.org/16, Retrieved May 2008.

[3.28] Milanovic J., Rimac-Drlje S., Bejuk K., "Comparison of Propagation Models Accuracy for WiMAX on 3.5 GHz", IEEE 14th International Conference on Electronics, Circuits and Systems, December 2007, pp. 111 - 114.

[3.29] Parsons J. D., "The Mobile Radio Propagation Channel", John Wiley & Sons Ltd., Chichester, U.K., 2000.

[3.30] Saunders S. R., "Antennas and Propagation for Wireless Communication Systems", John Wiley & Sons Ltd., Chichester, U.K., 1999.

[3.31] Electronic Communication Committee (ECC) within the European Conference of Postal and Telecommunications Administration (CEPT), "The Analysis of the Coexistence of FWA Cells in the 3.4 - 3.8 GHz Band", ECC Report 33, May 2003.

[3.32] Walfisch J., Bertoni H. L., "A Theoretical model of UHF Propagation in Urban Environments", IEEE Transactions on Antennas and Propagation, Vol. 36, No. 12, December 1988, pp. 1788 - 1796.

[3.33] Papoulis A., "Probability, Random and Macrodiversity for Mobile radio", 3rd Edition McGraw-Hill, New York, 1991.

[3.34] Ikegami F., Yoshida S., Takeuchi T., Umehira M., "Propagation Factors Controlling Mean Field Strength on Urban Streets", IEEE Transactions on Antennas and Propagation, Vol. 32, No. 8, August 1984, pp. 822 - 829.

[3.35] Simi I. S., Stani I., Zrni B., "Minimax LS Algorithm for Automatic Propagation Model Tuning", Proceeding of the 9th Telecommunications Forum (TELFOR 2001), Belgrade, November 2001.

[3.36] WINNER I and II – Public Deliverables, Website: http://www.ist-winner.org/deliverables.html

[3.37] Shankar P. M., "Introduction to Wireless Systems", John Wiley & Sons, USA, 2002.

[3.38] Papoulis A., "Probability, Random Variables, and Stochastic Processes 3rd", McGraw-Hill, New York, 1991.

[3.39] Sklar B., "Rayleigh Fading Channels in Mobile Digital Communication Systems Part I: Characterisation", IEEE Comms Magazine, Vol. 35, No. 7, July 1997, pp. 90-100.

[3.40] Loo C., "A Statistical Model for A Land Mobile Satellite Link", IEEE Transaction on Vehicular Technology, Vol. VT-34, No. 3, August 1985, pp. 122-127.

[3.41] Loo C.,"Measurements and Models of A Land Mobile Satellite Channel and Their Applications to MSK Signals", IEEE Transaction on Vehicular Technology, Vol. VT-35, No. 3, August 1987, pp. 114-121.

CHAPTER 4

Channel Sounder

Abstract:

This chapter describes the channel sounder that has been used in this research to perform radio channels measurements. In addition, the channel sounder back-to-back test results that illustrate the capabilities of the system are presented.

4.1 Introduction

To study fast varying broadband radio channel properties in the actual environments, a channel sounder is required. A channel sounder measures the channel response over a range of frequency in a very small time period within which the channel response is considered to be stationary. In this chapter, a brief description of the channel sounder used in this research is presented.

4.2 Channel Sounder in the Market

In wireless communication channels, the received signal is a combination of direct signal or line-of-sight (LOS) signal and non line-of-sight (NLOS) signals. The variation of the channel characteristics in time and space can be analysed by employing channel sounders to investigate signal components that arrive at the receiver antenna. A number of channel sounders were available on the market at the time that the University of Portsmouth sounder was developed. The main limitations of those available were the bandwidth, size, flexibility and prohibitive cost of purchase and maintenance.

There are several channel sounding techniques developed for characterising wireless propagation channels. These techniques can be classified based on the signals transmitted and can be divided into two groups: pulse and continuous wave. Pulse transmission is the basic method that has been used to examine the multipath characteristics of channels since the 1950s [4.1]. The limitation of pulse transmission includes the slow channel measurement rate, requirement for large transmission power and the fact that the resolution of multipath components depend on pulse width. However, pulse transmission techniques are still being used as they are easy to implement.

In the last few decades, modern channel sounding techniques that employed continuous wave such as Pseudo Random Binary Sequence (PRBS) and Pseudo Random Gaussian Noise (PRGN) signals have been invented to address the limitations of direct pulse sounding techniques. These include the multitone sounding method that has been used to developed the channel sounder at University of Portsmouth [4.5][4.6].

The market leader is the RUSK channel sounder [4.2] which is based on multitone signal produced by MEDAV [4.3]. In multitone channel sounders, if the transmitted signal is $X(f)$ and the received signal is $Y(f)$, then the transfer function of the channel can be determined by,

$$H(j\omega) = \frac{Y(f)}{X(f)} \tag{4.1}$$

However multitone signals lead to an undesirable large peak-to-average power ratio (crest factor). This is unwanted because linear power amplifiers operating with large power reserves are needed. The crest factor can be minimised by optimizing the phase of the spectral lines. The single channel RUSK sounder was capable of measuring the channel response over a bandwidth of 120 MHz at carrier frequencies of 5 and 6 GHz. This sounder was subsequently extended to a MIMO system.

Another example of channel sounder is Berkeley Varitronics Duet Channel sounder [4.4]. The duet channel sounder can be used to obtain channel details for personnel communication system (PCS) planning in indoor and also outdoor. However, it has a small bandwidth from 1930 MHz to 1960 MHz (30 MHz). Some of its features include selectable pseudo noise (PN) modulation sequence, bit error rate analysis for individual multipath components, and radio frequency (RF) spectrum analysis.

4.3 Channel Sounder

In this thesis, the wideband channel sounder developed by Stuart and Ndzi [4.5] [4.6] employed a multitone signalling technique called Spread Spectrum Time Averaging (SSTA) that was described in [4.7][4.8] and first used to investigate transhorizon propagation phenomena over the English Channel [4.8]-[4.10]. The block diagram illustrating the principles of a channel sounder is shown in Figure 4.1. The Pseudo Random Gaussian Noise (PRGN) signal is generated by a programmable dual channel Arbitrary Waveform Synthesiser (AWS) with bandwidth up to 200 MHz [4.11][4.12].

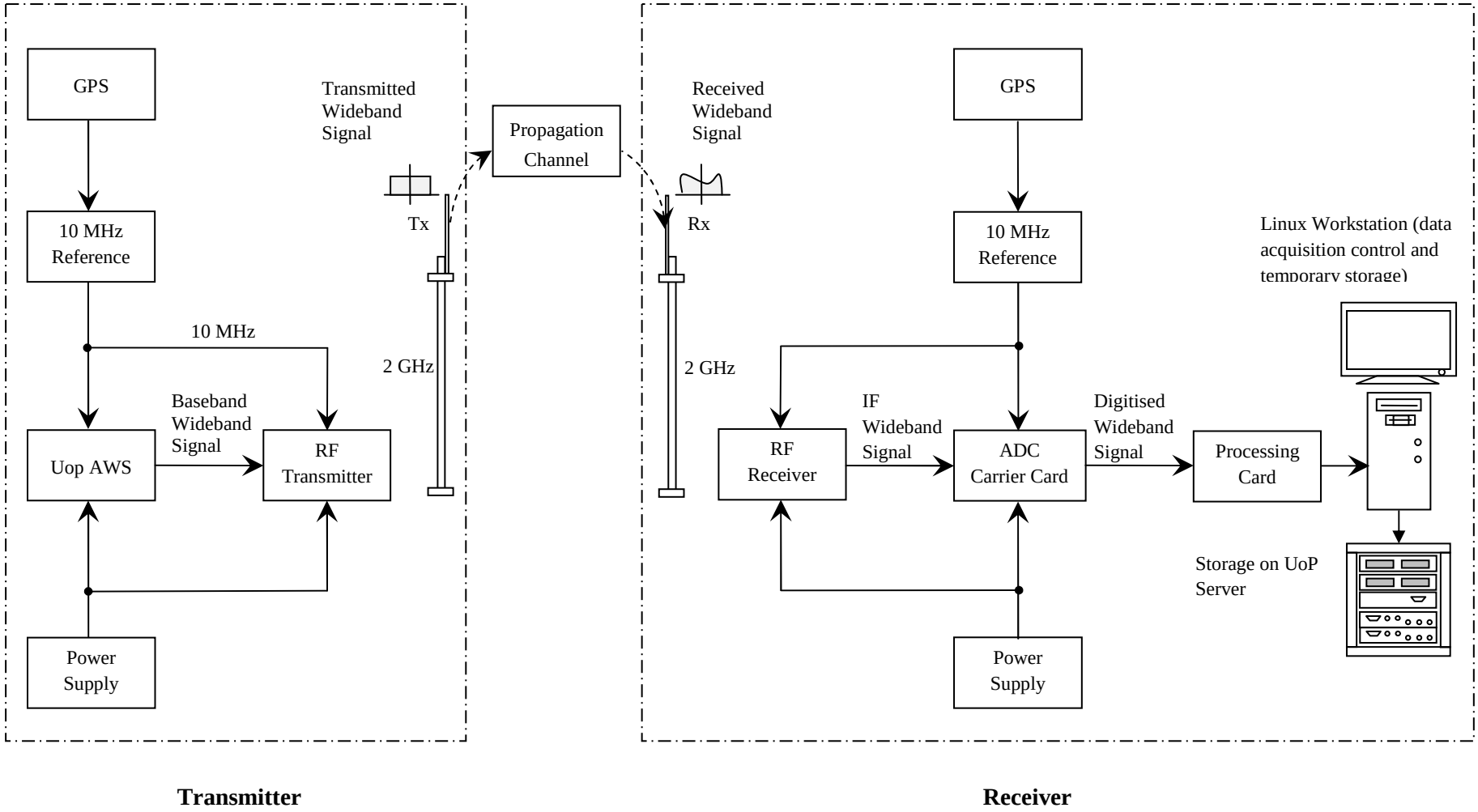

Figure 4.1 Channel sounder block diagram set up

This is up converter for transmission through the channel to investigate the channel characteristic.

4.3.1 Channel Sounder Transmitter and Receiver

The transmitter can be subdivided into two major parts; the Arbitrary Waveform Synthesizer (AWS) and the Radio Frequency (RF) unit, as shown in Figure 4.2.

The AWS is used to generate a PRGN waveform with a bandwidth of 200 MHz for transmission through the channel. At 2 GHz carrier frequency, the PRGN waveform occupies the frequency band from 1.9 GHz to 2.1 GHz. The transmitter RF system was designed and configured to minimise signal distortion, intermodulation product components, cost and to maximise output power. The output power of the RF unit is 21 dBm (126mW) and the dynamic range of the waveform is 22 dB. The baseband signal generated by the AWS is connected to the RF unit to be amplified and up-converted to 2 GHz. A 10 MHz reference frequency is used for frequency synchronisation of the unit to enable real-time averaging at the receiver.

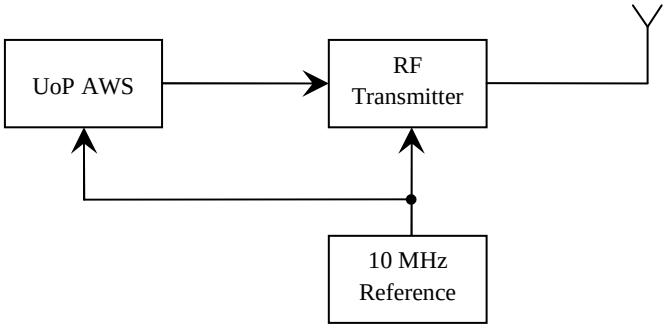

Figure 4.2 Block diagram of channel sounder transmitter

The block diagram of the channel sounder receiver is shown in Figure 4.3. The receiver system can be divided into the Analogue to Digital Converter (ADC), Processing card with a FPGA based Peripheral component interconnect Mezzanine Card (PMC) for real-time processing, a Linux workstation to store the measured data, the RF receiver and frequency reference unit.

The receiver RF system was designed to optimise the receiver sensitivity and adaptability. Therefore a programmable digital attenuator was incorporated to maintain the signal level within the linear range of the RF components and also to protect the ADC against damage by strong signals at short range. The received signal at 2 GHz is down-converted to an Intermediate Frequency (IF) of 100 MHz using a phase-locked 2.1 GHz

oscillator and is sampled at the rate of 400 MS/s. The PRGN waveform can be recovered by down conversion to baseband, using RF components. However this will increase the complexity of the receiver system. Therefore after sampling at IF, down conversion to baseband is implemented in software. The ADC input power is about 18 dBm (63mW) and the dynamic range of the PRGN is about 33 dB. For the channel sounder to be effective in low SNR conditions, averaging of the received signal is implemented in real-time using FPGA on the sampling card. This helps to reduce the need for high speed data transfer rate across the computer PCI bus, which is slower than the ADC output data rate. Xilinx Virtex II FPGA devices were selected and they are specified to support clock frequencies up to 420 MHz. In order to meet the Nyquist sampling criterion, the design objective was geared to support a maximum bandwidth of 200 MHz to minimise uncertainties associated with operating close to the limits of devices.

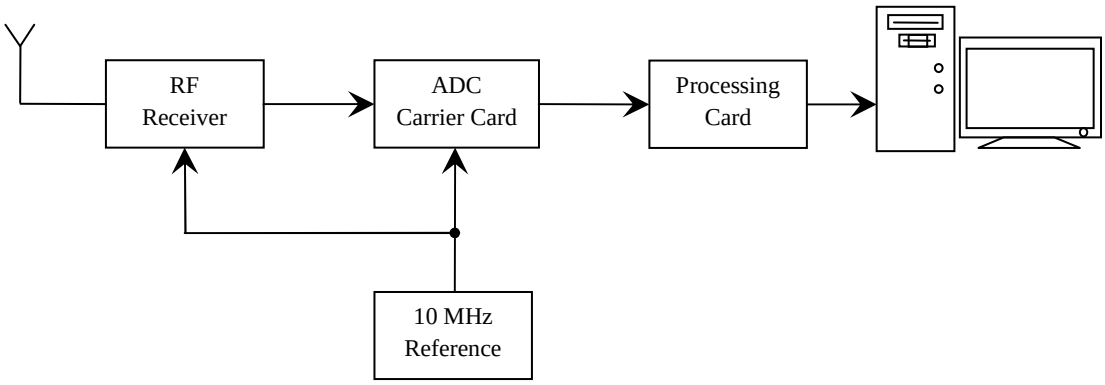

Figure 4.3 Block diagram of channel sounder receiver

From the development of the receiver, the user is allowed to adapt the system for different measurements by changing: 1) the number of real-time averages to be carried out; 2) time gap between successive channel measurements; 3) time gap between a continual block of successive channel response measurements; 4) the duration of the measurement or the number of data files to capture; and 5) when configured in conjunction with the transmitter, the bandwidth and sequence length of the waveform.

The complete-simplified channel sounder block diagram is shown in Figure 4.4 and the photograph of the transmitter and receiver units is shown in Figure 4.5, respectively.

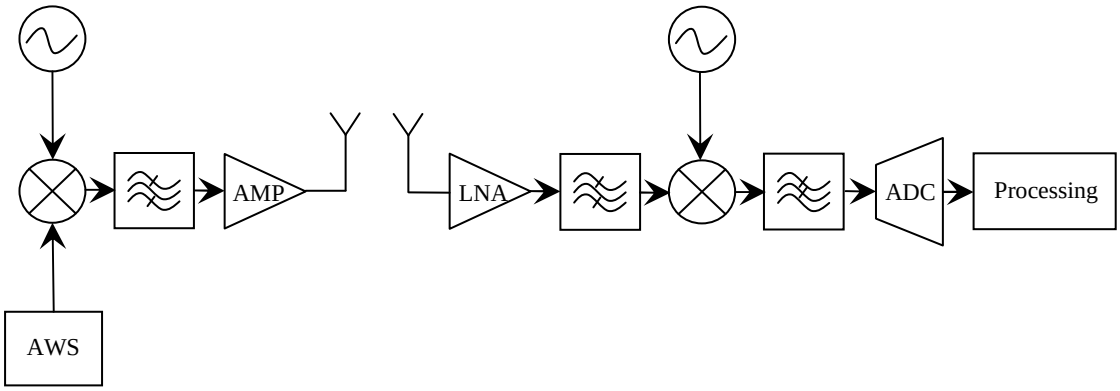

Figure 4.4 Simplified block diagram of the wideband channel sounder

Figure 4.5 Photograph of the built channel sounder

4.4 Channel Probing Waveforms

In this section, Pseudo Random Gaussian Noise (PRGN) signal [4.7] will be described. PRGN multitone signal was used in the channel sounder employed in this thesis. Although channel sounders that use multitone arbitrary waveforms are complicated to develop, they can provide higher channel resolution and simpler system architectures compared to other waveforms such as PRBS [4.13].

4.4.1 Pseudo Random Gaussian Noise

Pseudo Random Gaussian Noise (PRGN) waveform has a flat amplitude spectrum and low sidelobes outside the desired bandwidth [4.12]. The sampling rate can be set at exactly the Nyquist frequency which is lower than that of PRBS ($f_{PRGN} < f_{PRBS}$). The

sequence length is arbitrary and can be matched to a radix-2 FFT. Therefore a special clock frequency is not required. The PRGN waveform is defined with a flat amplitude in the frequency domain with uniformly distributed random phases in the interval $\pm \pi$.

The PRGN waveform with a bandwidth of 200 MHz is generated by the AWS which is phase-locked to a common 10 MHz frequency reference. The sequence length of the PRGN used was set to 4096 samples. The PRGN waveform from the AWS in the frequency domain has a flat amplitude spectrum across the bandwidth. The even harmonics are set to zero to avoid the generation of spectral lines at the Nyquist frequency and also at DC, thus permitting the suppression of the carrier frequency. Moreover, the data is zero-padded by a factor of 1 to allow analogue lowpass filtering. The waveform has a bandwidth of 200 MHz containing 1024 discrete spectral lines in the range ± 100 MHz with 195.313 kHz spaces between the spectral lines as shown in Figure 4.7.

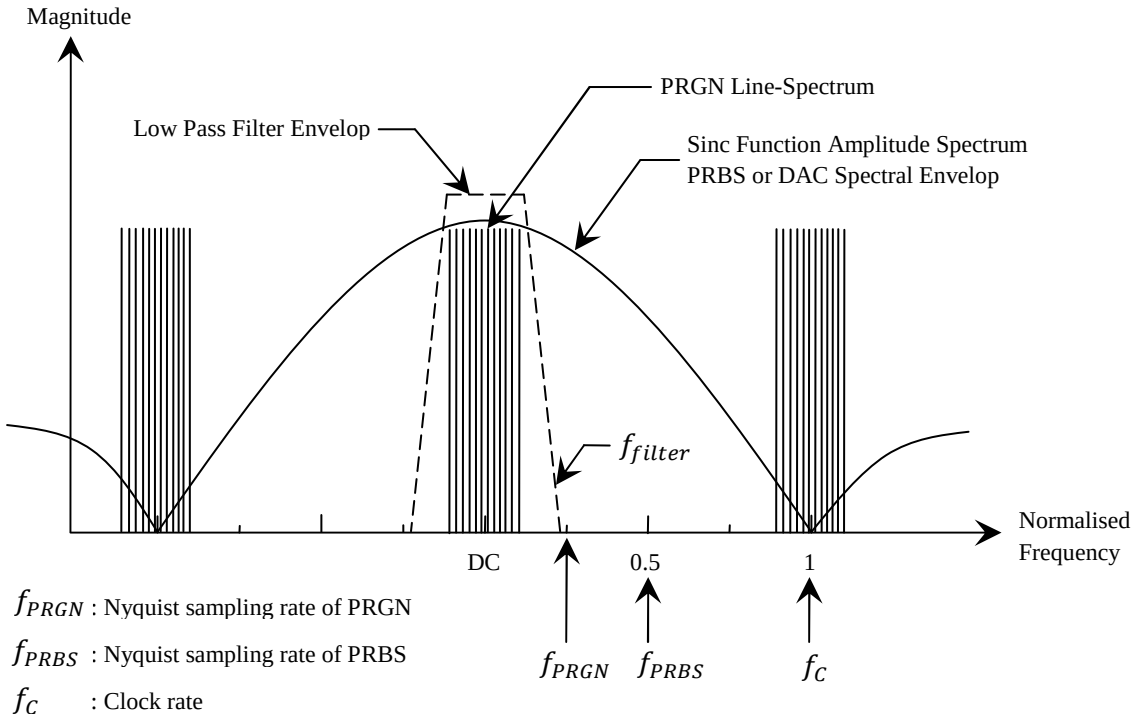

Figure 4.6 Relationship between the PRGN and PRBS spectra

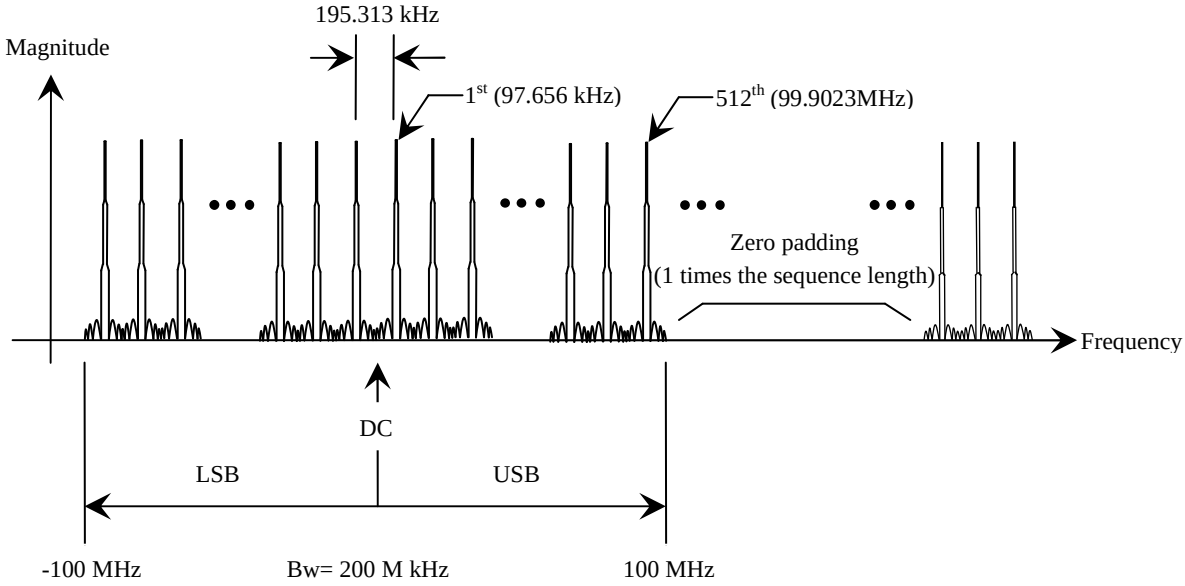

Figure 4.7 Illustration of the 200 MHz PRGN spectrum at baseband

PRGN signal in the time domain is shown in Figure 4.8 (a) and is similar to noise due to its random magnitude. The frequency domain PRGN signal is shown in Figure 4.8 (b).

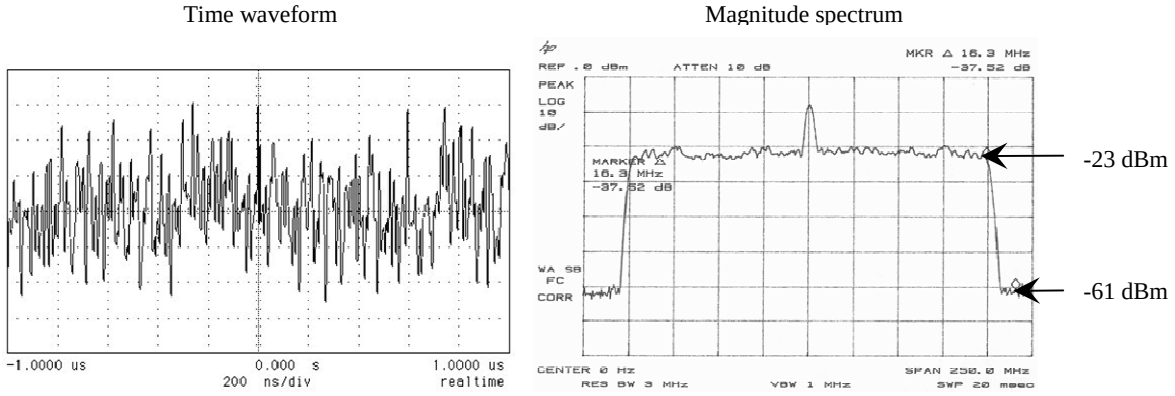

Figure 4.8 The 200 MHz PRGN waveform: (a) time domain signal, (b) magnitude spectrum

4.5 Data Acquisition

As mentioned earlier, one of the main objectives of the channel sounder design was to be able to capture and transfer the data to the storage device as fast as possible. The channel sounder used in the experiments was flexible for user to change the number of averages. Table 4.1 shows the counter settings required for the different number of averages, the time it takes to capture one averaged snapshot (T_{as}) and the theoretical improvement in

SNR (ΔSNR). The averaging counter values are calculated using equation (4.2), where N_s is the length of the sequence and N_a is the number of averages.

$$\text{counter value} = \left(\frac{N_s N_a + 2N_s}{2}\right) - 1 \tag{4.2}$$

The time taken to capture one averaged channel response (snapshot), T_{as}, is given by,

$$T_{as} = \frac{N_s N_a}{2f_c} + T_{sg} \tag{4.3}$$

where T_{sg} is the time required to reset the counters and First-IN-First-Out (FIFO) buffers, and f_c is the input clock frequency in Hz. Due to timing constraints, T_{sg} was set to a minimum value of 20.48 ms. Considering a sequence length of 4096, each snapshot has a size of 8.192 kB. The quantity of data generated for each value of N_a is shown in Table 4.2. It can be seen that when the number of averages is set to 32 or greater, data can be captured continually.

Table 4.1 Averaging counter value for possible number of averages, durations and expected improvement in SNR

N_a	Counter value (Hex)	$T_{as}(ms)$	Theoretical $\Delta SNR(dB)$
0	FFF	0.01024	0
2	1FFF	0.02048	3
4	2FFF	0.04096	6
8	4FFF	0.08192	9
16	8FFF	0.16384	12
32	10FFF	0.32768	15
64	20FFF	0.65536	18
128	40FFF	1.31072	21
256	80FFF	2.62144	24
512	100FFF	5.24288	27
1024	200FFF	10.48576	30

Table 4.2 Time to capture one channel response, number of averages and the volume of data generated per second

N_a	$T_{as}\ (ms)$	No. of snapshot per second	Data generated per second (MB)
0	0.03072	97656	266.666
2	0.04096	48828	200.000
4	0.06144	24414	133.333
8	0.10240	12207	80.0000
16	0.18432	6103	44.4444
32	0.34816	3051	23.5294
64	0.67584	1525	12.1212
128	1.33120	762	6.15385
256	2.64192	381	3.10076
512	5.26336	190	1.55642
1024	10.5062	95	0.77972

For number of averages less than 32, the quantity of data captured per second must be limited to 40 MB. This can be done by increasing the time gap (T_{sg}) between snapshots or block of continual channel response measurements such that the number of continual channel responses captured per second is less than 4882. During measurements a trade-off must be made between the channel sampling rate and quantity of data to be captured. Although the continual channel sampling rate is limited to 4.882 kHz, the user can achieve channel sampling rates up to 5.42 kHz for sub-second continual channel measurements. For a bandwidth of 100 MHz and 2048 long sequence, channel sampling rates up to 15 kHz are achievable. This provides the flexibility to investigate very high speed events. Figure 4.9 illustrates the data acquisition strategy.

The user can change the number of averages N_a, the time between snapshots (T_{sg}), and the time between data block (T_{dbg}) to suit the type of channel under investigation. The resulting time to capture one averaged snapshot (T_{as}), one data block (T_{db}) and one data file (T_{df}) can be calculated using Equations (4.3), (4.4) and (4.5) respectively.

$$T_{db} = 240T_{as} + 239T_{sg} \tag{4.4}$$

$$T_{df} = 4T_{db} + 3T_{dbg} \tag{4.5}$$

where,

$$T_{sg}\ and\ T_{dbg} = N_g\left(\frac{2N_s}{f_c}\right) \tag{4.6}$$

and N_g is the number of multiples of the time taken to reset all counters and FIFOs used in the averaging process. T_{sg} and T_{dbg} are independent of each other. Table 4.3 provides the details of the timing parameters for each number of averages, N_a, and the possible channel sampling rates for 180 MHz bandwidth signal transmission.

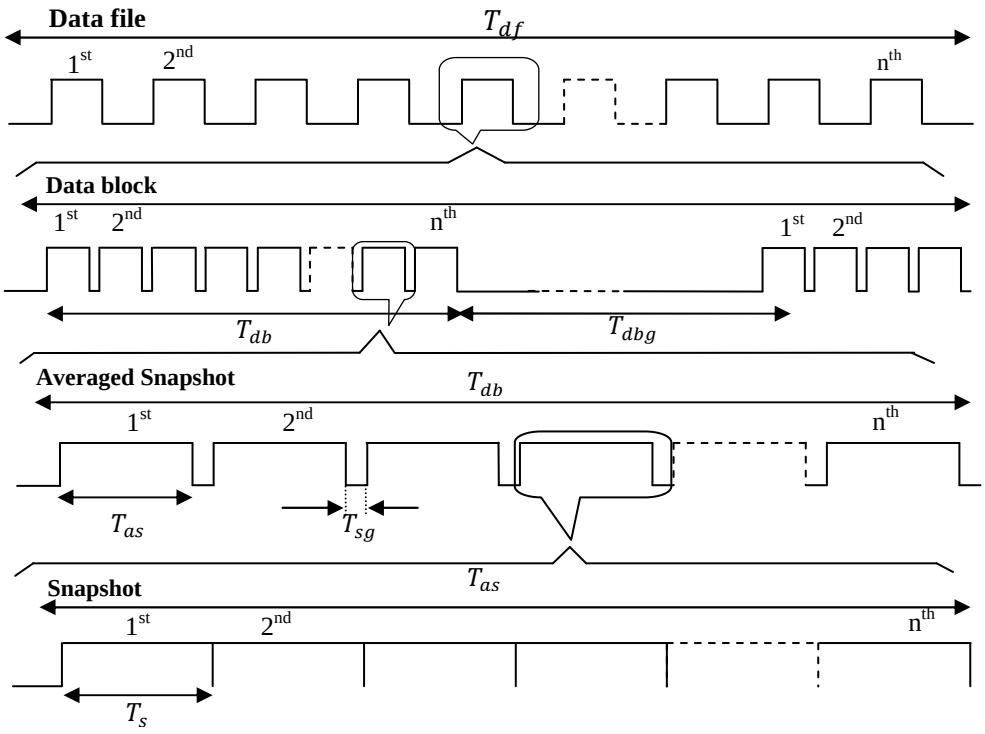

Figure 4.9 Data acquisition strategy for N_a averages

Table 4.3 Channel sampling rates for different number of averages for 180 MHz bandwidth configuration

N_a	Theoretical $\Delta SNR\ (dB)$	$T_{as}\ (ms)$	Channel sampling rate (Hz)
0	0	0.12288	8138
2	3	0.12288	8138
4	6	0.12288	8138
8	9	0.20480	4882
16	12	0.36864	2712
32	15	0.69632	1436
64	18	1.35168	739
128	21	2.66240	375
256	24	5.38384	189
512	27	10.5267	94
1024	30	21.0125	47

4.6 Sounder Tests and Results

Tests on the sounder highlighted a number of short comings in the software and hardware. The four areas of concern were the frequency stability of the sampling clock generated by the FPGA device on the ADC carrier card, the timing constraints of the software running on the PMC card, the data rate of the PCI bus and the rate at which data is written to disk. Frequency stability and the rate of data transfer to the storage device are critical to the implementation of a suitable data acquisition strategy, thus any associated problems had to be overcome. These included the addition of a new input clock for the ADC and revision of the VHDL design for the FPGA on the PMC card to improve the channel sampling rate. The following sections describe tests that were conducted, some of the issues that were identified, solutions implemented and the performance of the whole system.

4.6.1 Frequency Stability of the Experimental System

High stability of all the frequency sources is critical to the real-time averaging of PRGN signals. If the sources are not locked to a common phase reference, errors are introduced. Figure 4.10 shows measured channel transfer functions with and without the transmitter and receiver phase-locked to a common reference.

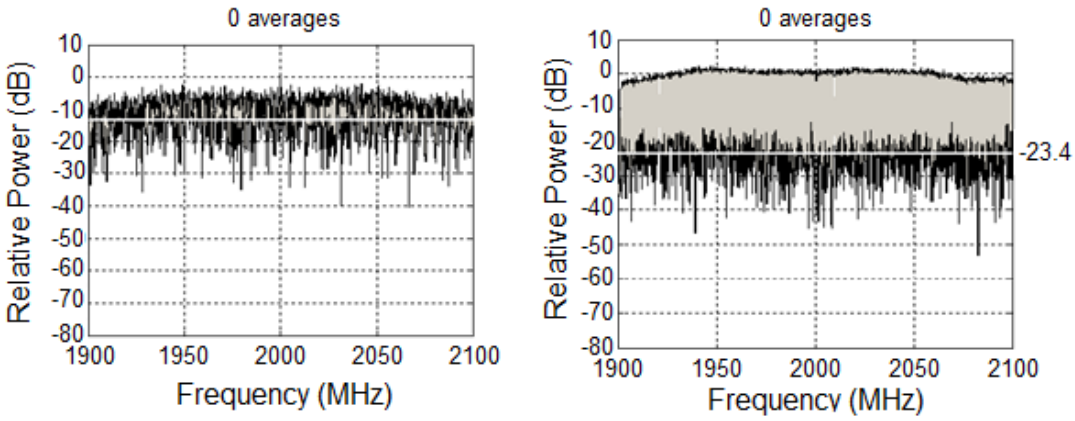

(a) (b)

Figure 4.10 Measured transfer functions (a) without and (b) with, the transmitter and receiver phase-locked to a common reference

Using a frequency counter, all the FPGA derived clocks on the AWS and the ADC carrier card were measured and found to be locked to the frequency reference. However, the data sampled by the ADC was found to contain errors. These errors are not observed when the sampling clock is obtained from a dedicated source e.g. signal generator. Tests revealed that the clock jitter was higher than the maximum recommended tolerance for the ADC. Figure 4.11 shows measurements taken with no signal applied to the input of the receiver. Errors with peak-to-peak values up to 3.25 V were obtained with the original FPGA generated clock. Since a low frequency clock from the FPGA had superior SNR and low jitter, a dedicated external clock multiplier could be used to generate the sampling clock for the ADC. Using the stable sampling clock, only the system noise with maximum peak-to-peak amplitudes of 0.005 V was present as shown in Figure 4.11 (b).

4.6.2 Signal to Noise Ratio

The transmitter and receiver RF units were designed to optimise the sensitivity of the receiver and minimise intermodulation products. In order to achieve this, measurement of input and output power and signal to intermodulation product ratios were evaluated at every stage in the RF chain.

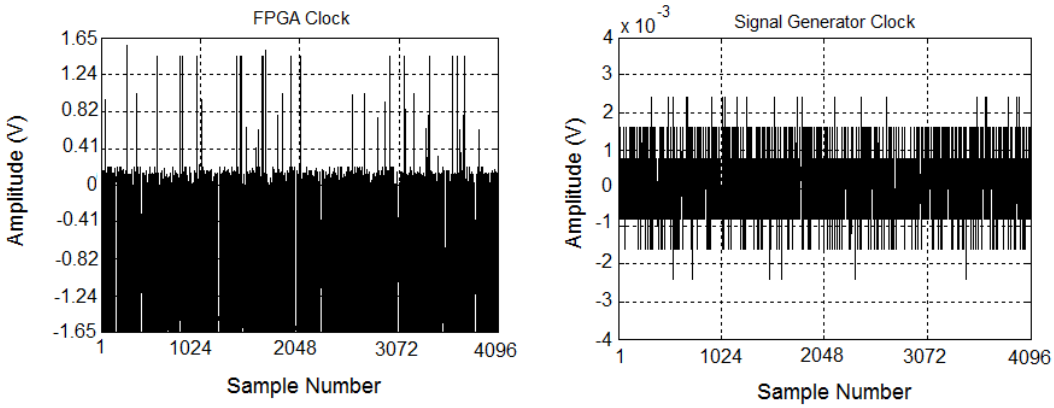

(a) (b)

Figure 4.11 Data captured with no signal input using clocks from: (a) the FPGA and, (b) the signal generator

All the components in a system have a noise figure and therefore generate noise that may not be band limited. The total noise power can be calculated by the integration of the continuous spectrum over a given bandwidth, B_w, which is taken to be the bandwidth of the last filter through which the signal plus noise is passed. The total noise power is given by,

$$P_N = \int_0^{B_w} S_{N|RWB=1Hz} \partial f = S_{N|RWB=1Hz} \times B_w \tag{4.7}$$

where $S_{N|RWB=1Hz}$ is the noise power spectral density at 1 Hz Resolution Bandwidth (RBW). Therefore, the SNR can be evaluated by,

$$SNR = 10 \log_{10} \left(\frac{P_s}{P_N} \right) \tag{4.8}$$

where P_s is the total signal power. Figure 4.12 shows the PRGN spectrum at the receiver IF and the corresponding expansion of the spectrum at the edge of the band. The mean output power, $\overline{P_S}$, across the bandwidth at IF is -9 dB. The mean noise power level, $\overline{P_N}$ is -30 dB, giving a SNR of 21 dB.

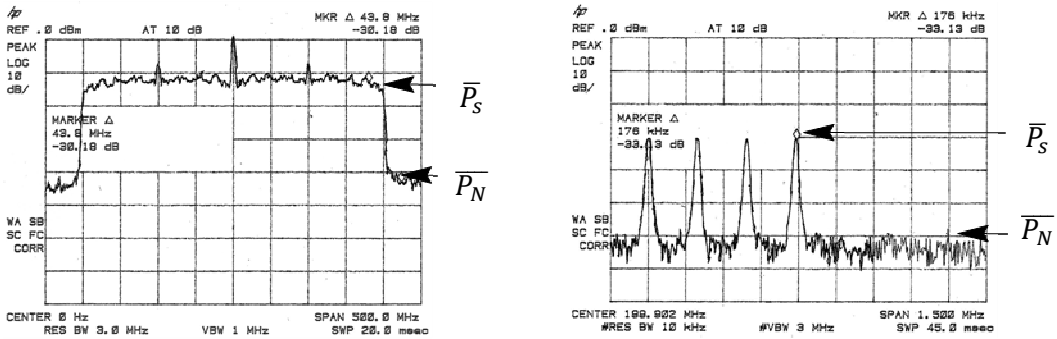

(a) (b)

Figure 4.12 IF: (a) spectrum of PRGN signal with a 200 MHz bandwidth, (b) spectrum at the edge of the band

4.6.3 Simulation of Flat Fading Channel

To test the performance of the system under flat fading channel conditions, 180 MHz and 200 MHz bandwidth PRGN waveforms were used. Tests were carried out with different numbers of averages, N_a, at a carrier frequency of 2 GHz. The back-to-back test configuration is shown in Figure 4.13.

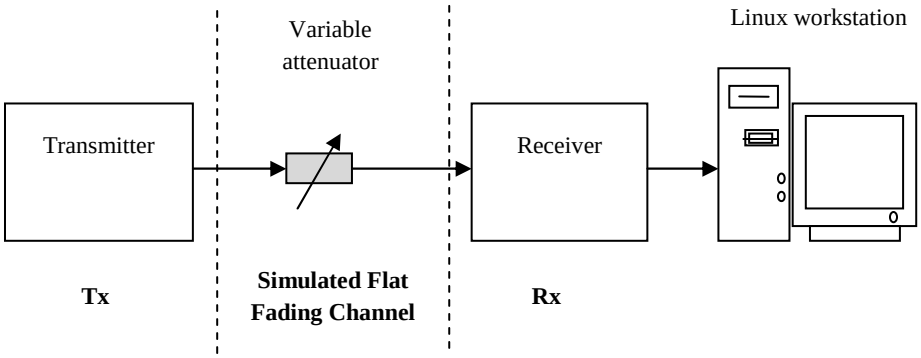

Figure 4.13 Block diagram of hardware for flat fading simulation

Figure 4.14 shows the transfer function of the waveform measured without averaging over a 180 MHz bandwidth. The system response introduces a slight amplitude variation across the band. These were not yet calibrated out. The magnitude of the components between the spectral lines represents noise plus any intermodulation products. Since it is not possible to separate intermodulation products from noise, the estimated mean level represents an equivalent Signal-to-Intermodulation and Noise Ratio (SINR). The estimated SINR is 22.8 dB.

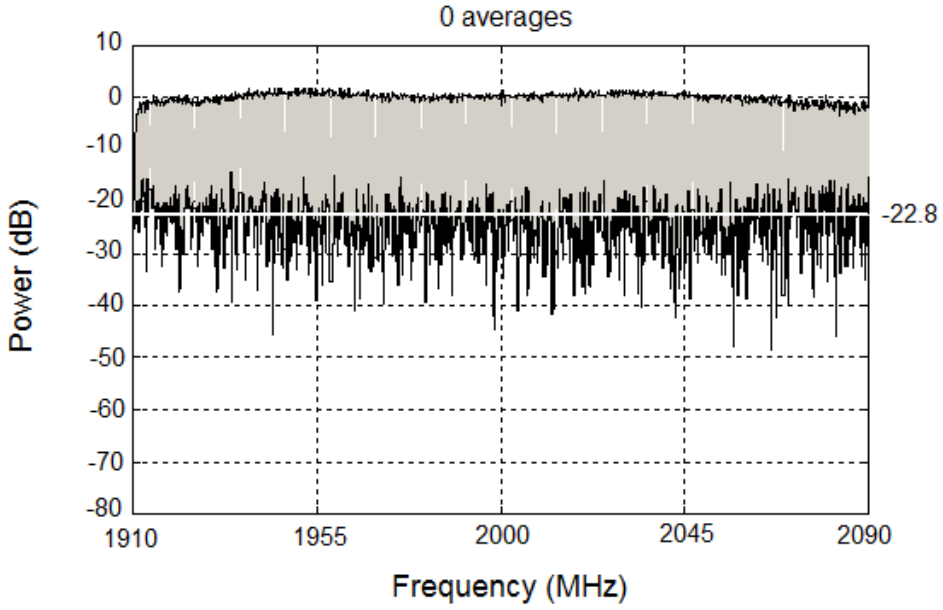

Figure 4.14 180 MHz bandwidth PRGN spectrum with no averaging ($N_a = 0$)

The results of measurements with 2 and 8 averages are shown in Figure 4.15. The improvement in SINR can be seen as the number of averages is increased from 0 (Figure 4.14) to 8 (Figure 4.15).

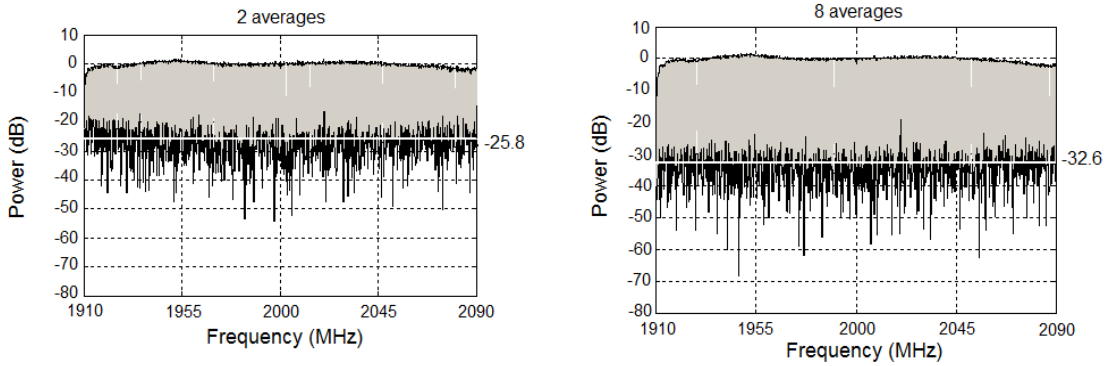

(a) (b)

Figure 4.15 180 MHz bandwidth spectrum with number of averages of (a) 2 and (b) 8 showing a 8.8 dB SNR improvement compared to 0 averages.

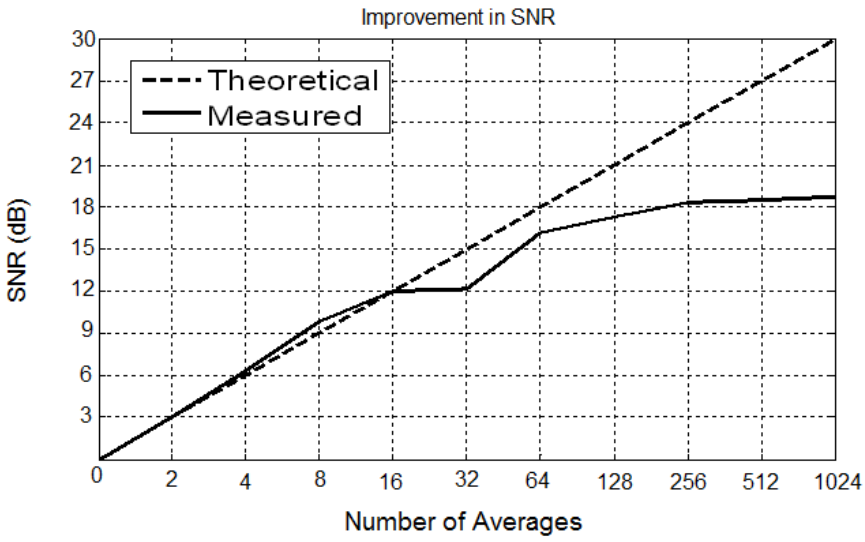

Figure 4.16 Comparison of theoretical and measured improvements in SNR for different number of averages

For white noise, the improvement in SNR due to averaging is by $10 \log N_a$, where N_a is the number of averages. Figure 4.16 shows the improvement in SNR for averages up to 1024 compared to the theoretical values. An improvement of 12.2 dB was achieved with 32 averages, which is 2.8 dB below the theoretical value. For higher number of averages, the measured SINR improvement flattened out at approximately 18.6 dB for 1024 averages. Since any intermodulation components present are coherent, signal averaging will only be effective in integrating out the noise. Therefore, the differences in levels between the SINRs for different number of averages represent the corresponding improvement in SNR. In addition, the theoretical improvement in SNR assumes that the noise is white Gaussian uncorrelated noise.

4.7 Summary

This chapter has briefly described the channel sounder developed at the University of Portsmouth (UoP). Channel probing signals like Pseudo Random Binary Sequence (PRBS), chirp, and Pseudo Random Gaussian Noise (PRGN) are described in brief. The different configurations of the UoP channel sounder are described together with the back-to-back tests carried out during its development and the results. These have been provided for completeness to emphasise the reliability and accuracy of the system that would be used to study space and time varying channels in subsequent chapters.

References

[4.1] DeLange O. E., “Propagation Studies at Microwave Frequency by Means of Very Short Pulse”, Bell System Technical Journal, Vol. 31, January 1952, pp. 91-103.

[4.2] RUSK Channel Sounder, MEDAV GmbH, Website: http://www.channelsounder.de

[4.3] MEDAV GmbH, Website: http://www.medav.de

[4.4] Berkeley Varitronics Duet Channel Sounder, Website: http://www.testequipmentconnection.com/63163/Berkeley_Varitronics_Duet_Channel_Sounder.php

[4.5] Stuart K., Ndzi D. L., Austin J., Savage N., “Development of a Fast and Adapable 200 MHz Sounder for Wideband Radio Channel Characterisation”, IADAT International Conference on Education (IADAT-e2004), Bilbao, Spain, 7-9 July 2004.

[4.6] Stuart K., Ndzi D. L., “Development and Evaluation of a Very Compact and Adaptable Low Cost 200 MHz Bandwidth Sounder”, IADAT International Conference on Telecommunications and Computer Networks (IADAT-tcn2004), San Sebastian, Spain, 1-3 December 2004.

[4.7] Austin J., Ditmar W. P. A., Lam W. K., Vilar E., Wan K. W., “A Spread Spectrum Communication Channel Sounder”, IEEE Transaction on Communications, Vol. COM-45, No. 7, July 1997, pp. 840-847.

[4.8] Lam W. K., “Wide-band Transhorizon Channel Sounding at X-band”, Ph.D. Thesis, Department of Electrical and Electronic Engineering, University of Portsmouth, U.K., May 1995.

[4.9] Ndzi D. L., “Statistical Characterisation of a Wideband Transhorizon Link at 11.647 GHz”, Ph.D. Thesis Department of Electrical and Electronic Engineering, University of Portsmouth, U.K., April 1998.

[4.10] Ndzi D. L., Austin J., Vilar E., “Wideband Transhorizon Channel Characterization”, Radio Science, Vol. 36, No. 5, September/October 2001, pp. 965-980.

[4.11] Stuart K., “Wideband Channel Sounder Development and Investigation of Spatial and Temporal Variations in Wireless Communication Channels”, Ph.D. Thesis Department of Electronic and Computer Engineering, University of Portsmouth, U.K., November 2007.

[4.12] Godfrey K., “Perturbation Signals for System Identification”, Prentice-Hall, London, UK., 1993.

[4.13] Pickholtz R., Schilling D., Minstein L., “Theory of Spread-Spectrum Communications – A Tutorial”, IEEE Transactions on Communications, Vol. 30, No. 5, May 1973, pp. 855-884.

CHAPTER 5

Channel Estimating Algorithm: Singular Value Decomposition Prony Algorithm

Abstract:

This chapter presents a brief introduction of channel impulse estimation using Fast Fourier Transform. Detailed formulation of the Singular Value Decomposition Prony algorithm is presented followed by the test results which confirm the superior performance of the SVDP algorithm when compared to the FFT technique.

5.1 Introduction

Channel sounder measurements are either done in the time or frequency domain. Measurements in the time domain often use the correlation technique. Measurements in the frequency domain benefits from high speed channel sampling. However, to gain insight into the channel structure, the channel impulse response must be estimated from the measured channel transfer function. Fourier transform is a classical method that is often used to transform channel responses between time and frequency domains. To address the problem of limited impulse response resolution and inherent assumption of periodicity of Fourier Transform technique, a number of parametric channel estimating algorithms have been developed. Amongst the most popular parametric methods is the Maximum Likelihood algorithms [5.1][5.2]. Key factors to take into consideration when selecting a parametric algorithm include the accuracy of the results, speed of convergence of the method and the computation time. In this research, the Singular Value Decomposition Prony (SVDP) algorithm, which is based on the Prony algorithm and was first proposed in [5.3], was selected for its accuracy and fast computational time. It is also an appropriate method for analysing wideband multipath fading channels characteristics [5.3][5.4].

5.2 Fourier Transform

Fourier transform (FT) is a classical method that is often used to transform channel responses between time and frequency domains. Conventionally, signal in time domain

and frequency domain are represented by $x(t)$, and $X(\omega)$, respectively. Fourier transform equation is given by

$$X(\omega) = \int_{-\infty}^{\infty} x(t)e^{-j\omega t}dt \tag{5.1}$$

The equivalent inverse Fourier transform that can be used to convert the signal from the frequency domain to time domain is given by

$$x(t) = \frac{1}{2\pi}\int_{-\infty}^{\infty} X(\omega)e^{j\omega t}d\omega \tag{5.2}$$

The discrete time signal is represent by the discrete Fourier transform (DFT)

$$F[n] = \sum_{k=0}^{N-1} f[k]e^{-j\frac{2\pi}{N}nk} \quad ; (n = 0{:}\, N-1) \tag{5.3}$$

and its inverse form is given by

$$f[k] = \frac{1}{N}\sum_{n=0}^{N-1} F[n]e^{j\frac{2\pi}{N}nk} \quad ; (k = 0; N-1) \tag{5.4}$$

where N is the number of sampled data. The problem of Fourier transform in wideband applications is the limitation of its resolution. The discrete Fourier transform time delay resolution is equal to

$$DFT\ resolution = \frac{1}{Measurement\ Bandwidth} \tag{5.5}$$

For example, for signals with bandwidths of 31.25 MHz and 200 MHz the maximum time delay resolutions will be 32 ns and 5 ns, respectively, assuming a perfect rectangular spectrum.

5.3 Singular Value Decomposition Prony (SVDP)

Due to the problems of limited resolution and sidelobes that are associated with the use of the Fast Fourier Transform (FFT) algorithm, an algorithm that does not suffer from these limitations was required. Some alternative approaches use fewer parameters such as the

fixed tap-delay model of Rummler [5.5] and the frequency domain polynomials of Greenstein [5.6] but they are not physically realistic although they are used to fit models to experimental data. The basic procedure of using parametric techniques to estimate any channel is a three stage process [5.7]:

i) choose a suitable parameterised model to fit to the measured data;
ii) formulate and implement an algorithm that gives the best fit of the model to the data; and
iii) use the parameter values from the best fit to characterise the channel and infer the underlying propagation mechanisms.

Singular Value Decomposition Prony (SVDP) algorithm [5.1][5.8][5.9] which is a parametric technique, can be formulated to follow this process.

The received multipath signals through wireless channels can be represented as a sum of finite set of multipath signals from the transmitter with different amplitudes and time delays (complex amplitude and phase). Each multipath component experiences one or a combination of reflection, refraction, diffraction or scattering mechanism or pure attenuation along its path. The set of finite multipath signals can be represented by discrete rays or a set of impulses, given by

$$h(t) = \sum_{n=1}^{N} a_n \delta(t - \tau_n) \tag{5.6}$$

where a_n is the ray amplitude, τ_n is the delay time an N is the number of multipath components. From Equation (5.6) and following the basic concept of parametric analysis, an algorithm must estimate the amplitude, a_n, and delay time, τ_n, for each multipath signal component (ray path). The unknown quantities are the number of multipath components, the complex amplitudes and their corresponding time delays.

The Fourier transform of Equation (5.6) is the channel transfer function $H(j\omega)$

$$H(j\omega) = \sum_{n=1}^{N} a_n e^{-j\omega\tau_n} \tag{5.7}$$

Each spectral line of the channel transfer function has a minimum frequency, f_0, and a corresponded fundamental angular frequency, $\omega_0 = 2\pi f_0$. The frequency of the spectral

lines increases by $i\omega_s$ across the bandwidth where ω_s is the sampling frequency in rad/s. Thus the angular frequency of the i^{th} spectral line can be represented by

$$\omega_i = \omega_0 + i\omega_s \tag{5.8}$$

Using this i^{th} component of the transfer function, H_i, can be expressed as

$$H_i = \sum_{n=1}^{N} a_n e^{-j(\omega_0 + i\omega_s)\tau_n} \qquad ; i = 0, 1, \dots, M-1 \tag{5.9}$$

Where M is the number of spectral components within the bandwidth of the transfer function. If two new parameters, b_n and z_n, are define as follows

$$b_n = a_n e^{-j\omega_0\tau_n} \tag{5.10}$$

$$z_n = e^{-j\omega_s\tau_n} \tag{5.11}$$

then

$$H_i = \sum_{n=1}^{N} b_n z_n^i \qquad ; i = 0, 1, \dots, M \tag{5.12}$$

From Equation (5.10) and (5.11), b_n can be used to represent the complex amplitude whilst z_n is a term having unity magnitude. From Equation (5.12), the index can be changed by replacing i with $i - m$

$$H_{i-m} = \sum_{n=1}^{N} b_n z_n^{i-m} \qquad ; i = 0, 1, \dots, M \tag{5.13}$$

Considering a linear combination of K arbitrary spectral components represented in Equation (5.13) by using a set of complex weighting coefficients, a_m, with $m = 0, 1, \dots, K$ and $a_0 = 1$, the equation can be rewritten as follows:

$$\sum_{m=0}^{K} a_m H_{i-m} = \sum_{m=0}^{K} a_m \sum_{n=1}^{N} b_n z_n^{i-m} \tag{5.14}$$

Equation (5.14) can also be represented by Equation (5.15).

$$\sum_{m=0}^{K} a_m H_{i-m} = \sum_{n=1}^{N} b_n z_n^{i-K} \sum_{m=0}^{K} a_m z_n^{K-m} \tag{5.15}$$

On the right hand side of Equation (5.15), the latter summation is represented in a form of a polynomial $P(z)$. This can be called the predictor polynomial and is given by

$$P(z) = \sum_{m=0}^{K} a_m z_n^{K-m} = \prod_{m=1}^{K} (z_n - z_m) \tag{5.16}$$

and from Equation (5.15), it can be represented by

$$H_i = -\sum_{m=1}^{K} a_m H_{i-m} \tag{5.17}$$

As shown in Equation (5.17) the channel transfer function is presented in terms of an autoregressive (AR) equation. This Equation is called the forward linear predictor (FLP) and it also shows that the value of each i^{th} spectral component can be related to its preceding K spectral components where K is the order of the FLP and $a_m$are called the AR coefficients. Using a similar analysis, its backward linear predictor (BLP), H_i^*, is expressed as

$$H_i^* = -\sum_{m=1}^{K} a_m H_{i+m}^* \tag{5.18}$$

The Prony method is based on the relationship between Equation (5.9), (5.12), (5.17), and (5.18) via the predictor polynomial (5.16).

In other words, assuming that the impulse response is represented by Equation (5.6), its equivalent channel transfer function samples H_i have an autoregressive (AR) structure. Equation (5.17), (5.18) and (5.16) are known as the forward prediction equation, the backward prediction equation and the predictor polynomial, respectively. These equations provide a means of processing measured versions of H_i according to the assumed ray model in Equation (5.6). The procedure can be summarised as follows:

iv) use the FLP Equation (5.17) and BLP Equation (5.18) to estimate the parameters a_m;

v) factorise the predictor polynomial, Equation (5.16), to obtain the z_n's and delays τ_n;
vi) use equations (5.9) and (5.12) to estimate the b_n's and the amplitudes a_n; and
vii) reconstruct the channel transfer function and compare with the measured data.

5.3.1 Estimation of the AR Coefficients

By taking advantage of the relationship between the AR structure of the sampled transfer function and the predictor polynomial, it can be deduced from Equation (5.11) that the ray time delays are closely related to the roots of the predictor polynomial $P(z)$.

As shown in [5.4] based on a fast algorithm published in [5.2] for finding these roots, it is necessary to estimate the AR coefficients from the empirical measurements. However in order to make the parameter estimation of the ray model more robust, a principal components approach has been introduced for estimating the AR coefficients [5.3]. To improve the resolution of closely spaced multipath signals, a combination of the FLP and BLP to estimate the AR coefficients is used. The forward-backward linear predictor (FBLP) which combines Equation (5.17) and (5.18), can be represented as a set of simultaneous equations that is written in matrix form as

$$\boldsymbol{Y} = \boldsymbol{S}\boldsymbol{\alpha} \tag{5.19}$$

Where $\boldsymbol{Y}$ is a data vector with dimensions of $2(M-K)\times 1$, whilst $\boldsymbol{S}$ is a data matrix of order $2(M-K)\times K$, and $\boldsymbol{\alpha}$ is the AR coefficient vector of order $K\times 1$. In the case of noiseless signal, the matrix $\boldsymbol{S}$ will have only K linearly independent columns but in practice the measured signals contain additive noise. In this case, the matrix $\boldsymbol{S}$ might contain more than K linearly independent columns. To remove the noise contributions, the K principal components from the matrix $\boldsymbol{S}$ are identified using the singular value decomposition (SVD) technique [5.12]. The signal component eigen values are separated from that of the noise. The data matrix $\boldsymbol{S}$ can be expressed as follows

$$\boldsymbol{S} = \boldsymbol{U}\Delta\boldsymbol{V}^H \tag{5.20}$$

From Equation (5.20) the columns of the unitary matrix $\boldsymbol{U}$ are denoted as the left singular vectors of matrix $\boldsymbol{S}$ which are equivalent to the eigenvectors of $\boldsymbol{S}\boldsymbol{S}^H$ whilst the columns of the unitary matrix $\boldsymbol{V}$ are the right singular vectors of matrix $\boldsymbol{S}$ which are equivalent to the eigenvector of $\boldsymbol{S}^H\boldsymbol{S}$ and finally Δ is a diagonal matrix given by

$$\Delta = \text{diag}(\lambda_1\ \lambda_2\ \ldots\ \lambda_w) \qquad \text{with } \lambda_1 \geq \lambda_2 \ldots \geq \lambda_w \tag{5.21}$$

For the eigenvalues, $\{\lambda_i : i = 1, 2, \ldots, w\}$, which are equivalent to the square root of the eigenvalues of $\boldsymbol{S}^H\boldsymbol{S}$, w is the rank of the matrix $\boldsymbol{S}$, whilst $\boldsymbol{S}^H$ is the Hermitian transpose of the matrix $\boldsymbol{S}$.

Although K is a number that represents the amount of singular values, the magnitude of the singular values can be used to distinguish the principal signal components from those of noise in the matrix $\boldsymbol{S}$. It can be separated into two groups, the one that contains all the large eigenvalues span the signal subspace whilst the rest span the noise subspace. By eliminating the noise subspace, the matrix $\boldsymbol{S}$ can be estimated by a lower rank matrix and then the SNR of the new matrix will be inherently increased. Finally the AR coefficients can be expressed and calculated using

$$\boldsymbol{\alpha} = \sum_{i=1}^{N} \frac{u_i^H \boldsymbol{X}}{\lambda_i^2} u_i \qquad with\ \boldsymbol{X} = -\boldsymbol{S}^H \boldsymbol{Y} \tag{5.22}$$

Where λ_i and u_i are the largest eigenvalues and the corresponding left eigenvectors of the matrix $\boldsymbol{S}$, respectively. The time delay for each impulse response can be calculated using Equation (5.23).

$$\tau_n = -\frac{arg(z_n)}{\omega_s} \tag{5.23}$$

Equation (5.12) can be written in a matrix form as

$$\boldsymbol{H} = \boldsymbol{Z}\boldsymbol{b} \tag{5.24}$$

where

$$\boldsymbol{H}^T = [H_1\ H_2\ \ldots\ H_M] \tag{5.25}$$

$$\boldsymbol{b}^T = [b_1\ b_2\ \ldots\ b_K] \tag{5.26}$$

$$\boldsymbol{Z} = \begin{bmatrix} z_1^0 & z_2^0 & \cdots & z_K^0 \\ z_1^1 & z_2^1 & \cdots & z_K^1 \\ \vdots & \vdots & \ddots & \vdots \\ z_1^{M-1} & z_2^{M-1} & \cdots & z_K^{M-1} \end{bmatrix} \tag{5.27}$$

In most channel measurements the number of rays is small compared to the number of spectral components in the transfer function i.e. $K \ll M$. Equation (5.27) therefore becomes an overdetermined system of equations. Vector b can be solved using a standard least-squares (LS) method as follows.

$$\boldsymbol{b} = (\boldsymbol{Z}^H \boldsymbol{Z})^{-1} \boldsymbol{Z}^H \boldsymbol{H} \tag{5.28}$$

Finally, the real amplitude a_n for each ray can be calculated using the relationship of Equation (5.10), $b_n = a_n e^{-j\omega_0 \tau_n}$.

5.3.2 Signal Zeros and Noise Zeros

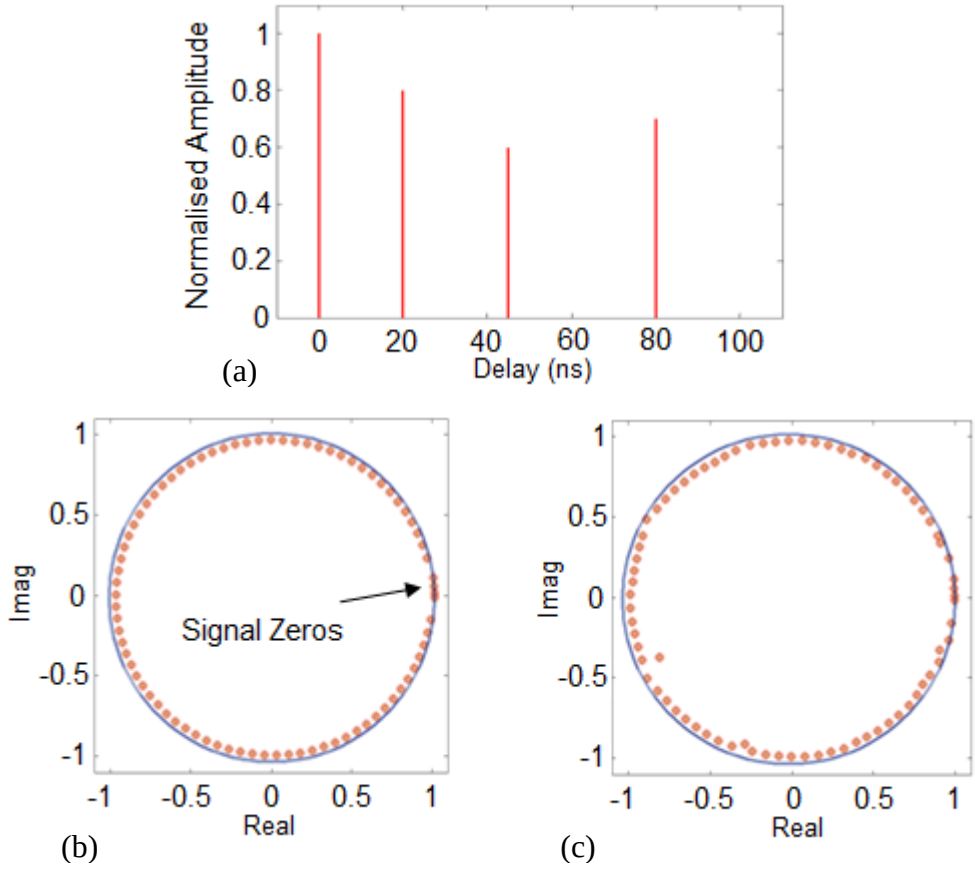

Figure 5.1 (a) Impulse Channel Response and its corresponding zeros in (b) without noise, and (c) with a signal to noise ratio of 25 dB

After determined the AR coefficients and factorizing ***P(z)***, the polynomial zeros can be plotted in a z-plane together with a unit circle. For a noiseless k-ray scenario, there should only be k zeros having unity magnitudes called signal zeros. While the rest of M-k zeros which are far away from the unit circle are called noise zeros. Figure 5.1 show channel impulse response and its related zeros with and without noise.

5.3.3 Noise effect and Model Order

In order to increase the resolution, the order of the forward-backward linear predictor (FBLP) K is set to be large although the number of the rays (signals), N, is small. Referring to Equation (5.11), if N ray scenario is assumed, there should only be N zeros with unity magnitude called signal zeros whilst the rest of $K - N$ extra zeros are noise zeros. This discrimination could easily be done by examining the closeness of the signal and noise zeros to the z-plane.

According to Equation (5.6), the analysis above is based on the noiseless ray model. If noise is taken into account, the sampled channel transfer function becomes an autoregressive-moving average (ARMA) [5.3] model process and the analysis above becomes invalid. From Wold's decomposition theorem in [5.1], it relates to the ARMA, MA and AR models and states that any stationary ARMA or MA process of finite variance can be used to represent a unique AR model of possibly infinite order. Similar to that, any ARMA or AR process can be used to represent a MA process of possibly infinite order. Therefore, an AR model with sufficiently high-order has been chosen because it can be used to represent a stationary ARMA process of finite variance. For the problems associated with the model order selection, if the order chosen is too high, a number of spurious rays may be produced. On the other hand, if the order chosen is too low, the rays may not be completely identified.

It is not easy to determine the order of the matrix by simply separating the signal and noise eigenvalues in low SNR conditions. This problem is known as *rank deficiency* [5.10].

A number of methods have been developed to calculate the most suitable rank and autoregressive coefficients number. The most popular methods are Akaike's final prediction error criterion (FPE), the Akaike Information Criterion (AIC), the criterion autoregressive transfer (CAT) of Parzen, and the Minimum Description Length (MDL) of Rissanen [5.11].

$$FPE(M) = \frac{N+M}{N-M}\xi_M \tag{5.29}$$

$$CAT(M) = \frac{1}{M}\sum_{m=1}^{M}\frac{N-m}{N\xi_m} - \frac{N-M}{N\xi_M} \tag{5.30}$$

$$AIC(M) = -2\log\left[\frac{\prod_{i=M+1}^{p}\lambda_i^{\frac{1}{(p-M)}}}{\frac{1}{p-M}\sum_{\iota=M+1}^{p}\lambda_\iota}\right]^{(p-M)N} + 2M(2p-M) \quad (5.31)$$

$$MDL(M) = -\log\left[\frac{\prod_{i=M+1}^{p}\lambda_i^{\frac{1}{(p-M)}}}{\frac{1}{p-M}\sum_{\iota=M+1}^{p}\lambda_\iota}\right]^{(p-M)N} + \frac{1}{2}M(2p-M)\log N \quad (5.32)$$

Where M is the model order, ξ_M is the linear prediction error of an M^{th} order model, $\lambda_1 > \lambda_2 > \ldots > \lambda_p$ are the eigenvalues and $\boldsymbol{p}$ is the rank of the data matrix.

In fact, the determination of the appropriate model order is not as easy as selecting one of the above criteria. However the high model order can increase the resolution, but too high an order may led to problems such as spurious spectral peaks and spectral line splitting.

The maximum order using the SVD approach should be $3/4M$ as suggested in [5.13]. However, if the length of data M is too large, K will also be too large and hence the noise zeros will be located closer to the unit circle that means it will compromise the advantage offered by the SVD technique in distinguishing between the signal and noise zeros.

Lam [5.10] suggested using MDL criterion for the rank determination, while for the model order selection criteria; Lau [5.9] used 10 randomly generated model orders between 1/3N to1/2N, and the best one chosen according to the lowest RMS Fitting Error. In this research, a decision was taken to use 10 model orders between 1/3N to 2/3N separated by a fix step. The best rank and model order values are chosen according to the lowest RMS fitting error after 10 iterations. A number of experiments have been carried out which showed that this criterion produces better results than the random selection method proposed in [5.9].

The SVDP algorithm developed in this research is shown in Figure 5.2. This is a more robust algorithm both in terms of identifying the number of rays and distinguishing between the signal and noise terms compared to the original Prony algorithm.

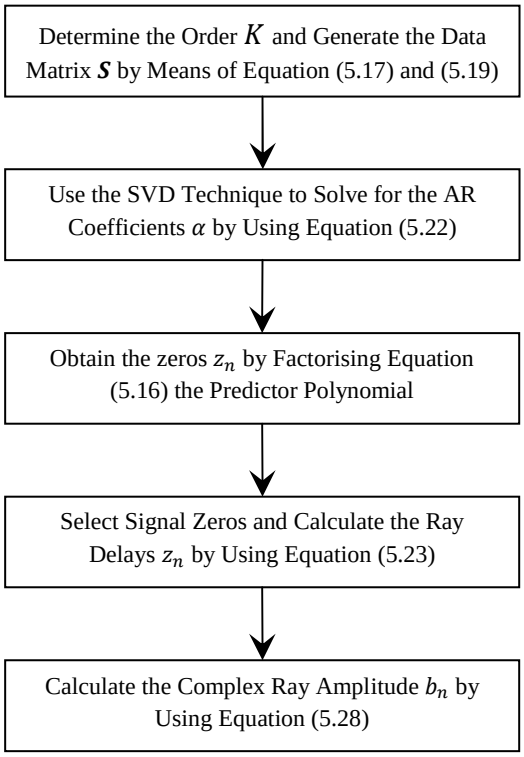

Figure 5.2 The Singular Value Decomposition Prony (SVDP) algorithm flowchart

5.3.4 Reconstructions of Channel Transfer Function

The accuracy of the SVDP algorithm can be assessed after the ray delays and amplitudes are obtained. If the reconstructed transfer function is represent by $\bar{\boldsymbol{H}}$, from Equation (5.24) it can be written as

$$\bar{\boldsymbol{H}} = Z\hat{\boldsymbol{b}} \tag{5.33}$$

where $\hat{\boldsymbol{b}}$ and $\hat{\boldsymbol{Z}}$ are the estimates of $\boldsymbol{b}$ and $\boldsymbol{Z}$, respectively, $\bar{\boldsymbol{H}}^T = [\bar{H}_1 \bar{H}_2 \ldots \bar{H}_M]$ and $\bar{H}_i$ represents the i^{th} reconstructed spectral component. Root mean square error between the measured and the reconstructed transfer functions is used to provide a quantitative measure of the accuracy of the algorithm using Equation (5.34).

$$e_{rms} = \sqrt{\frac{1}{M}\sum_{i=1}^{M}(H_i - \bar{H}_i)^2} \tag{5.34}$$

5.4 Algorithm Tests and Evaluation

In this section, the tests conducted to assess the accuracy of the SVDP algorithm are presented. Only a selected number of signal amplitude and time delay, and results are presented. The tests were designed to assess the following:

- ability to resolve closely spaced impulses;
- ability to correctly identify the number of multipath components and resolve their amplitudes and time delays; and
- performance of the algorithm in different SNR conditions.

The results obtained after processing the data using SVDP algorithm for signal transmissions over two different bandwidths are presented. An analysis of the algorithm's performance and behaviour under different signal to noise ratio (SNR) conditions is also presented.

In order to evaluate the performance of the SVDP algorithm, channel responses were simulated in the frequency domain. Assume that a channel response contains N_n components, each component of the channel response is represented in the frequency domain as

$$H_i(j\omega) = \sum_{n=0}^{N_n-1} a_n e^{j(\omega_0+i\omega_s)\tau_n} + n_0(i) \quad , i = 1, \dots, N_s \tag{5.35}$$

Where a_n and τ_n are the amplitude and time delay of the n^{th} multipath component, $\omega_0 = 2\pi f_0$ is the fundamental frequency of the signal, $\omega_s = 2\pi f_s$ is the frequency spacing between samples, $n_0(i)$ is the random noise component added to each sample scaled according to the required signal-to-noise ration and N_s is the number of samples in each sequence. In the channel response simulation used in this study, for 200 MHz, the parameter values were as follows: $f_0 = 1.900097656$ GHz and $f_s = 195.3$ kHz. The simulated TF is passed to the SVDP algorithm which estimates the time domain responds and reconstructs the channel TF (in red) as illustrated in Figure 5.4.

In this paragraph, the channel response simulation process used to evaluate the SVDP algorithm is explained. Firstly the amplitude and time delay of each component of channel impulse response are set, including the number of components. The noise free channel transfer function is computed using equation (5.35). The total power of the

transfer function is then computed. Using a random number generator, noise samples are generated. Depending on the desired signal-to-noise ratio, the noise signal is scaled and added to the simulated transfer function. The channel transfer function with the added noise is fed to the SVDP algorithm and the results are compared with the original.

The channel bandwidth used is 200 MHz at carrier frequency of 2 GHz with 1024 spectrum lines across the channel bandwidth. Examples of the reconstructed complex transfer functions are shown in red curves in the following sections. The results of 2-ray, 3-ray, and 4-ray simulations are presented in the next sections. Flow diagram of the simulated and estimated channel transfer function and impulse response described above is presented in Figure 5.3.

5.4.1 Multipath Resolution

Figure 5.4 shows the simulated and estimated transfer function and impulse response of a 2-ray model with the impulses separated by only 1 ns. The simulation was carried out with 50 dB signal to noise ratio. If FFT algorithm is used, the second ray will not be resolved because with a 200 MHz bandwidth, the multipath resolution of FFT is limited to 5 ns. The results of the simulation show that SVDP does not only resolve the multipath components but achieve an RMS error of 0.004 dB. As the SNR is reduced from 50 dB to 28 dB, the multipath components can still be resolved but the errors between the amplitude and delay of the second ray starts to increase. SVDP still achieves an RMS error of 0.08 dB. With the second multipath component having a time delay of 2 ns, similar results are obtained with SNR of 10 dB. Overall, when the time delay of the second ray is increased, the algorithm performs better and can achieve higher accuracies at lower SNRs. Table 5.1 shows the amplitudes and delay estimates for a 2-ray model with changing amplitude of the second ray. The simulations were carried out with a SNR of 25 dB. The table shows that SVDP maintains a good level of accuracy with varying multipath amplitude.

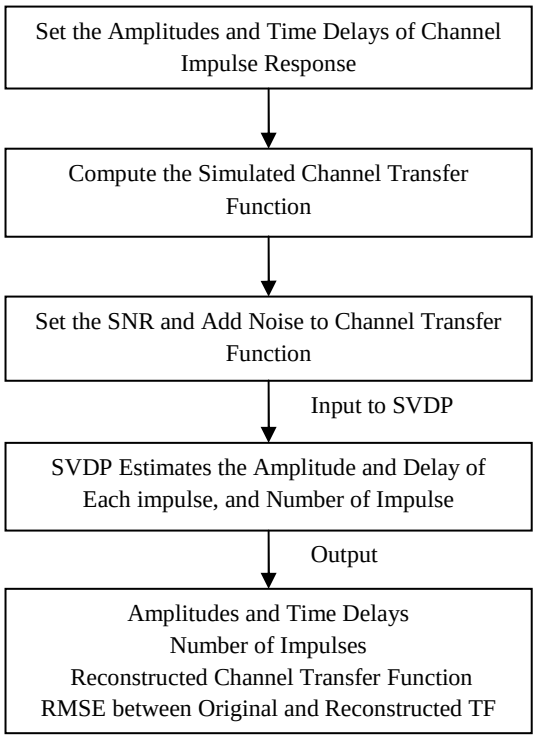

Figure 5.3 Flow diagram of the simulated and estimated transfer function and impulse response

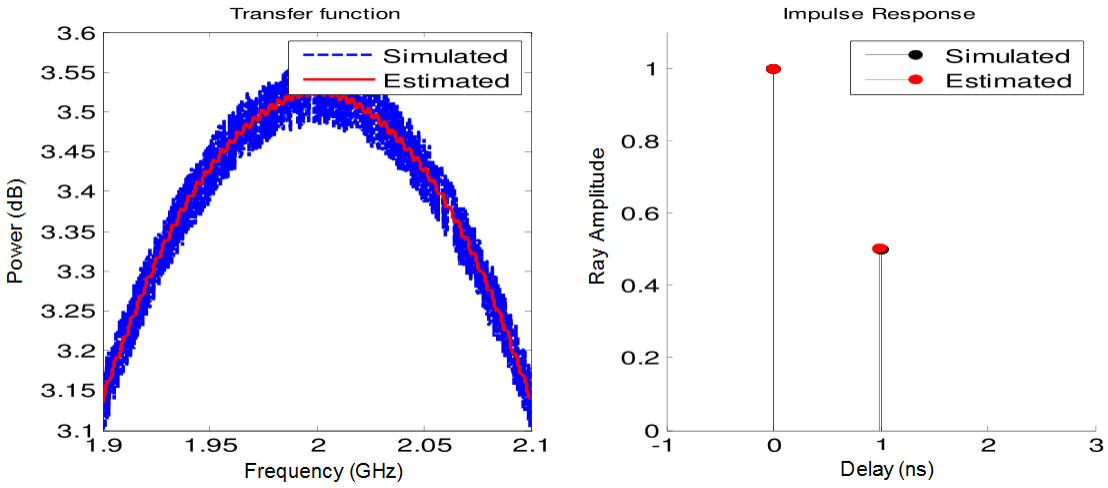

Figure 5.4 Simulated and SVDP estimated transfer function and impulse response (2-ray model $h(t) = 1 + 0.5\,\delta(t-1) + n(t)$, SNR= 50 dB)

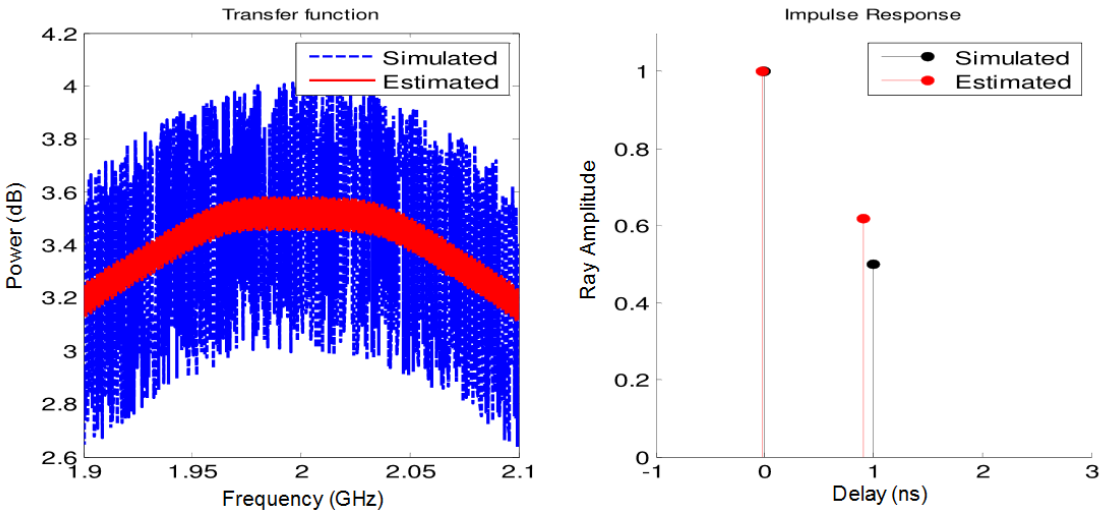

Figure 5.5 Simulated and SVDP estimated transfer function and impulse response (2-ray model $h(t) = 1 + 0.5\,\delta(t-1) + n(t)$, SNR= 28 dB)

At the time when the SVDP algorithm was being developed, another sounder with a bandwidth of 31.25 MHz was being used. The performance of the algorithm was assessed for use to process both the data measured using the 200 MHz channel sounder and the one with 31.25 MHz bandwidth. Some results of the assessment of the algorithm may include both bandwidths. In graphical form, the linear error (difference) between the simulated and estimated values of the amplitudes and time delay of the results presented in Table 5.1, Model 1 are shown in 0 for Ray 1 and 0 for Ray 2. It shows that the time delay errors between the simulated and estimated values are very small for 200 MHz bandwidth signal. In graphical form, it shows that the only high error was obtained for TF 101 Ray 2. However, on close examination of the values given in Table 5.1, it can be seen that this error was less than 0.006, hence considered to be negligible. The tests are well beyond the resolutions that could be expected for a 31.25 MHz and hence results using this bandwidth are inconclusive.

To assess the performance of SVDP for different SNR conditions, the following 2-ray model was used:

$$h(t) = 1 + 0.9\,\delta(t-2) + n(t) \tag{5.36}$$

In this model, Ray 2 has an amplitude of 0.9 and time delay of 2 ns. This was used to generate 32 transfer functions with SNR values between 5 and 50 dB in steps of 3 dB. The transfer function and, the estimated delays and amplitudes are presented in Figure 5.8. For clarity, the estimated amplitudes and delays are plotted in 2-dimensions in

Figure 5.9. It shows that at SNR less than 10 dB, the algorithm is not able to resolve the multipath components and hence identifies only one ray whose time delay is close to the centre between the two impulses but slightly skewed towards the one with the higher amplitude. The RMS error between the simulated and fitted transfer functions are plotted in Figure 5.10. For comparison, the study was repeated with Ray 2 amplitude set to 0.8 with a time delay of 8 ns. The results are presented in Figure 5.11. It shows that accurate estimates for both delay and amplitudes are obtained. At low SNR, only the amplitude of Ray 2 starts to loss accuracy.

Table 5.1 Simulated and estimate amplitudes and delays of a 2-ray model with SNR of 25 dB

	Model 1					**Model 2**				
	TF no.	Ray 1		Ray 2		TF no.	Ray 1		Ray 2	
		Simulate	SVDP Estimate	Simulate	SVDP Estimate		Simulate	SVDP Estimate	Simulate	SVDP Estimate
Amplitude	101	1.0	1.0	1.0	0.9949	301	1.0	1.0	1.0	0.81
Time		0	0	12	11.993		0	0.15	2.5	2.62
Amplitude	102	1.0	1.0	0.6	0.5996	302	1.0	1.0	0.6	0.55
Time		0	0	12	12.0075		0	0.04	2.5	2.53
Amplitude	103	1.0	1.0	0.3	0.3	303	1.0	1.0	0.3	0.31
Time		0	0	12	12.0001		0	-0.02	2.5	2.52
Amplitude	104	1.0	1.0	0.1	0.0981	304	1.0	1.0	0.1	0.06
Time		0	0	12	12.0188		0	0.05	2.5	3

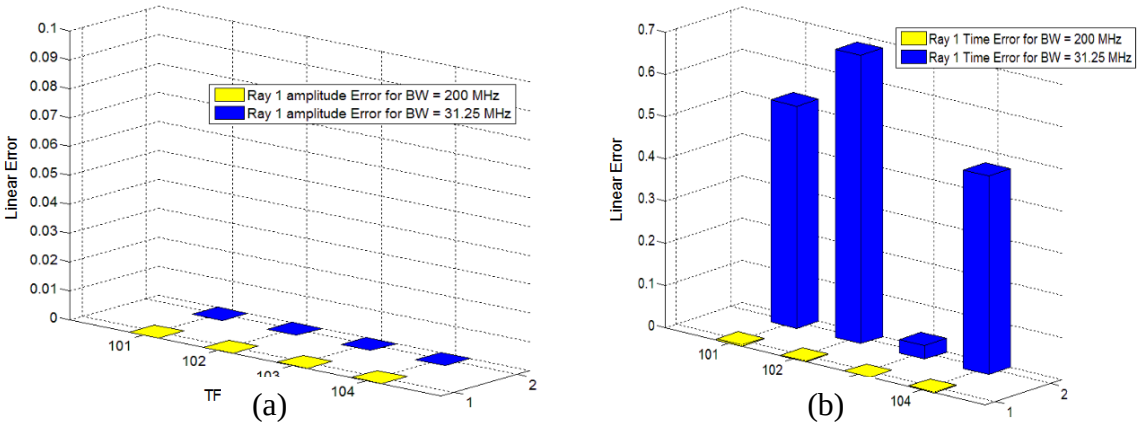

Figure 5.6 Linear error between simulated and SVDP estimated (a) amplitude, and (b) time delay of Ray 1 for 200 MHz and 31.25 MHz bandwidths

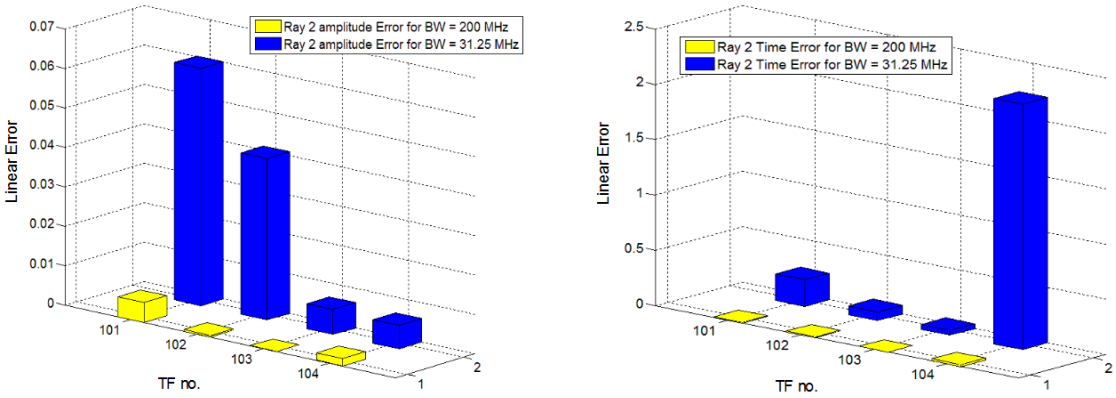

(a) (b)

Figure 5.7 Linear error between simulated and SVDP estimated (a) amplitude, and (b) time delay of Ray 2 for 200 MHz and 31.25 MHz bandwidths

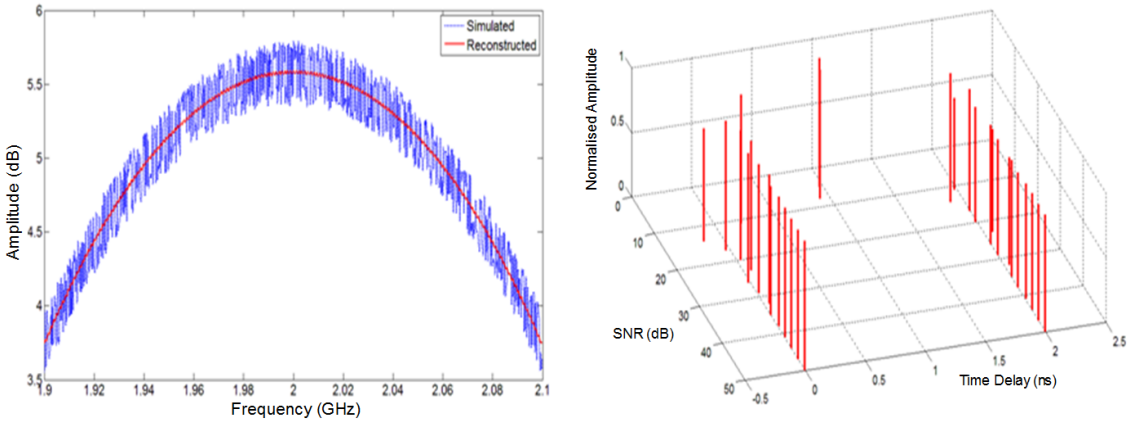

(a) (b)

Figure 5.8 (a) Simulated and reconstructed TF with 200MHz bandwidth, (b) estimated impulse response for different values of SNR

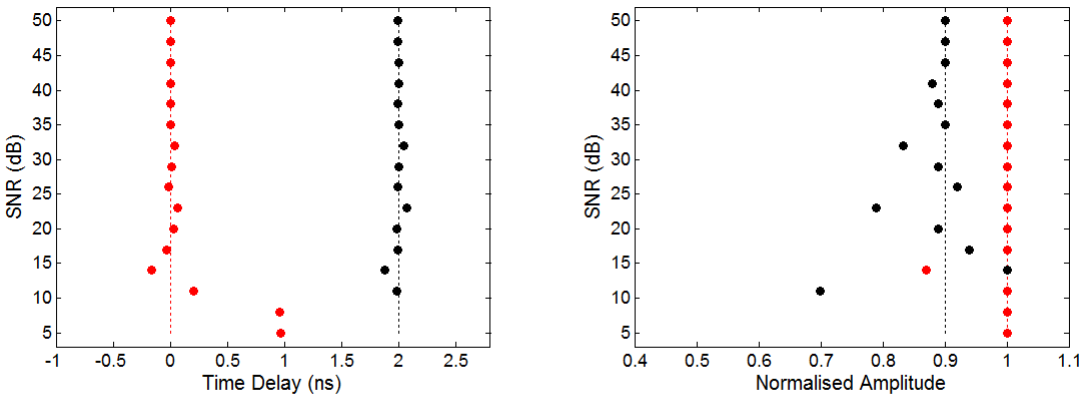

(a) (b)

Figure 5.9 Estimated parameter versus SNR (a) time delay, (b) amplitude for 200 MHz bandwidth

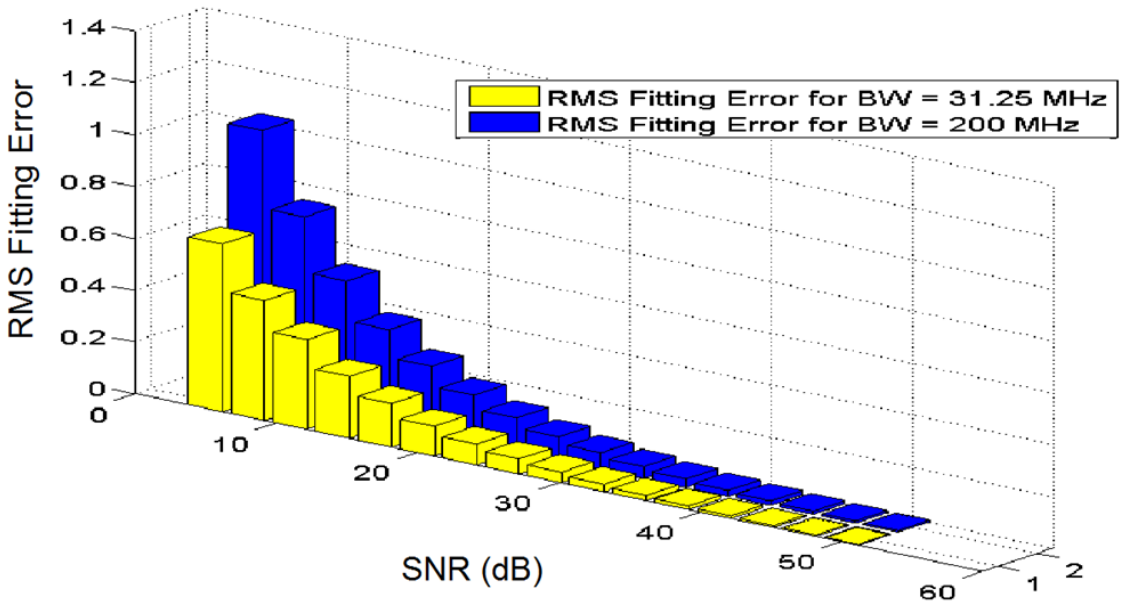

Figure 5.10 RMS error between the simulated and fitted transfer function for the 2-ray model for different SNR values

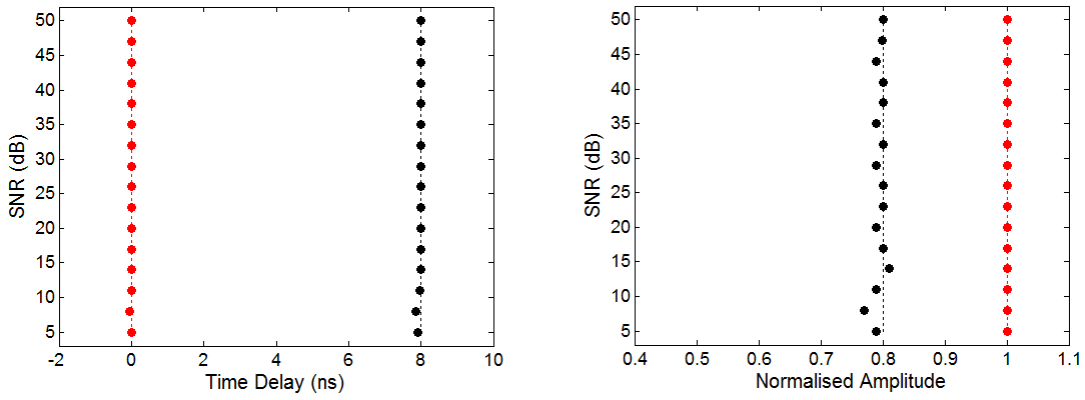

(a) (b)

Figure 5.11 Estimated parameter versus SNR (a) time delay, (b) amplitude for 200 MHz bandwidth and model $h(t) = 1 + 0.8\,\delta(t-8) + n(t)$

5.4.2 3-Ray Model

For large number of significant rays, the channel response starts to become more complex. To assess the performance of the algorithm, the following 3-ray model has been used:

$$h(t) = 1 + 0.8\,\delta(t-32) + 0.2\,\delta(t-80) + n(t) \tag{5.37}$$

The tests carried out using the 2-ray model were repeated. The results are presented in Figure 5.12 and Figure 5.13. It should be noted that there are significant separations

between these impulses. Nonetheless, the results show that SVDP achieve high accuracy for a wide range of SNR conditions. The simulated and fitted channel transfer functions are shown in Figure 5.14.

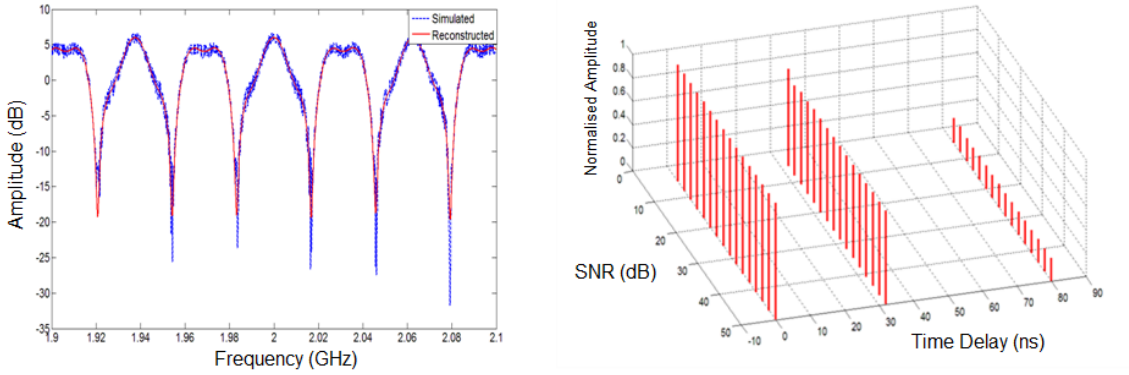

(a) (b)

Figure 5.12 (a) Simulated and reconstructed TF with 200MHz bandwidth, (b) estimated impulse response for different values of SNR for a 3-ray model

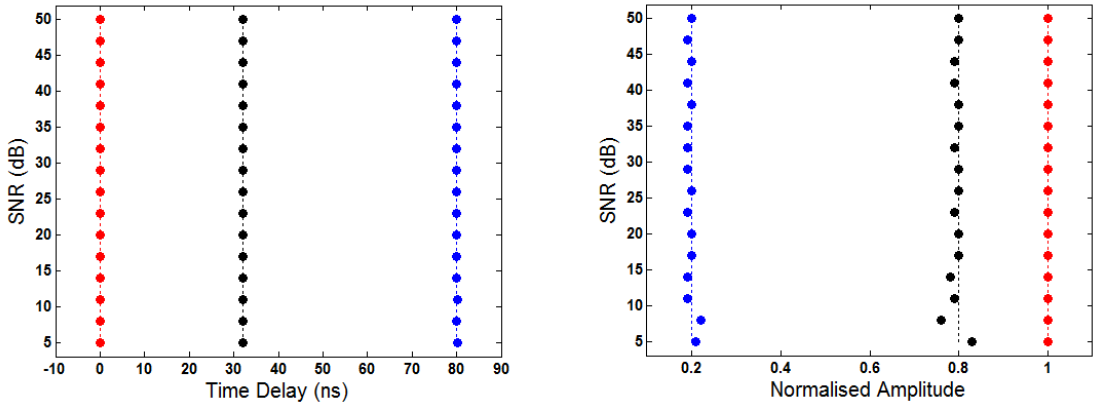

(a) (b)

Figure 5.13 Estimated parameter versus SNR (a) time delay, (b) amplitude for 200 MHz bandwidth for a 3-ray model

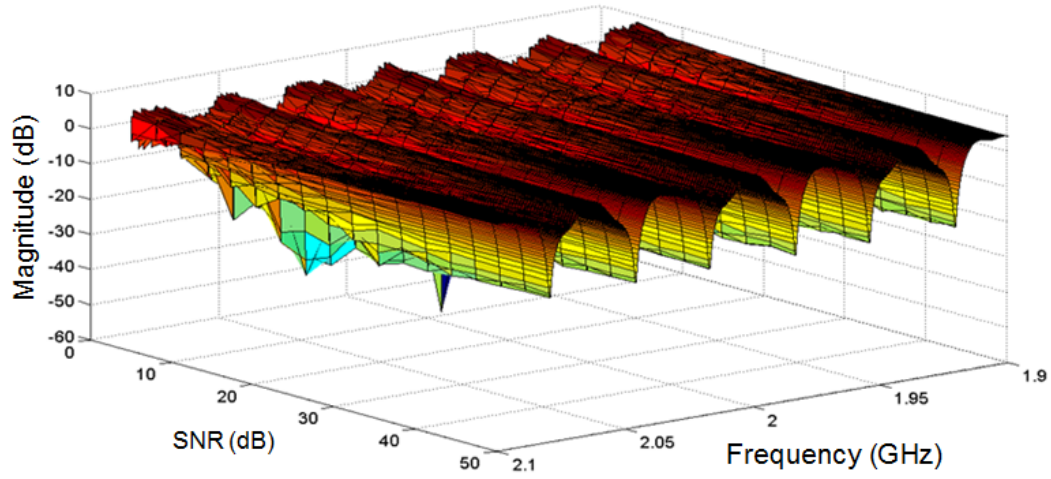

(a)

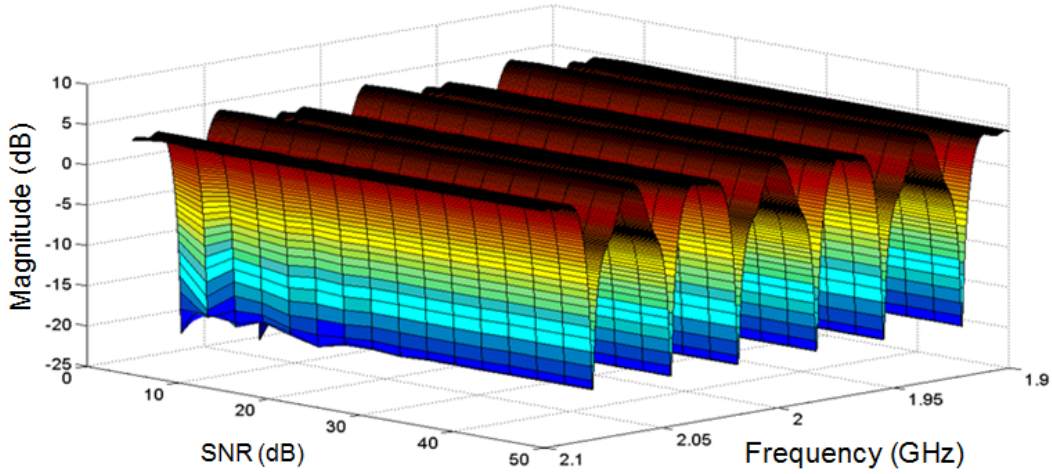

(b)

Figure 5.14 (a) Simulated channel transfer functions with different SNR values, and (b) SVDP fitted channel transfer functions (4-ray model)

5.4.3 4-Ray Model

The following 4-ray model has been simulated:

$$h(t) = 1 + 0.7\,\delta(t-4) + 0.5\delta(t-10) + 0.2\delta(t-20) + \ n(t) \qquad (5.38)$$

Figure 5.15 shows the results of the simulated and fitted channel transfer function and impulse response for SNR of 30 dB. The figure shows that accurate results are obtained. The simulated and estimated impulses superimpose on each other. For SNR=25 dB and SNR=10 dB, the results are given in Figure 5.16 and Figure 5.17. The algorithm

maintains its accuracy, resolving all multipath components even under low SNR conditions.

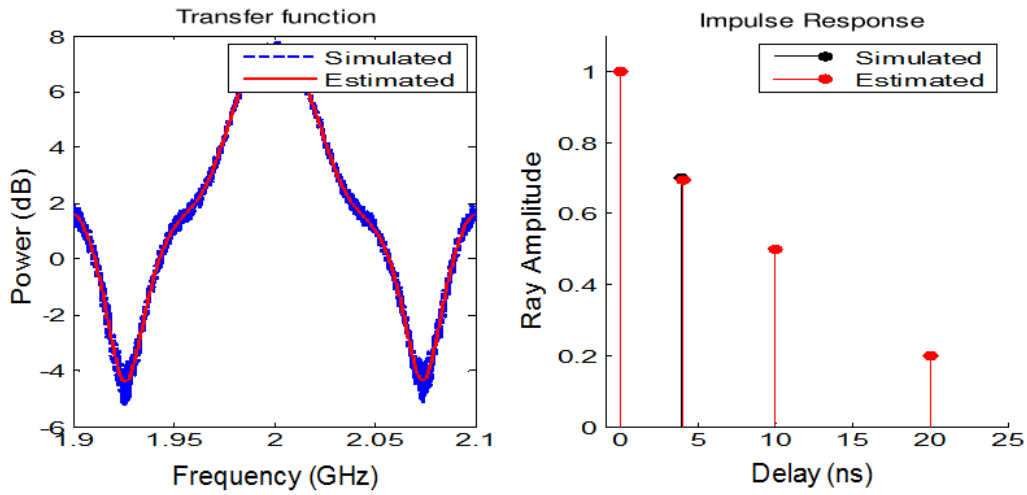

Figure 5.15 Simulated and SVDP estimated transfer function and impulse response (4-ray model, SNR=30 dB)

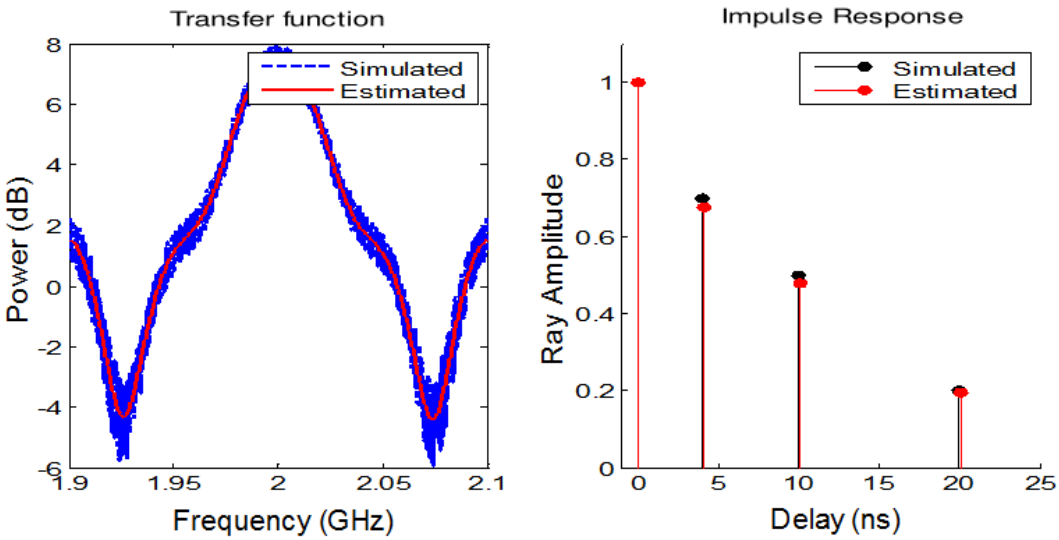

Figure 5.16 Simulated and SVDP estimated transfer function and impulse response (4-ray model, SNR= 25 dB)

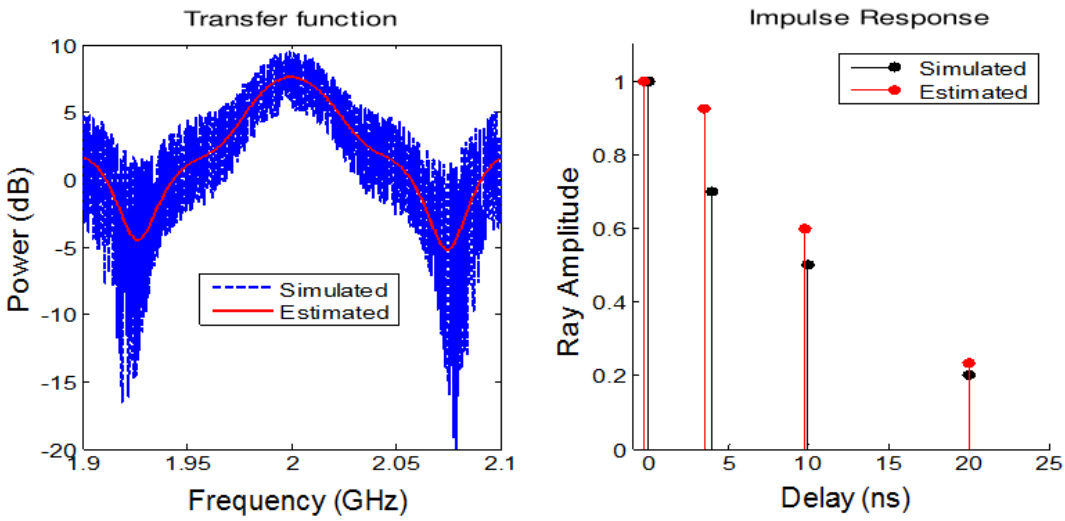

Figure 5.17 Simulated and SVDP estimated transfer function and impulse response (4-ray model, SNR= 10 dB)

5.5 Summary

The channel transfer function can be transformed to the corresponding impulse response using FFT algorithm or a parametric method. The development of a parametric algorithm requires an accurate model that describes the data. In this chapter, a parametric algorithm called Singular Value Decomposition Prony has been formulated and implemented for use to estimate the channel impulse response from measured channel transfer functions. Mathematical formulation and software implementation is often only half of the process. Through tests and evaluation, the algorithm has been fine tuned to give accurate estimates of the channel impulse response. Tests show that for signal to noise ratio of 10 dB and above, SVDP achieves accuracies up to 1 ns which, can only be achieve with signal bandwidth of 1 GHz with FFT algorithm. Most importantly, SVDP does not suffer from the periodic assumption problem of FFT. SVDP can also discriminate between signal and noise, an important capability in channel characterisation.

References

[5.1] Kay S. M., Marple, S. L., “Spectrum Analysis-A Modem Perspective”, Proc. IEEE, Vol. 69, November 1981, pp. 1380-1419.

[5.2] Marple L., “A New Autoregressive Spectrum Analysis Algorithm”, IEEE Transactions on Acoustics, Speech and Signal Processing, Vol. 28, No.4, August 1980, pp.441-454.

[5.3] Lau W. H., Austin J., Hewitt A., Vilar E., Martin L., “Analysis of the Time Variant Structure of Microwave Line-of-Sight Multipath Phenomena”, IEEE Transactions on Communications, Vol. 39, No. 6, June 1991, pp. 847-855.

[5.4] Hewitt A., Lau W. H., Austin J., Vilar E., “An Autoregressive Approach to the Identification of Multipath Ray Parameters from Field Measurements”, IEEE Transactions on Communications, Vol. 37, No. 11, November 1989, pp. 1136-1143.

[5.5] Rummler W. D., “A New Selective Fading Model: Application to Propagation Data”, Bell Syst. Tech. J., Vol. 58, No. 5, 1979, pp. 1037-1071.

[5.6] Greenstein L. J., Czekaj, B. A., “Modelling Multipath Fading Responses Using Mulitone Probing Signals and Polynomial Approximation”, Bell Syst. Tech. J., Vol. 60, No.2, February 1981, pp.193-214.

[5.7] Hewitt A., Lau, W. H., Austin, J., Vilar, E., “An Autoregressive Approach to the Identification of Multipath Ray Parameters from Field Measurements”, IEEE Transaction on Communications, Vol. 37, No. 11, November 1989, pp. 1136-1143.

[5.8] Hewitt A., Lau, W. H., Austin, J., Vilar, E., “An Autoregressive Approach to the Identification of Multipath Ray Parameters from Field Measurements”, IEEE Transaction on Communications, Vol. 37, No. 11, November 1989, pp. 1136-1143.

[5.9] Lau W. H., Austin, J., Hewitt, A., Vilar, E., Martin, L., “Analysis of the Time-Variant Structure of Microwave Line-of-sight Multipath Phenomena”, IEEE Transactions on Communications, Vol. 39, No. 6, June 1991, pp. 847-855.

[5.10] Lam, W. K. (1995). Wide-band Transhorizon Channel Sounding at X-Band. Ph.D. Thesis, Department of Electrical and Electronic Engineering, University of Portsmouth, UK.

[5.11] Raisanen, A. V. Lehto, A. (2002). Radio Engineering for Wireless Communication and Sensor Applications. London: ARTECH HOUSE, Inc

[5.12] Klema V. C., Laub, A. J., “The Singular Value Decomposition: Its Computation and Some Applications”, IEEE Transactions on Automatic Control, Vol. 25, No. 2, April 1980, pp. 164-176.

[5.13] Tufts D. W., Kumaresan R., “Estimation of Frequencies of Multiple Sinusoids: Making Linear Prediction Perform Like Maximum Likelihood”, IEEE Proceedings, Vol. 70, No. 9, September 1982, pp. 975-989.

CHAPTER 6

Channel Measurements and Data Calibration Processing

Abstract:

This chapter describes the measurements scenarios for both spatial and temporal variations. Details of the data acquisition strategy implemented are described together with the data calibration procedure used.

6.1 Introduction

The criterion for selecting measurement sites was to choose locations that represent possible sites for the deployment of high data rate wireless access point in an urban environment. The impact of moving vehicles on the radio channels is the main aspect to be investigated. Hence, a location with sufficient automotive traffic is necessary to enable the assessment of the impact on communication systems to be carried out. Moreover, measurements in controlled locations were conducted and compared to the measurements in the real traffic environment.

Although conceived to transmit up to 300 m, most WLAN access points are used within 30 m. In this study, path lengths up to 30 m were used to study the effects of vehicles moving parallel to the wireless transmission path. Most research studies have been done over longer path lengths [6.1] - [6.4] and no attention has been paid to picocell distances in urban environment.

6.2 The Measurement Scenarios

Omni-directional antennas were used at both the transmitter and the receiver. These were used for both spatial and temporal varying radio channel investigations. For the spatial variation assessments, the measurements were conducted in three locations as listed in Table 6.1.

Figure 6.1 shows a scenario in front of Burnaby Building and Figure 6.2 shows a scenario at rear of Anglesea Building. For both these scenarios, the transmitter and receiver antenna heights were set 2.5 m and 1.6 m.

Table 6.1 Measurement locations

Location	Maximum Distance (m)	Measurement Steps (m)	Figure
In front of Burnaby	30.5	0.5	Figure 6.1
In front of Anglesea	20	0.3	Figure 6.3
At rear of Anglesea	15	0.5	Figure 6.2

In front of Anglesea Building, the antenna heights for the transmitter and receiver were set, firstly at 2.5 m and 1.6 m with the distance separation increased in steps of 0.3 m, and secondly at 5.5 m and 1.6 m with the distance separation increased in steps of 2 m as shown in Figure 6.3 and Figure 6.4.

Vehicle induced temporal variation of radio channels were studied in two locations. The measurements were conducted at;

- the rear of Anglesea Building and
- in front of Anglesea Building.

Figure 6.1 The measurement scenario in front of Burnaby Building

To investigate the temporal variations [6.5]-[6.7] of a wireless communication link, a car and a van were used in a controlled experiment to assess the impact of vehicle size on the

radio channel. The separation distance was fixed at 10 m and 14 m as shown in Figure 6.5. This was conducted in the car park at the rear of Anglesea Building.

The measurements in front of Anglesea Building were to study a possible realistic urban channel scenario of a temporal varying channel induced by mobile traffic as shown in Figure 6.4.

Figure 6.2 The measurement at rear of Anglesea Building

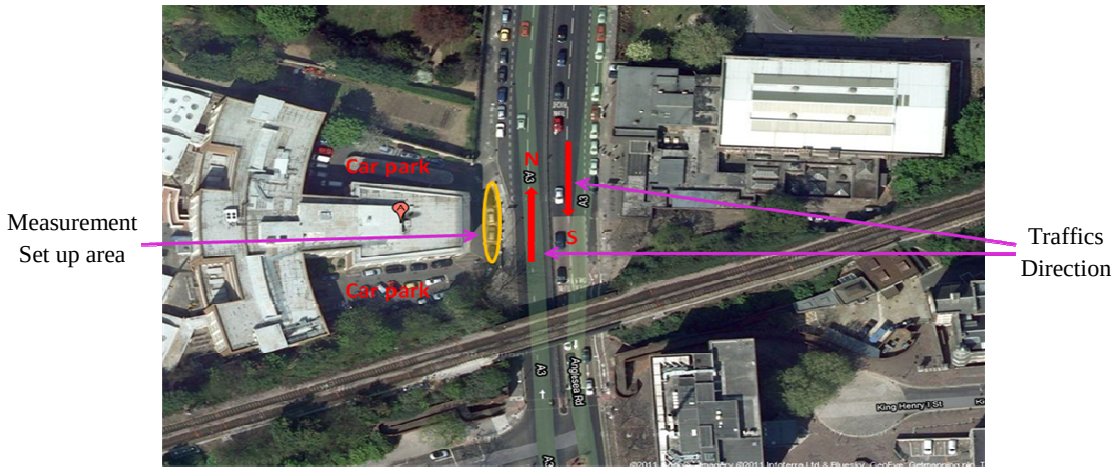

Figure 6.3 Top view of the measurement scenario in front of Anglesea Building

Figure 6.4 Transmitter and receiver position during measurement

Figure 6.5, Figure 6.6 and Figure 6.7 show the real controlled scenario employed to assess the impact of vehicle moving near the channel. The transmitter (Tx) was fixed and the receiver set up at position 1 (Rx1) and then at position 2 (Rx2).

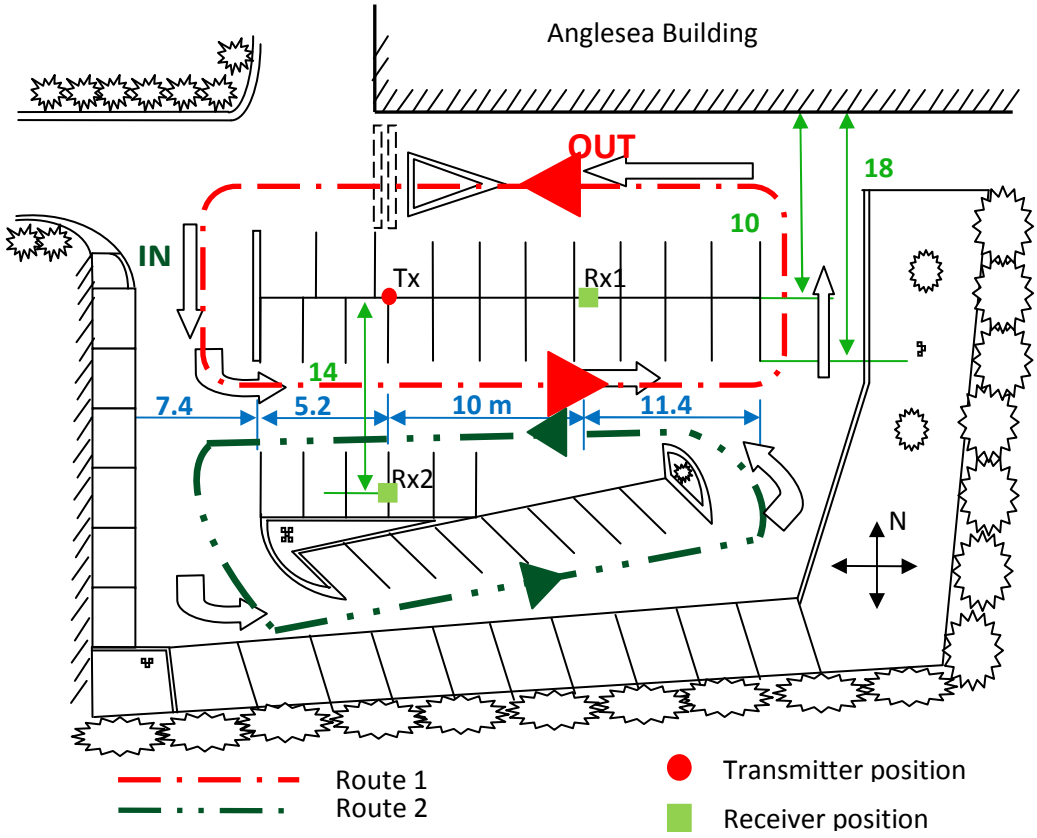

Figure 6.5 The measurement scenario at Anglesea Building rear car park

Figure 6.6 The measurement scenario at Anglesea Building rear car park with the transmitter and receiver set up at position 1

The directions of vehicles moving in the controlled area are shown in Figure 6.5. There are 2 routes, the first route is represented by the red oval and the second route is represented by the green oval. The distance separations between the transmitter and receiver are 10 m and 14 m for the measurements at positions 1 and 2, respectively.

Figure 6.7 The measurement scenario at Anglesea Building rear car park with the transmitter and receiver set up at position 2

Figure 6.8 and also Figure 6.3 and Figure 6.4 illustrate the real traffic measurement scenario used as an example of an urban area in front of Anglesea Building. In this location, the measurements were conducted for both spatial and temporal variations due to the real traffic influenced on the radio channel.

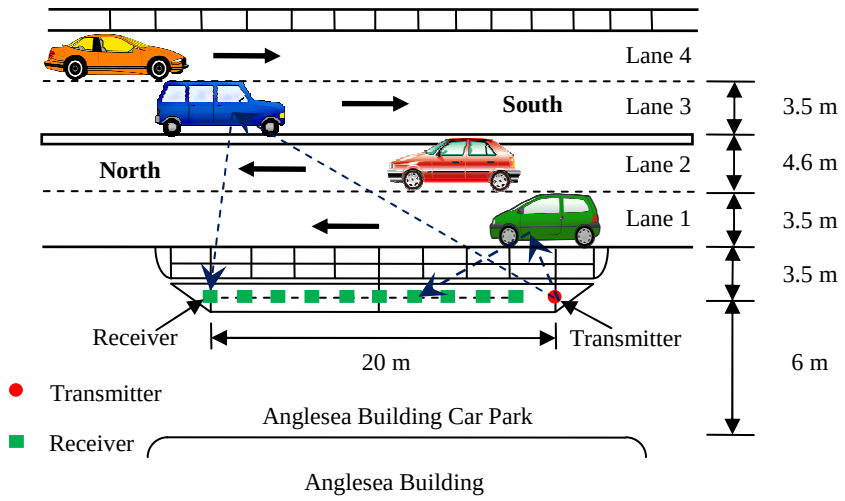

Figure 6.8 Measurement scenario in front Anglesea Building

Vehicle traffic induced variation can also affect WLAN systems in Buildings that are located close to roads. The results from the study would be applicable for mobile users that may be walking along a road with passing vehicles. The road has 4 lanes of which the nearest 2 lanes (lane 1-2) go north and the other 2 lanes in the far side (lane 3-4) go south. The measurement system was set up such that the transmission path was parallel to the direction of the traffic. Therefore, the LOS signal was never obstructed because the traffics did not traverse the LOS path between the transmitter and the receiver. The distances from the LOS path perpendicular to each lane of the road from the nearest to the furthest lane were 3.5 m, 7 m, 11.6 m and 15.1 m, respectively.

The vehicle speed was maintained at 10 mph (4.4704 m/s) in the controlled experiment whilst in the actual urban area in front of Anglesea Building the vehicle speeds were around 30 mph (13.4112 m/s).

6.3 Data Acquisition Strategy

The wideband channel sounder was used to measure the channel transfer function. With a 200 MHz bandwidth, the data captured are described using the following terms:

- snapshot – a complete sequence of the Pseudo Random Gaussian Noise (PRGN) signal containing 4096 complex data samples,
- averaged snapshot – the resulting 4096 complex samples produced by averaging N_a snapshots captured consecutively,
- data block consisting of 240 averaged snapshots, and
- data file made up of 4 data blocks.

As illustrated in Figure 6.9, the data acquisition process can be described as follows

- each averaged snapshot of channel transfer function is the average of N_a. Here N_a is the number of averaged snapshots,
- 240 averaged snapshots form a data block,
- 4 groups of data block form a data file,
- T_{sg} is the time between snapshots,
- T_{as} is the time to capture one averaged snapshot,
- T_{dbg} is the time between data block,
- T_{db} is the time to capture one data block, and
- T_{df} is the time to capture one data file.

To study time-variant channels, the channel must be sampled as fast as possible to capture changes in the channel and its evolution with time.

There was also a need to implement continuous measurement for long periods of time that can be used to gain a better insight into the events during the measurement. The channel was set up to measure at the rate of 5.425 kHz. Each averaged channel transfer function is captured every 184.32 µs and thus a data block containing 240 averaged channel transfer functions is captured in a total time of 44.24 ms. The vehicle speeds in urban areas can be expected to be around 30 mph (13.4112 m/s) and therefore a vehicle would travel a distance of 0.593 m in 44.24 ms. To ensure that the data is transferred to the computer hard-drive reliably via the PCI-bus, a time gap between each data block was chosen as 256 ms to keep the volume of data to a manageable level [6.8]. A total of 3840 channel transfer functions were measured at each position.

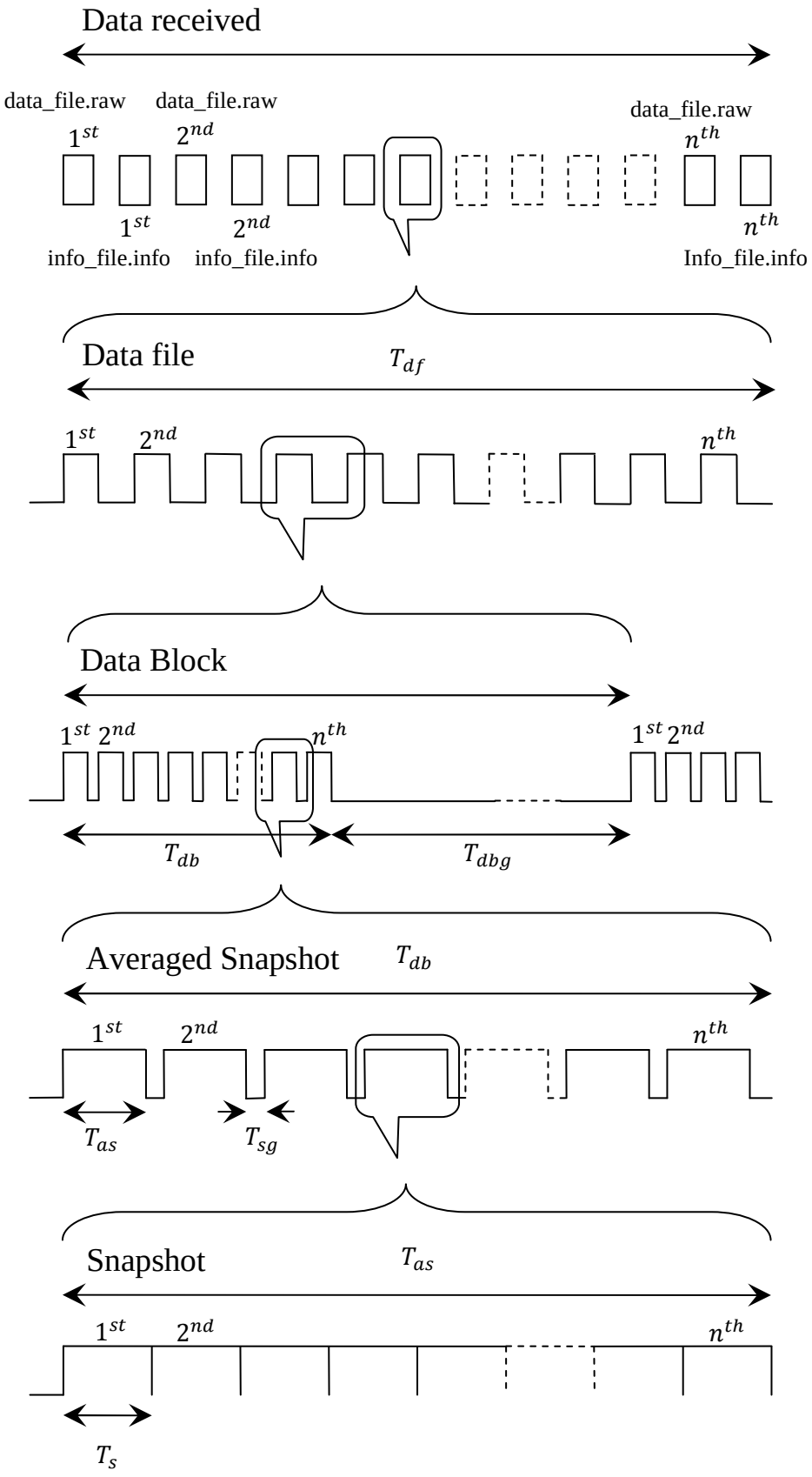

Figure 6.9 Data acquisition strategy

6.4 Omni-directional Antenna

Figure 6.10 shows the horizontal and vertical radiation patterns of the omni-directional antennas used at the centre frequency of 2 GHz. The measured radiation pattern shows that there is a slight drop in radiated power between 110° and 360° in azimuth with a maximum drop of approximately 6 dB occurring at 180°. In elevation, the radiation pattern is asymmetrical about its axis. At the mounted position, the maximum power dropped is approximately 20 dB at 180° and 345° in the zenith angles. This antenna pattern is only expected to have an effect on the signal components that may reach the receiver antenna from the direction where the gain is very different from that in the LOS. In the LOS direction the effect of the antenna is calibrated out during data processing.

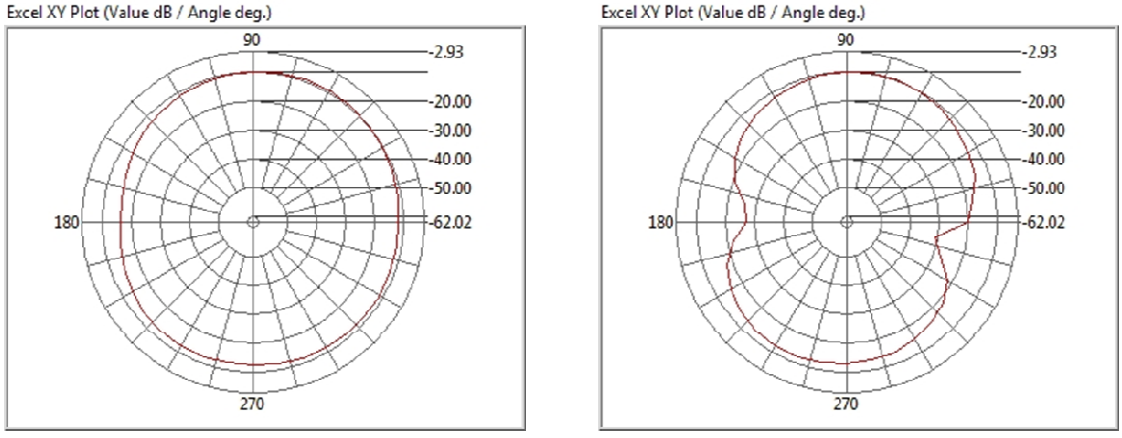

(a) Horizontal pattern (b) Vertical pattern

Figure 6.10 Omni-directional antenna pattern used in the experiments

6.5 Data Calibration

To calibrate out the system response, a reference file captured in an anechoic chamber can be used.

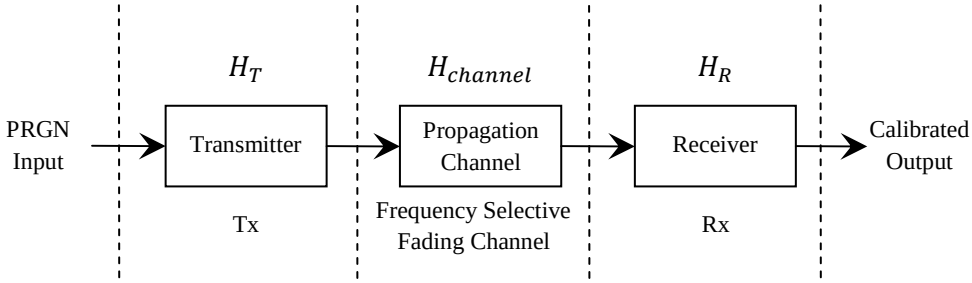

Figure 6.11 The channel transfer function's calibration

As shown in Figure 6.11, the calibration of the channel transfer function is necessary because the received signal transfer function is a combination of the whole system response including that of the transmitter, channel and the receiver. At the transmitter, out transfer function is

$$H_T = H_{Tx}H_{Tant} \tag{6.1}$$

This includes the transfer functions of the transmitter and the transmitter's antenna. At the receiver, its overall transfer function is

$$H_R = H_{Rant}H_{Rx}H_{spu} \tag{6.2}$$

which includes three components; the transfer functions of the receiver's antenna, the receiver and its averaging unit. Consider the input signal to be S_{PRGN} and the output of the receiver to be G_{mea}. Therefore,

$$G_{mea} = S_{PRGN}(H_T H_{channel} H_R). \tag{6.3}$$

It shows that the overall transfer function of the system is combined with the transfer function of the channel. The transfer function of the system needs to be eliminated to extract only the channel transfer function. A reference channel transfer function and calibrated output expressed as H'_{ref} and G'_{ref}, can be used to calibrate the measured signal. It is represented as

$$G'_{ref} = S_{PRGN}\left(H_T H'_{ref} H_R\right) \tag{6.4}$$

Dividing Equation (6.3) by (6.4) gives

$$\frac{G_{mea}}{G'_{ref}} = \frac{H_{channel}}{H'_{ref}} \tag{6.5}$$

Here H'_{ref} represents an ideal channel response measured under high signal-to-noise ratio (SNR) condition and exhibits a flat spectrum. Then

$$\frac{H_{channel}}{H'_{ref}} \approx H_{channel} \tag{6.6}$$

Obviously from Equation (6.6), all system responses, both magnitudes and phases, are eliminated and therefore the channel transfer function $H_{channel}$ can be estimated as the response of the channel.

6.6 Summary

Temporal varying channel measurements have been divided into two groups; measurement in a controlled environment and measurement in an actual urban area. Spatial and temporal variations of the radio channel will be studied to better understand the effects of moving objects on wireless channels. The measurement set-up at each location has been explained. The data acquisition strategy that has been implemented is presented. From the calculation, taking into account the speed of vehicles, the channel sampling speed used would allow the effect of vehicles to be measured every 0.0248 mm distance travelled. This is more than adequate to study channel variations. The data calibration procedure to eliminate the system response is presented. The results of the measurements will be presented in chapter 7.

References

[6.1] Torres R. P., Cobo B., Mavares D., Medina F., Loredo S., Engels M., "Measurement and Statistical Analysis of the Temporal Variations of a Fixed Wireless Link at 3.5 GHz", Wireless Personal Communications: Springer 2006, Vol. 37, 2006, pp. 41-59.

[6.2] Naz N., Falconer, D. D., "Temporal Variations Characterization for Fixed Wireless at 29.5 GHz", IEEE 51st, Vehicular Technology Conference Proceeding, Tokyo, Vol. 3, August 2002, pp. 2178 - 2182.

[6.3] Okumura Y., Ohmori E., Kawano T., Fukuda K., "Field Strength and Its Variability in VHF and UHF Land Mobile Radio Services", Review of the Electrical Communications Laboratory, Vol. 16, Sept - Oct 1968, pp. 825-873.

[6.4] Hata M., "Empirical Formula for Propagation Loss in Land Mobile Radio Services", IEEE Trans on Veh. Tech., Vol. 29, No. 3, March 1980, pp. 317-325.

[6.5] Sklar B., "Rayleigh Fading Channels in Mobile Digital Communication Systems Part I: Characterisation", IEEE Communications Magazine, Vol. 35, No. 7, July 1997, pp. 90-100.

[6.6] Sklar B., "Rayleigh Fading Channels in Mobile Digital Communication Systems Part II: Mitigation", IEEE Comm Mag, Vol. 35, No. 7, July 1997, pp.102-109.

[6.7] Shankar P. M., "Introduction to Wireless Systems", John Wiley & Sons, Inc., USA, 2002.

[6.8] Trulove J., "Build Your Own Wireless LAN", McGraw-Hill, New York, USA, 2002.

CHAPTER 7

Results and Discussions

Abstract:

This chapter presents the measurement results. The spatial and temporal analyses of the data have been carried out. The propagation models and statistical probability functions have been used to investigate and analyse the radio channel. The data measured from the real channels have been separated into event and non-event sets and have been used to discuss the impact of vehicles on wideband channels.

In this chapter, the results of the measurements in the controlled and real urban areas are presented and discussed from a signal propagation perspective. Qualitative and quantitative analysis of signal variation in both space and time are presented. To assess the spatial and temporal variations, empirical models and statistical probability density functions have been used.

7.1 Signal Variation

Figure 7.1 shows an example of signal power variation with time and the impact of a vehicle on received signal. It shows that a vehicle introduces variations in the signal levels with deep fades.

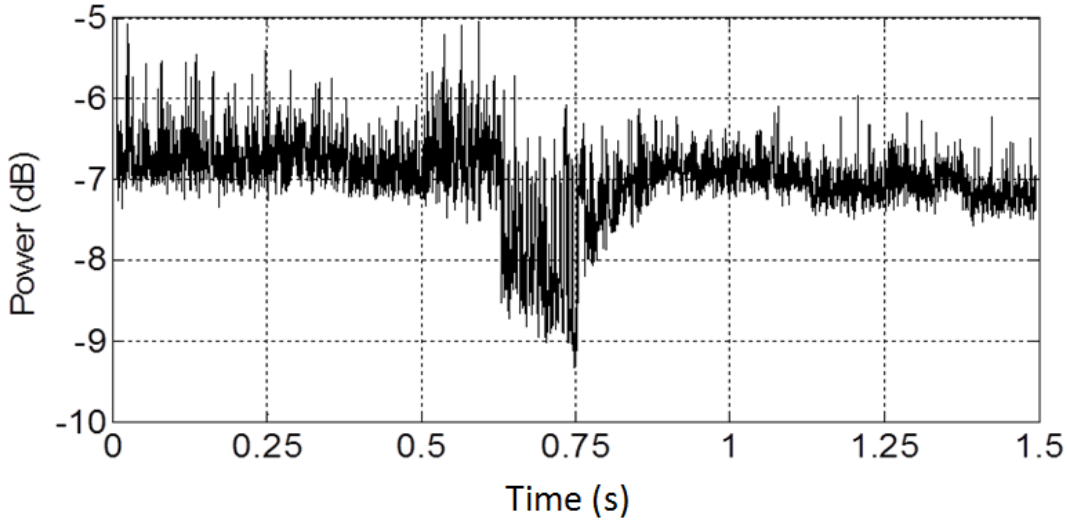

Figure 7.1 Averaged received power

Figure 7.2 shows the channel transfer functions and the corresponding impulse responses when no vehicle was passing (static channel) and when there was a vehicle travelling parallel to the transmitter to receiver path.

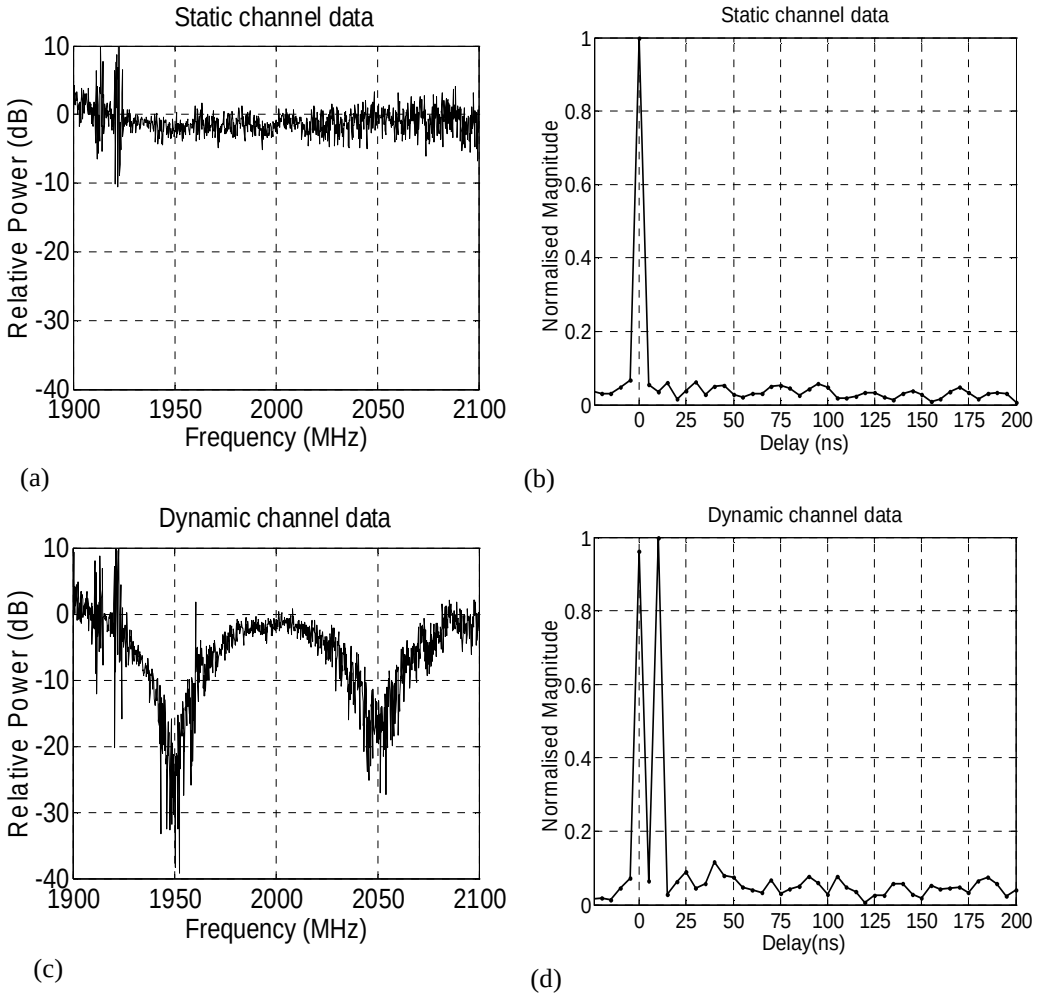

Figure 7.2 Field measurements (a) transfer function and (b) impulse response with no vehicles, (c) transfer function and (d) impulse response with a vehicles passing

The static channel transfer function (Figure 7.2a) exhibits small variations and very small fade depth. However, the dynamic channel response shows rapid fading with large fade depths due to multipath of up to 40 dB. The position of the nulls within the bandwidth changes with vehicle position and direction due to changes in the time delay of the multipath components. The impulse response from the static channel shows only one dominant path, LOS path, as would be expected (Figure 7.2b). However, when a vehicle is passing, the multipath component is very strong (Figure 7.2d). Figure 7.1 shows smaller amplitude variations than fade depths observed within the bandwidth because it is the average signal power across the bandwidth which masks the severity of frequency selective fading within the channel. The measured fade depths are similar to results reported in [7.1].

A section of averaged received power is shown in Figure 7.3 and the vehicles that were captured on video passing through the measurement zone are indicated. The video recording showed that the speed of traffic was between 30 km/h and 45 km/h. As the first vehicle in Figure 7.3 (3 door estate) moved through, the results show that the fade duration was approximately 30 ms. Examination of the data file showed that the start of the event was not captured but data acquisition did continue until the vehicle had left the measurement zone. The last vehicle to pass was an estate car which was travelling in Lane 4. Results show that longer vehicles have longer lasting effects on the received signal. An increase in the transmitter to receiver path length also increases the duration of the fading.

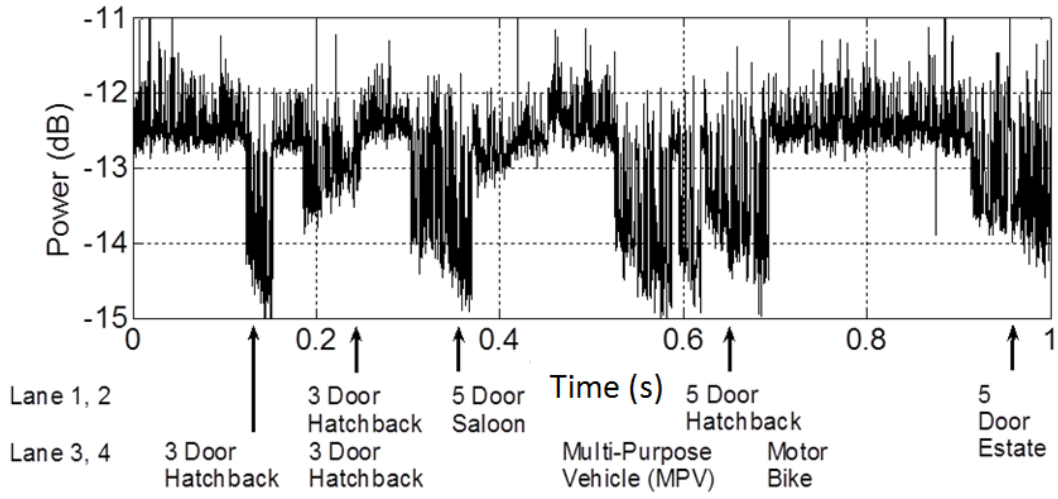

Figure 7.3 Averaged received power showing the impact of reflections from vehicles (Tx-Rx distance: 12m)

Considering the average signal power across the bandwidth, the presence of a vehicle in the channel introduces fade depths of up to 4 dB. Because the vehicle is not traversing the transmitter to receiver path, the decrease in the signal power is due to multipath fading caused by scattered and reflected components. There is also an increase in the standard deviation of the averaged signal power in the presence of traffic. A further increase was observed as the number of vehicles increased.

Table 7.1 Number of channel responses measured at each distance for event (vehicles passing) and non-event (no vehicles passing)

Distance (m)	Snapshot No. of Event	Snapshot No. of Non-event	Distance (m)	Snapshot No. of Event	Snapshot No. of Non-vent	Distance (m)	Snapshot No. of Event	Snapshot No. of Non-vent
2.0	519	3,101	8.3	0	3,840	14.6	445	3,395
2.3	236	3,604	8.6	79	3,761	14.9	171	3,669
2.6	768	1,665	8.9	0	3,840	15.2	398	2,740
2.9	5	3,711	9.2	245	3,595	15.5	374	3,466
3.2	0	3,604	9.5	491	3,349	15.8	265	3,575
3.5	303	3,537	9.8	553	3,287	16.1	208	3,431
3.8	0	3,840	10.1	602	3,065	16.4	510	3,094
4.1	0	3,840	10.4	240	3,599	16.7	413	3,421
4.4	0	3,840	10.7	245	3,595	17.0	362	3,478
4.7	54	3,786	11.0	470	3,370	17.3	765	3,075
5.0	516	3,324	11.3	0	3,840	17.6	101	1,819
5.3	480	3,360	11.6	0	3,840	17.9	938	2,667
5.6	200	3,640	11.9	0	3,840	18.1	864	2,976
5.9	32	3,808	12.2	44	3,464	18.4	242	3,598
6.2	125	3,715	12.5	0	3,840	18.7	1,079	2,289
6.5	0	3,840	12.8	23	3,817	19.0	238	3,602
6.8	546	3,294	13.1	0	3,840	19.3	539	3,301
7.1	0	2,880	13.4	343	3,261	19.6	354	2,526
7.4	0	3,840	13.7	0	3,840	19.9	684	3,000
7.7	245	3,359	14.0	136	3,468	20.2	854	2,986
8.0	0	3,389	14.3	558	3,282			

Table 7.1 shows the number of snapshot for event and non-event data at each position across the measurement path in front of Anglesea Building. The averaged received signal

power versus the distance between the transmitter and receiver is presented in Figure 7.4. The measured data was separated into event data (when there was at least a vehicle passing) and non-event data (when there was no vehicle passing). The event and non-event data are referred to as the data from a dynamic and static wideband channel, respectively.

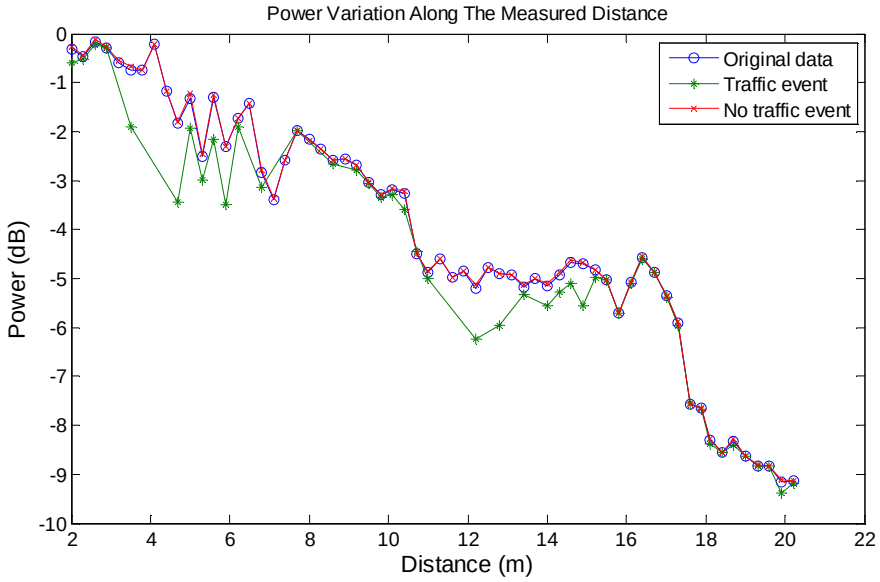

Figure 7.4 Signal power variation along the distance

Figure 7.4 shows the signal variation with distance for the combined (original) data, event and non-event data (after separation). The graphs shows that the effect of vehicles on the channel is signal fading. This can be attributed to the results of multipath fading due to the relative strength of the reflected components from the passing vehicles. However, the overlay of the original data and the non-event data shows that dynamic events occur in burst with relatively short durations. From the channel transfer functions at each position, the averaged received signal power was computed from 3840 transfer functions. The received signal power can be modelled using statistical distributions such as Gaussian, Rayleigh, Rician, Lognormal, Nakagami and Loo's distributions. These can be used to examine the variations of the received signals.

When evaluating models, a measure of accuracy has to be used. This includes Root Mean Square Error (RMSE). For statistical distributions, goodness-of-fit tests include Kolmogorov-Smirnov (KS) and Chi-Square (χ). In this research, KS and RMS tests have been used.

Kolmogorov-Smirnov (KS) test determines if two data sets differ significantly [7.2][7.3]. It has the advantages that it makes no assumption about the data distribution, does not depend

on the underlying cumulative distribution function being tested and it is an exact test. However it has limitations that include the fact that it only applies to continuous distributions, is more sensitive near the centre of the data distribution and the distribution must be fully specified. The Kolmogorov-Smirnov (KS) test statistic is defined by

$$D=\max_{1\le i\le N}\left(F(Y_i)-\frac{i-1}{N},\frac{i}{N}-F(Y_i)\right) \tag{7.1}$$

where F is the theoretical cumulative distribution of the distribution that is being tested and D represents the greatest distance between two data points. The null hypothesis H_0 is either accepted (rejecting H_1) or rejected (accepting H_1) based on the significance level, α. Normally the significant level α is set to 5% (0.05) or 10% (0.1). The 5% is usually chosen as a conventional level. If a test of significance gives a p-value lower than the significance level α, the null hypothesis is rejected.

Figure 7.5 shows that the average signal power variation about the mean at 2 m antenna separation can be model using Rice PDF. This is to be expected as the LOS path was unobstructed. Similar plots of the signal variations at 10 m and 19.9 m antenna separations are given in Figure 7.6 and Figure 7.7. Rice distribution best describes the spatial variation of the signal about the mean.

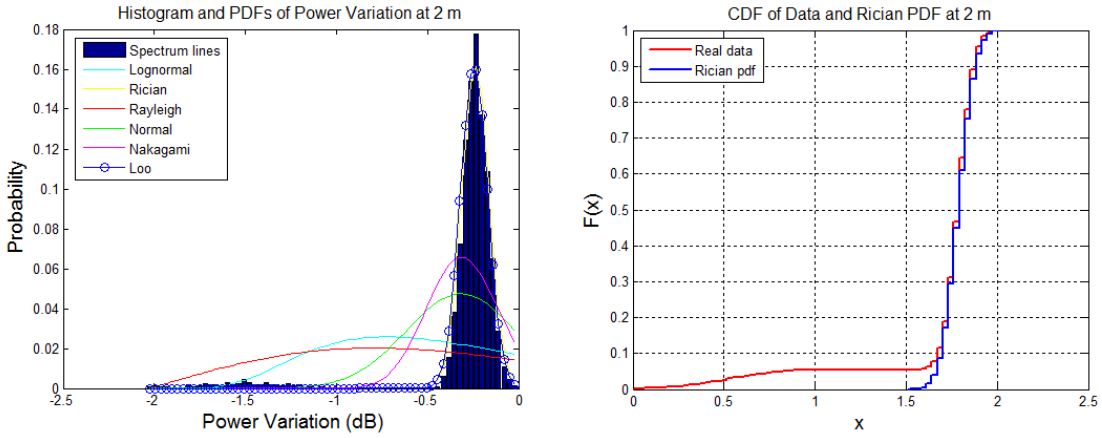

(a) (b)

Figure 7.5 Power variation about the mean (a) histogram with fitted PDFs and (b) fitted Rice cumulative distribution curve at 2 m distance.

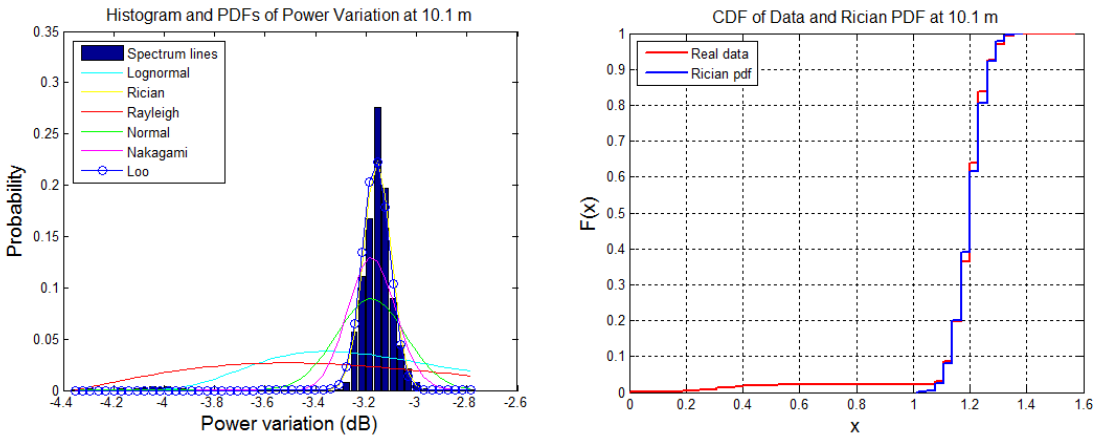

(a) (b)

Figure 7.6 Power variation about the mean (a) histogram with fitted PDFs and (b) fitted Ricean cumulative distribution curve at 10 m distance.

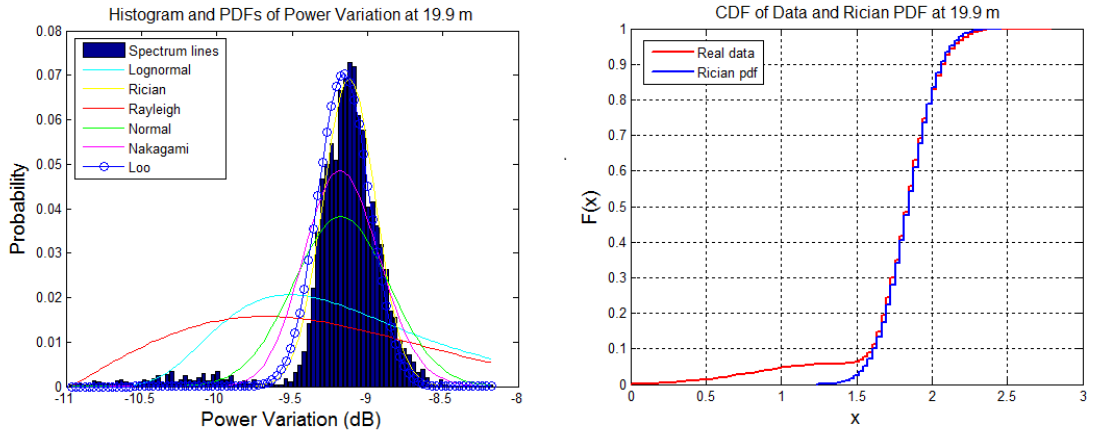

(a) (b)

Figure 7.7 Power variation about the mean (a) histogram with fitted PDFs and (b) fitted Ricean cumulative distribution curve at 19.9 m distance.

7.2 The Spatial Variation

Traditionally, communication channels have often been studied to understand and model path loss. Many path loss channel models have been developed as discussed in Chapter 3. These include Okumura [7.4], Hata [7.5], COST231-Hata [7.6], SUI [7.7], ECC-33 [7.8], Ericsson [7.9], WINNER II [7.10], and COST231 Walfisch-Ikegami [7.11]. Most of these models are not applicable to small wideband channels. Only the WINNER B3 model proposed for indoors has been designed for short path length channels. The average signal power across the bandwidth has been used to evaluate with path loss models.

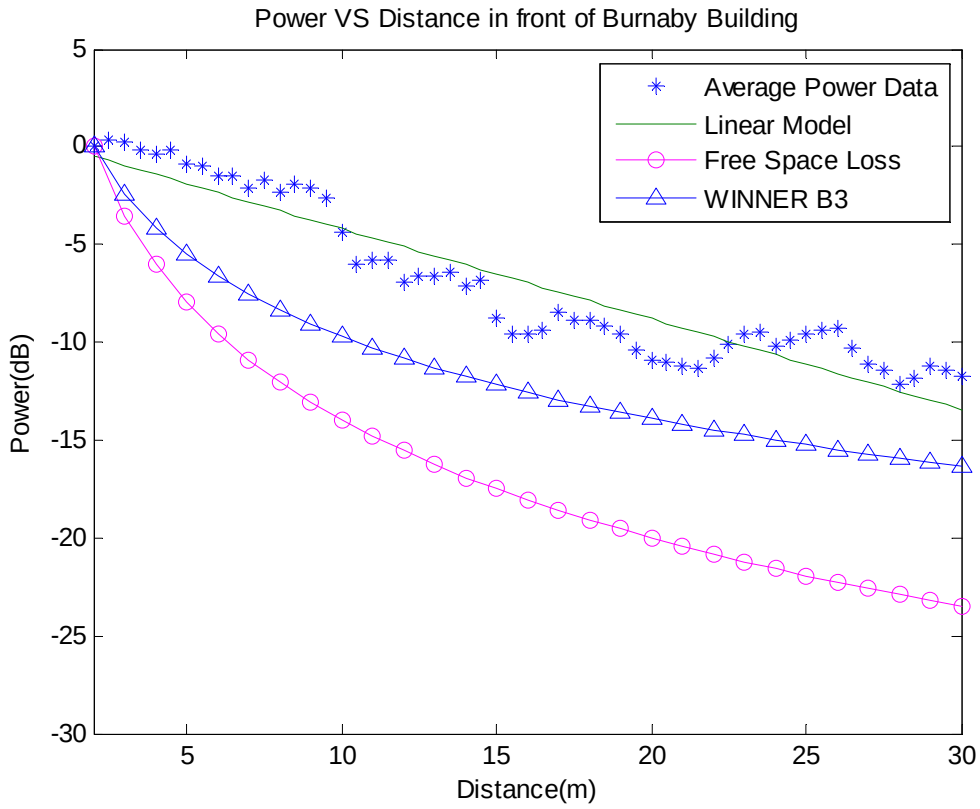

Figure 7.8 Power variation along the measurement path in front of Burnaby Building

Figure 7.8 shows the graphs of the measured data, linear regression method, and empirical channel models. It shows the signal power variation along the measurement path in front of Burnaby Building. In this area, there is no vehicle present at the time of the measurement. The best fit method that is close to representing the data measured is linear model. The second best model is the WINNER B3 model.

Figure 7.9 and Figure 7.10 show the signal power variations along the path length in front of Anglesea Building and rear of Anglesea Building (T-Hut area). The location at the rear of Anglesea Building is the controlled area without vehicle moving involved during the measurement. For the location in front of Anglesea Building, the effects from the real urban traffic can be examined. They also show that the best fit is the linear model whilst the second best is the WINNER B3 model.

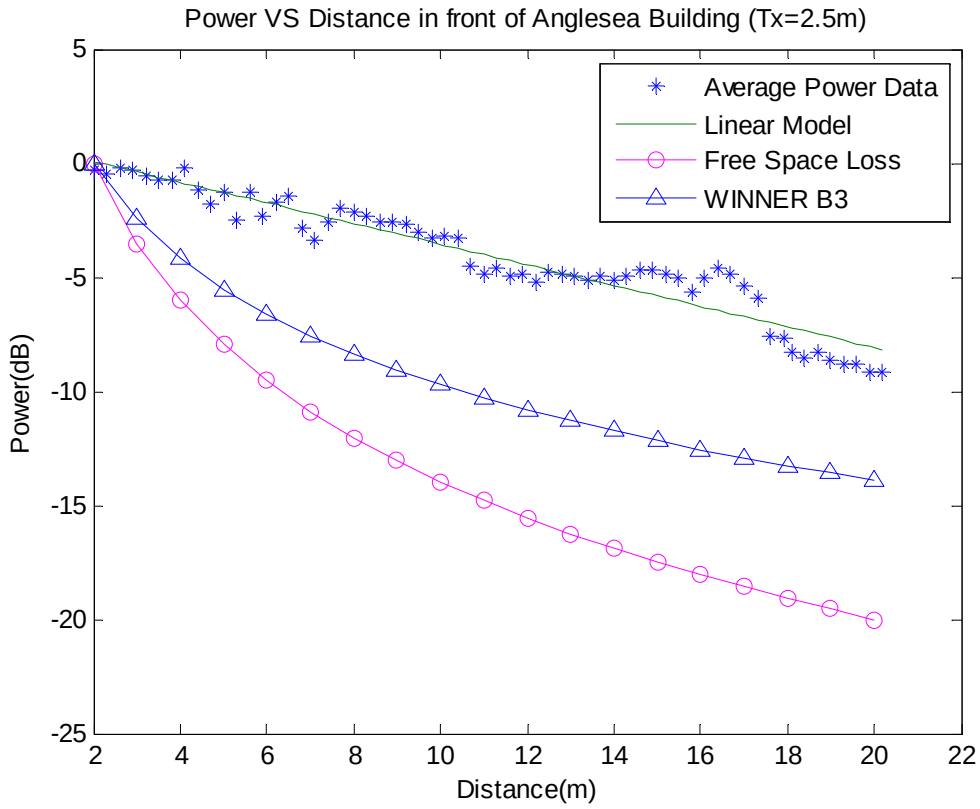

Figure 7.9 Power variation along the measurement path in front of Anglesea Building

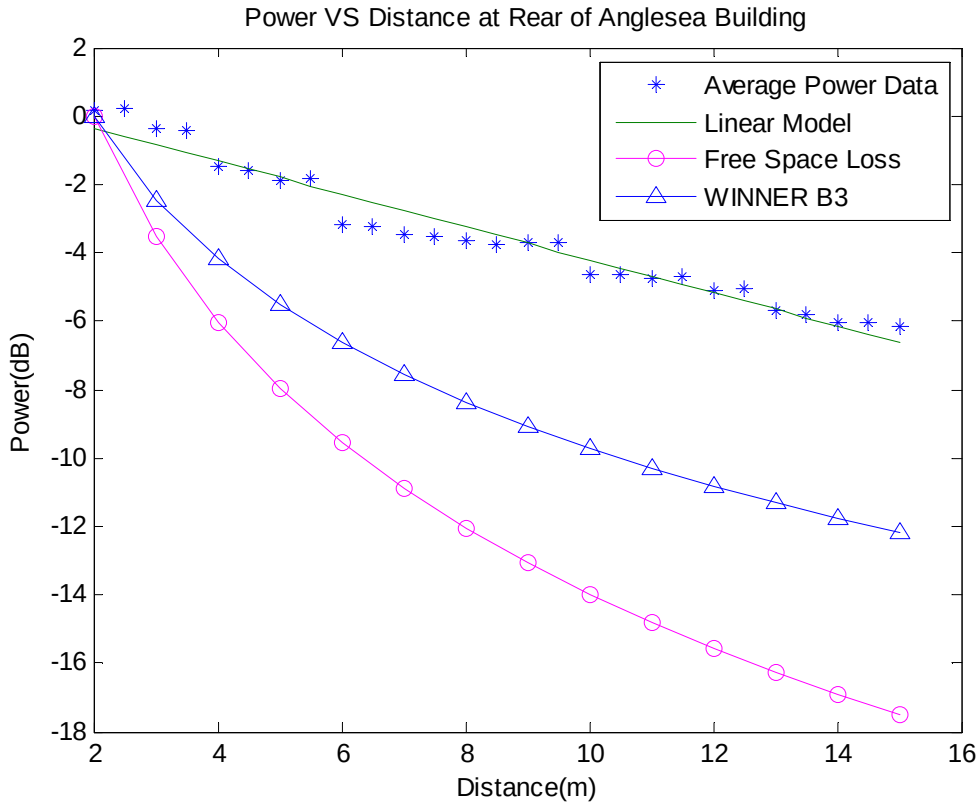

Figure 7.10 Power variation along the measurement path rear Anglesea Building

Table 7.2 Root-Mean-Square Error (RMSE) at each location compared to the data measured

Model	RMSE In front of Anglesea	RMSE In front of Burnaby	RMSE Rear of Anglesea
Linear model	0.7429	1.4121	0.4169
Free space loss	10.0223	9.7728	8.4533
WINNER B3	5.6451	4.6306	4.6862

The RMSE of the linear regression, WINNER B3 and free space path loss model are presented in Table 7.2. It shows that linear model is the best fit model that can be used to represent the spatial variation for all of these three locations. Measurements in front of Burnaby Building give the largest RMSE. The rear of Anglesea Building had the smallest number of objects in the vicinity of the transmission path, whilst in front of Burnaby Building there was a long wall running parallel to the transmission path.

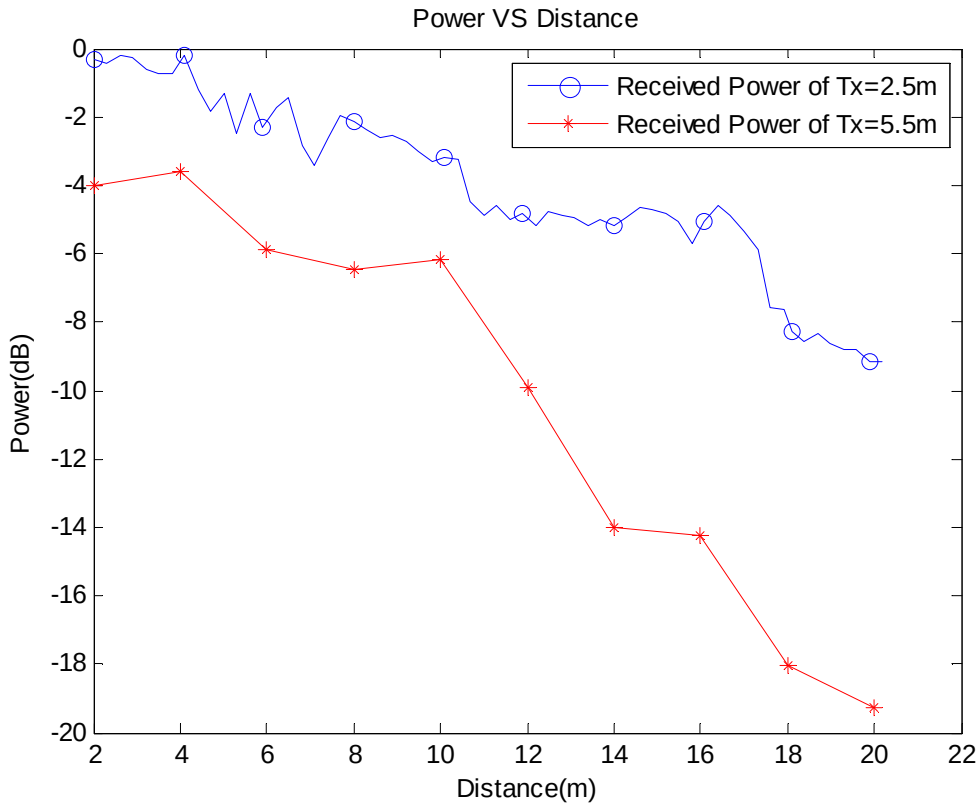

Figure 7.11 Power variation against distance for the transmitter antenna heights of 2.5 m and 5.5 m with fixed receiver antenna height of 1.6 m

Figure 7.11 shows the received signal power variation along the measurement path with the height of receiver antenna at 1.6 m for transmitter antenna heights of 2.5 m and 5.5 m. The received signal power from the 5.5 m transmitter height is lower than that from 2.5 m height

at all distances. This can be attributed to the receiver not being in the main lobe of the transmitting antenna at short distances.

7.3 Path Loss Models for Actual Urban Environments

Models based on prevailing propagation mechanisms cannot be directly applied to this study because they are based on work in which the transmitter heights were greater than 10 m or the systems used transmitted narrow band signals or very few measurements were taken at antenna separations less than 30 m.

Figure 7.8 - Figure 7.10 show that at ranges up to 20 m none of the channel models closely represents the signal variation with distance. It shows that a linear model provides the best fit. The signal loss with increased distance does not decay logarithmically as predicted by the models. The second and third models closer to the signal variations along the measurement path that were found were WINNER B3 and free space path loss, respectively.

Because of the short path length and the absence of clutter, the received signal was dominated by the LOS path. In the absence of automotive traffic, multipath components were very weak. In general, the gradient of the path loss for each measurement scenario was less than the values predicted by all the previously proposed models over short path lengths.

With the data separated into static and dynamic data sets from the scenario in front of Anglesea Building, individual modelling could be carried out. The gradients of the linear models that can be used to represent the average signal power of the dynamic and static channels are -0.45 for static channel and -0.42 for a dynamic channel. The picocell signal decay models for dynamic and static channels are given by Equations (7.2) and (7.3) respectively.

$$L_{\mathrm{apD}}(d) = -0.42\ \mathrm{d} + P_0 \tag{7.2}$$

$$L_{\mathrm{apS}}(d) = -0.45\ \mathrm{d} + P_0 \tag{7.3}$$

where d is the distance in metres and P_0 is the signal power in dBm at the reference distance d_0. Given that the signal variation about the mean at each measurement position can be described by a statistical distribution, picocell channel models can be developed for static and dynamic urban environments.

Models of signal power variation in front of Burnaby Building and at the rear of Anglesea Building are given by Equation (7.4) and (7.5).

$$L_{\mathrm{ap}}(d) = -0.46\ \mathrm{d} + P_0 \tag{7.4}$$

$$L_{\mathrm{ap}}(d) = -0.48\ \mathrm{d} + P_0 \tag{7.5}$$

In front of Anglesea Building, if the data measured is not separated into static and dynamic data, the gradient of the average signal power will be -0.45 and when the transmitter antenna height is 5.5 m, the gradient of the average signal power is -0.93.

7.4 Temporal Variation in the Controlled Area

The 200 MHz wideband channel sounder was used in the controlled area to investigate the impact of vehicles moving on radio channels. In the controlled traffic area, the vehicle speed was maintained at 10 mph (4.4704 m/s) with the directions of vehicle moving as shown in Chapter 6 (Figure 6.3). An average transfer function was captured every 184.32 µs.

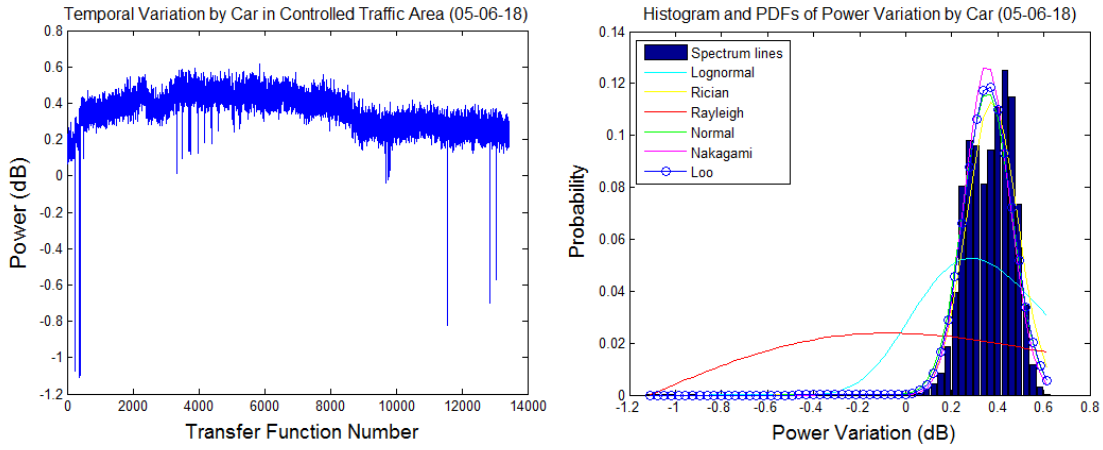

(a) (b)

Figure 7.12 Power variation of a car passing (a) average power, (b) histogram with fitted PDFs

Figure 7.12 shows the averaged received signal power and results of fitting possible PDFs to the data. The measurement was designed to use a car moving around the measurement system with the transmitter antenna height of 2.5 m and the receiver antenna height 1.6 m. Result shows that when a car was passing, the mean of the received signal power is around 0.35 dB with standard deviation equal to 0.11 dB, Figure 7.12 (b).

When a van was used instead with the same condition, result shows that the mean of received signal power is around 0.28 dB with standard deviation equal to 0.16 dB as presented in Figure 7.13.

This also shows that a bigger vehicle can induce fading duration that is longer and deeper.

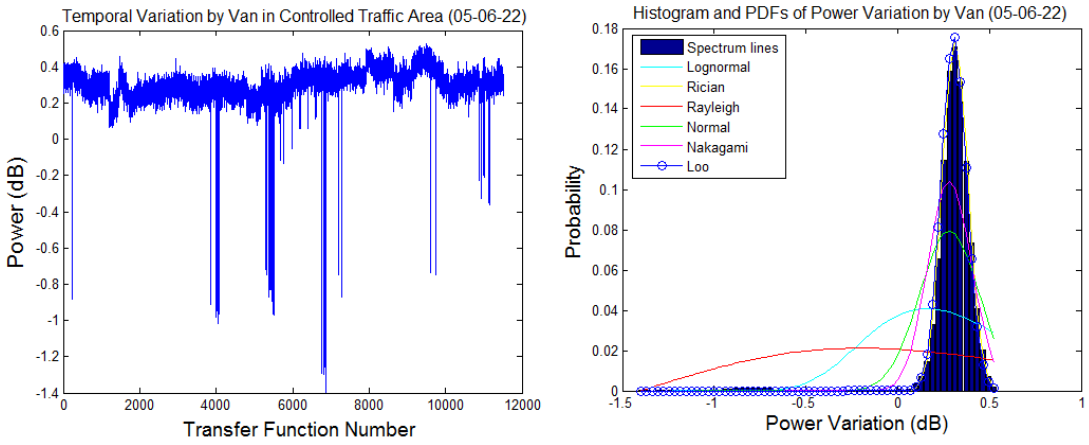

(a) (b)

Figure 7.13 Power variation of a van passing (a) average power and (b) histogram with fitted PDFs

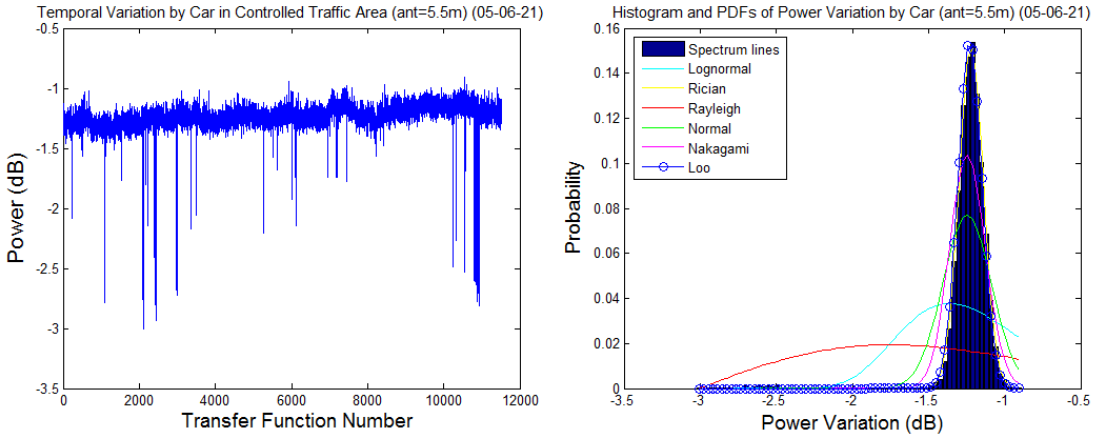

(a) (b)

Figure 7.14 Power variation of a car passing with 5.5 m received antenna height (a) average power and (b) histogram with fitted PDFs

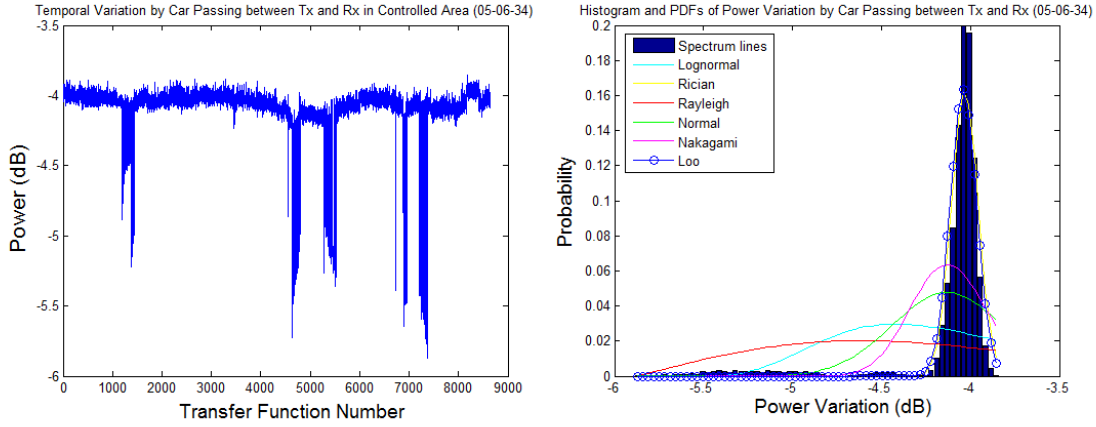

(a) (b)

Figure 7.15 Power variation of a car passing between Tx and Rx (a) average power and (b) histogram with fitted PDFs

From Figure 7.14, the mean of the received signal power decreases to -1.25 dB with the standard deviation of 0.16 dB when the transmitter antenna height was 5.5 m and fading also seems to be longer and deeper in this case when compared to that with transmitter antenna height of 2.5 m.

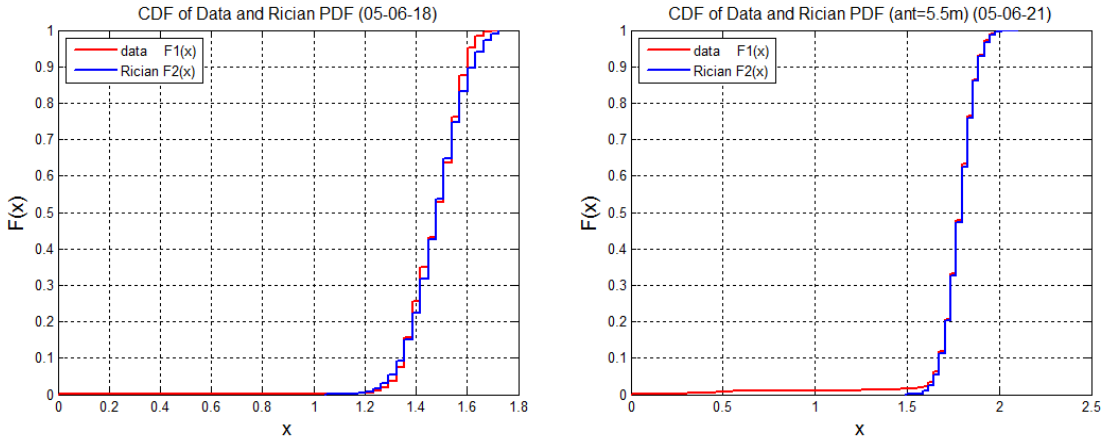

(a) (b)

Figure 7.16 The fitted cumulative distribution curves between signal power and Ricean pdf when a car passing in controlled area with the transmitter height of (a) 2.5 m and (b) 5.5 m

In Figure 7.15 the average received signal power is much smaller, -4.1 dB, with the standard deviation of 0.31 dB when the experiment was conducted with a car moving along route 2 (Figure 6.5) and passing between the transmitter and receiver as shown in Figure 7.15.

When the transmitter antenna height was set to 5.5 m, the mean of the average received signal power was -3.68 dB and the standard deviation was 0.11 dB. The duration of fading is similar at both transmitter antenna heights. From the results of fitting statistical PDFs, Rician PDF provides the best fitting as presented in Figure 7.16.

7.5 Temporal Variation in front of Anglesea Building

The ability of the wideband channel sounder to capture the channel transfer function as fast as possible has proved beneficial to investigate the impact of traffic on the channel. Temporal variations induced in the channel by passing vehicles manifest as rapid changes with short deep fade durations that requires rapid channel sampling. Figure 7.17 shows the average signal variation for the combined data and data that has been separated into static (no vehicles passing) and dynamic (when a vehicle was passing) sets. It shows that, on average, the passing vehicles cause severe signal fading rather than enhancements in wideband systems. The fades are due to the deep frequency selective fading that is experienced within the bandwidth.

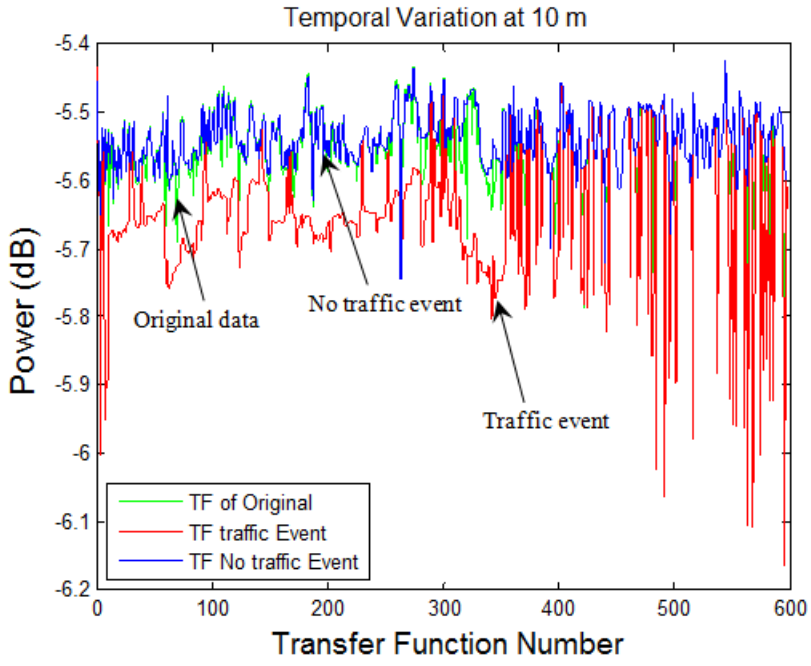

Figure 7.17 Temporal variation of signal power at 10 m

In the static case, the averaged received signal power variation is only about 0.3 dB peak-to-peak. During dynamic events the received power varies by up to 1.3 dB. From Figure 7.3, based on the study corroborated by video images, it shows that vehicles passing in any of the four lanes of the road will affect the channel. The effect depends on the close proximity

to the receiver and the size of the vehicle (reflecting surface). Under normal circumstances with no vehicle passing, the non-LOS signal will radiate in its launch direction and will not reach the receiver. However when it impinges on the vehicle, part of it is reflected into the receiver depending on the incident angle and the position of the vehicle within the channel. Irregularities on the vehicle surface will affect the strength of the reflected signal. Therefore the channel characteristics depend on:

- the distance between the transmitter and receiver;
- the distance of the vehicle from the transmitter to receiver path;
- the direction of the vehicle;
- the size and hence the reflecting surface of the vehicle;
- the vehicle surface geometry which determines the direction of the reflected signal; and
- the surface roughness or composition, as vehicle windows will not reflect the signal like the metal surface.

The results show that large vehicles will cause greater signal fading that has longer durations compared to smaller vehicles passing in the same lane because large vehicles have larger reflecting surfaces.

7.6 Channel Transfer Function and Impulse Response

The signal variations in Figure 7.17 are the averaged received signal power across the bandwidth. To gain a better understanding of the effects of vehicles, the impulse response of the channel needs to be studied.

Figure 7.18 and Figure 7.19 show examples of the estimated impulse responses which illustrate the ability of SVDP to resolve closely spaced multipath components. In Figure 7.19, it can be seen that the second multipath component is separated from the LOS component by 2.4 ns. Using FFT would require a bandwidth of at least 416 MHz to achieve this resolution.

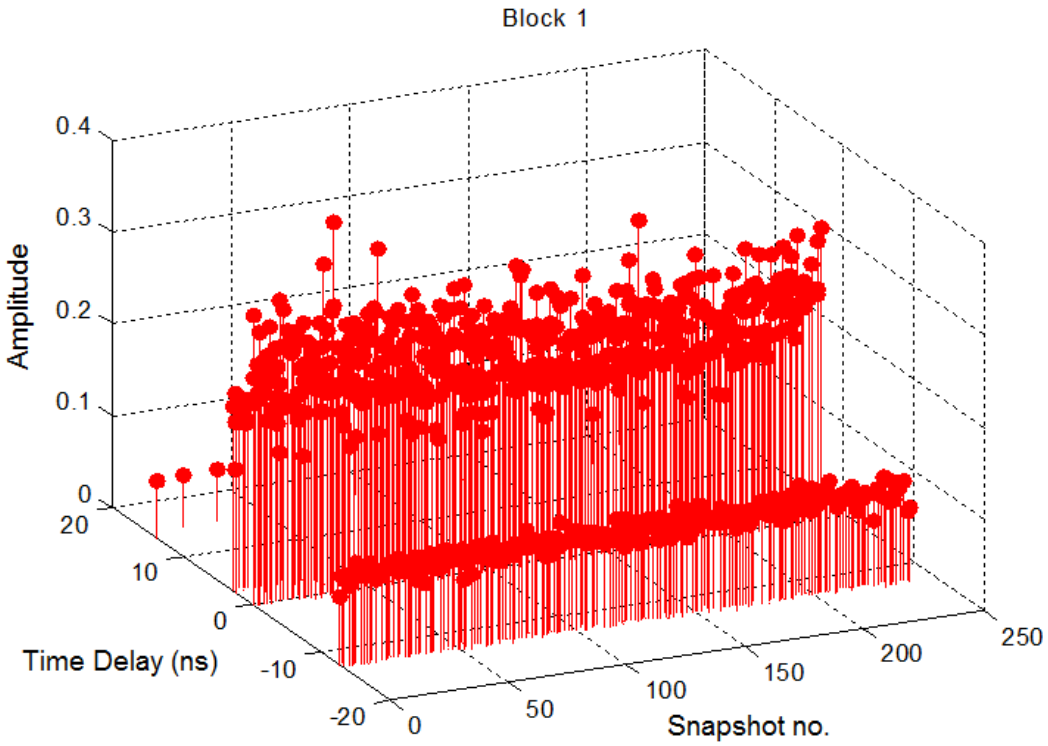

Figure 7.18 Impulse response in 3D of data block (112759 at 14.6 m)

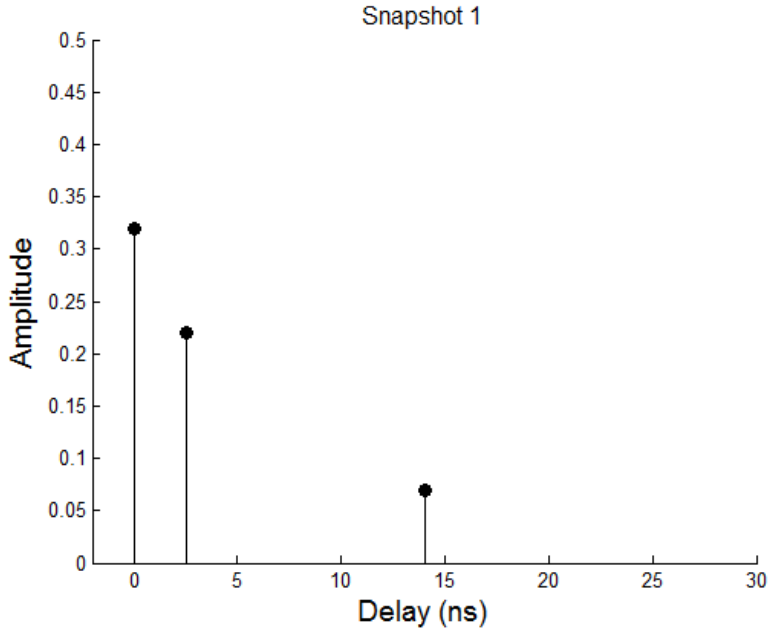

Figure 7.19 Impulse response of single channel response (112759 at 14.6 m)

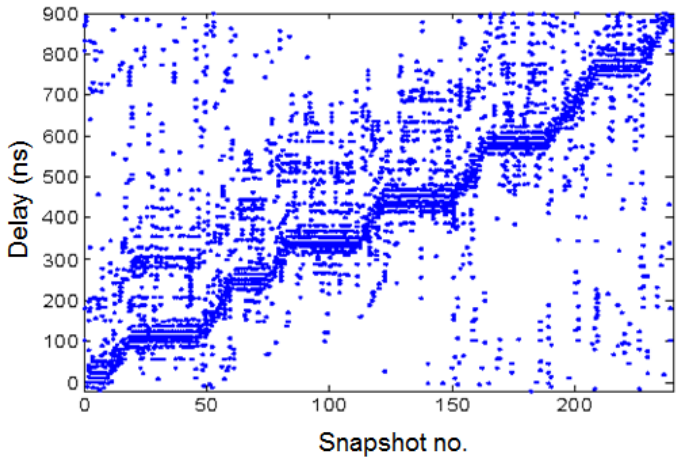

Figure 7.20 Evolution of impulse response time delay as a vehicle passes the measurement zone (103613)

From Chapter 5, the time delay of the multipath components are computed from the phase of the signal. Reflection from the vehicle changes the reference phase of the signal. When plotted together with impulses obtained without vehicle, it manifest as an evolution in the time delay as the vehicle traverses the zone. The change also encompasses the evolution of the multipath time delay owing to changes in the ray travel distance. This is exemplified in Figure 7.20.

7.6.1 Transfer Function and Impulse Response at Burnaby Building

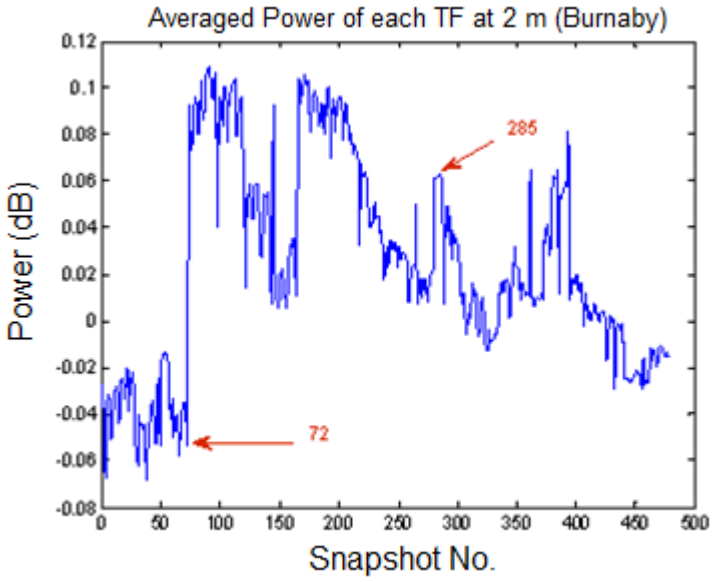

Figure 7.21 Averaged signal power variation at 2 m in front of Burnaby Building without vehicle passing (105523.tf, 105539.tf)

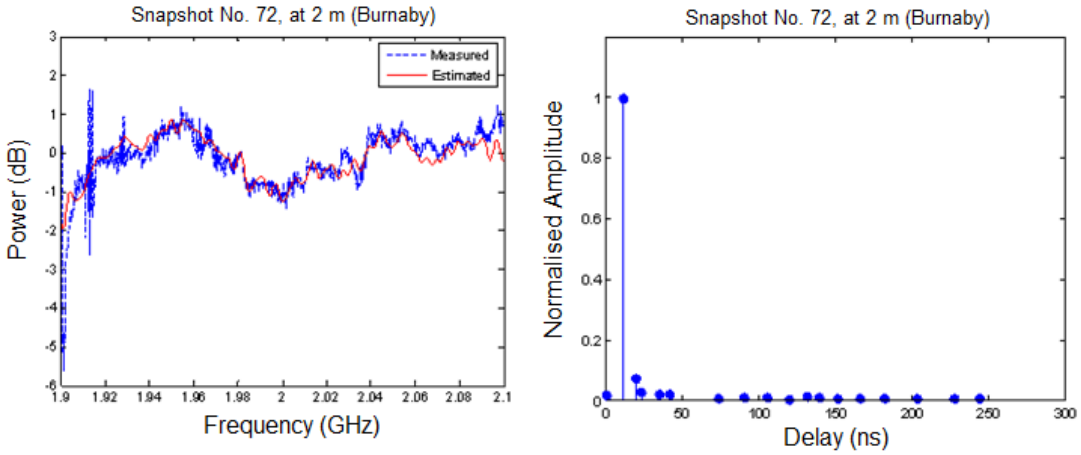

(a) TF of snapshot no. 72 (b) IR of snapshot no. 72

Figure 7.22 Measured and fitted TF and estimated impulse response at 2 m in front of Burnaby Building

Figure 7.22 shows an example of a channel transfer function at 2 m in front of Burnaby Building and the estimated channel impulse response. The scenario in front of Burnaby Building is without vehicle passing and the averaged signal power at 2 m only varies within 0.16 dB with time. The impulse response shows only one dominant signal path, the LOS path.

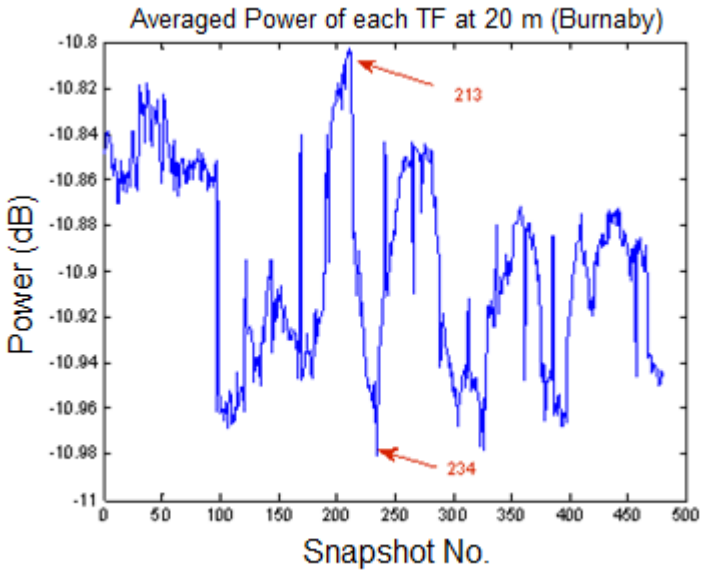

Figure 7.23 Averaged signal power variation at 20 m in front of Burnaby Building without vehicle passing (120146.tf, 120152.tf)

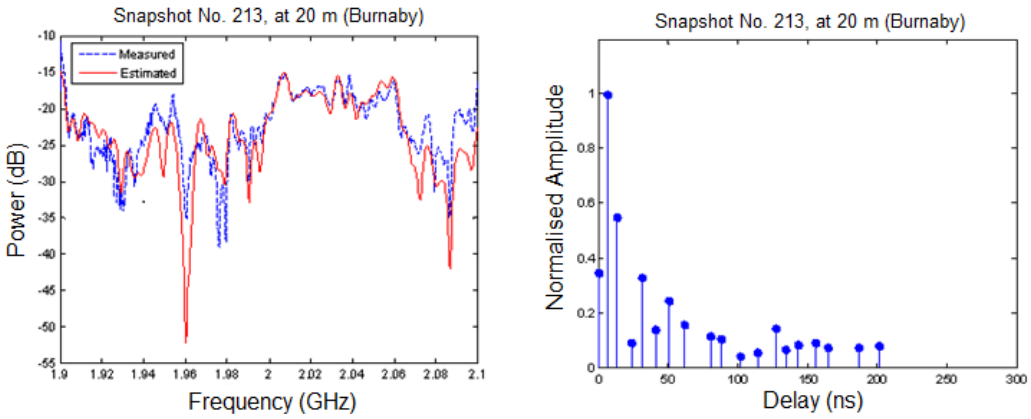

(a) TF of snapshot no. 213 (b) TF of snapshot no. 213

Figure 7.24 Measured and fitted TF and estimated impulse response at 20 m in front of Burnaby Building

For antenna separation of 20 m, the averaged signal power variation is shown in Figure 7.23 and varied between -10.98 dB to -10.80 dB. The SVDP algorithm has been used to estimate the channel transfer function and impulse response as shown in Figure 7.24. It shows that when the separation distance is longer the number of multipath signal components increases and the channel transfer function exhibits greater frequency selective fading. Overall, the results show that the SVDP algorithm performs fairly well based on the fitting of the measured and reconstructed transfer function.

7.6.2 Transfer Function and Impulse Response at Rear of Anglesea Building

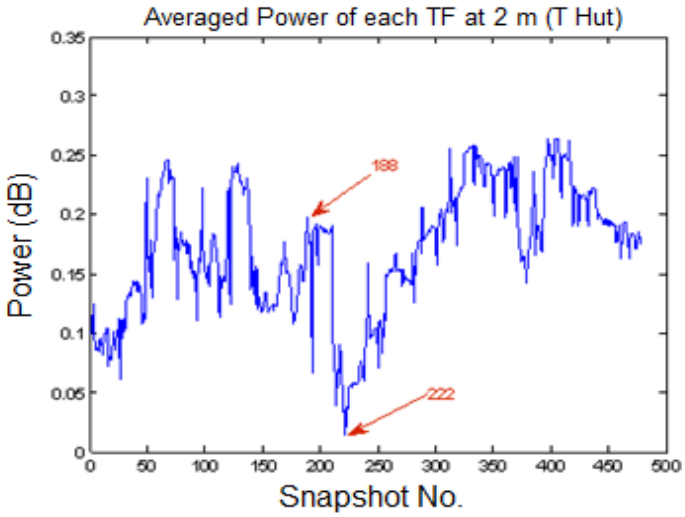

Figure 7.25 Averaged signal power variation at 2 m at rear of Anglesea Building without vehicle passing (112522.tf, 112537.tf)

The averaged signal power variation for antenna separation 2 m at rear of Anglesea Building is presented in Figure 7.25. The transfer function and impulse response of snapshot 188 are presented in Figure 7.26. At 2 m there is only one dominant signal components in the impulse response (Figure 7.26b) as would be expected.

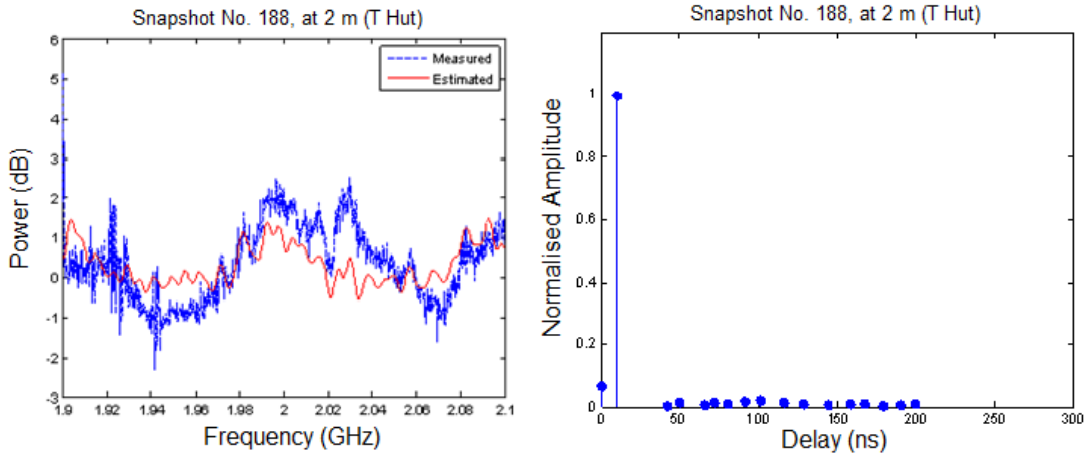

(a) TF of snapshot no. 188 (b) IR of snapshot no. 188

Figure 7.26 Measured and fitted TF and estimated impulse response at 2 m at rear of Anglesea Building

Figure 7.27 shows the averaged signal power at 10 m. At this position, although there is no vehicle passing, channel fading can be influenced by the multipath signals reflected or scattered from objects in the measurement area as shown in Figure 7.28b. Therefore, the channel transfer function still exhibits frequency selective fading.

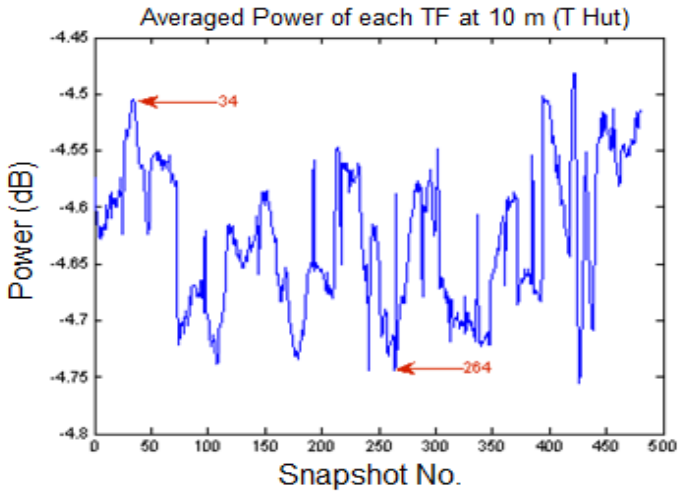

Figure 7.27 Averaged signal power variation at 10 m at rear of Anglesea Building without vehicle passing (115009.tf, 115025.tf)

The averaged signal power at 15 m varied between -6.40 dB to -6.01 dB is presented in Figure 7.29. The measured channel transfer function, the estimated channel transfer function and impulse response of snapshot 92 are presented in Figure 7.30. From the transfer function, the deepest fade null is nearly -30 dB. There are 2 components with amplitudes of approximately 0.35 which significantly contribute to the fading. In the following subsections, the transfer function and impulse response in front of Anglesea Building will be presented for transmitter antenna heights of 2.5 m and 5.5 m.

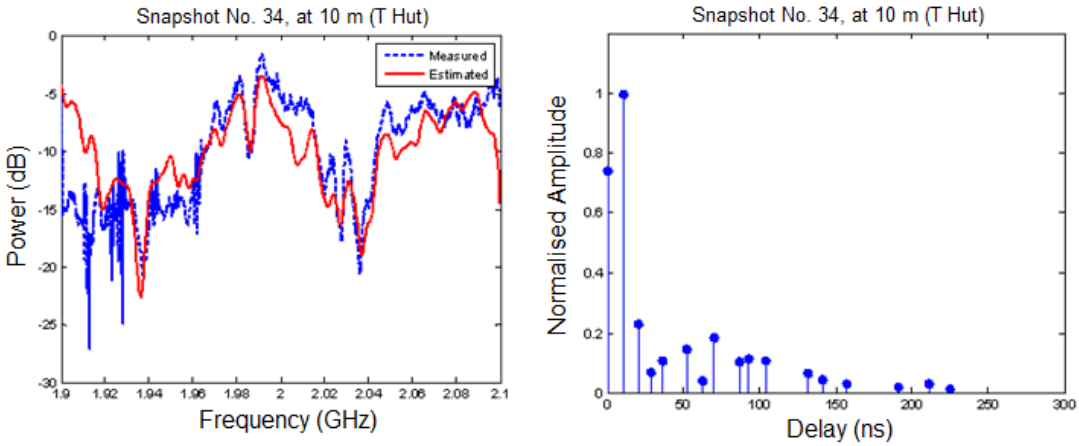

(b) TF of snapshot no. 34 (a) IR of snapshot no. 34

Figure 7.28 Measured and fitted TF and estimated impulse response at 10 m at rear of Anglesea Building

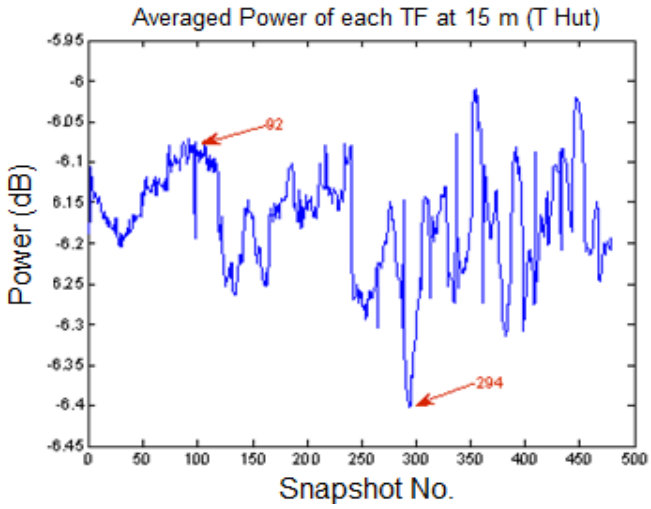

Figure 7.29 Averaged signal power variation at 15 m at rear of Anglesea Building without vehicle passing (121448.tf, 121514.tf)

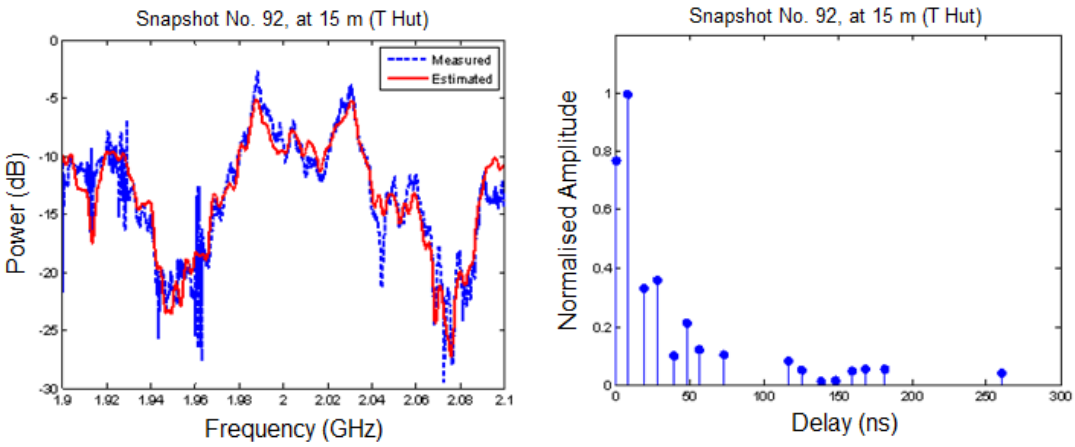

(a) TF of snapshot no. 92 (b) IR of snapshot no. 92

Figure 7.30 Measured and fitted TF and estimated impulse response at 15 m at rear of Anglesea Building

7.6.3 Transfer Function and Impulse Response in front of Anglesea Building with Transmitter Antenna Height at 2.5 m

Channel transfer function data measured in front of Anglesea Building are from a real traffic scenario. Figure 7.31 illustrates the averaged received signal power variation with time at 2 m antenna separation. The variation of the averaged received signal power is from -0.8 dB to -0.05 dB in the static period and between -2.8 dB and -0.25 dB when a vehicle passes.

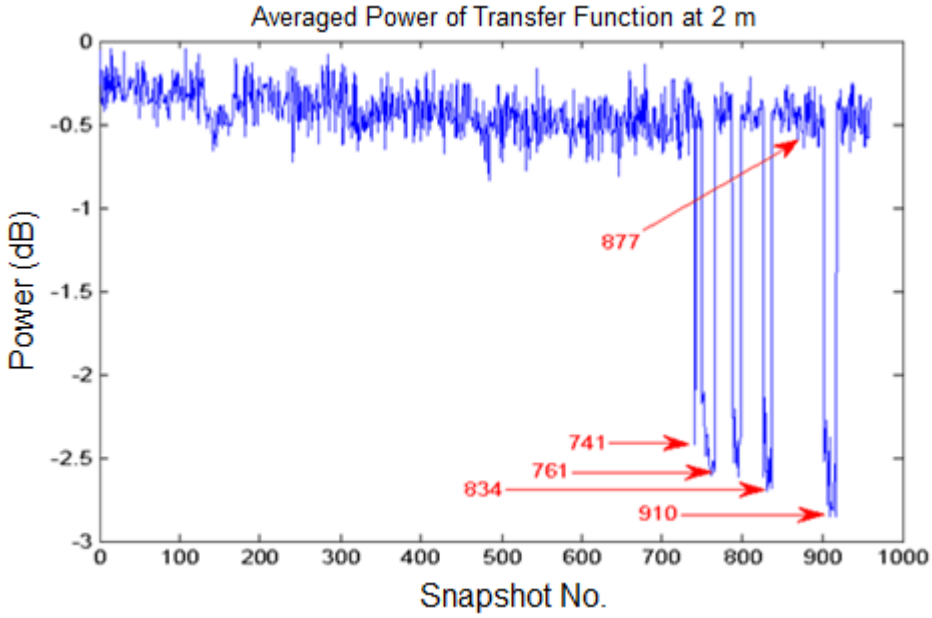

Figure 7.31 Averaged signal power variation at 2 m showing fading caused by vehicles passing parallel to the measurement system (103606.tf)

Figure 7.32 shows examples of the channel transfer functions from the data in Figure 7.31 and the estimated impulse responses when the channel is static. Note that in the impulse response, there is one impulse at 0 ns which is not the strongest. This is purely because the SVDP algorithm resolves multipath time delay based on the location of the signal zeros on a unit cycle. The relative time delay is what is important. Overall, the figure shows that there is strong signal component with the amplitude of LOS component normalised to 1.

Figure 7.33 shows that in the presence of a vehicle in close proximity to the channel, the channel transfer function experiences frequency selective fading. Of specific interest is the change in the power of the initial impulse response whose magnitude has increased from 0.1 (Figure 7.32b and d) to approximately 0.5 in Figure 7.33b (snapshot 761). The vehicle, in snapshot 761, had just entered the area where it influences the channel characteristics. In snapshot 834, the vehicle has moved closer to the channel sounder receiver. Because of the reduced distance, the reflected multipath component relative amplitude has increased to 0.58, as shown in Figure 7.33d, resulting in deeper fading in the channel transfer function.

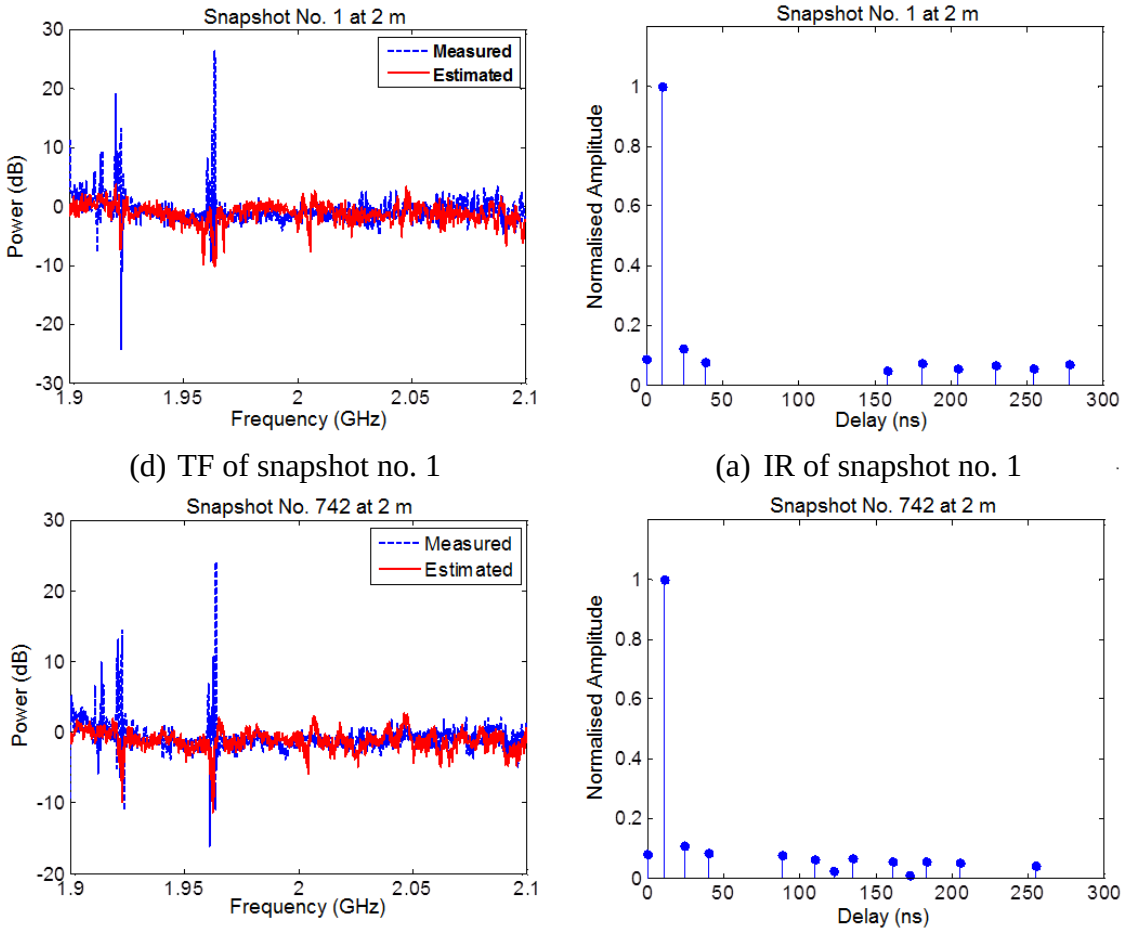

(d) TF of snapshot no. 1 (a) IR of snapshot no. 1

(b) TF of snapshot no. 742 (c) IR of snapshot no. 742

Figure 7.32 Measured and fitted TF and estimate impulse responses in a static channel

It should be noted that the spikes in the channel transfer functions at approximately 1.96 GHz is due to interference signal from mobile networks. Analysis shows that this has negligible effect on the estimated channel impulse response.

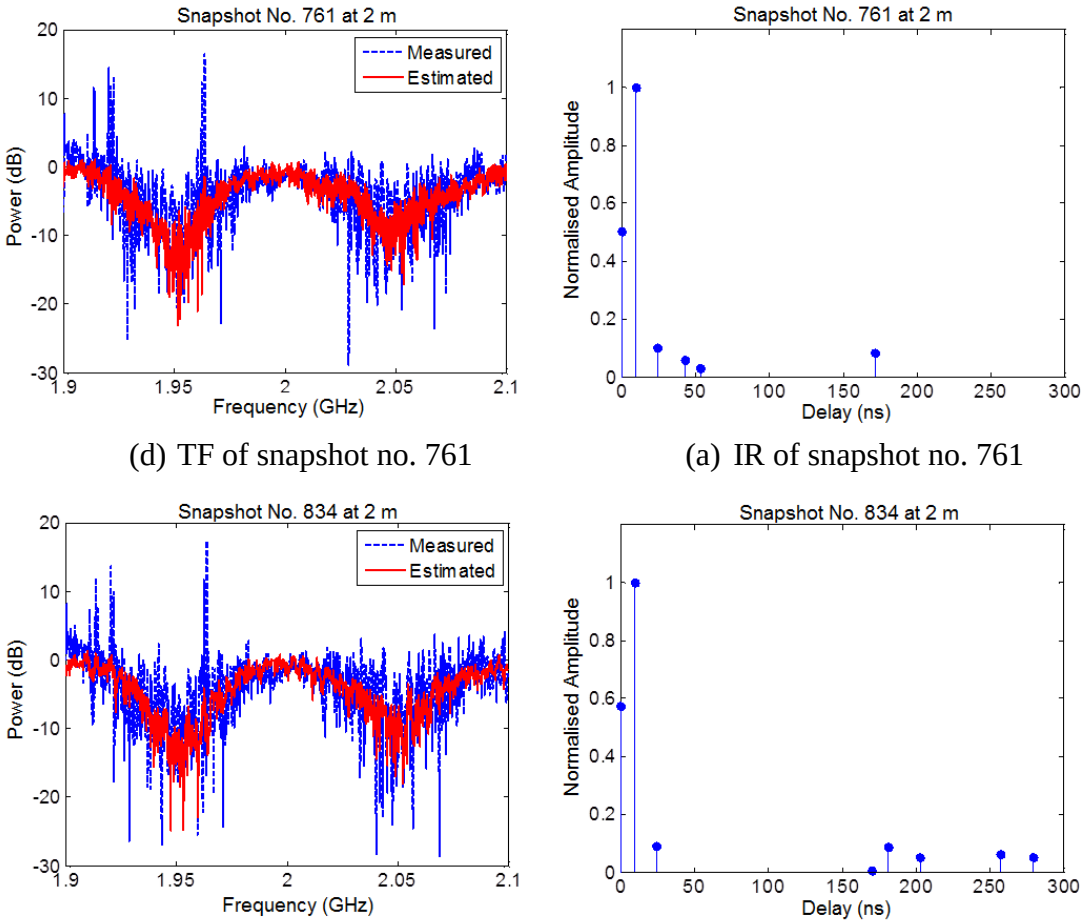

(d) TF of snapshot no. 761 (a) IR of snapshot no. 761

(b) TF of snapshot no. 834 (c) IR of snapshot no. 834

Figure 7.33 Measured and estimated TF and its impulse response at 2 m

Figure 7.34 shows the temporal signal variation at antenna separation of 10.1 m. As antenna separation increases, the impact of a multipath reflected from a passing vehicle is less pronounced due to the complex combination of all the multipath components at the receiver. This is illustrated by a reduction in the depth of the fade which is approximately 2 dB.

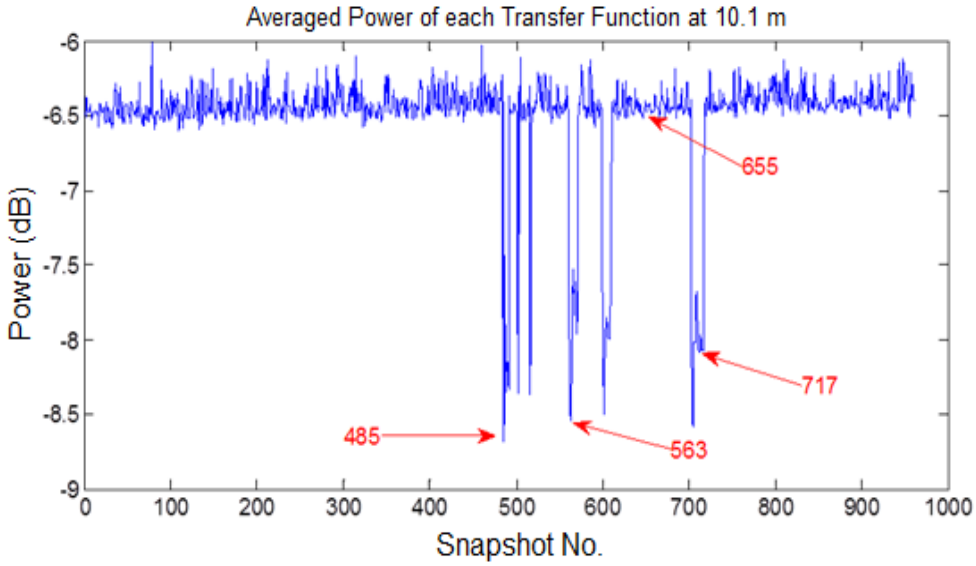

Figure 7.34 The averaged signal power variation at 10.1 m (file 110309.tf) representing fading caused by a vehicle passing the measurement system

Figure 7.35 gives an example of the channel response when there was no vehicle passing. It can be seen that there are two additional strong multipath components and the channel transfer function exhibits significant multipath fading. These multipath components are due to static objects within the environment.

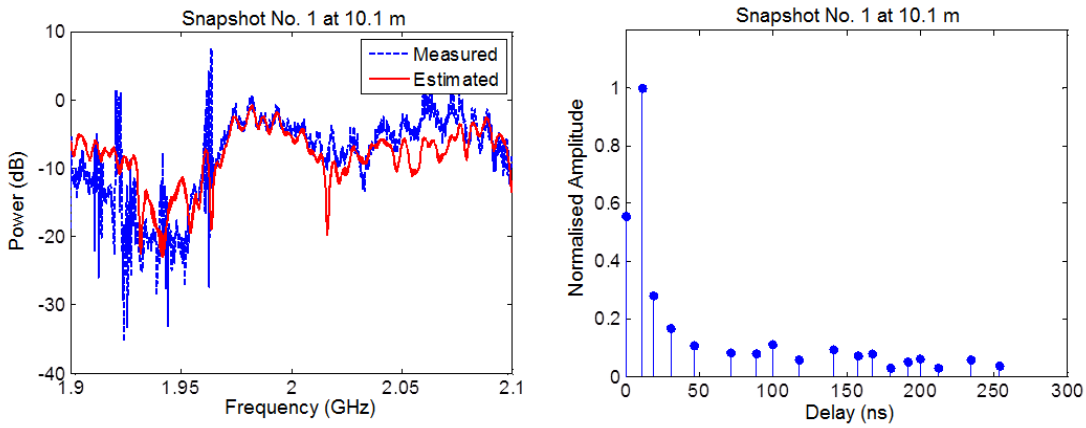

(b) TF of snapshot no. 1 (a) IR of snapshot no. 1

Figure 7.35 Measured and estimated TF and its impulse response at 10.1 (static channel)

Figure 7.36 shows the channel response when a vehicle is passing close to the measurements zone. It shows that the multipath structure of the channel is maintained but the amplitude of the first ray changes from 0.62 to 0.8. This could be attributed to the fact that the reflected component from the vehicle has a time delay that was too close and hence

could not be resolved as a different multipath. Tests have shown that in this case, SVDP will generate one impulse but the amplitude will be larger.

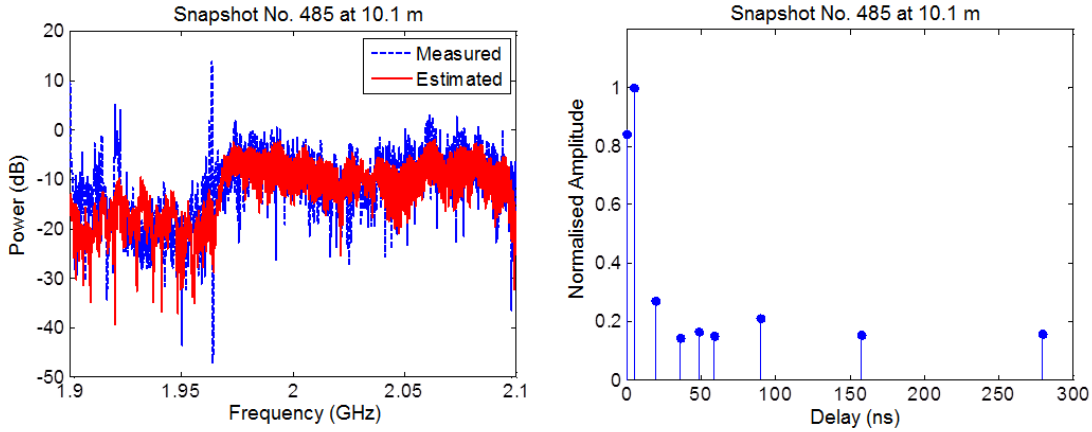

(b) TF of snapshot no. 485 (a) IR of snapshot no. 485

Figure 7.36 Measured and estimated TF and its impulse response at 10.1 (dynamic channel)

At 19.9 m antenna separation, the SNR has decreased. Figure 7.37 shows the signal variation with time. Figure 7.38 shows that the number of multipath components has increased further. Figure 7.39 shows that the time delay difference between the reflected component and the LOS component is very small and the impact on the channel transfer function is less obvious.

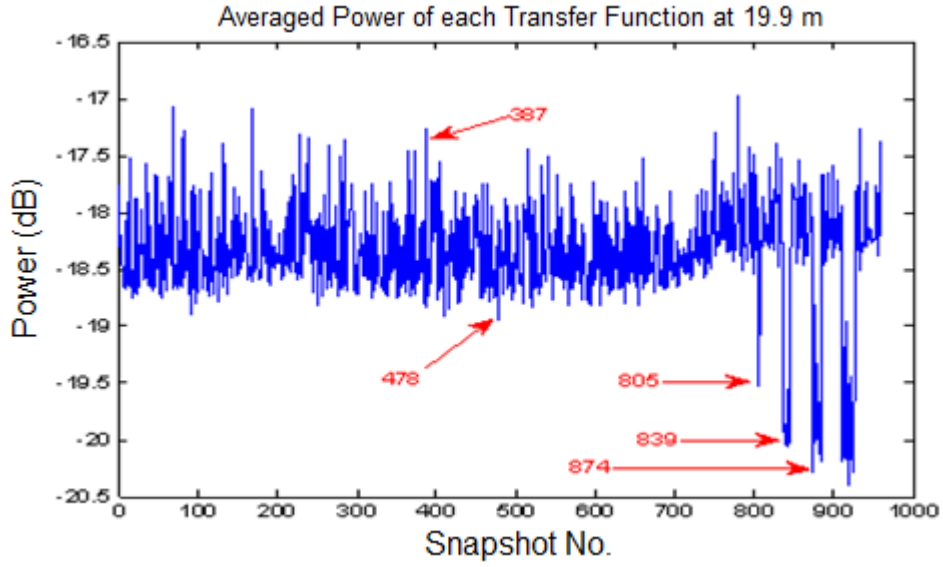

Figure 7.37 The averaged signal power variation at 19.9 m (120028.tf) representing fading caused by vehicles passing parallel to the measurement system

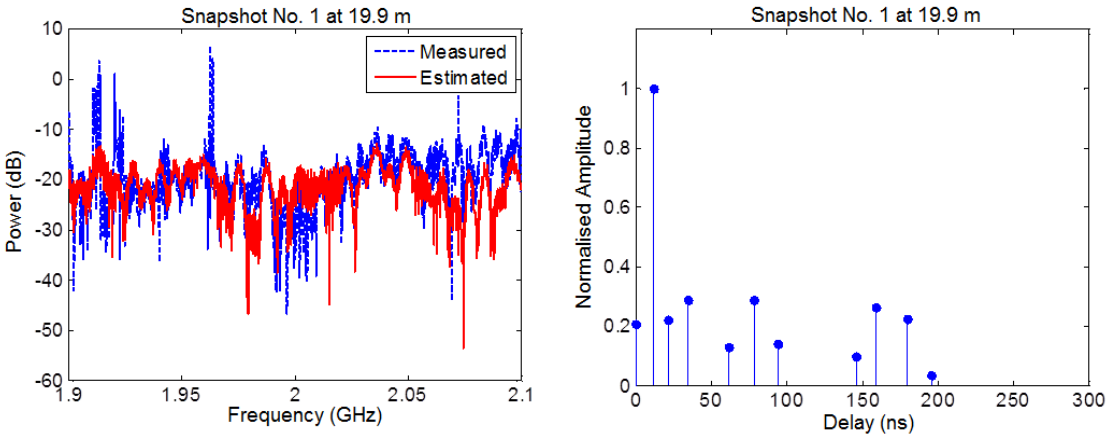

(a) TF of snapshot no. 1 (b) IR of snapshot no. 1

Figure 7.38 Measured and estimated TF and its impulse response at 19.9 m

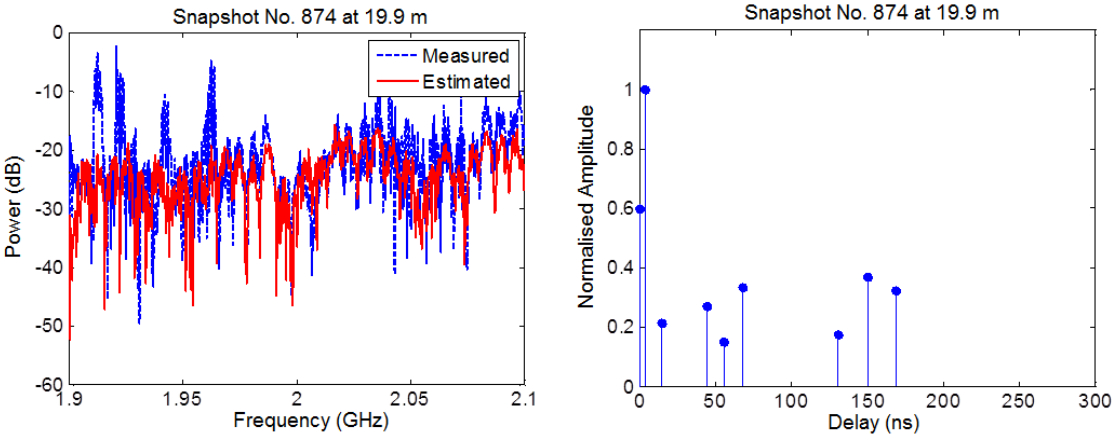

(a) TF of snapshot no. 874 (b) IR of snapshot no. 874

Figure 7.39 Measured and estimated TF and its impulse response at 19.9 m in the presence of a passing vehicle

7.6.4 Discussion of Channel Variation

The results show that short distances in static channels the signal power variation has very small standard deviation. When the separation distance is longer, signal power variation increases due to the effect of multipath.

The channel transfer function of static channels at short distances is nearly flat. But for long distances beyond 10 m, it exhibits frequency selective fading. Therefore the impulse responses of static channels at short distances have one dominant ray but shows additional significant multipath components as the distance increases. For dynamic channels due to the impact of moving vehicle, the signal power when the vehicle is passing fades from the averaged level.

The results show that the SVDP algorithm clearly provide much superior results than FFT. It does not only have a better time delay resolution, but it also does not assume periodicity and therefore resolve impulses based on their relative time of arrival. These have been instrumental in resolving the time evolution of the channel response as vehicles pass the measurement zone.

The impact of the fence in front of Anglesea Building is considered not to have a significant effect on the channel when compared with the static channel at the rear of Anglesea Building. In front of Burnaby Building, it shows that the wall had an impact on the channel response.

From the antenna pattern shown in Chapter 6, although there is a slight variation in the azimuth, the orientation of the antennas were not changed during each measurement set-up. Since the system response is calibrated out, it is considered that this did not significantly affect most of the results. However, where this could influence the results is when the multipath component angle corresponds to that of the antenna where the gain was small. That component would show up as having smaller amplitude than it was.

7.7 RMS Delay Spread and Coherence Bandwidth

Results of the RMS delay spread and coherence bandwidth have been calculated from the SVDP algorithm estimated channel impulse responses.

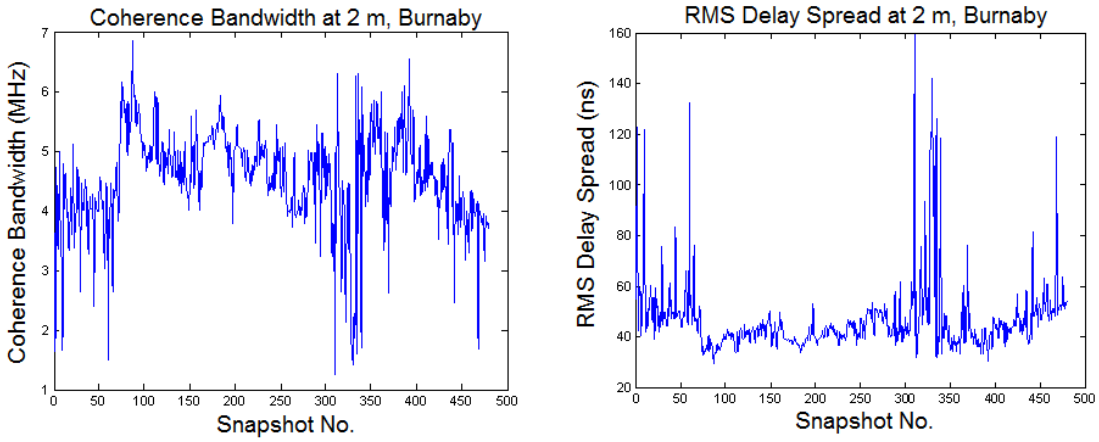

(b) Channel coherence bandwidth (a) RMS delay spread

Figure 7.40 Channel parameters at 2 m in front of Burnaby Building, (a) Channel coherence bandwidth and (b) RMS delay spread

The RMS delay spread and channel coherence bandwidth in front of Burnaby Building with the separation distance of 2 m are shown in Figure 7.40. The averaged values of RMS delay

spread and channel coherence bandwidth are 46.33 ns and 4.32 MHz, respectively. When the separation distance is longer the RMS delay spread increases and the channel bandwidth becomes smaller. For example at 10 m the RMS delay spread and channel bandwidth are 64.02 ns and 3.12 MHz and at 20 m they are 67.45 ns 2.97 MHz, respectively. Examples of impulse response at some positions in front of Burnaby Building are presented in Figure 7.41 to show the signal components of the impulse response at each position.

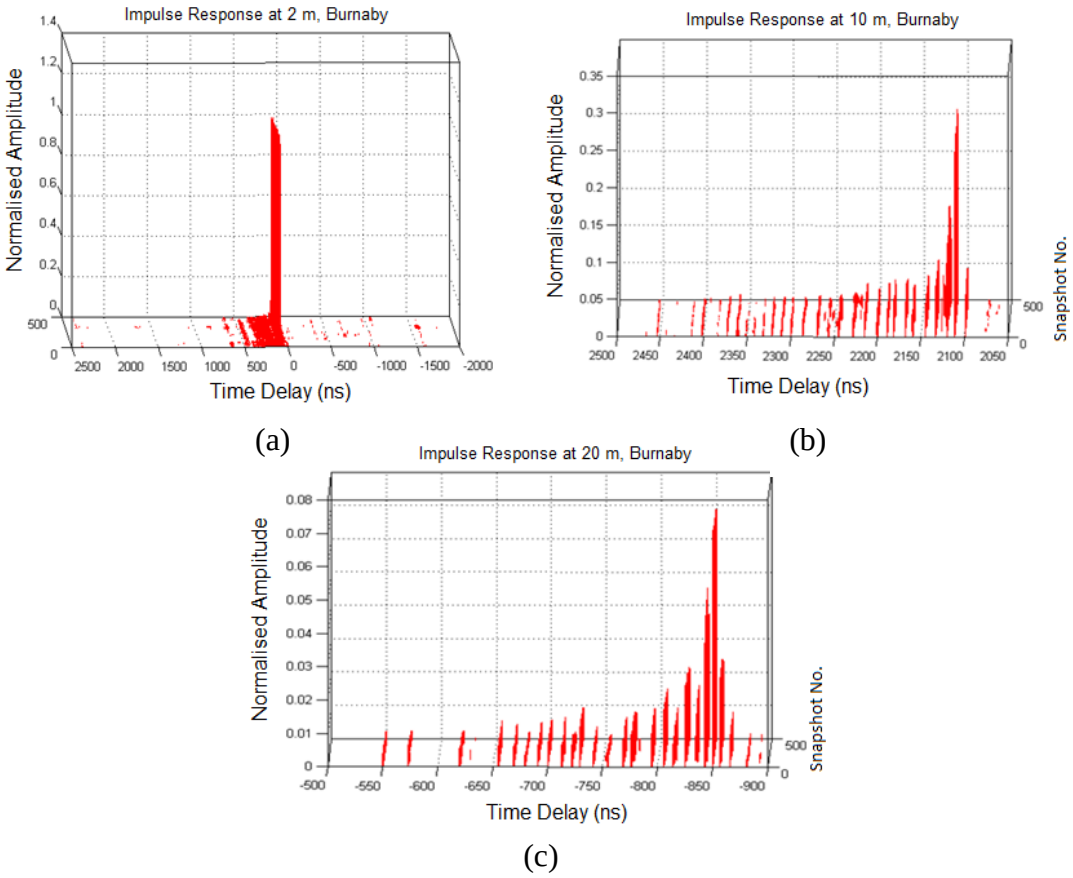

Figure 7.41 Impulse response in front of Burnaby Building, (a) at 2 m, (b) 10 m and (c) 20 m

For the measurement at the rear of Anglesea Building, at 2 m the RMS delay spread is 51.05 ns and become 55.46 ns at 15 m. For the results in controlled area, during the time of a car or a van moving parallel to the LOS path the RMS delay spread is about 1,500 ns for both 2.5 m and 5.5 m transmitter heights used. Whilst in the case of a car passing between the transmitter and the receiver for 14 m separation distance, the RMS delay spread for 2.5 m transmitter height is 1,183 ns and for 5.5 m transmitter height is 694.47 ns. It is about two times different.

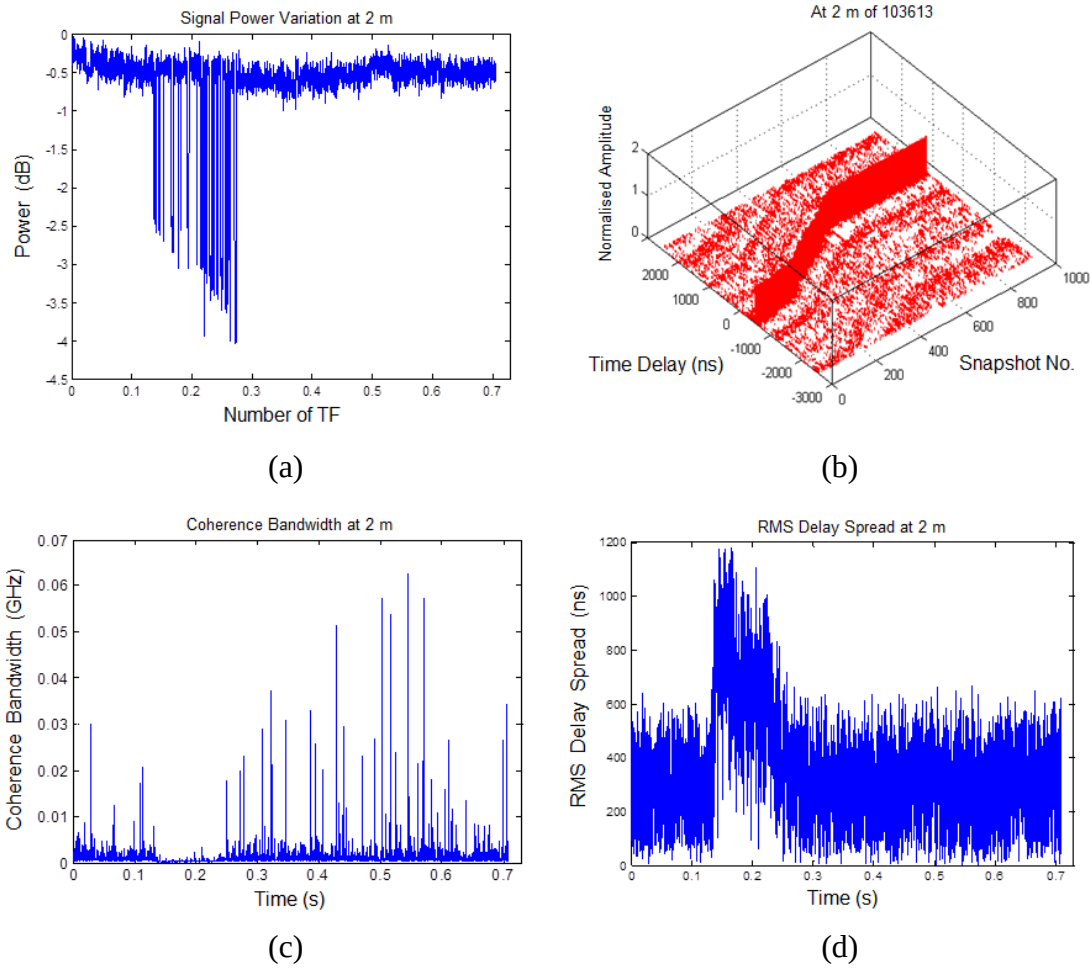

Figure 7.42 Evolution of the channel response and correlation between channel parameters, (a) average signal level, (b) channel impulse response, (c) channel coherence bandwidth and, (d) RMS delay spread (2 m)

Figure 7.42 shows the correlation between the signal level, evolution of the channel impulse response as a vehicle passes and the variation of the channel coherence bandwidth and RMS delay spread. The computation of the delay spread using channel impulse response normalised to the strongest signal when there was no vehicle passing has affected the computed value. As shown in Figure 7.42b, when the vehicle is passing, it introduces a dynamic evolution in the time delay of the channel impulse response by causing it to shift. Therefore, a true computation of the RMS delay spread would require the channel delay profile to be computed only for very short time periods. Because of the short range, when normalised, the RMS delay spread variation between channel measurements would be as shown in Figure 7.43. No further results of these parameters will be presented in this thesis. However, initial studies show that the RMS delay spread varies between 5 ns and 20 ns, owing to the short path length. Compared to other types of communication systems, this is

small but will have significant impact on the achievable data rate for high speed wireless systems.

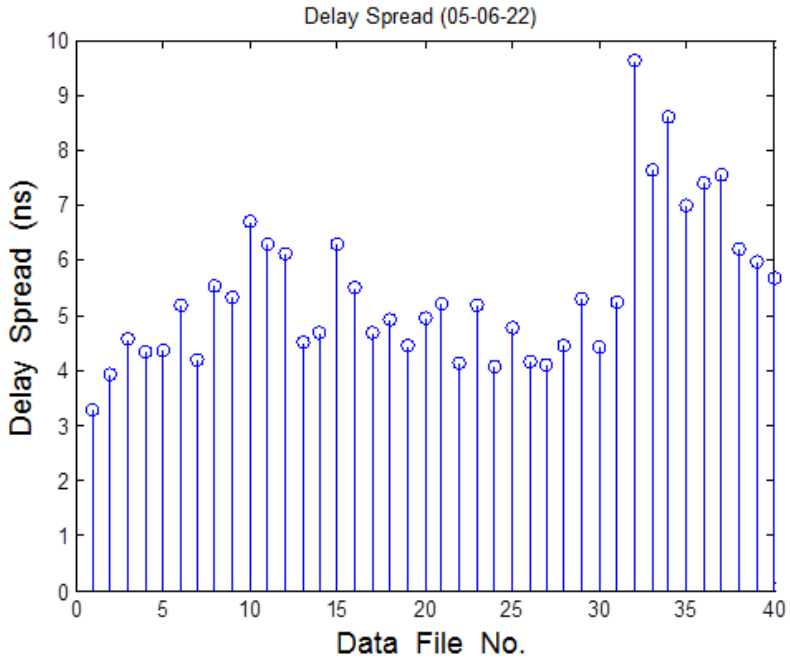

Figure 7.43 RMS delay spread variation between channel measurements

7.8 Doppler Frequency Shift and Scatter Function

Doppler frequency shift used as one of channel characterisation parameters is a deviation of signal frequency due to a change on the path length between the transmitter and receiver. Doppler frequency shift occurs when there is at least a movement of any or all of the following: the transmitter, the receiver, the reflector and scatter along the path. The Doppler shift can be given by the Equation (7.6).

$$f_d = f_c \frac{v}{c} \tag{7.6}$$

Where v is the speed or rate of change on path length between the transmitter and receiver, c is the speed of light, f_c is the carrier frequency of the signal and f_d is the Doppler frequency shift. The Doppler frequency shift is positive when the transmitter or object is moving towards to the receiver and is negative when the receiver is moving away from the transmitter. Thus the carrier frequency is shift from f_c to $f_c \pm f_d$.

To compute the Doppler frequency shift based on the length of the propagation path changed, it can be stated as the incremental distance given by the Equation (7.7).

$$d = v\Delta t \tag{7.7}$$

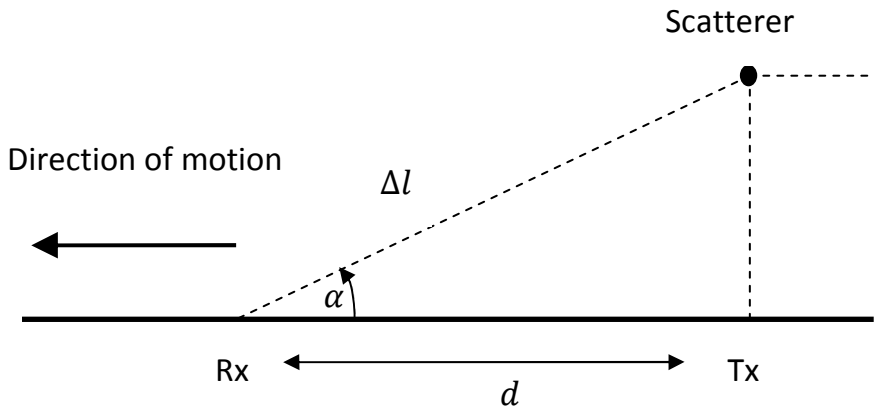

Figure 7.44 Doppler frequency shift on the length of propagation path changed

From Figure 7.44, d is the distance between the transmitter (Tx) and receiver (Rx), Δl is the distance between the scatterer and receiver, and α is the degree of angle measured from the straight line of Tx and Rx to the straight line of scatterer and Rx.

The Doppler frequency shift will be different according to the length of propagation path changed. As shown in Figure 7.44, the path length between the scatter and receiver can be given by

$$\Delta l = d\cos(\alpha) \tag{7.8}$$

Where the corresponding change of the received signal phase can be calculated by

$$\Delta\phi = -\frac{2\pi}{\lambda}\Delta l = -\frac{2\pi\Delta t}{\lambda}cos(\alpha) \tag{7.9}$$

And finally the Doppler frequency shift is given by,

$$\Delta f = -\frac{1}{2\pi}\frac{\Delta\phi}{\Delta t} = \frac{v}{\lambda}cos(\alpha) = f_d \tag{7.10}$$

As the Doppler frequency shift changed based on the length of propagation path, as shown in Figure 7.44 if the distance, d, is longer, the degree of angle, α, is become smaller. The

Doppler frequency shift, f_d, will be small and it will be high when the distance, d, is shorter.

From Figure 7.44, if there are several signal paths from many objects (scatterers), there will be frequency differences of Doppler frequency shifts from all of different signal paths. The summation of the different signals from different paths causes the fluctuations in amplitude of the delay component. The signal fluctuations in amplitude of a particular delay component can be analysed and accomplished by performing complex Fourier analysis over a period of time for each delay component as known as scatter plot.

The scatter function $S(\tau;\lambda)$ [7.12] of the channel represents a measurement of the average power output of the channel as a function of the time delay τ and the Doppler frequency λ given by

$$S(\tau;\lambda) = \int_{-\infty}^{\infty} S_C(\Delta f;\lambda)\, e^{j2\pi\Delta f}\, d\Delta f \qquad (7.11)$$

where $S_C(\Delta f;\lambda)$ is the Fourier transform of autocorrelation function of the measured channel transfer function. The scatter functions of the data file 103606.tf at 2 m, 110309.tf at 10.1 m, and 120028.tf at 19.9 m are given as the examples.

Figure 7.45 shows the scatter function of a static and dynamic channel (110309.tf data block no. 1 and 4). Figure 7.45 (a) and (b), show that there is no Doppler frequency shift in a static channel. Figure 7.45 (c) and (d), due to a moving vehicle, Doppler spectrum spread is introduced. The Doppler components are mainly around ± 50 Hz. Figure 7.46 and Figure 7.47 shows the scatter functions of the channel in the presence of a passing vehicle at antenna separations of 10.1 m and 19.9 m.

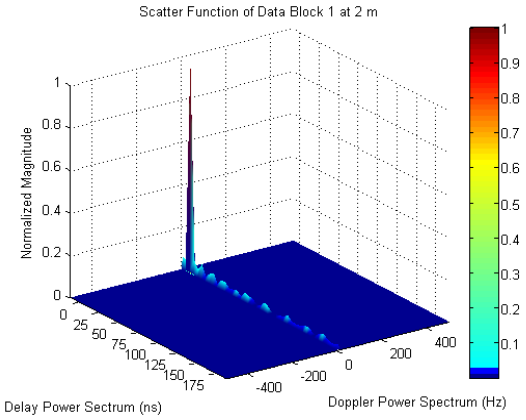

(a) SF of static channel

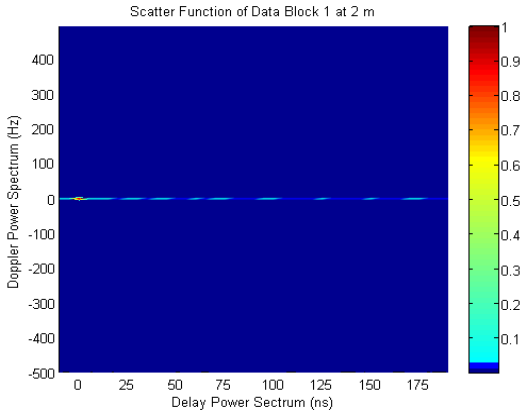

(b) SF of static channel (top view)

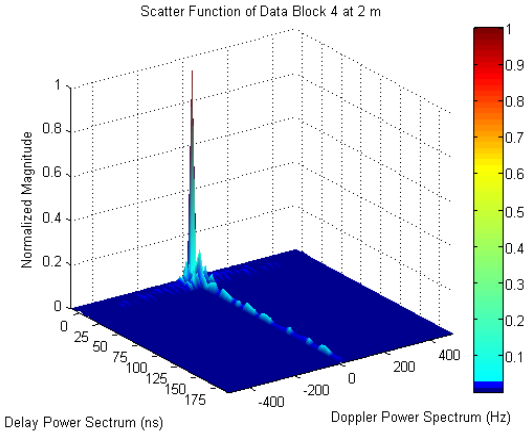

(c) SF of dynamic channel

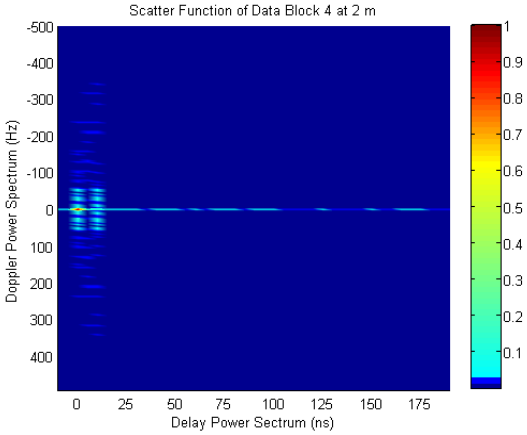

(d) SF of dynamic channel (top view)

Figure 7.45 Scatter function of static and dynamic channel at 2 m

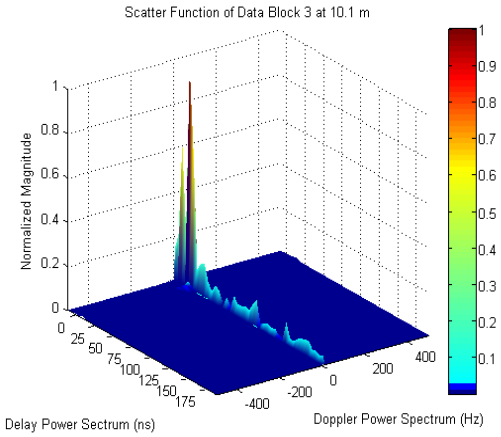

(a) SF of dynamic channel

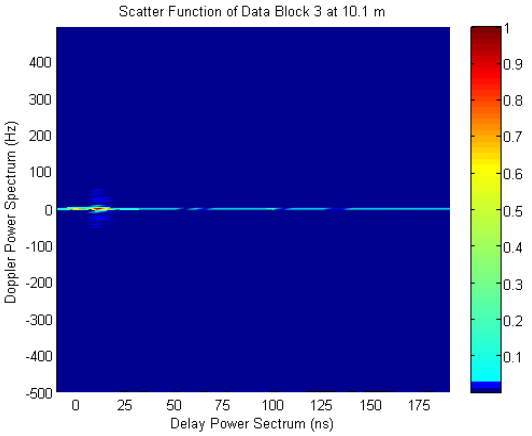

(b) SF of dynamic channel (top view)

Figure 7.46 Scatter function of static and dynamic channel at 10.1 m

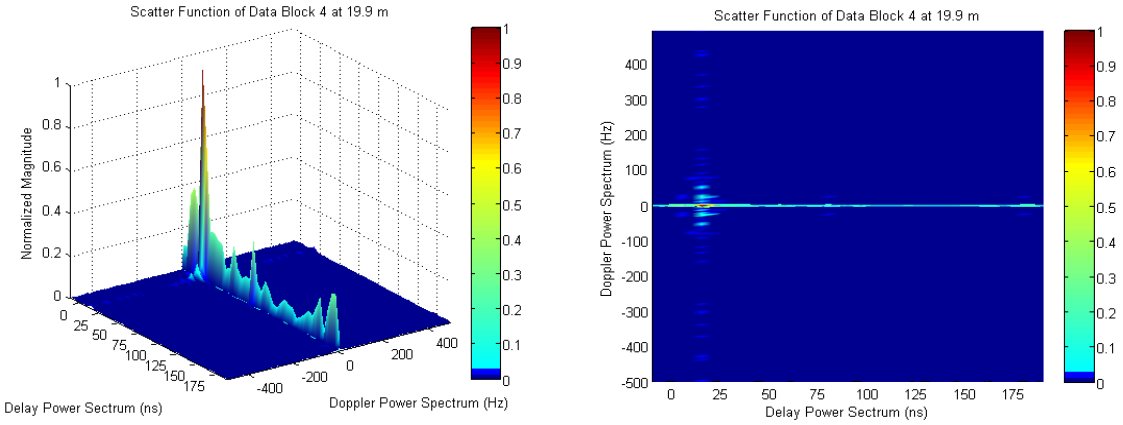

(a) SF of dynamic channel (b) SF of dynamic channel (top view)

Figure 7.47 Scatter function of static and dynamic channel at 19.9 m

7.9 Summary

In this chapter, spatial and temporal variations have been investigated and a number of empirical models have been evaluated. The empirical models and statistical PDFs have been used to analyse the data. The path loss models proposed in literature include WINNER, Hata, Ericsson urban model, and COST-231 Walfisch-Ikegami models. However the best fit model is the linear model. From the measurements in many environments, it can be concluded that environments with moving objects can significantly influence channel fading. To investigate the channel transfer function, the SVDP algorithm was used to estimate the channel impulse response from the measured channel transfer function.

Using SVDP algorithm, the channel impulse responses can be estimated much more accurately due to the ability of the algorithm to achieve better resolution compared to the Fast Fourier transform algorithm.

The RMS delay spread increases with path length and also when vehicles pass the measurement area. Fades up to 30 dB within the signal bandwidth are often measured when a vehicle passes the measurement zone.

References

[7.1] Torres R. P., Cobo B., Mavares D., Medina F., Loredo S., Engels M., "Measurement and Statistical Analysis of the Temporal Variations of a Fixed Wireless Link at 3.5 GHz", Wireless Personal Communications: Springer 2006, Vol. 37, 2006, pp. 41-59.

[7.2] Kolmogorov-Smirnov Goodness-of-Fit Test, Website: http://www.itl.nist.gov/div898/handbook/eda/section3/eda35g.htm

[7.3] Kolmogorov-Smirnov Test, Website: http://www.physics.csbsju.edu/stats/KS-test.html

[7.4] Okumura Y., Ohmori E., Kawano T., Fukuda K., "Field Strength and Its Variability in VHF and UHF Land Mobile Radio Services", Review of the Electrical Communications Laboratory, Vol. 16, September - October 1968, pp. 825 - 873.

[7.5] Hata M., "Empirical Formula for Propagation Loss in Land Mobile Radio Services", IEEE Transactions on Vehicular Technology, Vol. 29, No. 3, August 1980, pp. 317 - 325.

[7.6] COST Action 231, "Digital Mobile Radio Towards Future Generation Systems", Final Report, European Commission, EUR 18957, 1999.

[7.7] Erceg V., Hari K. V. S., Smith M. S., Sheikh K. P., Tappenden C., Costa J. M., Baum D. S., Bushue C., "Channel Models for Fixed Wireless Applications", IEEE 802.16 Broadband Wireless Access WG http://ieee802.org/16, Retrieved May 2008.

[7.8] Electronic Communication Committee (ECC) within the European Conference of Postal and Telecommunications Administration (CEPT), "The Analysis of the Coexistence of FWA Cells in the 3.4 - 3.8 GHz Band", ECC Report 33, May 2003.

[7.9] Milanovic J., Rimac-Drlje S., Bejuk K., "Comparison of Propagation Models Accuracy for WiMAX on 3.5 GHz", IEEE 14th International Conference on Electronics, Circuits and Systems, December 2007, pp. 111 - 114.

[7.10] WINNER II – Public Deliverables, Website: http://www.ist-winner.org/deliverables.html

[7.11] Erceg V., Hari K. V. S., Smith M. S., Baum D. S., Soma P., Greenstein L. J., Michelson D. G., Ghassemzadeh S., Rustako A. J., Roman R. S., Sheikh K. P., Tappenden C., Costa J. M, Bushue C., Sarajedini A., Schwartz R., Branlund D., Kaitz T., Trinkwon D., "Channel Models for Fixed Wireless Applications", Contribution IEEE 802.16a-03/01, June 2003.

[7.12] Proakis J. G., "Digital Communications," McGraw-Hill, Singapore, 1983.

CHAPTER 8

Conclusions and Future Work

Abstract:

A summary of the research carried out is presented in this chapter. The author's contributions are outlined and future work based on this research is suggested.

8.1 Wideband Channel Sounder

To investigate temporal varying urban channels due to the effects of moving objects, it is necessary to have a channel sounder that is capable of performing fast channel measurements. To achieve this, a channel sounder developed based on a proven technique, Spread Spectrum Time Averaging (SSTA) [8.1], implemented using Field Programmable Gate Array (FPGA) [8.2] was used.

Although the channel sounder development was not part of the work conducted in this thesis, the understanding of how it works was critical to the research studies carried out. Therefore detail of how it works has been described in Chapter 4 for completeness. In the configuration used for the channel measurements analysed in this thesis, the features and specifications of the sounder can be summarised as:

- transmits a PRGN signal,
- transmission bandwidth of 200 MHz,
- carrier frequency 2 GHz,
- number of averages 1024, and
- channel measurement rate 5.4 kHz.

The results presented in this thesis show that the channel sampling rate was sufficient for vehicle speed of more than 100 km/h. The channel sampling rate allows the evolution of vehicle induced multipath to be tracked, both, in amplitude and time delay.

8.2 Wideband Channel Measurements

A review of wireless channel models revealed that there are currently no channel models that can be applied in picocell modelling of dynamic variations induced by moving vehicles. Although there have been studies of the impact of automotive traffic on

channel characteristics using narrow band systems, the results of such studies cannot be used to infer the impact of the dynamic variations on wideband high data rate systems. The results presented in this thesis show that the average signal level can under represent frequency selective signal fading by a factor of more than 7. That is, for around 29 dB fade depth within the bandwidth, the average signal can, sometimes, only show a 4 dB fade.

8.3 Channel Impulse Response Estimating Algorithm

In order to accurately resolve multipath components in the received signal, an algorithm that offers a higher resolution than Fast Fourier Transform (FFT), and does not suffer from periodicity assumptions was required. A number of parametric estimation techniques were assessed and Singular Value Decomposition Prony (SVDP) algorithm was chosen. The advantage of SVDP is that it converges quickly to the solution. Although the formulation is documented, the implementation requires very careful fine tuning of the functions.

The results show that with a 200 MHz bandwidth signal, SVDP does achieve resolutions up to 1 ns for high signal to noise ratio signals, that is a factor 5 better than FFT. For well separated in time delay impulses, SVDP can resolve the multipath components at very low SNRs.

8.4 Channel Modelling

In this thesis, path loss models for LOS channels such as Okumura model [8.4], Hata model [8.5], COST231 Walfisch-Ikegami model [8.6], etc. have been described in chapter 3.

The data measured were separated into measurement with and without vehicles passing. Analyses show that the two sets of data can be model with a linear model. None of the models reviewed fits the data. One reason could be because of the short path which is smaller than the spatial resolution of most of the models in literature. This can be attributed to the fact that most of these models were developed for cellular network planning.

Probability distribution functions (PDFs) were used to examine the signal power spreading at each position along the measurement path. Komolgorov-Smirnov (KS) goodness of fit test has been used with the method of Root Mean Square Error (RMSE)

to assess the PDF. Rician PDF gives the best results. A combination of Rician PDF and linear regression can be used to represent the signal power spreading across the measurement path.

8.5 The Channel Transfer Function and Impulse Response

Analyses of channel transfer function and impulse response have been conducted to examine the effect of moving vehicles. At short distances, frequency selective fading might only due to reflections from vehicle passing. But for long distances, beyond 16 m, frequency selective fading is also due multipath components received due to other objects in the environment.

The transmitter antenna height has an impact the signal variation with distance owing mainly to the beam pattern of the antenna. At higher antenna heights, the receiver at short distances may not be in the direction of maximum power of the transmitter. This results in differences in received power between antennas mounted at the different heights in picocells.

8.6 Doppler shift and RMS Delay Spread

It has been observed that when there is a vehicle passing the RMS delay increases and coherence bandwidth decreases. This is expected as at least one multipath component becomes very strong relative to the LOS component.

Doppler frequency shift is a combination of frequency shift from each signal component as represented from the impulse response in detail of time delay. Doppler shift is changed based on the vehicle passing similar to the RMS delay spread.

For normalised delay power spectrum, RMS delays of the received signal vary between 5 ns and 20 ns. However, unless each channel response is individually normalised, the presence of a moving vehicle introduces an evolution not only in the reflected signal amplitude, but also in the time delay of all the channel responses. This, if not calibrated out results is exaggerated RMS delay spread values.

8.7 Author’s Contributions

The author’s contribution has been the successful assessment and validation of the data. In addition, the processing and analysis of the data measured, development of a high

resolution channel impulse response estimating algorithm and the study of an urban spatial and temporal varying channel. More specifically, the author's contributions are:

- the implementation of a suitable data calibration procedure;
- the research, design and development of a high resolution channel impulse response estimating algorithm, SVDP algorithm;
- implementation of software to process and analyse the measured channel data;
- analysis and interpretation of the measured data and assessment of the prevailing mode of propagation in the presence of vehicles;
- analysis of the relationship between signal power decay over distance in a picocell environment; and
- the provision of evidence of the dynamic evolution of the channel induced by traffic in an urban environment.

8.8 Future work

From the results of the spatial and temporal variations, a combination of Rician probability distribution function and linear model can be used to represent the signal power spreading across the measurement path. However more measurements are required to ensure that this model has a wide application with other urban channels.

To avoid mobile network interference, the transmission frequency of the channel sounder needs to be changed from the current value of 2 GHz. Since most of the RF components were not designed for this sounder, a rebuild of the RF unit will allow better SNR to be achieved.

An improve suite of software is required to allow fast data processing and channel characterisation. A more robust method of handling impulse response evolution should be developed to allow channel characterisation parameters such as RMS delay spread to be estimated.

References

[8.1] Austin J., Ditmar W. P. A., Lam W. K., Vilar E., Wan K. W., “A Spread Spectrum Communication Channel Sounder”, IEEE Transaction on Communications, Vol. COM-45, No. 7, July 1997, pp. 840-847.

[8.2] Stuart K., “Wideband Channel Sounder Development and Investigation of Spatial and Temporal Variations in Wireless Communication Channels”, Ph.D. Thesis Department of Electronic and Computer Engineering, University of Portsmouth, U.K., November 2007.

[8.3] Greenstein L. J., Andersen J. B., Bertoni H. L., Kozono S., Michelson D.G., Tranter W. H., “Guest Editorial Channel and Propagation Models for Wireless System Design I”, IEEE Journal on Selected Areas in Communications, Vol. 20, No. 3, April 2002, pp. 493 - 495.

[8.4] Okumura Y., Ohmori E., Kawano T., Fukuda K., “Field Strength and Its Variability in VHF and UHF Land Mobile Radio Services”, Review of the Electrical Communications Laboratory, Vol. 16, September - October 1968, pp. 825 - 873.

[8.5] Hata M., “Empirical Formula for Propagation Loss in Land Mobile Radio Services”, IEEE Transactions on Vehicular Technology, Vol. 29, No. 3, August 1980, pp. 317 - 325.

[8.6] Erceg V., Hari K. V. S., Smith M. S., Sheikh K. P., Tappenden C., Costa J. M., Baum D. S., Bushue C., “Channel Models for Fixed Wireless Applications”, IEEE 802.16 Broadband Wireless Access Working Group http://ieee802.org/16, Retrieved May 2008.

APPENDIX A

Conference Publication Relevant to this Thesis

[1] Toutaouchone S., D. Ndzi, K. Stuart, R. Khusainov, “Spatial and Temporal Variation of Urban Wideband Channels due to Automotive Traffic”, International Conference on Electrical, Computer and Communication Engineering (ICECCE-2011), Paris, France, 27-29 July 2011.

[2] Ndzi D. L., Stuart K., Toutaouchone S., Vuksanovic B., Sanders D. A., "Wideband sounder for dynamic and static wireless channel characterisation: urban picocell channel model," Progress In Electromagnetics Research, Vol. 113, 285-312, 2011.

[3] Ndzi D. L., Stuart K., Toautachone S., Yang Y., Dunn V., “An FPGA-Based Adaptable 200 MHz Bandwidth Channel Sounder for Wireless Communication Channel Characterisation”, International Journal of Reconfiguable Computing, Vol. 2011, Article ID 894530, 14 pages, 2011.

Spatial and Temporal Variation of Urban Wideband Channels due to Automotive Traffic

Somboon Toautachone, David Ndzi, Kenneth Stuart, Rinat Khusainov

Department of Electronic and Computer Engineering, University of Portsmouth
Anglesea Road, Portsmouth PO1 3DJ, United Kingdom

{Somboon.Toautachone, David.Ndzi}@port.ac.uk, kstuart@rftresearch.com, rinat.khusainov@port.ac.uk

Abstract— **Spatial and temporal variations of an urban wireless channel that is expected to support high data rate transmissions is studied and the results presented in this paper. The study examines the effects of vehicles travelling parallel to, but not traversing, the transmission path on the channel quality. It shows that multipath components reflected from passing vehicles introduce frequency selective fading with fade nulls up to 40 dB. However, these are masked when the average signal across the bandwidth is considered. Singular value decomposition Prony algorithm has been implemented and used to estimate the impulse response of the channel from the transfer function. This allows the variation in the channel response to be tracked as the vehicle passes due to its high multipath resolution. An assessment of the signal variation with distance shows that a linear model best describes the channel model over distances up to 20 m. Over this distance, most channel models assume free space loss. However the results presented in this paper show that the signal decays slower than predicted by the free space model. However a qualitative assessment shows that despite these strong levels, communication will be characterised by burst of errors that cannot be compensated using conventional fade mitigation techniques such as adaptive equalisation because of the dynamic nature of the channel.**

Keywords— **Spatial Variation, Temporal Variation, Singular Value Decomposition Prony (SVDP), Channel Transfer Function-Impulse Response**

I. INTRODUCTION

Over the past decade there has been a phenomenal rise in the use of wireless communications systems favoured for its flexibility and mobility over wired communication system. Although wireless communication system can fulfil most user requirements, the capacity for supporting high data applications on the move is limited both by variations in the wireless channels hitherto be accurately modelled and required system complexities. Wireless signal transmissions experiences at least one or a combination of mechanisms which includes reflection, refraction, diffraction and scattering. Multipath reception as a result, introduces inter-symbol interference (ISI), and depending on the dynamics of the objects within the environment or terminals, Doppler frequency shift may also be present. Although adaptive techniques e.g. equalization, antenna diversity and coding techniques are widely used to compensate for these problems, the techniques are ineffective in dynamic channels. Therefore there is a need to better understand multipath channel fading behaviour in particular scenarios e.g. dynamic temporal and spatial varying urban channels. This knowledge can then be used to develop models that can be applied to predict and mitigate the detrimental effects of channel variations caused by mobile and fixed objects such as vehicles, buildings, vegetation and people on wireless systems e.g. in urban environment.

Most of the research on the effects of objects (such as foliage, buildings, vehicles) on wireless signal propagation has been based on fixed point wireless systems in a variety of environments both, indoors and outdoors [1]-[3]. Most wireless propagation channel models [4]-[6] are focused on specific microwave frequency range, for example broadband fixed wireless access (BFWA) [7] standards for the 2 to 11 GHz in Europe, HiperMAN in the United State of America, IEEE 802.16 (or WiMAX) Channel. There has been renewed interest in time and space dispersion, and also in Doppler frequency shift [1][8][9][17]. This is because most wireless systems are set up at heights where these variations are easily induced. Therefore there is a need to improve the quality of wireless communication services.

Experimental studies have resulted in the development of empirical and statistical wireless channel models [4] such as the Stanford University Interim (SUI) channel model [16]. Although a number of studies have led to the proposal of a number of channel models e.g. COST 231 Walfisch-Ikegami, Hata-Okumura [10][11], none of the models can be applied to a wide range of scenarios.

This paper presents results of a wideband channel measurements conducted to study the impact of temporal variations induced by automotive traffic on a mobile system. Fast Fourier Transform (FFT) is widely used to estimate the impulse response of wideband channels. However, FFT suffers from poor impulse response resolution that is limited to 1/bandwidth. In addition, FFT suffers from spectral leakage which masks weak multipath components. In this study, Singular Value Decomposition (SVDP) algorithm has been developed and used to estimate the impulse response from the measured channel transfer functions [12]. SVDP achieve resolution that is up to a factor 3 better than FFT in high signal to noise ratio conditions.

This paper also presents results of large scale fading that have been computed from measured channel transfer function. The data processing technique implemented separates the data into static (no event) data when the channel was considered to

be wide sense stationary with no moving objects and dynamic (event) data when there were moving objects within the channel. Emphasis of the analysis is on the study of the impact of automotive traffic on wireless communication systems. Such a study is important for the effective implementation of mobile high data rate broadband wireless communication in urban environment [13].

This paper is organised as follows; Section II describes the measurement system used to conduct channel measurements whilst the measurement environment is described in Section III. Section IV describes the Singular Value Decomposition Prony algorithm that has been implemented to estimate the impulse response from the measured channel transfer functions. The spatial and temporal measurement results are presented in Section V. Conclusions are given in Section VI.

II. MEASUREMENT SYSTEM

The channel sounder was developed at the University of Portsmouth. The main objectives were to simplify the sounder system architecture and develop a fast and highly adaptable channel sounder that can be used to measure the channel transfer function over the widest bandwidth as possible. The speed of the channel acquisition system enables the sounder to be used to study both slow and fast channel variations. Details of the channel sounder are presented in [14]. Some of the details are presented in this paper for completeness.

The channel sounder transmits a pseudo random Gaussian noise (PRGN) waveform which is generated by an arbitrary waveform generator. Field programmable gate array (FPGA) was selected [15] because it supports high clock frequencies and concurrent processes. A block diagram of the transmitter is shown in Fig. 1. Fig. 2 illustrates the receiver with three main units: RF receiver, analogue to digital converter (ADC) on a carrier card and the processing card. The key objectives of the transmitter and the receiver system design were to minimize the system set-up time and to develop a highly flexibility data acquisition system [15] that could be adapted for measurements in a wide range of scenarios.

Fig. 3 and Fig. 4 show the 200 MHz PRGN signal in the time domain and frequency domain, respectively. The waveform contains 1024 discrete spectral lines in the range ± 100 MHz. For the study reported in this paper, the waveform was transmitted at a carrier frequency of 2 GHz using omni-directional antennas at the transmitter and the receiver.

A. Data Acquisition and Processing

The channel was measured at the rate of 5.425 kHz. This generates a large volume of data and to ensure that the data is transferred reliably to the computer hard-drive across the PCI-bus, time gaps of 256 ms were used to separate 240 continuous channel response acquisitions. Each stored channel transfer function was the results of 16 averages. An averaged channel transfer function was captured every 184.32 μs. Therefore a data file containing 240 averaged channel transfer functions took 44.24 ms to capture. The averaging process runs in real-time and this allows the sounder to be used in low signal to noise ratio conditions.

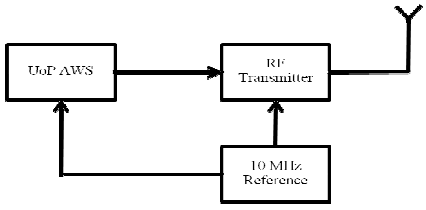

Fig. 1 The channel sounder transmitter

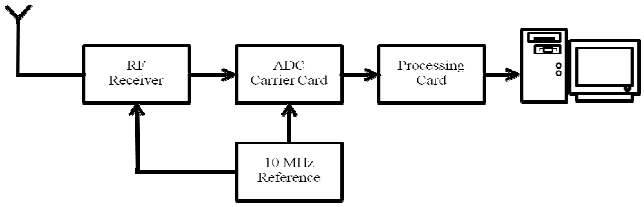

Fig. 2 The channel sounder receiver

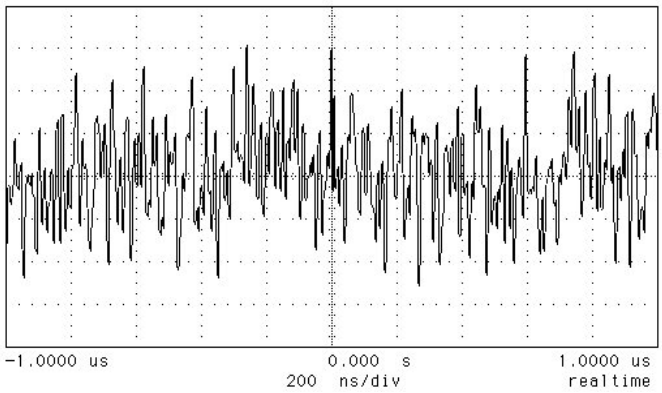

Fig. 3 200 MHz PRGN signal: time waveform

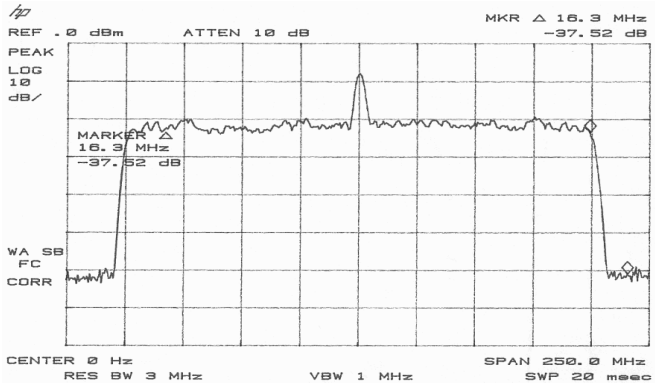

Fig. 4 200 MHz PRGN signal: magnitude spectrum

B. Data Calibration

The received signal from the transmitter to the receiver through the channel is a combination of channel transfer function and system transfer function. Hence, to obtain the channel transfer function the system response must be calibrated out. The block diagram in Fig. 5 presents the overall transfer function which includes 3 transfer functions: the transmitter, channel, and the receiver.

At the transmitter: $H_T = H_{Tx}H_{Tant}$, including the antenna response.

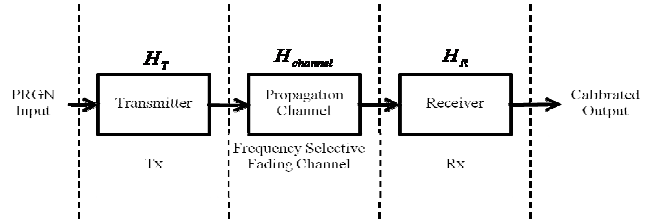

Fig. 5 Set-up for calibration

At the receiver: $H_R = H_{Rant}H_{Rx}H_{spu}$ include the transfer function of the antenna, the receiver and its averaging unit, respectively.

If S_{PRGN} and G_{mea} are the input signal and output signal of system in the frequency domain respectively, from Fig. 5 the output signal can be represented by,

$$G_{mea} = S_{PRGN}(H_T H_{channel} H_R) \tag{1}$$

The overall transfer function of system is combined with the transfer function of the propagation channel. The transfer function of the system needs to be eliminated to get the channel transfer function. A reference channel transfer function and calibrated output, H'_{ref} and G'_{ref}, are used to calibrate the measured signal where,

$$G'_{ref} = S_{PRGN}(H_T H'_{ref} H_R) \tag{2}$$

Dividing (1) by (2) means,

$$\frac{G_{mea}}{G'_{ref}} = \frac{H_{channel}}{H'_{ref}} \tag{3}$$

As H'_{ref} represented an ideal channel response measured under high signal to noise ratio (SNR) condition with a flat spectrum, then

$$\frac{H_{channel}}{H'_{ref}} \approx H_{channel} \tag{4}$$

All system responses, magnitudes and phases, are eliminated leaving only the channel transfer function.

III. MEASUREMENT SCENARIO

The measurement scenario is illustrated in Fig. 6. The system was set up parallel to an urban dual carriage road (Anglesea Road) which has 4 lanes. The nearest 2 lanes go north and the other 2 lanes go south. The set up was to investigate the effects of moving vehicles on the propagation channel when the traffic does not traverse the transmitter to receiver path. The perpendicular distances from the transmission paths to each lane from the nearest lane to the furthest were 3.5 m, 7 m, 11.6 m and 15.1 m, respectively. The transmitter was fixed in one position during the measurements whilst the receiver was moved away from the transmitter in steps of 0.3 m from 2 m to 20 m.

The transmitter antenna height was set at 2.5 m and the receiver antenna height used was 1.6 m. The receiver antenna height was selected to be as close as possible to the height of a mobile user.

From the measurement scenario, the line of sight (LOS) was never obstructed and this study was aimed at investigating the impact of off-path scattering/reflections on communication systems.

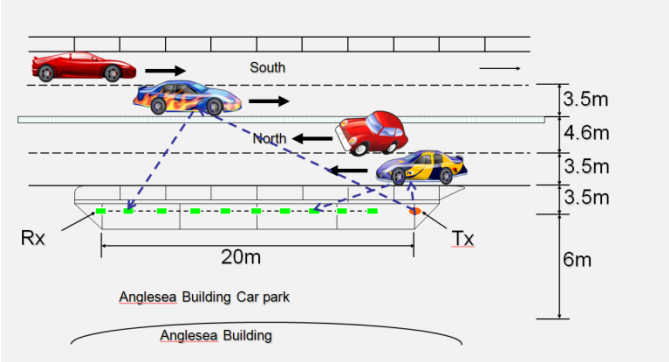

Fig. 6 The measurement scenario in front of Anglesea building

The speed limit for vehicles travelling on the road is 30 mph (48 km/h). However because of the presence of traffic lights and a junction not far from the measurement area, vehicles normally travel at slower speeds. If the speed of a vehicle is 20 mph (8.889 m/s), the vehicle would travel 0.39 m in the time that it takes to capture 240 channel responses (snapshots). During the measurements, a time gap of 251.66 ms was introduced between each data block of 240 snapshots.

IV. SINGULAR VALUE DECOMPOSITION PRONY ALGORITHM

Singular value decomposition Prony (SVDP) algorithm has been used as an alternative to the Fast Fourier Transform (FFT) algorithm. It is used to estimate the channel impulse response from the measured transfer function. FFT suffers from spectral leakage which can mask weak multipath components. In addition, it assumes that the multipath components arrive with only fixed values of time delay due to its limited resolution. If it is assumed that the multipath signals have different amplitudes and delays, then the impulse response of the channel can be represented by,

$$h(t) = \sum_{n=1}^{N} a_n \delta(t - \tau_n) \tag{5}$$

where a_n and τ_n are the ray amplitudes and time delays of the impulses. According to (5), its Fourier transform (transfer function) can be represented by (6).

$$H(j\omega) = \sum_{n=1}^{N} a_n e^{-j\omega\tau_n} \tag{6}$$

Each i^{th} spectral line can be represented by (7) where ω is replaced by $\omega_0 + i\omega_s$; ω_0 is the lowest angular frequency and ω_s is the angular sampling frequency.

$$H_i = \sum_{n=1}^{N} a_n e^{-j(\omega_0 + i\omega_s)\tau_n} \qquad i = 0,1,\dots,N-1 \tag{7}$$

N is the number of multipath components. Equation (7) can be rewritten as shown in (8).

$$H_i = \sum_{n=1}^{N} b_n z_n^i \tag{8}$$

With $b_n = a_n e^{-j\omega_0\tau_n}$ and $z_n = e^{-j\omega_s\tau_n}$. To change its index, then (8) becomes

$$H_{i-m} = \sum_{n=1}^{N} b_n z_n^{i-m} \tag{9}$$

Consider a linear combination of K arbitrary components represented in (9) by using a set of complex weighting coefficients, a_m, with m = 0,1, ..., K where $a_0 = 1$.

$$\sum_{m=0}^{K} a_m H_{i-m} = \sum_{m=0}^{K} a_m \sum_{n=1}^{N} b_n z_n^{i-m} \tag{10}$$

And can also be represented by (11).

$$\sum_{m=0}^{K} a_m H_{i-m} = \sum_{n=1}^{N} b_n z_n^{i-K} \sum_{m=0}^{K} a_m z_n^{K-m} \tag{11}$$

The latter summation of (11) represents a polynomial $P(z)$. It is called the predictor polynomial and is given by

$$P(z) = \sum_{m=0}^{K} a_m z_n^{K-m} = \prod_{m=1}^{K} (z_n - z_m) \tag{12}$$

From (11),

$$H_i = -\sum_{m=1}^{K} a_m H_{i-m} \tag{13}$$

It can be seen that in (13) the channel transfer function is presented in the form of an autoregressive (AR) equation. This is called the forward linear predictor (FLP) where K is the order of the FLP and a_m are called the AR coefficients whilst its backward linear predictor (BLP) is given as

$$H_i^* = -\sum_{m=1}^{K} a_m H_{i+m}^* \tag{14}$$

The Prony method is based on the relationship between (7), (8), (13) and (14) via the predictor polynomial (12).

To estimate the AR coefficients, by combination of the FLP and BLP, a forward-backward linear predictor (FBLP) is formed and can be used to represent the set of simultaneous equations written in matrix form as

$$Y = S\alpha \tag{15}$$

Where Y is a data vector with a dimension of $2(M-K) \times 1$, S is a data matrix of order $2(M-K) \times K$, and α is the AR coefficient vector of order $K \times 1$ respectively. By using the singular value decomposition (SVD) technique, the data matrix S can be represented by

$$S = U\Delta V^H \tag{16}$$

U is the left singular vectors of S which is equivalent to the eigenvectors of SS^H and V is the right singular vectors of S which is equivalent to the eigenvectors of $S^H S$ and Δ is a diagonal matrix given in form of $\{\lambda_i : i = 1,2,\dots,K\}$ called the singular values which are equivalent to the square root of the eigenvalues of $S^H S$ whilst ^{H} represents the Hermitian transpose of the matrix.

Thus, the AR coefficients, α, can be calculated as follows

$$\alpha = \sum_{i=1}^{N} \frac{u_i^H X}{\lambda_i^2} u_i \qquad with\ X = -S^H Y \tag{17}$$

The time delay for each impulse response can be calculated using (18).

$$\tau_n = -\frac{arg(z_n)}{\omega_s} \tag{18}$$

From (8) which is written in form $H = Zb$, b can be solved as follows:

$$b = (Z^H Z)^{-1} Z^H H \tag{19}$$

Finally the amplitude a_n for each ray can calculate using the relationship $b_n = a_n e^{-j\omega_0\tau_n}$.

V. MEASUREMENT RESULTS

A. Signal Variation and Channel Response Estimate

Fig. 7 shows the averaged signal power variation across the bandwidth with time. It shows that the overall impact of automotive traffic results in significant fading. This is cause by frequency selective fading within the bandwidth due to the reflected multipath component from the passing cars. It should be noted that in the absence of a car, the receiver will receive the line of sight component and relatively weak scattered components from objects in the environment.

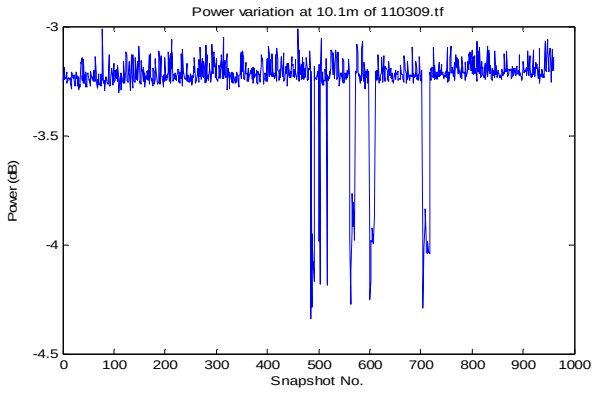

Fig. 7 Signal power level variation showing fading caused by cars passing parallel to the transmission path

In order to better understand the channel structure, SVDP algorithm was used to estimate the channel response. Root mean square error was used to assess the accuracy of the estimated channel impulse response. To achieve this, the estimated impulse response is used together with equations (7) to reconstruct the transfer function. Fig. 8 shows an example of an estimated transfer function superimposed on the measured channel transfer function. The corresponding estimated impulse response is shown in Fig. 9.

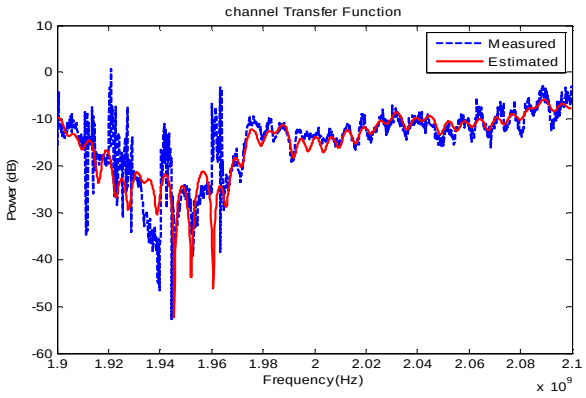

Fig. 8 Measured and estimated transfer function

In Fig. 9, the impulse response of the channel is normalised to the strongest component. It shows that there are a number of components with one that has strong amplitude compared to the strongest multipath component. This relatively strong multipath component results in deep fades within the bandwidth at a frequency that is close to 1.94 GHz in Fig. 8. Fig. 9 also shows that the first component is not always the strongest component.

B. Spatial and Temporal Variations

The averaged received signal power as a function of distance is shown in Fig. 10. In order to assess the impact of automotive traffic on wideband signals, the data was separated into event (when there was a vehicle passing) and non-event (when there was no vehicle passing). To enable accurate data separation software to be developed, controlled experiments were conducted in which video recordings, synchronised with the data acquisitions, were used. This enabled a corroboration of the variation in signal levels with the traffic.

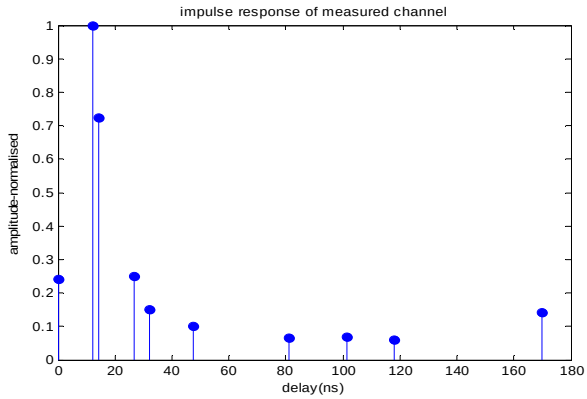

Fig. 9 Impulse response of measured channel using SVDP algorithm

Fig. 10 shows that automotive traffic causes fading in the averaged received signal power. This can be attributed to the multipath fading due to the relative strength of the reflected components from the passing vehicle. The impact of cars is more clearly shown in Fig. 11. For this data, the transmitter and receiver were fixed and any change in the signal strength was due to changes in the environment. In the static case the averaged received signal power variation is small, between -5.45 dB and -5.74 dB whilst in dynamic scenario it varies between -5.43 dB and -6.16 dB. This variation is smaller than the fade depths obtained within the bandwidth which can be up to 40 dB. The reason for the small variation is due to the averaging effect.

Analysis of the results show that moving vehicle on each lane affect the averaged received signal power levels differently with a vehicle in the nearest lane to the transmitter-receiver path having the greatest effect. This is because reflected components from the vehicle travel only very short additional distances compared to the line of sight path and therefore have strong amplitudes. The results also show that large vehicles cause greater signal fades compared to smaller vehicles. This can be attributed to the large signal reflection surfaces of large vehicles. The duration of the fades is also longer for large vehicles.

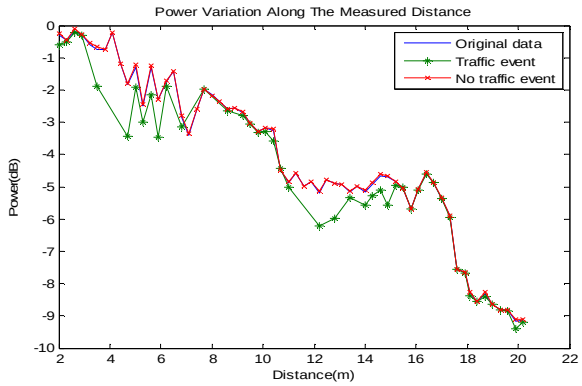

Fig. 10 Signal power variation with antenna separation

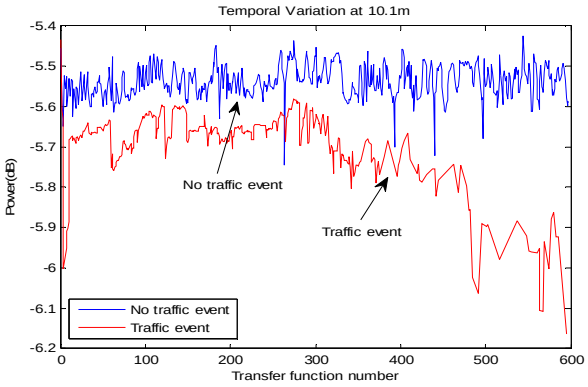

Fig. 11 Temporal variation of signal power at 10m

The measured data has been used to model the signal variation with distance in an urban environment. The models that have been fitted to the data include a linear model, free space path loss, WINNER project scenarios B1 and B3, and COST 231 Walfisch-Ikegami models [16]. These are illustrated in Fig. 12. It shows that the linear model gives a more accurate representation of signal variation with distance. This is followed by WINNER B3 scenario model proposed for indoor channels. It is worth noting that the signal decay with distance is less than predicted by the free space model. However caution must be exercised because the presence of moving vehicles introduces a burst of error in the transmission that cannot be mitigated using conventional fade mitigation techniques such as adaptive equalisation.

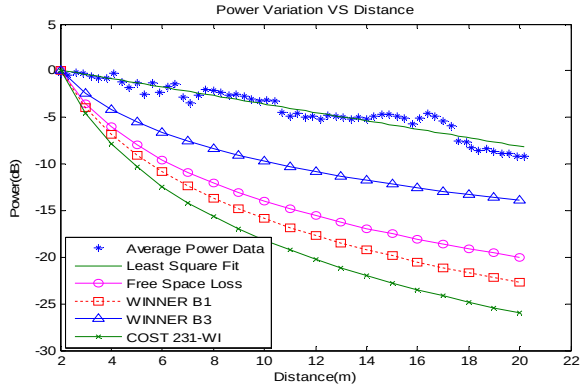

Fig. 12 Evaluation of channel variation models

VI. CONCLUSION

The results of spatial and the temporal variations of an urban channel have been presented in this paper to show the effects of vehicles moving parallel to the transmitter-to-receiver path. Singular value decomposition Prony algorithm that has been implemented and used to estimate the impulse response from the measured channel transfer function has been presented. The results show that SVDP can achieve multipath delay resolution of 2 ns compared to 5 ns by FFT for signal transmission bandwidth of 200 MHz. Measurement results show that a vehicle travelling parallel to the transmission path can introduce fade depths up to 40 dB within the signal bandwidth. However, when the signal is averaged across the bandwidth, these fades are masked. Nonetheless these fades are significant enough to introduce a burst of errors in high data rate digital transmission. To maintain a high quality of services for high data rate services in urban environment, a greater understanding of this dynamic variation is required and should be accurately modelled. An assessment of some of models that have been proposed or are widely used to model signal variation with distance show that none of the models gives a good fit to the measured data. Average signal variation with distance is better represented by a linear model with decay rate that is smaller than predicted by Free Space Loss model. This paper has focused on the qualitative assessment of the channel. Future work will focus on a more detailed qualitative and quantitative analysis of spatial and temporal varying urban short range wireless channels.

ACKNOWLEDGMENT

The authors express their sincere gratitude to Dr John Austin for his vision and contribution to the development of the channel sounder.

REFERENCES

[1] P. Marinier, G. Y. Delisle, and C. L. Despins, “Temporal Variations of the Indoor Wireless Millimeter-Wave Channel,” IEEE Trans. Antennas Propagat., vol. 46, No. 6, pp 928-934, June 1998.

[2] M. J. Gans, N. Amitay, Y. S. Yeh, T. C. Damen et al., “Propagation Measurements for Fixed Wireless Loops (FWL) in a Suburban Region With Foliage and Terrain Blockages,” IEEE Wireless Commun., vol. 1, No. 2, pp. 302-310, April 2002.

[3] L. Ahumada, R. Feick, R. A. Valenzuela, and C. Morales, “Measurement and Characterization of the Temporal Behavior of Fixed Wireless Links,” IEEE Trans. Vehicular Technology, vol. 54, No. 6, pp. 1913-1922, Nov. 2005.

[4] E. Biglieri, J. Proakis, and S. Shamai, “Fading Channels: Information-Theoretic and Communications Aspects,” IEEE Trans. Information Theory, vol.44, No. 6, Oct 1998.

[5] L. J. Greenstein, J. B. Andersen et al., “Guest Editorial Channel and Propagation Models for Wireless System Design I.” IEEE Journal on Selected Areas in Comm., vol. 20, No. 3, April 2002.

[6] L. J. Greenstein and S. S. Ghassemzadeh, “Comparing Three Models for UWB Indoor Power Delay Profile.” Conference on Information Sciences and Systems, 40th Annual, March 2006.

[7] P. Soma, Y. W. M. Chia and L. C. Ong, “Recommendation on Time Varying Radio Propagation Channel Models and Study of System Performance for LMDS,” Contribution IEEE 802.16.1pc-00/24r1,April,2000.

[8] N. Naz, and D. D. Falconer, “Temporal Variations Characterization for Fixed Wireless at 29.5 GHz,”in 2000 IEEE51st Vehicular Technology Conference Proceedings, vol. 3, pp. 2178-2182, Tokyo, May 2000.

[9] D. C. Cox, “Delay Doppler Characteristics of Multipath Propagation at 910 MHz in a Suburban Mobile Radio Environment,” IEEE Trans. Antennas Propagation, vol. AP-20, No. 5, pp. 625-635, Sep. 1972.

[10] V. Erceg, L. J. Greenstein et al., “An Empirically-Based Path Loss Model for Wireless Channels in Suburban Environments.” IEEE Global Telecommunications Conference, vol. 2, Aug 2002.

[11] M. Hata, “Empirical Formula for Propagation Loss in Land Mobile Radio Services.” IEEE Trans. Vehicular Tech., vol. VT-29, No. 3, Aug 1980.

[12] W. H. Lau, J. Austin, A. Hewitt, E. Vilar et al., “Analysis of the Time-Variant Structure of Microwave Line-of-Sight Multipath Phenomena,” IEEE Trans. Commun., vol. 39, No. 6, June 1991.

[13] M. Shafi, A. Hashimoto, M. Umehira, S. Ogose et al., “Wireless Communications in the Twenty-First Century: A Perspective,” IEEE Proceedings, vol. 85, No. 10, Oct. 1997.

[14] D. L. Ndzi, K. Stuart, S. Toautachone, Y. Yang, and V. Dunn, " An FPGA-Based Adaptable 200 MHz Bandwidth Channel Sounder for Wireless Communication Channel Characterisation," International Journal of Reconfigurable Computing, vol. 2011, Article ID 894530, 14 pages, 2011.
[15] K. Stuart, "Wideband Channel Sounder Development and Investigation of Spatial and Temporal Variations in Wireless Communication Channels," Ph.D. Thesis, Department of Electrical and Computer Engineering, Univer of Portsmouth, U.K., Nov. 2007.
[16] V. Erceg, K. V. S. Hari, M. S. Smith, D. S. Baum et al., "Channel Models for Fixed Wireless Applications," Contribution IEEE 802.16a-03/01, June. 2003.
[17] R. P. Torres, B. Cobo, D. Mavares, F. Medina, S. Loredo and M. Engels, "Measurement and Statistical Analysis of the Temporal Variations of Fixed Wireless Link at 3.5 GHz," Wireless Personal Communications: Springer, 2006,vol. 37, pp. 41-59, 2006.
[18] F. Aryanfar, and K. Sarabandi, "A Millimeter-Wave Scaled Measurement System for Wireless Channel Characterization," IEEE Trans. Microwave Tech., vol. 52, No. 6, June 2004.

Progress In Electromagnetics Research, Vol. 113, 285–312, 2011

WIDEBAND SOUNDER FOR DYNAMIC AND STATIC WIRELESS CHANNEL CHARACTERISATION: URBAN PICOCELL CHANNEL MODEL

D. L. Ndzi, K. Stuart, S. Toautachone, B. Vuksanovic and D. Sanders

Microwave Telecommunication Systems Research Group
Department of Electronic and Computer Engineering
University of Portsmouth, Anglesea Building
Anglesea Road, Portsmouth, PO1 3DJ, UK

Abstract—This paper presents a high speed configurable FPGA-based wideband channel sounder with signal bandwidths up to 200 MHz and results of a study of dynamic urban picocell channel. The use of FPGA allows the sounder to be adaptable for measurements in different scenarios. Adaptable options include changes to the waveform, bandwidth, channel sampling rate and real-time averaging to improve signal-to-noise ratio in weak signal conditions. The implemented architecture has led to a 60% reduction in size and weight compared to sounders in use elsewhere making it ideal for mobile channel measurements. The study of an urban picocell channel has shown that dynamic variation due to automotive traffic introduces average signal fades of up to 5 dB but causes frequency selective fading with depths of up to 40 dB. Existing channel models assume antenna heights of more than 6 m and path lengths of more than 30 m. Therefore there is a need for shorter path models and this paper proposes a linear picocell channel model for static and dynamic urban environment.

1. INTRODUCTION

Growth in wireless communication use has seen a shift in telecommunication pricing model from connectivity to data rate and quality of service model. The widespread use of smart-phones has also accelerated growth in high data rate applications. Significant

Received 29 December 2010, Accepted 31 January 2011, Scheduled 4 February 2011
Corresponding author: David L. Ndzi (david.ndzi@port.ac.uk).

studies have been carried out in short-range indoor environment [1, 2]. However studies in short-range outdoor environment where most of the mobile devices are used have received relatively little attention. In outdoor urban environment many studies have focused on macrocells [3].

Substantial research activities have produced numerous models relating to a variety of wireless channels [4–10]. In outdoor urban environment, a number of scenarios have been developed which can be broadly categorised as over roof-tops with static or mobile receivers for path lengths that are greater than 100 m [11–13]. In fixed wireless access channel models [14] where the transmitter and the receiver are static, the transmitter to receiver distance is too large. In addition to these, for distances less than 20 m most models, including the COST231-Walfisch-Ikegami-Model (COST231-WI), assume free-space path loss [15, 16]. The antenna heights and distances are not typical of current and future high data rate wireless access system set ups [17, 18].

Urban channels exhibit both spatial and temporal variations. Studies of induced dynamic variations in the channels due to movements within the urban picocell areas are limited. References can be found for indoor channels in [19–22]. Temporal variation of the channel can have significant impact on the performance of wireless systems resulting in a burst of errors in digital systems. Therefore, there is a need to understand the temporal variability of the channel response in order to assess its impact on wireless data rates [23]. Considerable studies have been carried out using Multiple-Input Multiple-Output (MIMO) systems resulting in a large number of publications of MIMO channel models [24]. A large study of spatial channels with path lengths, mainly, from 30 m up to 8 km have also been undertaken under the 3GPP group for bandwidths of 5 MHz [25]. This has been extended by the WINNER project for bandwidths up to 100 MHz and a number of models have been proposed for a range of communication channels in urban and suburban environment [26].

The diversity of the urban environment and the dynamic nature of the channels make the measurement and analysis approach critical to ensure that results obtained are representative and can be applied to similar channels. Wideband channel sounders are often used to study broadband wireless channels. Channel sounding take many forms and the systems that are used have evolved in parallel with the interest in wireless communication [27–29]. Some techniques, such as pulse or frequency swept transmissions, have been widely used in many measurement studies [30–34]. Although simple to construct and low cost, these techniques suffer from poor multipath delay resolution and slow channel measurement rates. These make

their use in the investigation of fast dynamic channels impractical. When the received signal is digitised, the hardware complexity becomes disproportionately high due to the spectral inefficiency of the signals [35, 36].

Sounders based on the cross-correlation techniques have been widely used over the years [37–41]. In this technique the received signal is correlated with an identical transmitted sequence clocked at a slower rate or at the same rate as in the transmitter but such that the two sequences pass each other on a step-by-step basis rather than continuously. Digital frequency synthesisers have also been used with this technique to increase signal bandwidth, multipath resolution and channel sampling speed. However the use of waveforms such as phase codes and Chirp increases the complexity of the receiver [42].

Multitone channel sounders have recently become practical with the advent of technology that enables complex waveform generation [43]. Channel sounders that use multitone waveforms have many advantages over other systems because of the spectral efficiency of the waveforms which reduce hardware complexity. Further advantages include the ability to operate without carrier acquisition and code/carrier recovery circuitry, which is necessary when a Chirp signal is used. However these systems require experience and expertise to construct and are often expensive to purchase making them unaffordable for most organisations.

There are a number of other channel sounders of differing architectures that are commercially available [43–46]. In general channel sounders are expensive, big and heavy with complex receiver architectures. There are other channel sounding techniques that are comparatively cheaper to implement [47, 48], although with limited channel resolution, sampling rate and sensitivity. These highlighted the need for the development of a simpler architecture that can be adapted for different studies [49].

In this paper, the development of an adaptable wideband channel sounder with signal bandwidths up to 200 MHz based on the transmission of a Pseudo Random Gaussian Noise (PRGN) waveform is presented. The objective of the development was to build a system which is compact and yet adaptable that addresses the problem of restricted mobility, speed, range restriction and cost inherent in many channel sounders. The sounder is designed to be configured to implement real-time processing of data that improves the Signal-to-Noise Ratio (SNR) by up to 30 dB in weak signal conditions. Channel sampling rates up to 5.4 kHz can be achieved. This paper also presents results of urban channel measurements designed to investigate spatial channel variation over short path distances and temporal variations

induced by automotive traffic. The processing approach used allows the detection of induced channel variation as vehicles pass in close proximity of the transmitter to receiver path, although they do not traverse the path. The study is of benefit to researchers, system designer and network providers who are working on the optimisation of data rates and provision of wideband services in urban environment. The papers is organised as follows; Section 2 describes the wideband channel sounder that has been developed. The design objectives, implementation and tests carried out to evaluate the performance of the sounder are provided. Spatial and temporal channel variation measurements are described in Section 3. This is followed by the results of signal variations, analysis and description of a picocell outdoor urban channel model in Section 4.

2. SYSTEM DESCRIPTION

The objective of the new sounder design was to overcome the limitations of channel sounders in use, in general. Thus the design objective was: *"to developed a very compact, low cost and adaptable sounder to measure the channel transfer function of a channel, over the widest possible bandwidth in the shortest possible time and as often as possible with the ability to improve the channel signal-to-noise ratio"*. This rendered most of the channel sounding implementation techniques unsuitable.

The approach adopted in the development of the channel sounder uses a synthesized multitone waveform called PRGN [50]. Field Programmable Gate Array (FPGA) technology has been used, in preference to Digital Signal Processors, to minimise the number of discrete components in the system, enable adaptability and provide real-time data processing capability [51–53]. The PRGN characteristics include a rectangular spectrum which allows sampling to be carried out at exactly the Nyquist frequency thereby minimising the complexity of the receiver system.

2.1. Transmitter

The transmitter is made up of an Arbitrary Waveform Synthesizer (AWS) and a Radio Frequency (RF) unit. The dual channel AWS generates a PRGN signal with an optimised crest factor which has a flat amplitude spectrum and low sidelobes outside the desired bandwidth. The AWS can generate two independent simultaneous waveforms with bandwidths of up to 150 MHz from channel A and 200 MHz from channel B, a capability that is important for co-located

channel investigation. However for the study reported in this paper only channel B was used. A simplified block diagram and the image of the AWS that has been developed are shown in Figure 1. The PRGN waveform used consists of 1024 spectral lines with 195.313 kHz frequency resolution over a bandwidth of 200 MHz [50]. The DAC is driven by a 400 MHz clock generated using FPGA from a 10 MHz input reference clock. The 200 MHz PRGN time and frequency domain signal that is generated by the AWS is shown in Figure 2. The transmitter unit has been built to transmit at a carrier frequency of 2 GHz. The use of a phase-locked 10 MHz reference signal that can be locked to a GPS receiver eliminates the transmitter and receiver synchronisation problem inherent in most channel sounding techniques. A simplified block diagram of the transmitter and an image of the built system are shown in Figure 3.

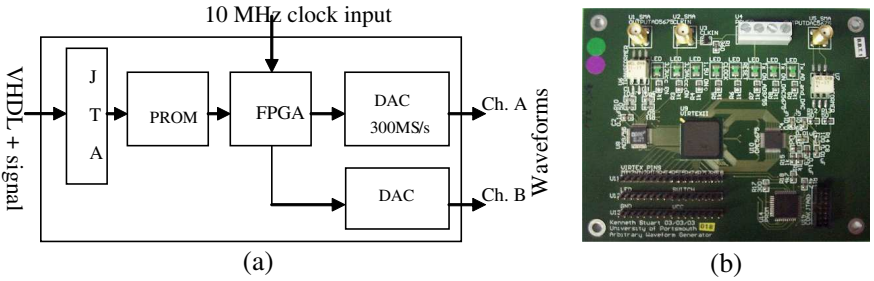

Figure 1. (a) Simplified block diagram and (b) image of the arbitrary waveform synthesizer card (10×12 cm).

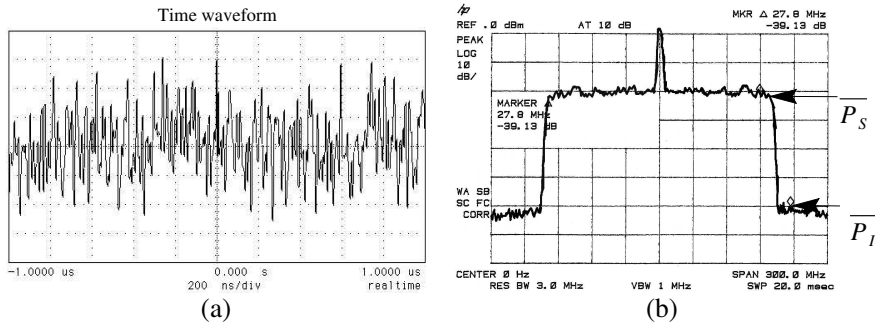

Figure 2. (a) PRGN time domain signal and (b) frequency magnitude spectrum generated by the AWS.

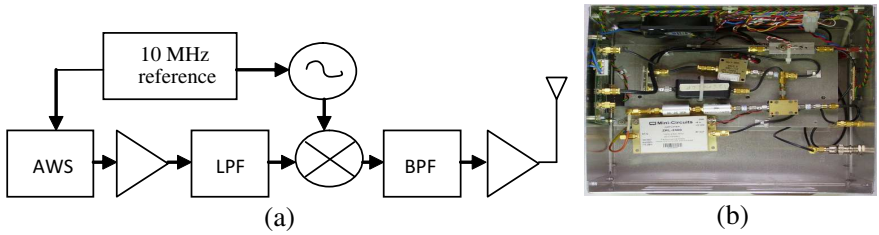

Figure 3. (a) Simplified block diagram and (b) the realised transmitter unit.

2.2. Receiver

The receiver system is comprised of a RF unit, a 12-bit resolution Analog-to-Digital Converter (ADC) [54], ADC carrier card, PCI Mezzanine Card (PMC) [55, 56] and a computer. A simplified block diagram of the receiver unit, ADC carrier card and built receiver unit is shown in Figure 4. The ADC has sampling rates up to 400 MS/s and is used to sample the signal at an Intermediary Frequency (IF). The sampled data is output through two channels thereby halving the frequency. The PMC card is used to implement real-time averaging of the sampled data using FPGA. The data is transferred to the computer

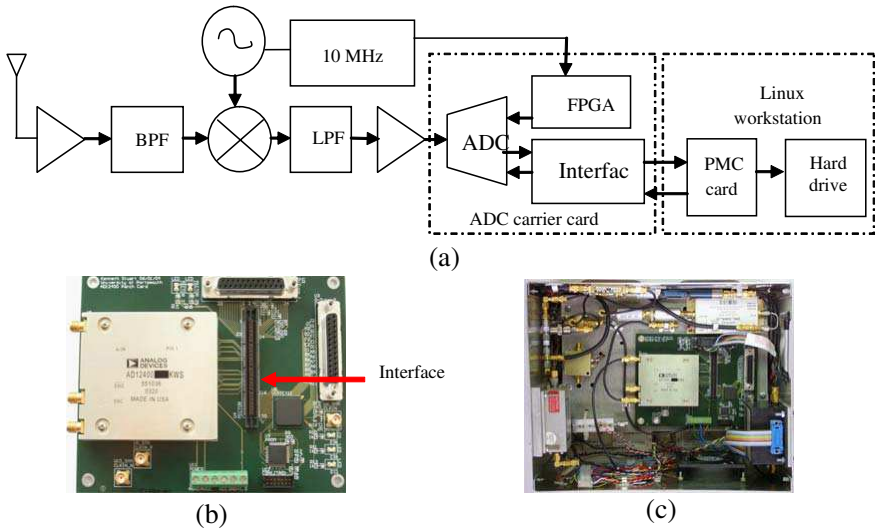

Figure 4. (a) Simplified block diagram of the receiver unit, (b) ADC carrier card and, (c) receiver unit.

across the PCI data bus for storage using demand-mode direct memory access. The acquisition time for each channel measurement (without averaging) is 10.24 µs. The user can select the number of real-time averages to be preformed up to 1024. This gives a theoretical improvement in SNR of between 3 dB and 30 dB. A block diagram of the averaging process and the PMC is shown in Figure 5 and illustrates how First-In-First-Out (FIFO) memory blocks are used in the averaging process.

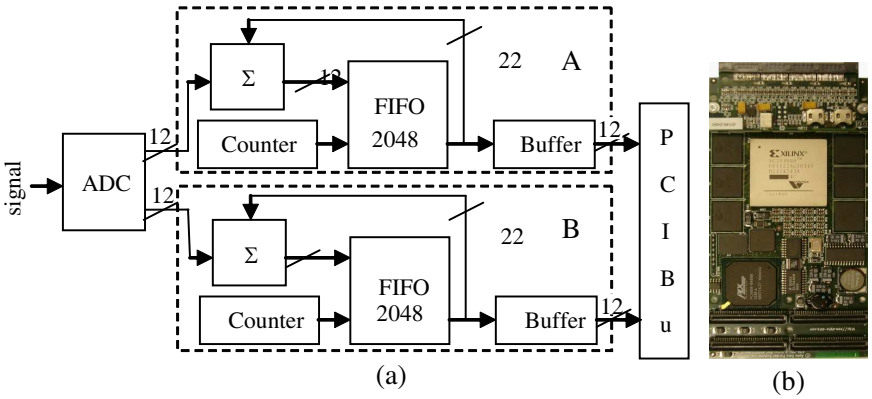

Figure 5. (a) Simplified block diagram of averaging unit and, (b) PCI Mezzanine Card.

2.3. Data Acquisition and Real-time Averaging

The developed software allows the user to implement a data acquisition strategy that optimises the speed of channel measurements, the amount of captured data and signal-to-noise ratio for the channel under investigation. It provides the flexibility for the user to control the data acquisition strategy by changing:

- the number of real-time averages to be carried out;
- time gap between successive channel transfer function measurements;
- time gap between a continual block of successive measurements;
- the number of data files to be captured and hence, the duration of the measurements; and
- when configured in conjunction with the transmitter, the bandwidth and sequence length of the waveform.

Periodic averaging is performed in real-time on the PMC card. This helps to reduce the amount of data that needs to be transferred across the PCI bus.

Tests were carried out to determine the sustainable data rates from the ADC to the computer hard drive. They revealed that the average PCI bus data rate was 55.7 MB/s and the average hard disk write speed was 40 MB/s. When sampling at 400 MS/s, the ADC generates 600 MB of data per second. With a hard disk write speed of 40 MB/s, 15 times reduction in data rate is required from the ADC to the computer hard disk. This can be achieved as a consequence of performing real-time averaging. The time taken to capture one averaged snapshot, T_{as}, is given by Equation (1).

$$T_{as} = \frac{N_s N_a}{2 f_c} + T_{sg} \tag{1}$$

where N_s is the sequence length, N_a is the number of averages, T_{sg} is the time required to reset the counters and FIFO, and f_c is the sampling frequency in Hz. Due to timing constraints when using clock frequencies greater than 390 MHz, T_{sg} has been set to a minimum value of 20.48 µs. The quantity of data generated for each value of N_a is shown in Table 1. It shows that data can be captured continually for number of averages greater than 16. For number of averages less than 32, the quantity of data per second must be limited to 40 MB. This can be achieved by increasing the time gap (T_{sg}) between each snapshot or continual measurements such that the number of channel responses captured per second is less than 4882.

With a 200 MHz bandwidth, the FPGA device speed grade used on the PMC card is operating at a frequency that is close to its limit. Thus, for different numbers of averages, the design had to be individually optimised. This could be alleviated by using a faster FPGA device. Fully adaptable data acquisition software has therefore been developed for all number of averages, up to 1024, at bandwidths up to 180 MHz. For 200 MHz bandwidth, the sounder has been designed to be adaptable for 1, 16 and 1024 averages. Table 2 provides details of the timing parameters for each number of averages (N_a) for 200 MHz signal bandwidth transmission.

The following terms are used to describe the data:

- snapshot: — a complete sequence (4096 sample long) of the PRGN waveform;
- averaged snapshot: — a complete sequence (4096 sample long) produced from the averaging process;
- data block: — 240 snapshots (averaged or not);
- data file: — 4 data block.

Table 1. Number of averages, time to capture one channel response and volume of data generated per second.

N_a	T_{as} ms	No. of snapshot per second	Data generated per second (MB)
1	0.03072	97656	266.666
2	0.04096	48828	200.000
4	0.06144	24414	133.333
8	0.10240	12207	80.0000
16	0.18432	6103	44.4444
32	0.34816	3051	23.5294
64	0.67584	1525	12.1212
128	1.33120	762	6.15385
256	2.64192	381	3.10076
512	5.26336	190	1.55642
1024	10.5062	95	0.77972

Table 2. 200 MHz bandwidth data acquisition; number of averages, theoretical improvement in SNR and timing.

N_a number of averages	Theoretical ΔSNR dB	T_{as} (ms)	Channel sampling rate (Hz)
1	0	0.18432	5425
16	12	0.18432	5425
1024	30	10.5062	95

The user can increase the number of averages (N_a), the time between snapshots (T_{sg}), and the time between data block (T_{dbg}) to suit the environment under investigation. The resulting time to capture one averaged snapshot (T_{as}), one data block (T_{db}) and one data file (T_{df}) can be calculated using Equations (1), (2) and (3), respectively.

$$T_{db} = 240T_{as} + 239T_{sg} \tag{2}$$

$$T_{df} = 4T_{db} + 3T_{dbg} \tag{3}$$

where,

$$T_{sg} = T_{dbg} = N_g \left(\frac{2N_s}{f_c} \right) \tag{4}$$

and N_g is the number of multiples of the time taken to reset all counters and FIFOs used in the averaging process. T_{sg} and T_{dbg} are independent of each other.

For a 200 MHz bandwidth signal the values of T_{sg} and T_{dbg} are given by Equations (5) and (6).

$$T_{sg} = 2T_s \tag{5}$$

$$T_{dbg} = 0.2517 - T_{db} \tag{6}$$

2.3.1. Data Processing and Calibration

Before the channel parameters can be estimated, each transfer function is first down converted to baseband and calibrated to remove the system response (magnitude and phase). These operations are done in software. The down-conversion of the signal from IF to baseband is realised by multiplying each sample of the measured sequence by conceptual orthogonal phased oscillators for in-phase (7) and quadrature-phase (8).

$$f_{loI} = \sin\left(\frac{2\pi f_c}{4}\right) \tag{7}$$

$$f_{loQ} = \cos\left(\frac{2\pi f_c}{4}\right) \tag{8}$$

The local oscillators (f_{loI} and f_{loQ}) are required to be one quarter of f_c, for down-conversion of the in-phase and quadrature-phase channels.

Each transfer function is then calibrated using a reference transfer function measured with the channel sounder in an anechoic chamber. The configuration of the measurement set-up used is shown in Figure 6.

From Figure 6, the relationship between the input PRGN waveform, S_{PRGN}, and the calibrated output, G_{mea}, is given by,

$$G_{mea} = S_{PRGN}\left(H_{Tx}H_{ant}H_{channel}H_{ant}H_{Rx}H_{spu}H_{cal}\right) \tag{9}$$

If a reference transfer function measured from the channel is G'_{ref}, and the corresponding ideal calibrated channel transfer function is H'_{ref}, then,

$$G'_{ref} = S_{PRGN}\left(H_{Tx}H_{ant}H'_{ref}H_{ant}H_{Rx}H_{spu}H_{cal}\right) \tag{10}$$

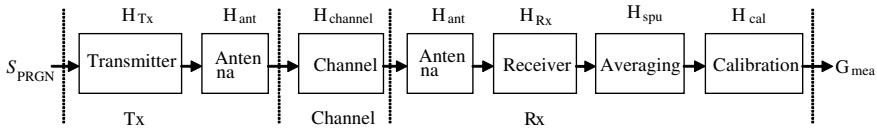

Figure 6. Configuration for calibration measurements.

Dividing (9) by (10) gives,

$$\frac{G_{mea}}{G'_{ref}} = \frac{H_{channel}}{H'_{ref}} \tag{11}$$

Since, H'_{ref} represents an ideal channel response measured under high SNR condition and exhibits a flat spectrum, therefore,

$$\frac{H_{channel}}{H'_{ref}} \approx H_{channel} \tag{12}$$

All system responses (magnitudes and phases) are eliminated and the transfer function, $H_{channel}$, represents only the response associated with the measured channel.

2.4. System Tests and Evaluation

Exhaustive tests were carried out to assess the functions and capability of the sounder. The transmitter and receiver RF units were designed to optimise the power sensitivity of the receiver and minimise intermodulation products. In order to achieve this, measurement of input and output power, and signal to intermodulation product ratios were evaluated at every stage in the RF chain.

An example of the 200 MHz PRGN spectrum at the output of the AWS is shown in Figure 2(b). The arbitrary waveform contains 1024 discrete spectral lines in the range ±100 MHz with a frequency resolution of 195.313 kHz. The noise power associated with the waveform is defined by the Signal-to-Intermodulation Ratio (SIR) or the SNR. The total signal power (P_s) of the waveform is given by,

$$P_S = \sum_{i=1}^{1024} \overline{P_S} = 1024\overline{P_S} \tag{13}$$

where $\overline{P_S}$ is the mean level of the wideband signal components.

Intermodulation products are coherent and hence cannot be minimised by periodic averaging of the signal. The total power of the intermodulation products and noise is given by,

$$P_I = \int_0^{B_w} \overline{P_I(f)} df \tag{14}$$

where $\overline{P_I(f)}$ is the mean level of any intermodulation components and/or noise at all frequencies within the bandwidth. Since it is not possible to separate intermodulation products from noise, the estimated mean level of the components represents an equivalent

Signal-to-Intermodulation and Noise Ratio (SINR). Thus, the SINR can be expressed as,

$$SINR = 10 \log \left(\frac{P_S}{P_I} \right) \tag{15}$$

If the value shown in Figure 2(b) is assumed to be the mean level of the intermodulation components plus noise, the estimated SINR is 39 dB. The transmitted power is 21 dBm. Figure 7 shows the PRGN spectrum at the input of the ADC. The SINR is 28 dB. Without averaging, the sensitivity of the receiver is −81 dBm.

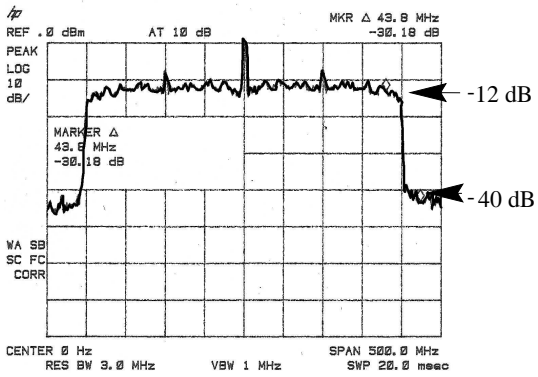

Figure 7. PRGN at the input to the ADC in the receiver.

2.4.1. Simulation of Channel Fading

Back-to-back tests were conducted to assess the performance of the system under simulated flat fading and frequency selective fading conditions using the set-ups shown in Figure 8. The delays and magnitudes of the signals in the primary and secondary paths were controlled using attenuators and different lengths of semi-rigid cables. Figure 9 shows a photo of the laboratory set-up. Comparisons were made between the measured improved SNR and the theoretical values.

Figures 10 and 11 show the measured transfer functions with 1 (no averaging) and 16 averages for flat fading and frequency selective fading channels, respectively. The magnitude response of the system was not calibrated out and can be seen in the spectrum. For frequency selective fading, a 2-ray model was simulated.

The magnitudes of the components between the spectral lines in the transfer function represent the level of noise plus any intermodulation products. The estimated SINR is 23.4 dB, Figure 10.

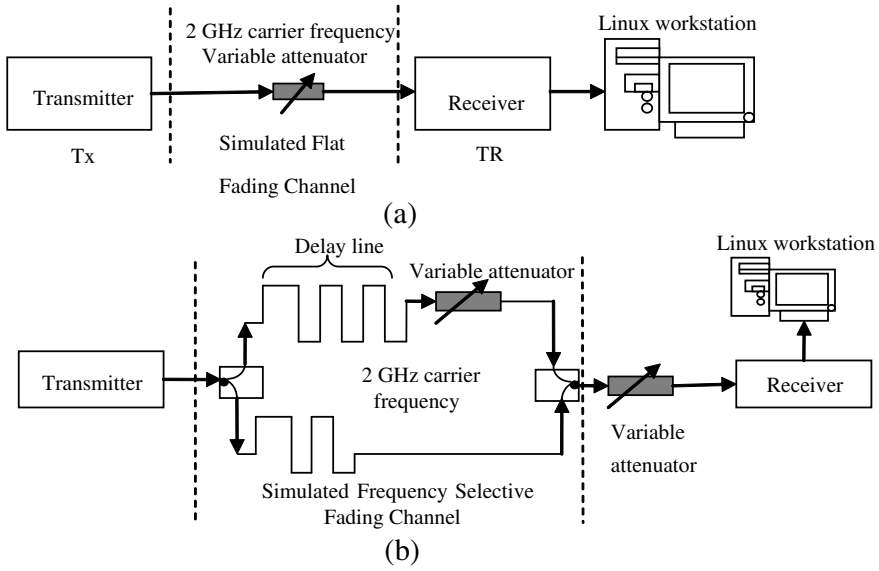

Figure 8. Set-up for (a) flat fading and, (b) frequency selective fading channel simulation.

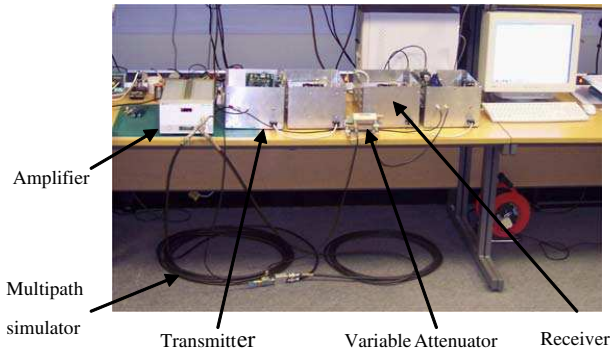

Figure 9. Configuration of hardware for multipath simulation.

An improvement in SNR of 11.2 dB is achieved with 16 averages which is 0.8 dB below the theoretical value of 12 dB. Figure 11(b) shows that the processing gain enables the depth of the fade nulls within the bandwidth to be determined.

Figure 12 shows the improvement in SNR for averages up to 1024 compared to the theoretical values. An improvement of 12.2 dB was achieved with 32 averages, which is 2.8 dB below the theoretical value.

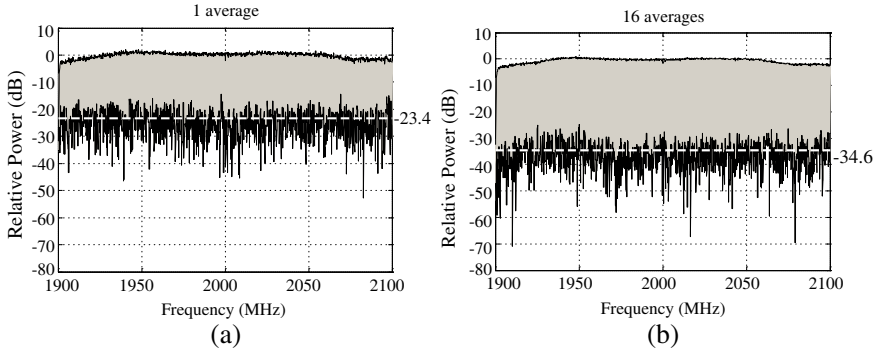

Figure 10. Transfer function of simulated flat fading channel with; (a) 1 averages and, (b) 16 averages.

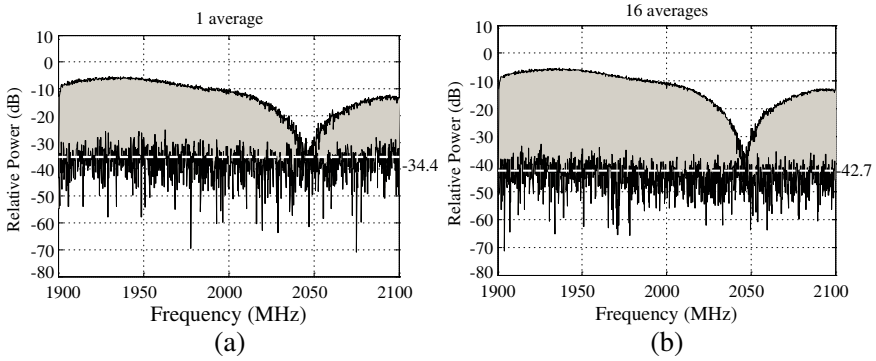

Figure 11. Transfer function of simulated 2-ray multipath channel with: (a) 1 averages and, (b) 16 averages.

For higher number of averages, the measured SINR improvement flattened out at approximately 18.6 dB for $N_a = 1024$. Since any intermodulation components present are coherent, signal averaging will only be effective in integrating out the noise. Therefore, the differences in levels between the SINRs for different number of averages represent the corresponding improvement in SNR. In addition, the theoretical improvement in SNR assumes that the noise is white Gaussian uncorrelated noise.

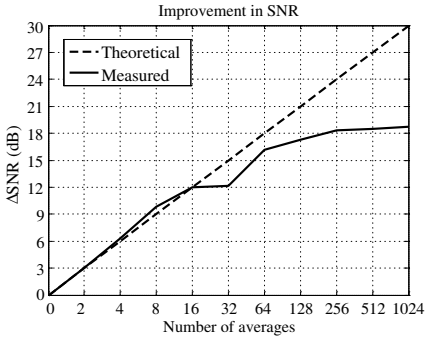

Figure 12. Comparison of theoretical and measured improvements in SNR for different number of averages.

3. CHANNEL MEASUREMENTS

In an outdoor wireless environment, the movement of people, objects and vehicles cannot always be controlled. The movement and, hence, position of the user and surrounding objects will vary and introduce both spatial and temporal variations. To study these changes, measurements were conducted in a position typical of an urban high data rate wireless access hotspot. For long range or wide area coverage transmissions, little or no attention is paid to short paths variations. However as cell sizes have reduced, the ability to accurately characterise path loss over specific short distances has become more important than general models over larger distances, particularly in high data rate wireless access environments.

Measurements were carried out in front of a building (Anglesea Building) which is adjacent to a dual carriage road in an urban area. The environment is typical of an urban area with relatively high number of mobile wireless communication users and hence, a most likely position for a high speed access hotspot. The area is also similar in size to a bar, cafe or shop front where WLAN access points are widely used. The speed at which the vehicles travel is typically between 20 and 45 km/h and the distance of the traffic from the transmitter to receiver path ranges from 3.5 m to 15.1 m. The number of vehicles travelling in both directions varied throughout the measurement period. Figure 13 provides an illustration of the routes and, the positions of the transmitter and receiver.

Video recordings synchonised with the channel measurements were made and used to corroborate the signal variations observed. The transmitter antenna height was 2.5 m and the receiver antenna height was 1.6 m. Omni-directional antennas were used.

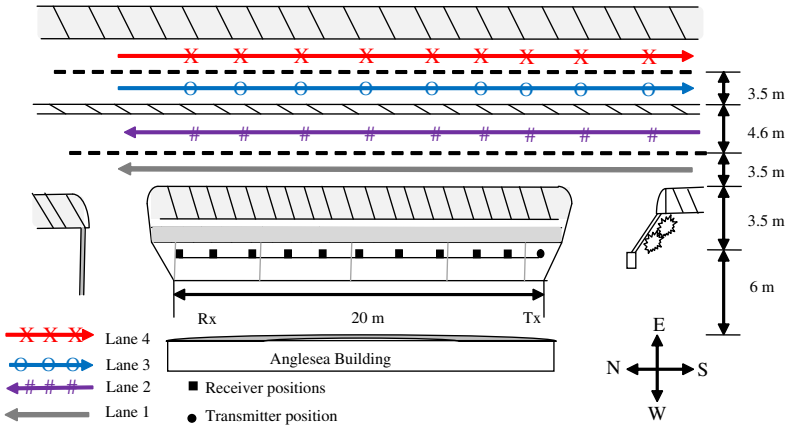

Figure 13. Measurement Set-up.

The distance between the transmitter and receiver was increased from 2 m to 20 m in steps of 0.3 m parallel to the direction of traffic. At each receiver position, the channel was sampled for approximately 20 s, that is 19200 channel response measurements. Figure 14 shows an example of the transmitter and receiver positions.

Figure 14. Transmitter and receiver position during measurement.

4. MEASUREMENT RESULTS

Observed temporal variations at each position were induced by moving objects, vehicles, and not due to the movement of the transmitter or receiver. In addition, no vehicles cross the transmitter to receiver path during the study.

Figure 15 shows an example of signal power variation with time and the impact of a vehicle on received signal. It shows that multipath

components introduce significant variations in the signal levels with deep fades. Figure 16 shows the channel transfer functions and corresponding impulse responses when no vehicle was passing (static

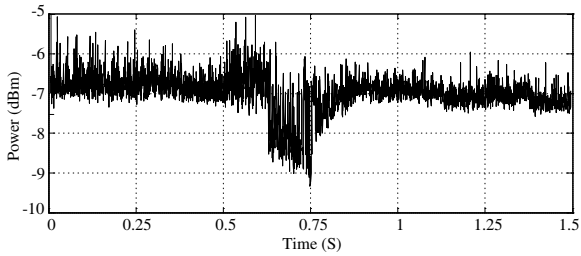

Figure 15. Averaged received power.

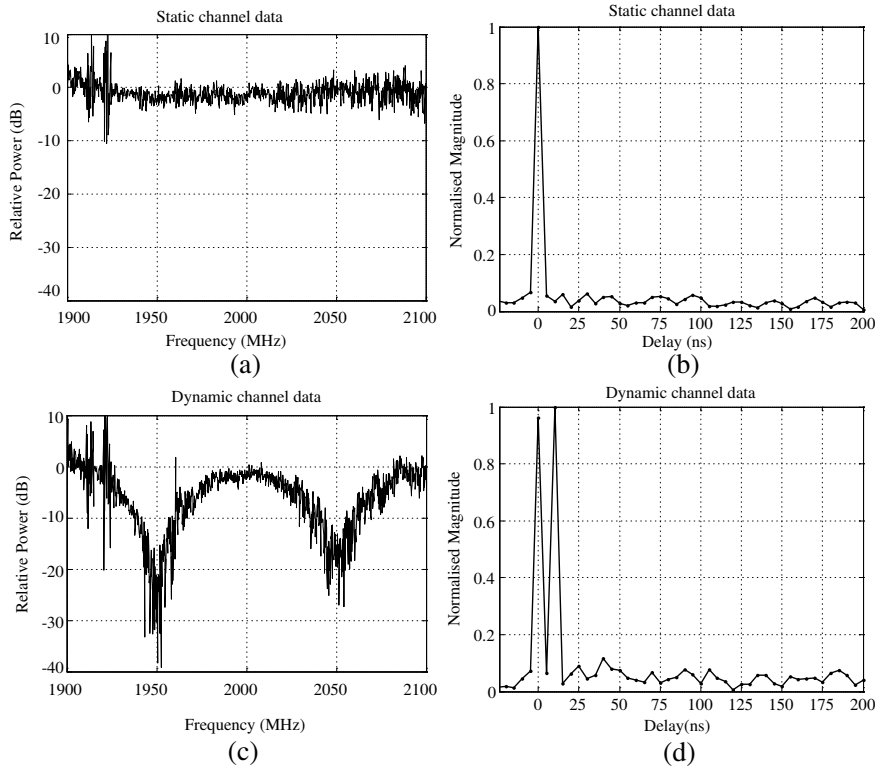

Figure 16. Field measurements (a) transfer function and, (b) impulse response with no vehicles, and (c) transfer function, and (d) impulse response with a vehicles passing.

channel) and when there was a vehicle travelling parallel to the transmitter to receiver path. The static channel transfer function (Figure 16(a)) exhibits small variations and very small fade depth. However, the dynamic channel response shows rapid fading with large fade depths due to multipath of up to 40 dB. The position of the nulls within the bandwidth changes with vehicle position and direction due to changes in the time delay of the multipath components. The impulse response from the static channel shows only one dominant path, Line-Of-Sight (LOS) path, as would be expected (Figure 16(b)). However, when a vehicle is passing, the multipath component is very strong (Figure 16(d)). Figure 15 shows smaller amplitude variations than fade depths observed within the bandwidth because it is the average signal power across the bandwidth which masks the severity of frequency selective fading within the channel. The measured fade depths are similar to results reported in [57].

A section of averaged received power is shown in Figure 17 and the vehicles that were captured on video passing through the measurement zone are indicated. The video recording showed that the speed of traffic was between 30 km/h and 45 km/h. As the first vehicle in Figure 17 (3 door estate) moved through, the results show that the fade duration was approximately 30 ms. Examination of the data file showed that the start of the event was not captured but data acquisition did continue until the vehicle had left the measurement zone. The last vehicle to pass was an estate car which was travelling in Lane 4 (Figure 13). Results show that longer vehicles have longer lasting effects on the received signal. An increase in the transmitter to receiver path length also increases the duration of the fading. When the path length was reduced to less than 6 m, the duration of the effects of vehicles on the channel was also reduced.

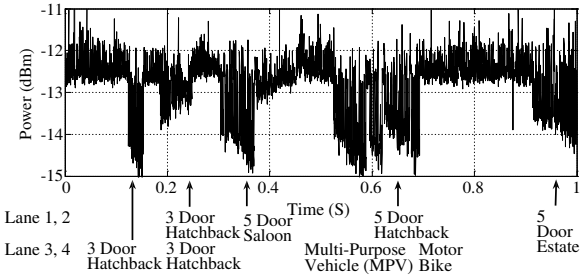

Figure 17. Averaged received power showing the impact of reflections from vehicles (Tx-Rx distance: 12 m).

Considering the average signal power across the bandwidth, the presence of a vehicle in the channel introduces fade depths of up to 4 dB. Because the vehicle is not traversing the transmitter to receiver path, the decrease in the signal power is due to multipath fading caused by scattered and reflected components. There is also an increase in the standard deviation of the averaged signal power in the presence of traffic. A further increase was observed as the number of vehicles increased.

4.1. Path Loss Model

Most of the models published in open literature for urban environments are either for path lengths greater than 1 km or assumptions have been made about the prevailing propagation mechanisms. Models based on prevailing propagation mechanisms cannot be directly applied to this study because they are based on work in which the transmitter heights were greater than 10 m or the systems used transmitted narrow band signals or very few measurements were taken at antenna separations less than 30 m.

The models published for short path lengths include the COST231-Walfisch-Ikegami and Wideband Microcell (WM) [58, 59]. They proposed a log-distance model. The COST231-Walfisch-Ikegami model uses free-space for distances less than 20 m and assumes transmitter antenna heights between 4 and 50 m. The model is described by (16). The WINNER project model for urban microcell is described by (17) [26].

$$PL_{COST231\_W} = 42.6 + 26\log_{10} d\,[\text{km}] + 20\log_{10} f_c\,[\text{MHz}] \quad (16)$$

$$PL_{WINNER} = A\log_{10} d\,[\text{m}] + C\log_{10}\left(\frac{f_c\,[\text{GHz}]}{5}\right) + B \quad (17)$$

where d is the distance between the antennas and f_c is the carrier frequency. For urban microcell environment (WINNER B1), the values of $A = 22.7$, $B = 41.0$ and $C = 20$ and, the transmitting antenna is assumed to be below surrounding buildings roof tops and in LOS. The model has been developed to be valid for antenna separations from 10 m. The values of $A = 13.9$, $B = 64.4$ and $C = 20$ have been proposed for indoor channel (WINNER B3)for base station antenna height of 6 m and mobile antenna height of 1.5 m for distances between 5 m and 100 m.

In this study, to evaluate the channel models, the data was separated into measurements in the presence of traffic (dynamic) and measurements when there was no vehicle passing (static). The results of signal variation with distance are presented in Figure 18. They show

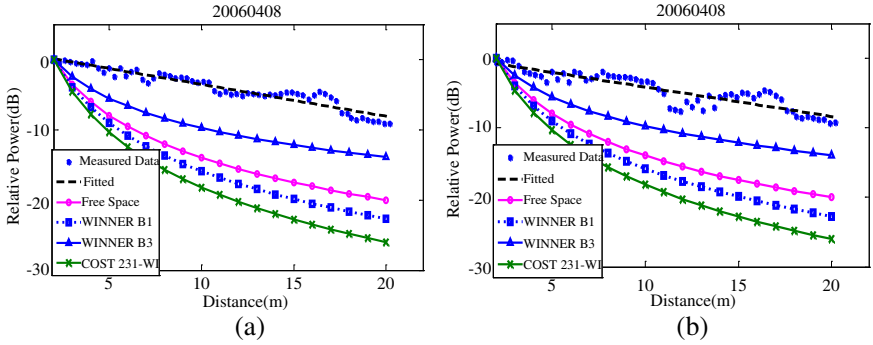

Figure 18. Signal variation with distance for (a) static and, (b) dynamic channels.

that at ranges up to 20 m none of the channel models closely represents the signal variation with distance. It was found that a linear model provides a best fit. The signal loss with increased distance did not decay logarithmically as predicted by the models.

Because of the short path length and absence of clutter, the received signal was dominated by the LOS path. In the absence of automotive traffic, multipath components were very weak. Linear path loss was also obtained during dynamic channel variation, as shown in Figure 18(b). However greater variations of signal power which depended on the size, number and direction of vehicles passing were observed. In general, the gradient of the path loss for each measurement scenario was less than the values predicted by free space path loss, WINNER and COST231-Walfisch-Ikegami models over short path lengths.

4.1.1. Small-scale Variations

Small-scale variations of the signal have been computed from measurement results. This has been used to calculate the signal power distribution about its mean, across the bandwidth, in a narrow band sense.

Results show that for dynamic channels, for path lengths up to 10 m, signal variation is best described by a Rician distribution. However in a static channel the signal variation is best described by a Normal distribution. Figure 19 shows results from measurements at an antenna separation of 8 m. At large antenna separations the small-scale variations of a dynamic channel have been found to be best described by a Nakagami distribution. Nakagami distribution

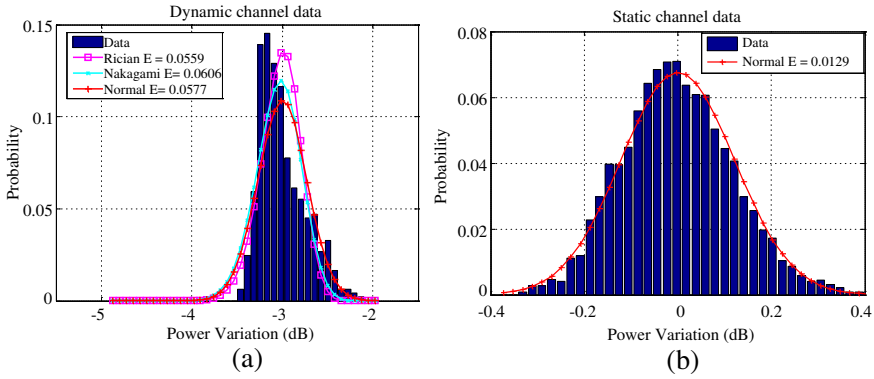

Figure 19. Small-scale variation: (a) dynamic channel, (b) static channel.

has Rice and Rayleigh distributions as extreme cases. The change in statistical distribution with path length in the presence of traffic can be attributed to an increase in multipath components due to reflection and scattering. However, for measurement conducted in static environment Normal distribution still gives the best results. Figure 20 shows typical results from measurements at 20 m.

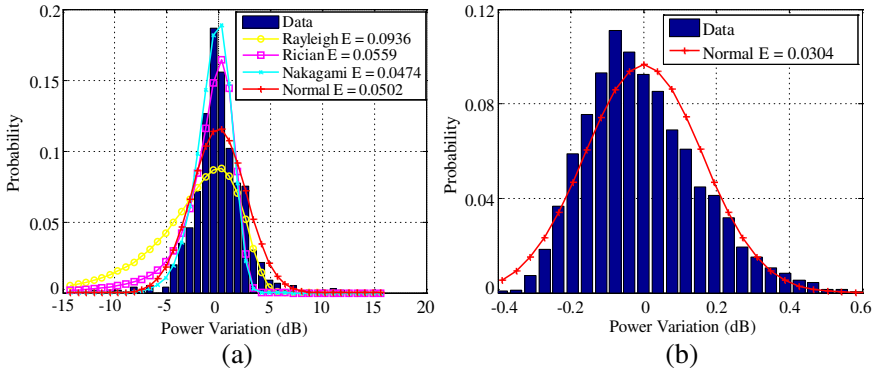

Figure 20. Small-scale variation: (a) dynamic channel, and (b) static channel.

The signal power variations at short path lengths up to 10 m showed that moderate variations about the mean in a static channel was generally within 2 dB. Overall an increase in signal variations with antenna separations was observed due to greater contributions from scattered components. This was more significant in dynamic channels where standard deviation of up to 12 dB were obtained.

The gradient of the average signal power is -0.45 for static channel and -0.42 for a dynamic channel. The smaller gradient of dynamic channel is due to average signal level enhancement by multipath components. The picocell signal decay models for dynamic and static channels are given by (18) and (19) respectively.

$$L_{apD}(d) = -0.42d + P_0 \tag{18}$$

$$L_{apS}(d) = -0.45d + P_0 \tag{19}$$

where d is the distance in meters and P_0 is the signal power in dBm at the reference distance d_0. Given that the signal variation about the mean at each measurement position can be described by a statistical distribution, picocell channel models can be developed for static and dynamic urban environments. The resulting static channel model can be described using Equation (20);

$$L_S\,(\text{dB}) = p_{no}(x|x_a) + L_{apS}(d) \quad 2 \le d \le 20 \tag{20}$$

and the urban dynamic channel model by Equation (21).

$$L_D\,(\text{dB}) = \begin{cases} p_{ri}(x|x_a) + L_{apD}(d) & 2 \le d \le 10 \\ p_{na}(x|x_a) + L_{apD}(d) & 10 < d \le 20 \end{cases} \tag{21}$$

where $p_{no}(x|x_a)$, $p_{ri}(x|x_a)$ and $p_{na}(x|x_a)$ are the distributions describing the variation in signal power about the average power x_a at each position. The signal power distributions are defined as follows,

$$p_{no}(x|x_a) = \frac{1}{\sigma\sqrt{2\pi}} e^{-\left[\frac{(x|x_a-\mu)^2}{2\sigma^2}\right]} \tag{22}$$

$$p_{ri}(x|x_a) = \frac{(x|x_a)}{\sigma^2} e^{-\left[\frac{(x|x_a)^2+A^2}{2\sigma^2}\right]} I_0\left(\frac{(x|x_a)A}{\sigma^2}\right) \tag{23}$$

$$p_{na}(x|x_a) = \frac{2m^m}{\Gamma(m)\Omega^m}(x|x_a)^{2m-1} e^{-\frac{m}{\Omega}(x|x_a)^2} \tag{24}$$

where μ and σ are the mean and standard deviation of $(x|x_a)$; A is the amplitude of the LOS component, I_0 is the modified Bessel function of the first kind and zero order, Ω is the scale parameter equal to the mean value of $(x|x_a)^2$ and m is the Nakagami parameter.

5. CONCLUSIONS

A wideband channel sounder capable of capturing the evolving response of a rapidly changing radio link has been described. It uses a Pseudo Random Gaussian Noise waveform that has a rectangular spectrum and negligible side-lobes. This allows the receiver to sample the waveform at exactly the Nyquist frequency providing

better sampling efficiency compared to other waveforms e.g., Chirp. Configurable technology (FPGA) has been used which enables the sounder to be adapted for measurements in different scenarios by changing the waveform, bandwidth, channel sampling rate and number of real-time averages. The use of FPGA improves the reliability of the sounder and allows for compact design and future upgrades without changing the architecture. The problem of transmitter and receiver synchronisation has been eliminate by using frequency references that can be obtained from GPS receivers or similar transmissions thereby eliminating link path length restriction inherent in wideband channel measurements. Back-to-back test results have shown that the improvement in signal-to-noise ratio achievable with up to 16 periodic averaging in the presence of random Gaussian noise can be represented by $10 \log_{10} N_a$, where N_a is the number of averages.

One of the main contributions of this paper is that the developed channel sounder architecture has allowed a more than 60% reduction in the size, weight and cost of the channel sounder systems whilst providing more flexibility in channel measurement. The architecture has been used to shift channel sounder system complexity from hardware to software. The application of programmable technology allows advantages to be taken of future faster devices in channel characterisation without changing the fundamental architecture of the sounder.

Measurements carried out in an urban environment has shown that automotive traffic, although not bisecting the transmitter-to-receiver path, can introduce frequency selective fading of up to 40 dB. Results show that the duration of the fade and depth depend on the size of the passing vehicle. Although the fade depths within the bandwidth are large, the averaged received power across the bandwidth exhibits relatively smaller variations. This shows that the impact of dynamic variations on wideband signals within picocell environment is dominated by the quality of the signal rather than signal strength. The temporal nature of the impact of dynamic variation will introduce error burst in digital receptions.

Channel models for urban microcell and picocell have largely assumed large antenna heights and long path lengths. For small distances less than 20 m, free space path loss is assumed. Results from the study reported in this paper show that for path length up to 20 m a linear path loss model with a gradient that is less than 1 dB/m can be used. The results also show that path loss is smaller than predicted by the WINNER model for indoor channels (B3). Overall, in static conditions, the small scale signal variation can be modeled using a Gaussian distribution about the mean. However

under dynamic conditions, signal variation is Rician distributed for antenna separations up to 10 m and Nakagami distributed for antenna separations beyond 10 m. This paper has produced useful results relevant to system planning and design for urban picocell high data rate transmissions. In particular, the results are relevant to high data rate ad-hoc network systems which use short range transmissions.

REFERENCES

1. Ndzi, D. L., N. Savage, and B. Gremont, "Spatial and temporal variation of wideband indoor channels," *International Journal of Antennas and Propagation*, Vol. 2010, Article ID 735434, 11, 2010.
2. Ndzi, D., J. Austin, and E. Vilar, "Hyper-resolution indoor channel impulse responses: Multipath components and k-factors," *Electronics Letters*, Vol. 35, No. 9, 698–699, April 1999.
3. Maciel, L. R., H. L. Bertoni, and H. H. Xia, "Unified approach to prediction of propagation over buildings for all ranges of base station antenna height," *IEEE Transactions on Vehicular Technology*, Vol. 42, No. 1, 41–45, January 1993.
4. Kurner, T., D. J. Cichon, and W. Wiesbeck, "Concepts and results for 3d digital terrain-based wave propagation models: An overview," *IEEE Journal on Selected Areas in Communications*, Vol. 11, 1002–1012, September 1993.
5. Hashemi, H., "The indoor radio propagation channel," *IEEE Proceedings*, Vol. 81, No. 7, 941–968, July 1993.
6. Cichon, D. J. and T. Kurner, "Propagation prediction models," *COST 231 Final Report*, Chapter 4, 134, 1999.
7. Goncalves, N. C. and L. M. Correia, "A propagation model for urban microcellular systems at the UHF band," *IEEE Transactions on Vehicular Technology*, Vol. 49, No. 4, 1294–1302, July 2000.
8. Juan-Llacer, L., L. Ramos, and N. Cardona, "Application of some theoretical models for coverage prediction in macrocell urban environments," *IEEE Transactions on Vehicular Technology*, Vol. 48, No. 5, 1463–1468, September 1999.
9. Berg, J., "A recursive method for street microcell path loss calculations," *IEEE International Symposium on Personal, Indoor and Mobile Radio Communications, PIMRC-95*, 140–143, Toronto, Canada, September 195.
10. Lee, W. C. Y. and D. J. Y. Lee, "Microcell prediction in dense urban area," *IEEE Transactions on Vehicular Technology*, Vol. 47, No. 1, 246–253, February 1998.

11. Okumura, Y., E. Ohmori, T. Kawano, and K. Fukuda, "Field strength and its variability in VHF and UHF land mobile radio services," *Review of the Electrical Communications Laboratory*, Vol. 16, 825–873, September–October 1968.
12. Hata, M., "Empirical formula for propagation loss in land mobile radio services," *IEEE Transactions on Vehicular Technology*, Vol. 29, No. 3, 317–325, September 1981.
13. COST Action 231, "Digital mobile radio towards future generation systems," *Final Report*, European Commission, No. 18957, 1999.
14. Electronic Communication Committee (ECC) within the European Conference of Postal and Telecommunications Administration (CEPT), "The analysis of the coexistence of FWA cells in the 3.4–3.8 GHz band," *ECC Report 33*, May 2003.
15. Rappaport, T. S., *Wireless Communications: Principles and Practice*, Prentice Hall, New Jersey, USA, 2002.
16. Wireless World Initiative New Radio (WINNER), 6th Framework Programme, Information Society Technologies, IST-2003-507591, Website: https://www.ist-winner.org/
17. The Working Group for WLAN Standards (IEEE 802.11), Website: http://www.ieee802.org/11/.
18. 3rd Generation Partnership Project, Website: http://www.3gpp.org/.
19. Papantoniou, S. J., "Modelling the mobile-radio channel," Ph.D. Thesis, No. 9120, ETH Zürich, 1990.
20. Fleury, B. and U. B. R. Heddergott, "Advanced radio channel model for magic WAND," ACTS Mobile Telecommunications Summit, 600–607, November 1996, Granada, Spain.
21. Nielsen, J. Ø., V. Afanassiev, and J. B. Andersen, "A dynamic model of the indoor channel," *Wireless Personal Communications*, Vol. 19, No. 2, 91–120, November 2001.
22. Chong, C. C., D. I. Laurenson, and S. McLaughlin, "The implementation and evaluation of a novel wideband dynamic directional indoor channel model based on a markov process," *14th IEEE Proceedings on Personal, Indoor and Mobile Radio Communications*, Vol. 1, 670–674, September 2003.
23. Wireless Local Area Network Hotspot Directory, W-Squared Inc., Website: http://www.wifi411.com/.
24. Calcev, G., D. Chizhik, B. Goransson, S. Howard, H. Huang, A. Kogiantis, A. F. Molisch, A. L. Moustakas, D. Reed, and X. Hao, "A wideband spatial channel model for system-

wide simulations," *IEEE Transactions on Vehicular Technology*, Vol. 56, No. 2, 389–403, March 2007.

25. 3GPP, "Spatial channel model for MIMO simulations," ftp://ftp.3gpp2.org/TSGC/Working/2001/TSG-C_0108/TSG-C-0801-Portland/WG5/.
26. WINNER II Channel Models, September 30, 2007, http://www.ist-winner.org/WINNER2-Deliverables/D1.1.2v1.1.pdf.
27. DeLange, O. E., "Propagation studies at microwave frequency by means of very short pulse," *Bell System Technical Journal*, Vol. 31, 91–103, January 1952.
28. Hewitt, A. and E. Vilar, "Sective fading on LOS microware links: Classical and spread_spectrum measurements techniques," *IEEE Trans. on Comms.*, Vol. 36, No. 7, 789–796, July 1988.
29. Crawford, A. B. and W. C. Jakes, "Selective fading of microwaves," *Bell System Technical Journal*, Vol. 31, 68–90, January 1952.
30. Bailey, R. J. and G. R. Summers, "Radio channel characterisation for the digital european cordless telecommunications system," *British Telecommunications Technology Journal*, Vol. 8, No. 1, 25–30, January 1990.
31. Turin, G. L., F. D. Clapp, T. L. Johnson, S. B. Fine, and D. Lavry, "A statistical model of urban multipath propagation," *IEEE Transactions on Vehicular Technology*, Vol. 21, No. 1, 1–9, February 1972.
32. Falconer, D. D. and S. Lek Ariyavisitakul, "Broadband wireless using singal carrier and frequency domain equalization," *5th International Symposium on Wireless Personal Multimedia Communications*, Vol. 1, 27–36, Honolulu, HI, USA, October 2002,.
33. Matic, D. M., H. Harada, and R. Prasad, "Indoor and outdoor frequency measurements for MM-waves in the range of 60 GHz," *48th IEEE Vehicular Technology Conference: Pathway to a Global Wireless Revolution*, Vol. 1, 567–571, Ottawa, Canada, May 1998.
34. Bajwa, A. S. and J. D. Parsons, "Small-area characterization of UHF urban and suburban mobile radio propagation," *IEE Proceedings*, Vol. 129, No. 2, 102–109, April 1982.
35. Godfrey, K., *Perturbation Signals for System Identification*, Prentice-Hall, London, UK, 1993.
36. Ditmar, W. P. A., M. Khoshlahjeh-Motamed, and R. R. Pettitt, "Design and Application of multi-frequency signals for power plant indentification," *IEE International Conference on Control'91*, Vol. 1, 665–670, Edinburgh, United Kingdom, March 25–28, 1991.

37. Nielson, D. L., "Microwave propagation measurements for mobile digital radio application," *IEEE Transactions on Vehicular Technology*, Vol. 27, No. 3, 117–131, August 1978.
38. Martin, G. T. and M. Faulkner, "Delay spread measurements at 1890 MHz in pedestrian areas of the central business district in the city of melbourne," *44th IEEE Vehicular Technology Conference*, Vol. 1, 145–149, Stockholm, Sweden, June 1994.
39. Cox, D. C., "Delay-doppler characteristics of multipath delay spread and average excess delay for 910 MHz urban mobile radio paths," *IEEE Transactions on Antennas and Propagation*, Vol. 20, No. 5, 625–635, September 1972.
40. Nche, C., A. M. D. Turkmani, and A. A. Arowojolu, "Channel sounder for PCN networks," *IEE Colloquium on High Bit Rate UHF/SHF Channel Sounders Technology and Measurements*, 5/1–6, Savoy Place, London, UK, December 1993.
41. Løvnes, G., S. E. Paulsen, and R. H. Rækken, "A millimeter wave channel sounder based on chirp/correlation technique," *IEE Colloquium on High Bit Rate UHF/SHF Channel Sounders Technology and Measurements*, 8/1–7, Savoy Place, London, UK, December 1993.
42. Salous, S. and V. Hinostroza, "Bi-dynamic indoor measurements with high resolution channel sounder," *5th International Symposium on Wireless Personal Multimedia Communications*, Vol. 1, 262–266, Honolulu, HI, USA, October 2002.
43. RUSK Channel Sounder Ordering Information, MEDAV GmbH, Website: http://www.channelsounder.de/.
44. Trulove, J., *Build Your Own Wireless LAN*, McGraw-Hill, New York, USA, 2002.
45. Duet Channel Sounder Technical Description, Berkeley Varitronics Systems, Inc., Website: http://www.bvsystems.com/Products/CDMA/Duet/duet.htm.
46. Elektrobit Propsound Channel Sounder Technical Description, Elektrobit Corporation, Website: http://www.elektrobit.com/index.php?209.
47. Van Rees, J., "Measurements of the wideband radio channel characteristics for rural, residental, and suburban areas," *IEEE Transactions on Vehicular Technology*, Vol. 36, No. 1, 2–6, February 1987.
48. Safer, H., G. L. Berger, and F. Seifert, "Propagation measurement-based probability of error predictions for the tactical VHF-range," *IEEE Military Communication Conference Proceed-*

ings, 331–335, November 1999.

49. Dinis, M. and J. Fernandes, "Provision of sufficient transmission capacity for broadband mobile multimedia: A step toward 4G," *IEEE Comm. Magazine*, Vol. 39, No. 8, 46–54, August 2001.
50. Austin, J., W. P. A. Ditmar, W. K. Lam, E. Vilar, and K. W. Wan, "A spread spectrum communication channel sounder," *IEEE Transactions on Communications*, Vol. 45, No. 7, 840–847, July 1997.
51. Hunt Engineering, "Choosing FPGA or DSP for your application," 2010, http://www.hunteng.co.uk/info/fpga-or-dsp.htm.
52. Parker, M., "FPGA versus DSP design reliability and maintenance," 2010, http://www.dsp-fpga.com/articles/id/?2207.
53. Bilsby, D. C. M., R. L. Walke, and R. W. M. Smith, "Comparison of a programmable DSP and a FPGA for real-time multiscale convolution," *IEE Colloquium on High Performance Architectures for Real-Time Image Processing*, No. 1998/197, 4/1–4/6, London, February 1998.
54. Analog Devices, "AD12401 data sheet," 2010, http://www.analog.com/en/analog-to-digital-converters/ad-converters/ad12401/products/product.html.
55. Technobox Inc., "64-bit PMC-to-PCI adapter card data sheet," 2010, Website: http://www.technobox.com/cat3673.pdf.
56. Alpha Data Ltd., "ADM-XRC-II xilinx virtex-II PMC data sheet," Alpha Data, 2010, Website: http://www.alpha-data.com/adm-xrc-ii.html.
57. Torres, R. P., B. Cobo, D. Mavares, F. Medina, S. Loredo, and M. Engels, "Measurement and statistical analysis of the temporal variations of a fixed wireless link at 3.5 GHz," *Wireless Personal Communications*, Vol. 37, Nos. 1–2, 41–59, April 2006.
58. Ikegami, F., S. Yoshida, T. Takeuchi, and M. Umehira, "Propagation factors controlling mean field strength on urban streets," *IEEE Transactions Antennas and Propagation*, Vol. 32, No. 8, 936–942, August 1984.
59. Feuerstein, M. J., K. L. Blackard, T. S. Rappaport, S. Y. Seidel, and H. H. Xia, "Path loss, delay spread, and outage models as functions of antenna height for microcellular system design," *IEEE Transactions on Vehicular Technology*, Vol. 43, No. 3, 487–498, August 1994.
60. Walfisch, J. and H. Bertoni, "A theoretical model of UHF propagation in urban environments," *IEEE Transactions Antennas and Propagation*, Vol. 36, No. 12, 1788–1796, December 1988.

Hindawi Publishing Corporation
International Journal of Reconfigurable Computing
Volume 2011, Article ID 894530, 14 pages
doi:10.1155/2011/894530

Research Article

An FPGA-Based Adaptable 200 MHz Bandwidth Channel Sounder for Wireless Communication Channel Characterisation

David L. Ndzi, Kenneth Stuart, Somboon Toautachone, Yanyan Yang, and Victor Dunn

Microwave Telecommunication Systems Research Group, Department of Electronic and Computer Engineering, University of Portsmouth, Anglesea Building, Anglesea Road, Portsmouth PO1 3DJ, UK

Correspondence should be addressed to David L. Ndzi, david.ndzi@port.ac.uk

Received 21 September 2010; Accepted 10 January 2011

Academic Editor: Fernando Pardo

This paper describes the development of a fast adaptable FPGA-based wideband channel sounder with signal bandwidths of up to 200 MHz and channel sampling rates up to 5.4 kHz. The application of FPGA allows the user to vary the number of real-time channel response averages, channel sampling interval, and duration of measurement. The waveform, bandwidth, and frequency resolution of the sounder can be adapted for any channel under investigation. The design approach and technology used has led to a reduction in size and weight by more than 60%. This makes the sounder ideal for mobile time-variant wireless communication channels studies. Averaging allows processing gains of up to 30 dB to be achieved for measurement in weak signal conditions. The technique applied also improves reliability, reduces power consumption, and has shifted sounder design complexity from hardware to software. Test results show that the sounder can detect very small-scale variations in channels.

1. Introduction

Channel sounders are used to study wideband signal transmission channels [1]. Although simple to design, in theory, they are complex to build and hence, expensive to purchase. Most channel sounders are developed using bespoke electronic systems. Although the use of wideband wireless communication systems is widespread and is expected to continue to grow, research into the channels that support these high data rate transmissions is limited, in most part, to simulations [2, 3]. Many wideband channel studies involve the use of general purpose instruments such as a vector network analyzer that can only be used for short-range investigations and are not suitable for fast channel sampling and mobile measurements [4, 5].

Compared to narrow band systems, channel sounders have to measure all frequencies within the bandwidth in a very short time during which the channel is assumed to be stationary [6]. For any given bandwidth, the Nyquist sampling criterion must be met. Channel probing signals that are widely used include Pseudorandom Binary Sequence (PRBS) and chirp [7]. Since the frequency spectra of these signals are not perfectly rectangular, the sampling frequency (f_s) must be more than twice the signal bandwidth (B_w). This generates large volumes of data in a short time and transferring this data from a sampling system for storage presents a unique challenge.

To facilitate further studies into the causes and impact of high-speed channel variations on wireless communication, an adaptive and fast channel sampling sounder was required. The objective was "*to developed a very compact, low cost and highly adaptable sounder to measure the transfer function of a channel, over the widest possible bandwidth in the shortest possible time and as often as possible with the ability to improve the channel signal-to-noise ratio*". To meet the compact and adaptable objectives, the design required the use of reconfigurable hardware. There are two main technologies that could have been used: Digital Signal Processors (DSP) and Field Programmable Gate Array (FPGA). DSP devices are specialised microprocessors that are typically programmed in C and are well suited to mathematically intensive tasks and offer robust software programmability [8]. However, DSP architecture capable of supporting high-speed accumulators are complex and limited compared to FPGA [9]. In contrast,

an FPGA device is programmed by connecting logic gates to form digital blocks such as multipliers, registers, and adders [10, 11]. FPGA devices support high clock frequencies and, both concurrent and parallel processes. Their capabilities are only limited by their logic capacities. There are also a wide range of FPGA devices available with high numbers of gates which offer more flexibility and quicker reconfiguration, both of which are essential for an adaptive system. Although FPGA and microprocessors are integrated on some devices such as MicroBlaze [12], FPGA was chosen for use in the implementation of the sounder. This marked a shift from hardware to software specification in channel sounder development. The use of FPGA also allows the system to be easily upgraded to keep pace with future communication system development needs. Most importantly, the use of FPGA devices enables a combination of many discrete components in the system on a single device. This contributes to a reduction in size, power consumption, hardware complexity, cost, and improvement in reliability of the system. Part of the design objective was to achieve an optimum performance at low cost with minimum hardware and software complexity using an architecture that can be ported to new devices to take advantage of the higher speeds and processing power that they may offer.

This paper is organised as follows: Section 2 gives an overview of the design objectives of the sounder and Section 3 describes the development of the transmitter and the receiver. Details of the software development and the data acquisition configurations that are available to the user are given. Section 4 describes the tests conducted to ascertain the performance of the sounder and the results obtained. These are followed by Section 5.

2. Sounder Specification and Design Objectives

A channel sounder is made up of the transmitter and the receiver as shown in Figure 1. The transmitter generates a waveform that is up-converted using appropriate Radio Frequency (RF) components to a suitable carrier frequency and transmitted. For this particular sounder, the waveform that is transmitted is a Pseudorandom Gaussian Noise (PRGN) [6]. PRGN has a noise-like characteristic in the time domain and a rectangular spectrum in the frequency domain. An example of a time domain and frequency spectrum of a PRGN signal is shown in Figure 2. The receiver down converts the received signal to a suitable intermediary frequency, where it is digitised, preprocessed (averaged), and stored.

2.1. Transmitter. The main requirement of the transmitter was to be reconfigurable to transmit signals with different bandwidths and spectral resolution (number of spectral lines within the bandwidth). To achieve this, a programmable Arbitrary Waveform Synthesizer (AWS) was required. Because of the noise-like characteristics of the PRGN waveform, a high resolution Digital-to-Analog Converter (DAC) was needed to maintain the accuracy of the signal. All frequencies used within the transmitter must be phase-locked to an external reference (10 MHz) to eliminate

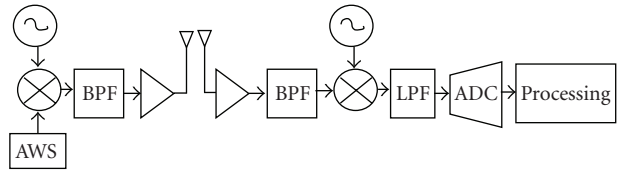

Figure 1: Simplified block diagram of the wideband channel sounder.

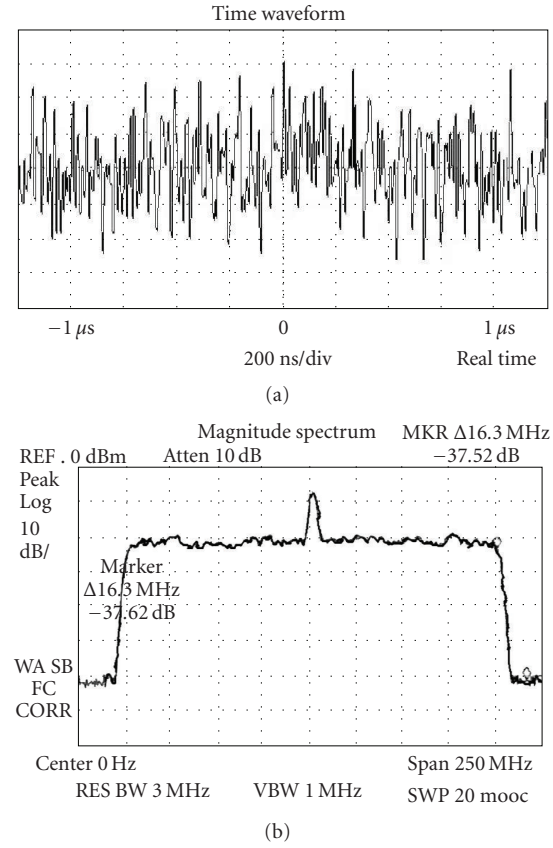

Figure 2: 200 MHz PRGN signal: (a) time domain signal and (b) magnitude spectrum.

transmitter to receiver range restriction. The generated waveform was to be up-converted to a carrier frequency of 2 GHz for transmission or as an Intermediary Frequency (IF) for further up-conversion.

2.2. Receiver. The design aims of the receiver are encompassed in the objectives of the system which require the receiver to be "*compact and highly adaptable to measure the transfer function of a channel, over the widest possible bandwidth in the shortest possible time and as often as possible with the ability to improve the channel signal-to-noise ratio*". To meet the compact objective, RF sampling was selected to minimise the number of components and reduce the complexity inherent in hardware in-phase and quadrature-phase demodulation [13]. The largest bandwidth was decided based upon the maximum clock frequency that a reasonably

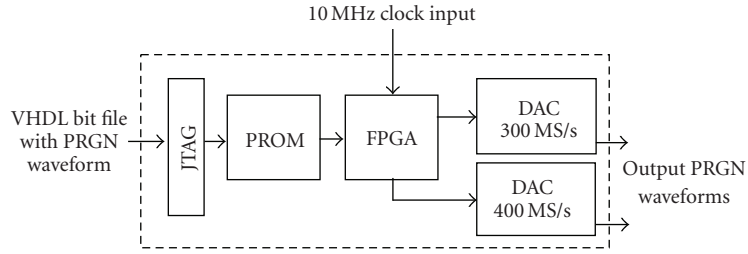

Figure 3: Simplified block diagram of the arbitrary waveform synthesizers.

priced FPGA device and a high-resolution Analog-to-Digital Converter (ADC) can support. Xilinx Virtex II FPGA devices were selected and they are specified to support clock frequencies up to 420 MHz. In order to meet the Nyquist sampling criterion, the design objective was geared to support a maximum bandwidth of 200 MHz to minimise uncertainties associated with operating close to the limits of devices.

The receiver must also be configurable to implement real-time averaging to improve the signal-to-noise ratio (SNR) in weak signal conditions. Other requirements include providing the ability for the user to adapt the receiver for different measurements by changing:

(i) the number of real-time averages to be carried out,

(ii) time gap between successive channel measurements,

(iii) time gap between a continual block of successive channel response measurements,

(iv) the duration of the measurement or the number of data files to capture,

(v) when configured in conjunction with the transmitter, the bandwidth and sequence length of the waveform.

3. Sounder Implementation

FPGA has been extensively used in the sounder to provide the flexibility required, minimize size, and improve reliability. Most importantly the developed architecture must be able to take advantage of current and future high-speed devices to increase the bandwidth, provide additional flexibility, and extend real-time processing capability of the system.

3.1. Transmitter. The main component in the transmitter is the arbitrary waveform generator. Although the RF unit is critical to the operation of the sounder, the main configuration that would be required is to change the carrier frequency. Therefore, more efforts were put into the design and construction of the AWS.

3.1.1. Arbitrary Waveform Synthesizer. The AWS was designed to be programmed through a Joint Test Action Group (JTAG) cable interface. A PROM is used to store the code that runs on the FPGA and the waveforms that are generated by the card. To ensure that the transmitter and receiver can be locked to one common frequency phase reference, a connection was provided for a 10 MHz input clock. The simplified block diagram of the implemented AWS card is shown in Figure 3.

A Xilinx Virtex II FPGA device was selected and used for its simplicity and low cost. Two 14-bit resolutions DACs with speeds of 400 MS/s and 300 MS/s were selected to provide flexibility and also allow robust testing to be carried out during development. The developed dual channel AWS can be used to generate two independent waveforms with bandwidths of up to 150 MHz and 200 MHz.

The operations of the AWS card and the functions of the VHDL software can be summarized as follows: at power up

(i) load the programme code and digital waveforms from the PROM into the FPGA;

(ii) check the status of the input 10 MHz clock;

(iii) if clock is available, generate the loaded waveform.

To generate the 150 MHz and 200 MHz bandwidth signals, 300 MHz and 400 MHz clocks are required. VHDL code was written to multiple the 10 MHz input reference to generate these high frequency clocks using the Digital Clock Management (DCM) modules. The FPGA device that has been used has 2 clock multiplier modules:

(i) low frequency module with output clock frequencies from 24 MHz to 240 MHz,

(ii) high frequency module with output clock frequencies from 24 MHz to 420 MHz.

The 300 and 400 MHz clocks could be generated using one low- and one high-frequency multiplier clock modules. However, for low-frequency module outputs of 130 MHz and above, the clock jitter is very high, more than 10% of the clock period. This is outside the jitter tolerance of the high-frequency module. Thus stable 75 MHz and 100 MHz clocks were first generated and two high frequency modules were then used to provide the final times 4 multiplication factor. Tests showed that changing the voltage reference of the FPGA device from 1.5 V to 1.65 V improved the stability of the generated clocks.

The width of the data bus of the DACs is 14 bits wide. Tests showed that clocking the data from a single register onto the data bus at 300 MHz and 400 MHz introduced high skew. This was overcome by using Double Data Registers (DDR). This enabled the clock frequency to be halved with data clocked from one register on the rising edge of the clock

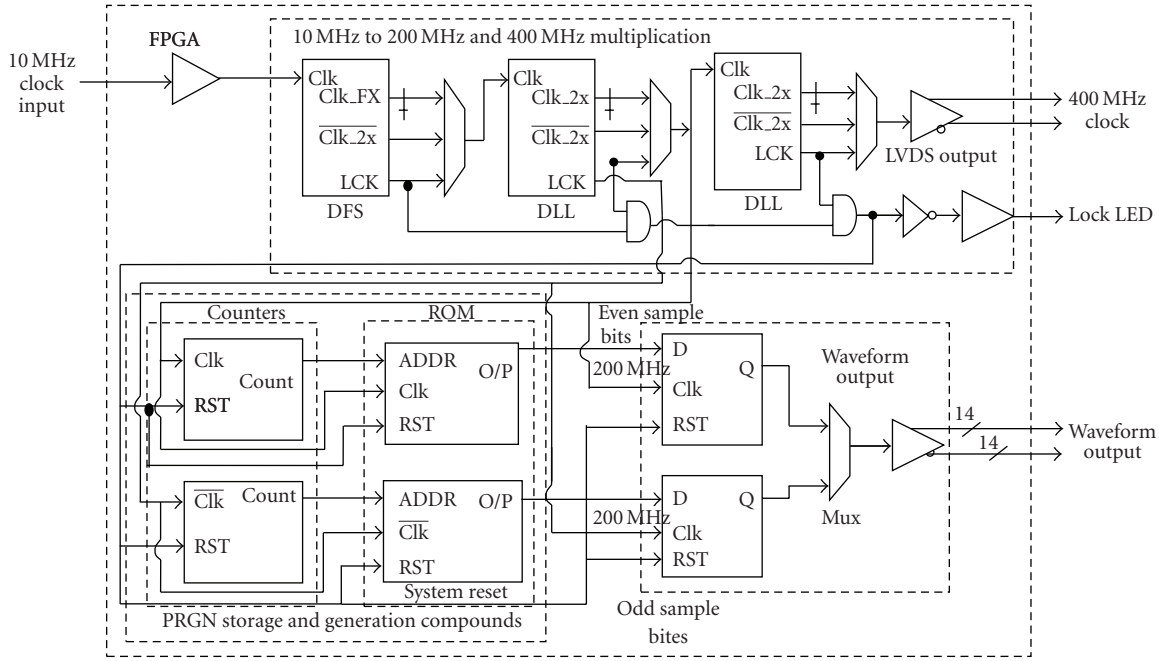

Figure 4: Block diagram of the 200 MHz bandwidth AWS VHDL design.

and from the second register on the falling edge, thus reducing jitter and data skew. The VHDL logic for the 200 MHz bandwidth signal generation is illustrated in Figure 4.

In the frequency domain, the PRGN waveform from the AWS has a "flat" amplitude spectrum. When clocked at 400 MHz, the waveform has a bandwidth of 200 MHz and has been designed to have 1024 discrete spectral lines in the range ±100 MHz, spaced by 195.313 kHz. Figure 2 shows the 200 MHz PRGN baseband time domain signal and the magnitude spectrum generated by the AWS, and Figure 5 is a photo of the built AWS card. The card has dimensions of 10 cm by 12 cm.

3.2. Receiver. The main goal of the receiver design was to develop a highly flexible data acquisition system that would enable the channel sounder to be adaptable for measurements in a wide range of scenarios. This required hardware that could be readily reconfigured. The receiver can be divided into; the RF unit, frequency reference unit, ADC, FPGA-based Peripheral Component interconnect Mezzanine Card (PMC) for real-time data processing, and a Linux workstation as shown in Figure 6.

3.2.1. RF Unit. The design philosophy of the receiver RF system was to optimise the sensitivity and adaptability of the receiver. Thus, a programmable digital attenuator was incorporated into the design for automatic gain control to maintain the signal within the linear range of the RF components and to protect the ADC from high input signals.

For a 200 MHz bandwidth signal transmission, the received signal is down converted to an IF of 100 MHz using a phase-locked oscillator. Frequency stability and phase synchronisation are achieved by using a stable 10 MHz reference phase-locked to the same source as the transmitter.

3.2.2. ADC and ADC Carrier Card. A 12-bit ADC with sampling speeds of up to 400 MS/s was selected to minimise quantization errors [14]. Due to the rectangular nature of the PRGN spectrum, the sampling frequency is set at exactly the Nyquist frequency. An ADC carrier card with an onboard FPGA device was designed to be used to generate the sampling clock required by the ADC [15]. The sampling clock is generated using the same technique developed for the AWS.

The carrier card was also designed to route control signals and data between the ADC and the PMC cards. In addition, the carrier card acts as an automatic gain controller. Figure 7 shows a simplified block diagram of the ADC carrier card.

3.2.3. PMC Card. To minimise cost, it was important to use standard computer components. To provide flexibility and ensure data integrity, an interface card was selected to be used between the ADC and the computer to process and buffer the captured data. To provide the data acquisition flexibility required, the interface card also had to

(i) have a data processing engine (DSP and/or FPGA),

(ii) have an external clock input to synchronise internal data processing and transfers with the rest of the system,

(iii) be programmable such that the data sequence, number of averages, and data transfer rates could be changed when required,

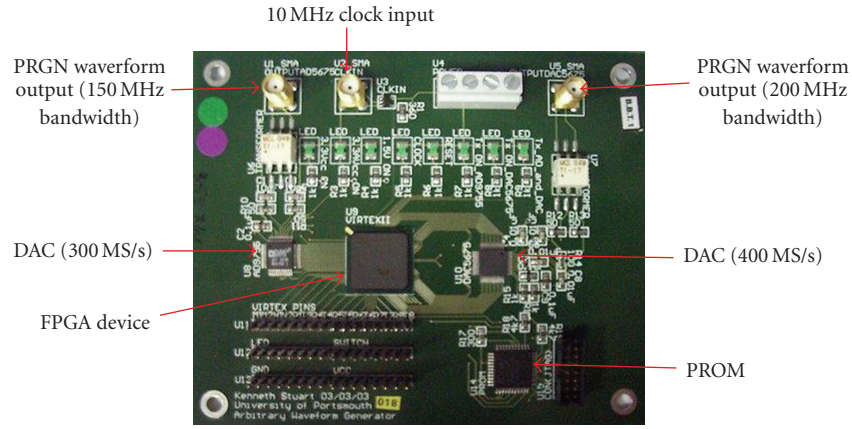

Figure 5: Photograph of the dual channel arbitrary waveform synthesizers.

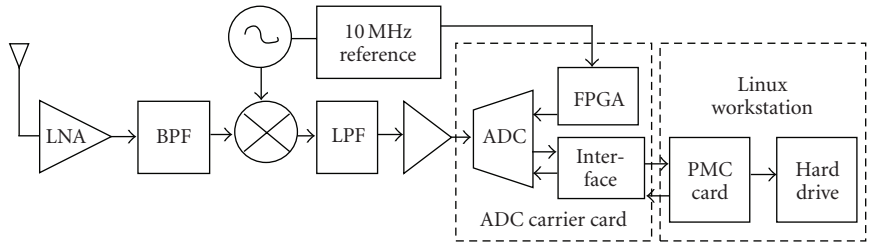

Figure 6: Simplified block diagram of the receiver system.

(iv) have a large memory to store a significant amount of data to provide fast channel sampling capability,

(v) support the computer data bus protocol.

After evaluating a number of programmable cards available on the market, the Alpha Data Ltd PMC-XRC card with an onboard FPGA device and memory banks was selected [16]. The PMC is mounted on a PMC-to-PCI bridged adapter card for connection to a computer motherboard [17].

3.2.4. Real-Time Averaging. One of the main design objectives was for the channel sounder to be effective in low SNR conditions. This could be achieved by performing periodic averaging of the received signal. Although averaging could be done offline, there was a need to reduce the quantity of data that has to be transferred and stored. With this in mind, processing of the data is done on the PMC card and has been implemented entirely in VHDL.

The ADC output has two channels which halve the speed of data output compared to the sampling rate. Therefore, the data averaging logic in the FPGA was doubled to process each channel as shown in Figure 8. The ADC produces Data Ready signals for each channel (DRA and DRB for channel A and B, resp.) that indicate when data samples are valid at the outputs. These are synchronised with the sampling clock and have frequencies that are half the ADC sampling frequency. These clocks are used to drive the data accumulator logic.

Table 1 shows the counter settings required for the different number of averages, the time it takes to capture one averaged snapshot (T_{as}), and the theoretical improvement in SNR (ΔSNR) [18]. The averaging counter values are calculated using (1), where N_s is the length of the sequence and N_a is the number of averages.

Table 1: Averaging counter value for possible number of averages, durations, and expected improvement in SNR.

N_a	Counter value (Hex)	T_{as} (ms)	Theoretical ΔSNR (dB)
0	FFF	0.01024	0
2	1FFF	0.02048	3
4	2FFF	0.04096	6
8	4FFF	0.08192	9
16	8FFF	0.16384	12
32	10FFF	0.32768	15
64	20FFF	0.65536	18
128	40FFF	1.31072	21
256	80FFF	2.62144	24
512	100FFF	5.24288	27
1024	200FFF	10.48576	30

$$\text{counter value} = \left(\frac{N_s N_a + 2N_s}{2}\right) - 1. \tag{1}$$

3.2.5. Data Transfer and Storage. The rate at which captured data can be transferred from the PMC to the host computer and written to the hard disk is key to the data acquisition strategy and, in particular, the channel sampling rate. If data

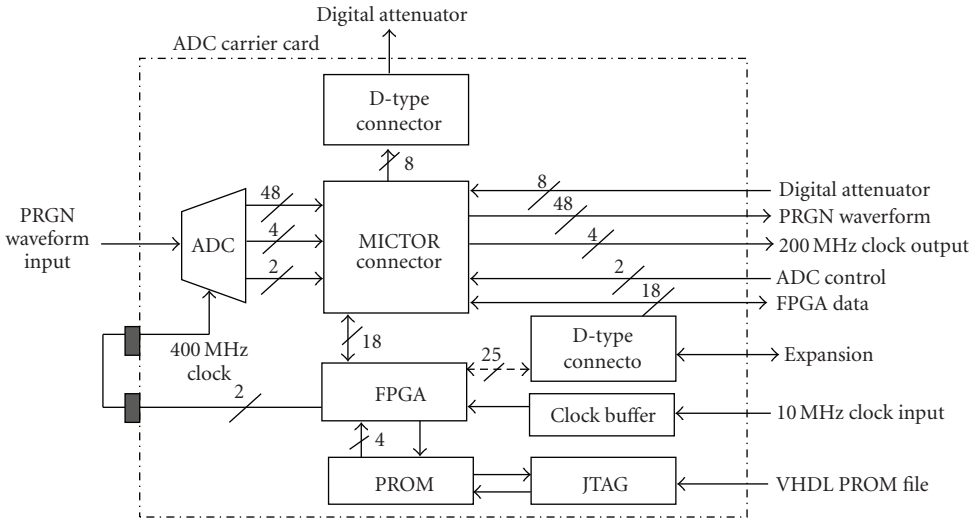

Figure 7: Simplified block diagram of the ADC carrier card.

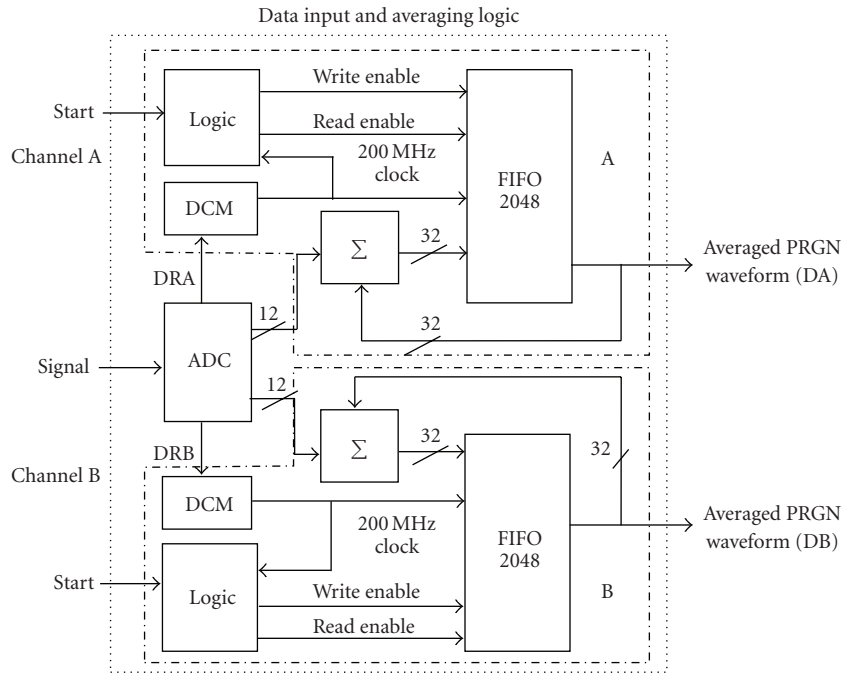

Figure 8: Block diagram of the averaging process.

is not read from the PMC card memory before the next set is captured, it will be overwritten. To prevent lost or corruption of data, two issues had to be resolved: the data transfer clock frequencies and the timing of when data should be transferred to the host computer.

The clock frequency options that are available when using a 32-bit PCI bus are 33.3 MHz and 66.6 MHz. The clocks used in the averaging process have a maximum frequency of 200 MHz. This means that, at least, three snapshots can be captured in the same time that one is transferred across the PCI bus. Furthermore, the two clock domains are separate and are not phase-locked. To overcome this asynchronous problem, First-In-First-Out (FIFO) buffers were used. The write clocks into the FIFOs are the DRA and DRB, and the read clock is the PCI bus clock. A block diagram of the data transfer logic is shown in Figure 9.

The read enable of the FIFOs is controlled by the value of the averaging counter such that on the last average, the data is transfered to the asynchronous FIFO. If the computer is the bus master, and the PMC card is the slave, the data contained in the asynchronous FIFOs will not be necessarily completely read before new data is available to be written to the FIFOs. This is because the computer uses a polled interrupt routine to service the PCI bus. Since it is critical

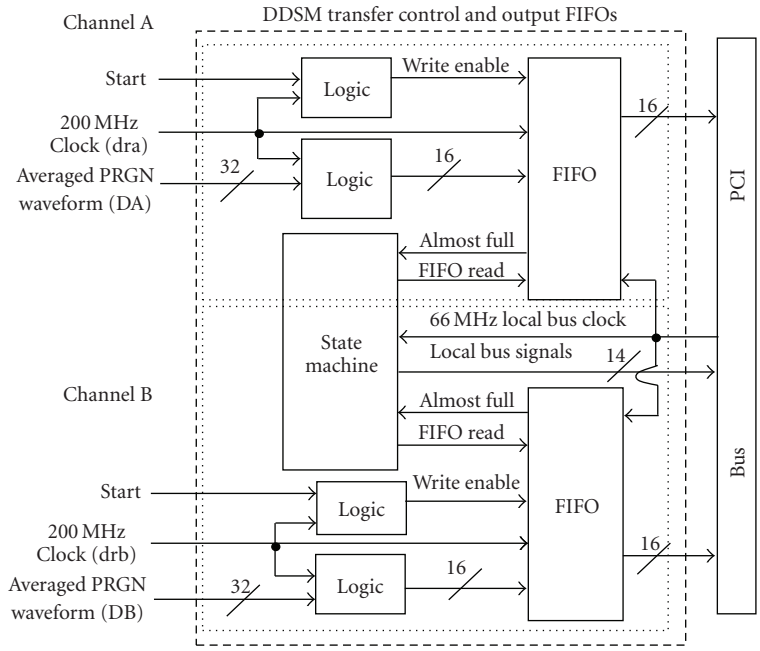

Figure 9: Block diagram of the output buffer VHDL.

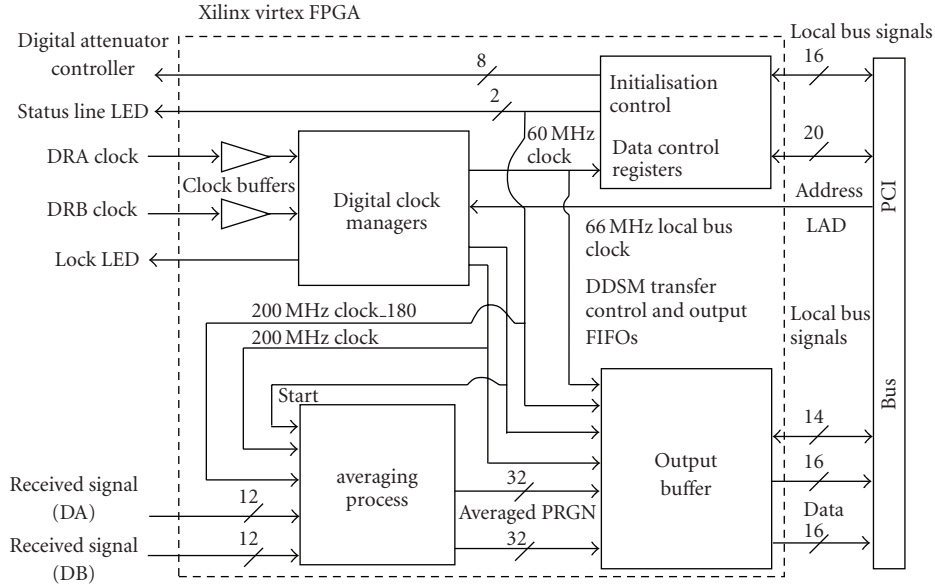

Figure 10: Block diagram of the PMC VHDL design.

that no sample is overwritten, the PMC card must be the PCI bus master. This was achieved by using Demand-mode Direct Memory Access (DDMA), where the PMC initializes a read transaction when one complete data sequence has been written to the asynchronous FIFOs. The computer then writes the data to disk and no samples are lost.

The data output of the ADC is 12-bit signed binary. To perform 1024 averages, a 22-bit adder is required. To complete the averaging process, the summed result must be divided by the number of averages. However, if this is performed in the FPGA, the averaged result will be truncated to a whole number. This is undesirable in low SNR conditions where an actual representation of the signal in comparison to the noise level is required [19]. Saving the data and carrying out floating point division in the computer provide the best solution. However, this would require 22 bits per sample to be transferred. Since the PCI bus used is 32 bits wide, only one sample would be transferred per clock period.

Since the ADC generates two samples per clock, the channel sampling rate would need to be halved for number of averages greater than 16. This was undesirable and hence the width of each sample was limited to 16 bits. For a number

of averages greater than 16, only the most significant 16 bits are transferred. Discarding some of the bits in this manner corresponds to predivision by a factor of 2^{nb}, where nb is the number of bits discarded. When 8 or less averages are performed, the number of data bits per sample is less than 16. Thus, to ensure data integrity the sign bit for each sample is duplicated to make the sample 16 bits wide.

Figure 10 shows a block diagram of the top level VHDL design for the PMC card illustrating how each part of the VHDL logic is linked together.

3.2.6. Data Acquisition. During measurements, a user must be able to implement a data acquisition strategy that is suitable for the channel under investigation. A combination of C and VHDL was used to implement the software. To achieve the design goals of the receiver as outline in Section 2.2, emphasis was placed upon transferring the measured data from the output of the ADC to the computer hard drive as fast as possible.

The PCI data bus rate and the hard drive read/write speed are the two most critical factors in the receiver. Tests were carried out to determine the sustainable data rate from the ADC to the hard drive. This was achieved by using a VHDL design that transfers data using DDMA from memory across the host machine's PCI bus. In addition, an operating system tool (hdparm) was used to test the read/write speed from/to the computer hard drive. The tests revealed that the average PCI bus data rate was 55.7 MB/s and that an average of 40 MB could be written to the hard disk per second. The data acquisition strategy was then designed around these results.

When sampling at 400 MS/s, the 12-bit ADC can generate over 600 MB of data per second. Since the hard disk writing speed is only 40 MB/s, a 15-time reduction in data rate was required. Due to the dual channel nature of the ADC, the first reduction in the data rate is achieved within the ADC from the interleaving configuration [14]. Further reduction could be achieved as a consequence of performing real-time averaging on the PMC card. The time taken to capture one averaged channel response (snapshot), T_{as}, is given by

$$T_{\text{as}} = \frac{N_s N_a}{2 f_c} + T_{\text{sg}}, \tag{2}$$

where N_s is the sequence length, N_a is the number of averages, T_{sg} is the time required to reset the counters and FIFO, and f_c is the input clock frequency in Hz. Due to timing constraints, T_{sg} was set to a minimum value of 20.48 ms. Considering a sequence length of 4096, each snapshot has a size of 8.192 kB. The quantity of data generated for each value of N_a is shown in Table 2. It can be seen that when the number of averages is set to 32 or greater, data can be captured continually. For number of averages less than 32, the quantity of data captured per second must be limited to 40 MB. This can be done by increasing the time gap (T_{sg}) between snapshots or block of continual channel response measurements such that the number of continual channel responses captured per second is less than 4882. During measurements, a trade-off must be made between the channel sampling rate and quantity of data to be captured.

Table 2: Time to capture one channel response, number of averages, and the volume of data generated per second.

N_a	T_{as} (ms)	No. of snapshot per second	Data generated per second (MB)
0	0.03072	97656	266.666
2	0.04096	48828	200.000
4	0.06144	24414	133.333
8	0.10240	12207	80.0000
16	0.18432	6103	44.4444
32	0.34816	3051	23.5294
64	0.67584	1525	12.1212
128	1.33120	762	6.15385
256	2.64192	381	3.10076
512	5.26336	190	1.55642
1024	10.5062	95	0.77972

Although the continual channel sampling rate is limited to 4.882 KHz, the user can achieve channel sampling rates up to 5.42 KHz for subsecond continual channel measurements. For a bandwidth of 100 MHz and 2048 long sequence, channel sampling rates up to 15 KHz are achievable. This provides the flexibility to investigate very high speed events.

Figure 11 illustrates the data acquisition strategy that has been developed. The following terms, defined in the diagram, are used to describe the data sets:

(i) snapshot: a complete sequence (4096 samples long) of the PRGN waveform,

(ii) averaged snapshot: a complete sequence (4096 samples long), produced by the averaging process,

(iii) data block: 240 snapshots,

(iv) data file: 4 data block.

The user can change the number of averages (N_a), the time between snapshots (T_{sg}), and the time between data block (T_{dbg}) to suit the type of channel under investigation. The resulting time to capture one averaged snapshot (T_{as}), one data block (T_{db}), and one data file (T_{df}) can be calculated using (2), (3), and (4) respectively.

$$T_{\text{db}} = 240 T_{\text{as}} + 239 T_{\text{sg}}, \tag{3}$$

$$T_{\text{df}} = 4 T_{\text{db}} + 3 T_{\text{dbg}}, \tag{4}$$

where

$$T_{\text{sg}},\ T_{\text{dbg}} = N_g \left(\frac{2 N_s}{f_c} \right), \tag{5}$$

and N_g is the number of multiples of the time taken to reset all counters and FIFOs used in the averaging process. T_{sg} and T_{dbg} are independent of each other. Table 3 provides the details of the timing parameters for each number of averages, N_a, and the possible channel sampling rates for 180 MHz bandwidth signal transmission.

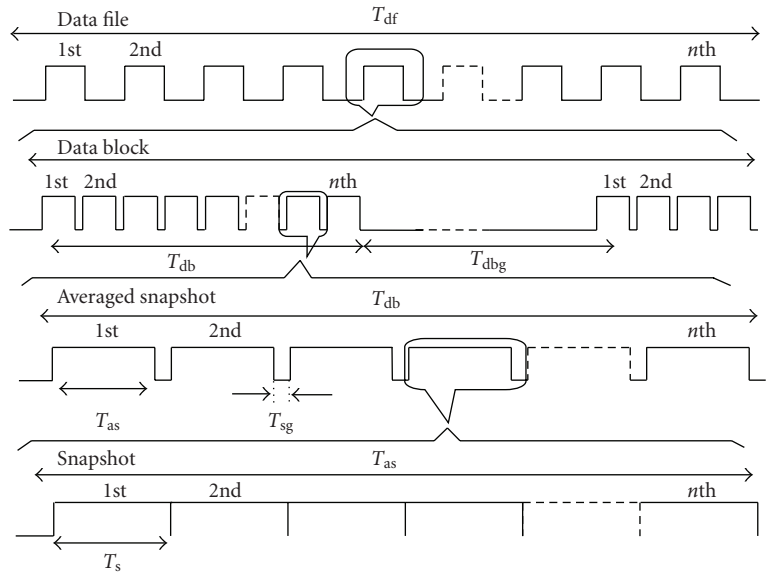

Figure 11: Data acquisition strategy for N_a averages.

Table 3: Channel sampling rates for different number of averages for 180 MHz bandwidth configuration.

N_a	Theoretical ΔSNR (dB)	T_{as} (ms)	Channel sampling rate (Hz)
0	0	0.12288	8138
2	3	0.12288	8138
4	6	0.12288	8138
8	9	0.20480	4882
16	12	0.36864	2712
32	15	0.69632	1436
64	18	1.35168	739
128	21	2.66240	375
256	24	5.38384	189
512	27	10.5267	94
1024	30	21.0125	47

4. Sounder Test and Results

Tests on the sounder highlighted a number of short comings in the software and hardware. The four areas of concern were the frequency stability of the sampling clock generated by the FPGA device on the ADC carrier card, the timing constraints of the software running on the PMC card, the data rate of the PCI bus, and the rate at which data is written to disk.

Frequency stability and the rate of data transfer to the storage device are critical to the implementation of a suitable data acquisition strategy, thus any associated problems had to be overcome. These included the addition of a new input clock for the ADC and revision of the VHDL design for the FPGA on the PMC card to improve the channel sampling rate. The following sections describe tests that were conducted, some of the issues that were identified, solutions implemented, and the performance of the whole system.

4.1. Frequency Stability of the Experimental System. High stability of all the frequency sources is critical to the real-time averaging of PRGN signals [18]. If the sources are not locked to a common phase reference, errors are introduced. Figure 12 shows measured channel transfer functions with and without the transmitter and receiver phase-locked to a common reference.

Using a frequency counter, all the FPGA derived clocks on the AWS and the ADC carrier card were measured and found to be locked to the frequency reference. However, the data sampled by the ADC was found to contain errors. These errors are not observed when the sampling clock is obtained from a dedicated source for example, signal generator. Tests revealed that the clock jitter was higher than the maximum recommended tolerance for the ADC input [20]. Figure 13 shows measurements taken with no signal applied to the input of the receiver. Errors with peak-to-peak values up to 3.25 V were obtained with the original FPGA generated clock. Since a low frequency clock from the FPGA had superior SNR and low jitter, a dedicated external clock multiplier could be used to generate the sampling clock for the ADC. Using the stable sampling clock, only the system noise with maximum peak-to-peak amplitudes of 0.005 V was present as shown in Figure 15(b). The tests were repeated with the PRGN signal connected to the input of the receiver. The results in Figure 14 show that the errors are eliminated when a stable clock is used.

4.2. Real-Time Averaging. In order to perform real-time averaging, consecutively captured snapshots must be added together and the result is divided by the number of snapshots. Since the PRGN waveform has noise-like characteristics, the tests carried out on the averaging logic were conducted using known test signals (counter). Included in the VHDL design and substituted for the ADC input to the adders, the Most Significant Bit (MSB) of the counter value was considered

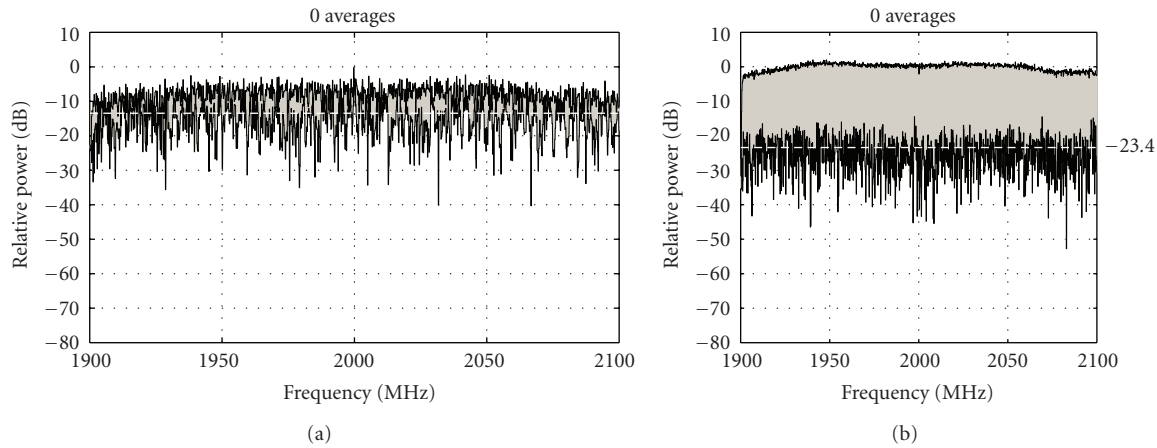

Figure 12: Measured transfer functions (a) without and (b) with the transmitter and receiver phase-locked to a common reference.

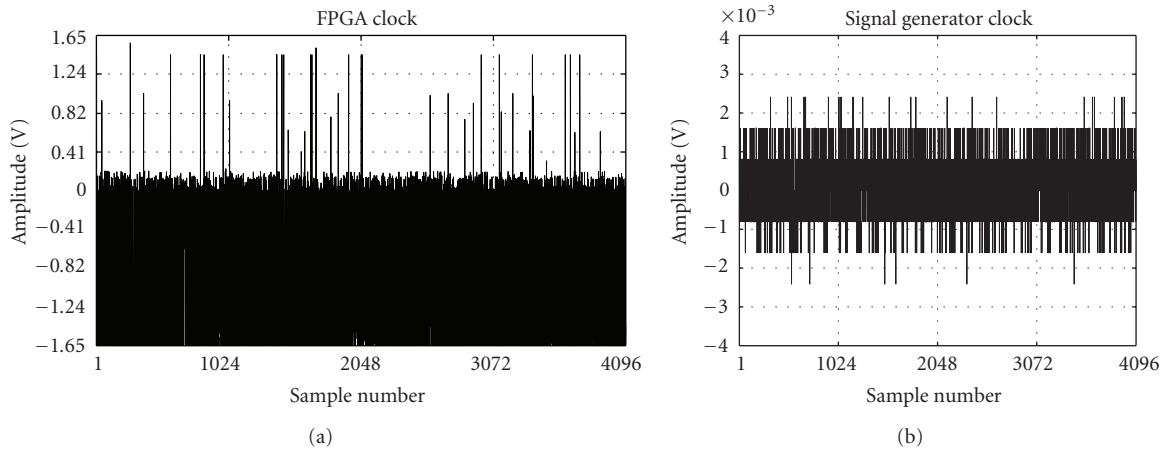

Figure 13: Data captured with no signal input using clocks from: (a) the FPGA and (b) the signal generator.

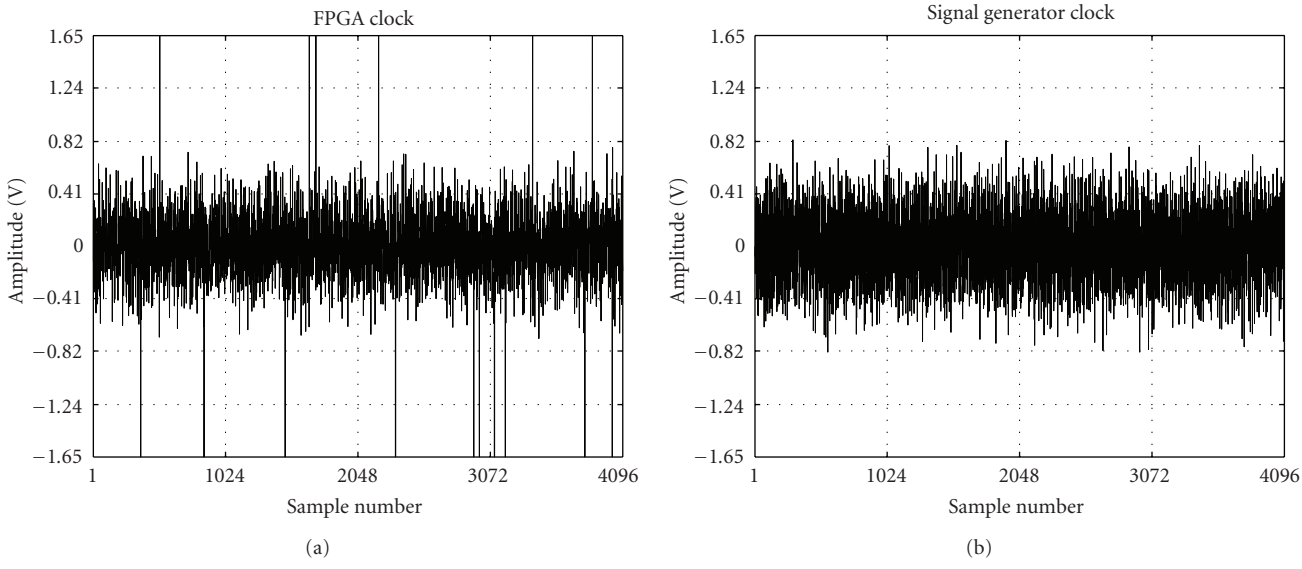

Figure 14: PRGN time domain signal captured with signal applied to ADC input with clocks from: (a) the FPGA and (b) signal generator.

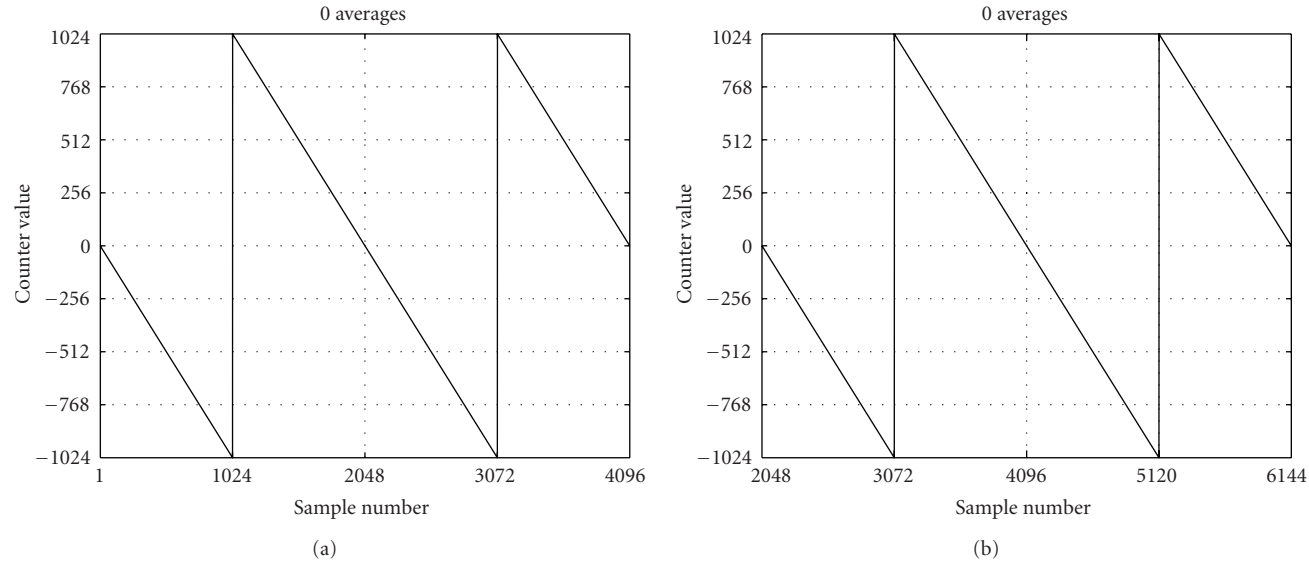

Figure 15: Averaging logic output (a) one sequence and (b) output showing transition between two sequences.

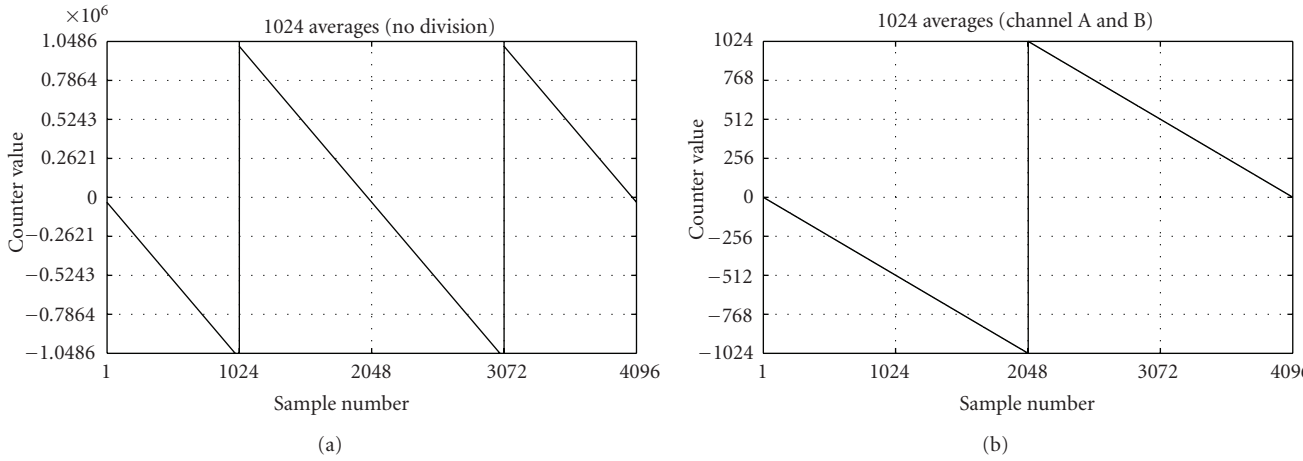

Figure 16: Averaging logic output for: (a) 1024 averages and (b) one sequnce from combined channels A and B.

as the sign bit of the data. The expected saw-tooth signal values lay between −1024 and +1023. Since the data is split into two channels, and the length of each sequence is 2048 samples long, each counter turns over twice to produce 4096 samples. This is equivalent, in length, to the PRGN sequence. Since the two channels use different clocks, they were tested separately. Figure 15(a) shows the output from the counter when no averaging was preformed. Figure 15(b) shows that accuracy is maintained across the sequence boundary which is critical for averaging.

In view of the fact that the division of the added snapshots is preformed after the set number of averages, the expected measured values that are written to file when the counters are used as the input to the adders (emulating the averaging process) are the original counter values multiplied by the number of averages. The expected output for 1024 averages is from −1048576 to +1048575. Note that all the sample bits were transferred to the computer for this test. The output from channel A after 1024 averages is shown in Figure 16(a). Test results using both data channels in an interleaving configuration, similar to when data is captured, is shown in Figure 16(b) after dividing by the number of averages. The results show that the averaging software is working as intended.

4.3. Signal to Noise Ratio. The transmitter and receiver RF units were designed to optimise the sensitivity of the receiver and minimise intermodulation products. In order to achieve this, measurement of input and output power and signal to intermodulation product ratios were evaluated at every stage in the RF chain.

All the components in a system have a noise figure and therefore generate noise that may not be band limited. The total noise power can be calculated by the integration of the

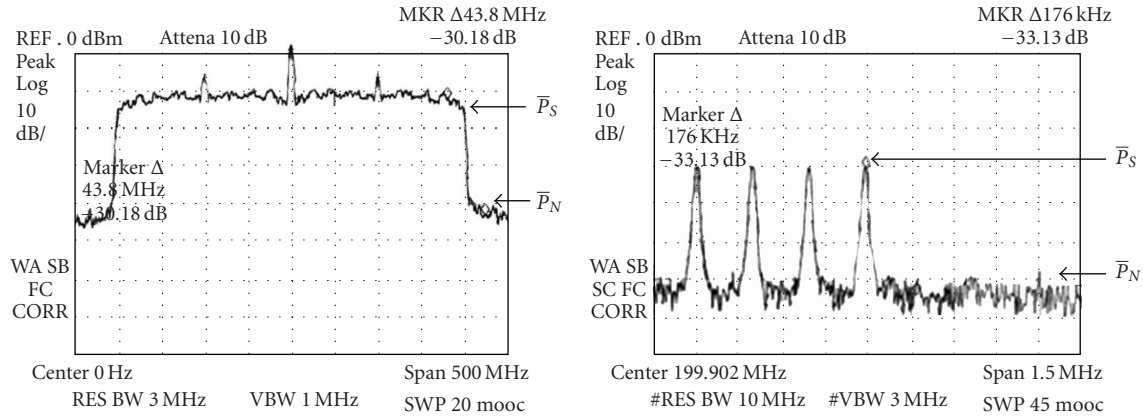

Figure 17: IF: (a) spectrum of PRGN signal with a 200 MHz bandwidth and (b) spectrum at the edge of the band.

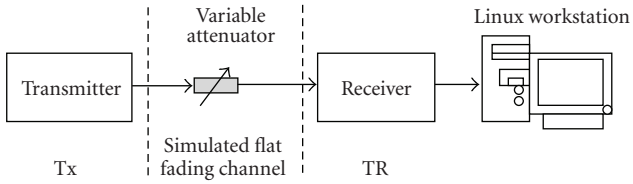

Figure 18: Block diagram of hardware for flat fading simulation.

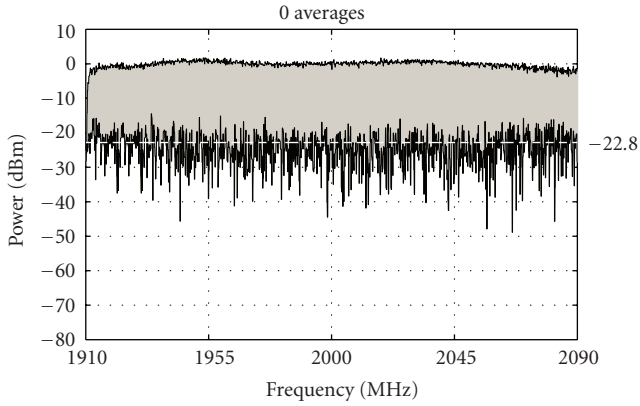

Figure 19: 180 MHz bandwidth PRGN spectrum with no averaging ($N_a = 0$).

continuous spectrum over a given bandwidth, B_W, which is taken to be the bandwidth of the last filter through which the signal plus noise is passed. The total noise power is given by

$$P_N = \int_0^{B_w} S_{N|\mathrm{RWB}=1\,\mathrm{Hz}} \partial f = S_{N|\mathrm{RWB}=1\,\mathrm{Hz}} \times B_w, \quad (6)$$

where $S_{N|\mathrm{RWB}=1\,\mathrm{Hz}}$ is the noise power spectral density at 1 Hz Resolution Bandwidth (RBW). Therefore, the SNR can be evaluated by

$$\mathrm{SNR} = 10 \log_{10}\left(\frac{P_S}{P_N}\right), \quad (7)$$

where P_S is the total signal power. Figure 17 shows the PRGN spectrum at the receiver IF and the corresponding expansion of the spectrums at the edge of the band. The mean output power, $\overline{P_S}$, across the bandwidth at IF is −9 dB. The mean noise power level, $\overline{P_N}$, is −30 dB, giving an SNR of 21 dB.

Back-to-back tests were conducted to assess the performance of the data acquisition hardware and software under simulated fading conditions. Indoor channel measurements were also conducted to evaluate the sounder. Comparisons were made between the measured improved SNR and the theoretical value.

4.4. Simulation of Flat Fading Channel. To test the performance of the system under flat fading channel conditions, 180 MHz and 200 MHz bandwidth PRGN waveforms were used. Tests were carried out with different numbers of averages, N_a, at a carrier frequency of 2 GHz. The back-to-back test configuration is shown in Figure 18.

Figure 19 shows the transfer function of the waveform measured without averaging over a 180 MHz bandwidth. The system response introduces a slight amplitude variation across the band. These were not yet calibrated out. The magnitude of the components between the spectral lines represents noise plus any intermodulation products. Since it is not possible to separate any intermodulation products from the noise, the estimated mean level represents an equivalent Signal-to-Intermodulation and Noise Ratio (SINR). The estimated SINR is 22.8 dB.

The results of measurements with 2 and 8 averages are shown in Figure 20. The improvement in SINR can be seen as the number of averages is increased from 0 (Figure 19) to 8 (Figure 20). The results are comparable to theoretical values which show that improvement in SNR is given by $10 \log N_a$. This validates the performance of the system and proves that improvement in SNR is close to the theoretical values with averaging.

To test the ability of the sounder to detect small changes in the channel, measurements were taken in indoor environment at an antenna separation of 5 m at 3 cm intervals

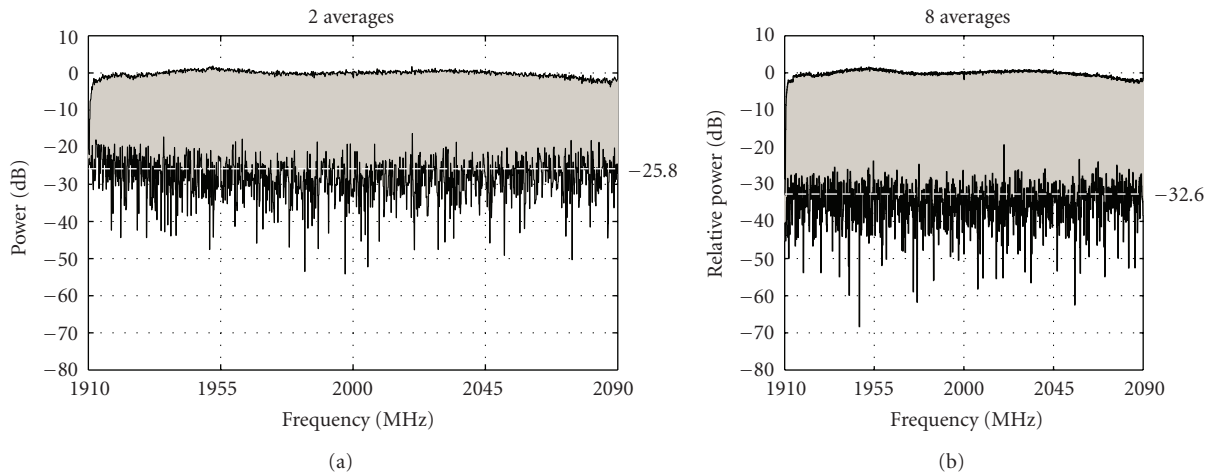

Figure 20: 180 MHz bandwidth spectrum with number of averages of (a) 2 and (b) 8 showing a 8.8 dB SNR improvement compared to 0 averages.

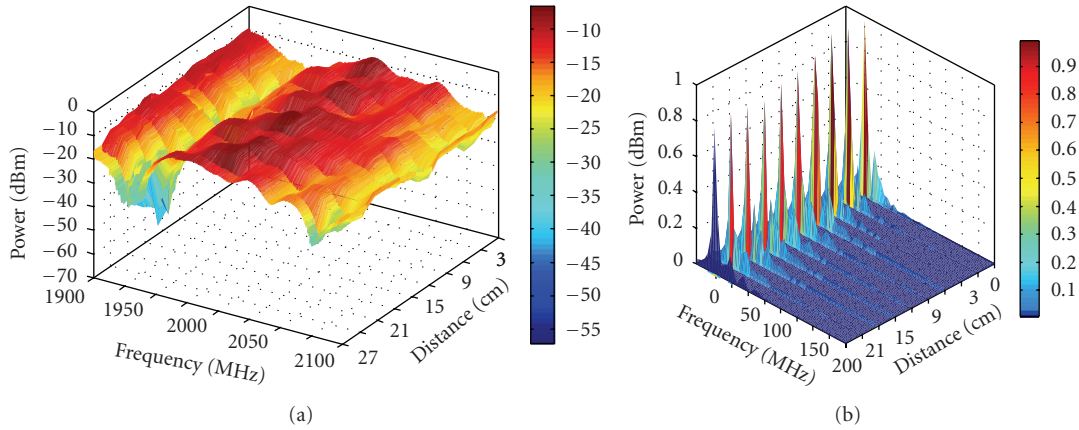

Figure 21: Small-scale variation measurement in an indoor channel; (a) channel transfer function and (b) impulse response.

over a distance of 27 cm at 2 GHz. The transfer functions and the corresponding channel impulse responses are given in Figure 21. It can be seen that the system can clearly detect the evolution of the channel response over small distances. A good understanding of small-scale indoor channel variation is key to the effective delivery of wireless high data rate services [21, 22].

5. Conclusions

The development of a compact, adaptable and low cost channel sounder with transmission bandwidths of up to 200 MHz has been presented. The sounder has been developed using FPGA technology which allows future upgrades to be achieved simply by replacing the FPGA devices with newer and faster devices. The extensive use of FPGA at both the transmitter and receiver marked a shift in sounder development from hardware specification to software. Because of the high cost of channel sounders, efforts were put into reducing the complexity of the system from hardware to software. In addition, to meet the low-cost design objective of the system and maintain low hardware complexity, simpler FPGA devices were used.

The transmitter unit is built around a dual channel arbitrary waveform synthesizer card that can generate two independent waveforms with bandwidths up to 150 MHz and 200 MHz simultaneously. This would facilitate colocation of more than one transmitter. The main challenges faced in the development of the arbitrary waveform synthesizer included difficulties with generating stable high frequency clocks to drive the digital-to-analog converters. In the receiver, the signal is sampled at an intermediary frequency for example, 100 MHz for a 200 MHz bandwidth signal. The signal is digitised using a 12-bit analog-to-digital converter with sampling speeds up to 400 MS/s. The data is transferred to an FPGA-based data processing card for real-time averaging. It is buffered before it is transferred across the PCI bus for storage on the computer hard disk. All the control signals on the sampling cards were derived from a 10 MHz input frequency reference. A robust data acquisition system has

been developed to ensure data integrity. Test results show that the real-time averaging process improves the signal-to-noise ratio inline with expected value defined by $\Delta\text{SNR} = 10\log N_a$, where N_a is the number of averages. Channel measurements over small spatial intervals of 3 cm in indoor environment have shown that the sounder performance is very high and it is capable of detecting small changes in the channel.

This sounder will be invaluable in the study of wideband channels that support current and future broadband wireless systems. The design approach has resulted in more than 60% reduction in the weight of the sounder compared to similar systems used elsewhere [23]. Channel sampling rates of 5.4 kHz over 200 MHz bandwidth have been achieved with the capability of up to 15 kHz with 100 MHz bandwidth signal transmissions. The sounder is ideally suited to the study of mobile wireless channels because of its light weight and fast channel sampling capability. The use of a faster device such as Xilinx Virtex 6 or 7 Series FPGA will boost not only the channel sampling rates but allow for more extensive real-time processing to be carried out.

References

[1] P. Kyösti, J. Meinilä, L. Hentilä et al., "WINNER II Channel Models," D1.1.2 V1.1, Information Society Technologies, November 2007.

[2] C. A. Middleton and A. Bryne, "An exploration of user-generated wireless broadband infrastructures in digital cities," *Telematics and Informatics*, vol. 28, no. 3, pp. 163–175, 2011.

[3] N. Savage, D. Ndzi, E. Vilar, and J. Austin, "Comparison of wideband indoor channel characteristics along two corridors with different wall surfaces," in *UK National USRI Symposium*, Mavern, UK, December 2001.

[4] A. G. Siamarou and M. Al-Nuaimi, "A wideband frequency-domain channel-sounding system and delay-spread measurements at the license-free 57- to 64-GHz band," *IEEE Transactions on Instrumentation and Measurement*, vol. 59, no. 3, pp. 519–526, 2010.

[5] I. Parez, S. Loredo, L. Valle, and R. P. Torres, "Experimental estimation of wideband radio channel parameters with the use of a spectrum analyzer and the Hilbert transform," *Microwave and Optical Technology Letters*, vol. 34, no. 5, pp. 393–397, 2002.

[6] J. Austin, W. P. A. Ditmar, W. K. Lam, E. Vilar, and K. W. Wan, "A spread spectrum communications channel sounder," *IEEE Transactions on Communications*, vol. 45, no. 7, pp. 840–847, 1997.

[7] A. Hewitt and E. Vilar, "Sective fading on LOS microware links: classical and spread_spectrum measurements techniques," *IEEE Transactions on Communications*, vol. 36, no. 7, pp. 789–796, 1988.

[8] Hunt Engineering, "Choosing FPGA or DSP for Your Application," 2010, http://www.hunteng.co.uk/info/fpga-or-dsp.htm.

[9] Mango DSP, September 2010, http://www.mangodsp.com/default.asp?id=11&item=24.

[10] M. Parker, "FPGA versus DSP design reliability and maintenance," November 2010, http://www.dsp-fpga.com/articles/id/?2207.

[11] D. C. M. Bilsby, R. L. Walke, and R. W. M. Smith, "Comparison of a programmable DSP and a FPGA for real-time multiscale convolution," *IEE Colloquium*, no. 197, pp. 4/1–4/5, 1998.

[12] P. Mu, M. Raulet, J.-F. Nezan, and J.-G. Cousin, "Automatic code generation for multi-microblaze system with syndex," in *Proceedings of the 15th European Signal Processing Conference (EUSIPCO '07)*, Poznañ, Poland, September 2007.

[13] P. Naraine, "Direct modulation radio hardware architectures for 3G communications systems," RF Design (Defense Electronics), February 2005, http://rfdesign.com/ar/502rfdf2.pdf.

[14] Analog Devices, "AD12401 Data Sheet," 2010, http://www.analog.com/en/analog-to-digital-converters/ad-converters/ad12401/products/product.html.

[15] "Advanced Filter Bank Technical Description," V CORP Technologies, Inc., http://www.v-corp.com/afb.htm.

[16] Alpha Data Ltd, ADM-XRC-II Xilinx Virtex-II PMC Data Sheet, Alpha Data, 2010, http://www.alpha-data.com/adm-xrc-ii.html.

[17] Technobox Inc., 64-Bit PMC-to-PCI Adapter Card Data Sheet, 2010, http://www.technobox.com/cat3673.pdf.

[18] K. Godfrey, *Perturbation Signals for System Identification*, Prentice-Hall, London, UK, 1993.

[19] Y. Lee, Y. Choi, M. Lee, and S. Ko, "Performance analysis of bit-width reduced floating-point arithmetic units in FPGAs: a case study of neural network-based face detector," *EURASIP Journal on Embedded Systems*, vol. 2009, Article ID 258921, 11 pages, 2009.

[20] Xilinx Inc., "Virtex-II CLKFX Jitter Calculator," 2010.

[21] D. Ndzi, J. Austin, and E. Vilar, "Hyper-resolution indoor channel impulse responses: multipath components and k-factors," *Electronics Letters*, vol. 35, no. 9, pp. 698–699, 1999.

[22] D. L. Ndzi, N. Savage, and B. Gremont, "Spatial and temporal variation of wideband indoor channels," *International Journal of Antennas and Propagation*, vol. 2010, Article ID 735434, 11 pages, 2010.

[23] H. Farhat, G. Grunfelder, A. Carcelen, and G. El Zein, "MIMO channel sounder at 3.5 GHz: application to WiMAX system," *Journal of Communications*, vol. 3, no. 5, pp. 23–30, 2008.